

Fakultät für Physik



**On-Surface Synthesis of One- and Two-Dimensional
Organic Nanoarchitectures: Reaction Progression,
Steric Hindrance, and a Novel Reaction Pathway**

Dissertation

von

Massimo Enrico Fritton



TECHNISCHE
UNIVERSITÄT
MÜNCHEN



Technische Universität München

Fakultät für Physik

Oskar-von-Miller Lehrstuhl für Wissenschaftskommunikation

**On-Surface Synthesis of One- and Two-Dimensional Organic
Nanoarchitectures: Reaction Progression, Steric Hindrance,
and a Novel Reaction Pathway**

Massimo Enrico Fritton

Vollständiger Abdruck der von der Fakultät für Physik der Technischen
Universität München zur Erlangung des akademischen Grades eines

Doktors der Naturwissenschaften

(Dr. rer. nat.)

genehmigten Dissertation.

Vorsitzender: Prof. Dr. Martin Zacharias

Prüfer der Dissertation:

1. Priv.-Doz. Dr. Markus Lackinger

2. Prof. Dr. Johannes Barth

Die Dissertation wurde am 23.06.2020 bei der Technischen Universität München
eingereicht und durch die Fakultät für Physik am 09.09.2020 angenommen.

I confirm that this PhD thesis is my own work and I have documented all sources and material used.

München, den.....2020,

Massimo Enrico Fritton

Abstract

In the present thesis, on-surface chemistry of functionalized aromatic molecules is investigated by state-of-the-art surface science techniques in ultra-high vacuum (UHV). More specifically, the formation of one- and two-dimensional organometallic and covalent nanostructures on metal and metal halide surfaces is studied. A decisive advantage of on-surface polymerization is that the final morphology of the nanostructure is predefined by the combination of substrate and molecular precursor. As standard tool, scanning tunneling microscopy (STM) is used to characterize the surface-supported nanoarchitectures in real space. The submolecular resolution of STM allows to identify the topology of both self-assemblies of intact molecular precursors and polymerized structures. Temperature programmed X-ray photoelectron spectroscopy (TP-XPS) measurements are used to gain insights into the progression of thermally induced on-surface Ullmann-type coupling.

In the first study, it was demonstrated that *ortho*-methyl substitution significantly improves the quality of self-assembled organometallic networks on the (111) facets of silver and copper, by high resolution STM images. Organometallic networks, where molecules are connected *via* surface adatoms, are commonly observed on Cu(111) and Ag(111) surfaces. Even though the reversibility of the carbon-metal-carbon (C-M-C) bonds enables healing of defects, topological defects in 2D networks are still observed. The organometallic networks obtained from the *ortho*-methyl substituted molecule were compared with those of the unsubstituted analogue on Cu(111) and Ag(111) surfaces. Statistical analysis of defects showed marked differences in network quality, i.e. strongly varying amounts of topological defects in the systems under investigation. This could be made plausible by calculating the energetic cost for bond angle (C-M-C) distortions associated with steric hindrance, complemented by density functional theory (DFT)-optimized adsorption geometries.

In the second study, the complementary nature of XPS and STM was used to comparatively study the elementary steps of surface-assisted Ullmann coupling and its thermal progression on Ag(111) and Au(111) surfaces, respectively. From TP-XPS measurements, we learned that, besides the known differences in onset temperatures, also

the progression of thermally induced dehalogenation is vastly different on the two surfaces. Debromination occurred in a narrow temperature window on Ag(111), whereas on Au(111), a more gradual debromination over an extended temperature range was observed. DFT and experiments concur in explaining the observed differences by first-order reaction kinetics on Ag(111) and a thermodynamically controlled reaction on Au(111).

In the end, the principle of a radical deposition source (RDS), i.e. an instrument that allows to directly dose radicals onto the surface, is introduced and discussed. As a model compound for first tests, the highly relevant 6,11-Diiodo-1,2,3,4-tetraphenyltriphenylene (DITTP) precursor, for chevron-type graphene nanoribbons (GNRs), was used. The basic idea of the RDS was to activate precursors spatially separated from the target substrate, rendering the catalytic activity of the substrate redundant for dehalogenation. Experiments were carried out on iodine passivated Au(111) and Ag(111) surfaces to validate the functionality of the RDS on inert substrates.

Zusammenfassung

In der vorliegenden Arbeit werden chemische Reaktionen von adsorbierten aromatischen Molekülen mit hochmodernen Techniken der Oberflächenwissenschaft im Ultrahochvakuum untersucht. Präziser formuliert, die Synthese von ein- und zweidimensionalen organometallischen und kovalenten Nanostrukturen wird auf Metall- und iodierten Metalloberflächen untersucht. Ein entscheidender Vorteil der Oberflächensynthese ist, dass die finale Morphologie der Nanostruktur durch die Kombination von Substrat und Vorläufermolekül vordefiniert wird. Als Standardmethode wird die Rastertunnelmikroskopie (STM) verwendet, um die vom Substrat stabilisierten Nanoarchitekturen im Realraum zu charakterisieren. Die submolekulare Auflösung des STM erlaubt es, Selbstassemblierungen von Vorläufermolekülen sowie polymerisierte Strukturen zu identifizieren und zu charakterisieren. Temperaturprogrammierte Röntgenphotoelektronenspektroskopie (TP-XPS) wird verwendet, um Einblicke in den Verlauf von thermisch induzierter Ullmann-Kupplung auf Oberflächen zu gewinnen.

In der ersten Studie wurde mittels STM gezeigt, dass eine Methyl-Substituierung in *ortho*-Stellung die Qualität von selbstassemblierten organometallischen Netzwerken auf den (111)-Facetten von Silber- und Kupfer-Einkristallen signifikant erhöht. Organometallische Netzwerke, in welchen Moleküle über ein Oberflächenatom verknüpft sind, werden üblicherweise auf Cu(111)- und Ag(111)-Oberflächen beobachtet. Trotz der Möglichkeit topologische Fehlstellungen aufgrund der Bindungsreversibilität der Kohlenstoff-Metall-Kohlenstoff (C-M-C)-Bindung zu heilen, werden solche dennoch beobachtet. Die mit dem *ortho*-Methyl-substituierten Molekül synthetisierten organometallischen Netzwerke wurden mit Netzwerken von dem nicht substituierten Analogen auf Cu(111) und Ag(111) verglichen. Eine statistische Analyse der Defekte zeigte signifikante Unterschiede in der Netzwerkqualität, das heißt stark schwankende Anteile an topologischen Defekten. Dies konnte mittels Berechnungen des energetischen Aufwandes für Bindungswinkelabweichungen aufgrund sterischer Hinderung plausibel gemacht werden. Ergänzt wurde dies durch Dichtefunktionaltheorie (DFT)-optimierter Adsorptionsgeometrien.

In der zweiten Studie wurde die komplementäre Natur von XPS und STM genutzt, um die elementaren Reaktionsschritte der oberflächenunterstützten Ullmann-Kupplung und deren Verlauf mit der Temperatur auf Ag(111)- und Au(111)-Oberflächen vergleichend zu untersuchen. Von den TP-XPS Messungen auf beiden Metalloberflächen wissen wir, dass neben den bekannten Onsettemperaturunterschieden auch der Verlauf der thermisch induzierten Dehalogenierung äußerst unterschiedlich abläuft. Die Debromierung vollzog sich auf Ag(111) innerhalb eines schmalen Temperaturfensters, wohingegen auf Au(111) eine graduelle Debromierung über einen ausgedehnten Temperaturbereich beobachtet werden konnte. Übereinstimmend erklären DFT und Experimente die beobachteten Unterschiede durch Reaktionskinetik erster Ordnung auf Ag(111) und einer thermodynamisch kontrollierten Reaktion auf Au(111).

Am Ende wird das Prinzip einer Radikalabscheidungsquelle (RDS), also einem Gerät, mittels dem Radikale direkt auf die Oberfläche aufgebracht werden können, eingeführt und erklärt. Als Modellsystem für erste Versuche, wurde das höchst relevante 6,11-Diiodo-1,2,3,4-tetraphenyltriphenylene Vorläufermolekül verwendet, welches chevronartige Graphene Nanoribbons (GNRs) formt. Die Grundidee der RDS war es, die Vorläufermoleküle räumlich getrennt vom Zielsubstrat zu aktivieren. Das macht die katalytische Aktivität des Substrats für die Dehalogenierung überflüssig. Experimente wurden auf Iod passivierten Au(111)- und Ag(111)-Oberflächen durchgeführt, um die Funktionalität auf inerten Substraten zu bestätigen.

Contents

Abstract	i
Zusammenfassung	iii
1 Introduction	1
2 Techniques to study surface-supported nanoarchitectures	5
2.1 Scanning tunneling microscopy	5
2.1.1 Overview.....	5
2.1.2 Theoretical principle	6
2.1.3 Experimental setup UHV-STM	10
2.1.4 Sample and tip preparation in UHV	11
2.1.5 Benefits and limitations of STM.....	12
2.2 X-ray Photoelectron Spectroscopy	15
2.2.1 Overview.....	15
2.2.2 Theoretical principle	16
2.2.3 Surface sensitivity.....	18
2.2.4 Characteristics of XP spectra	19
2.2.5 Spin-orbit splitting	21
2.2.6 FWHM of XPS peaks	23
2.2.7 Chemical shifts	24
2.2.8 Synchrotron-based XPS.....	26
2.2.9 Benefits and limitations of XPS.....	30
3 Bottom-up synthesis of carbon-based nanoarchitectures	33
3.1 The role of the surface	34
3.2 On-surface Ullmann coupling	36
3.3 Molecule-surface interactions	42
3.4 Thermodynamically versus kinetically controlled processes	45
4 On-surface synthesis of two-dimensional organometallic networks	51
4.1 Abstract.....	52

4.2 Introduction	52
4.3 Results and Discussion	53
4.4 Conclusion	64
4.5 Experimental details	65
5 On-surface synthesis of two-dimensional polyphenylene networks	67
5.1 Abstract.....	68
5.2 Introduction	69
5.3 Results and Discussion	71
5.4 Conclusion	87
5.5 Experimental details	89
6 On-surface synthesis of chevron-type graphene nanoribbons <i>via</i> direct deposition of radicals.....	93
6.1 Introduction	94
6.2 Basic principle of the RDS	96
6.3 Graphene nanoribbons	98
6.4 Results and Discussion	99
6.5 Conclusion and Outlook	113
7 Conclusion and Outlook	117
Appendix A.....	123
Appendix B.....	131
Appendix C.....	145
List of Abbreviations	147
List of Figures.....	149
References.....	153
Publications.....	173
Curriculum Vitae	175
Acknowledgments.....	177

Chapter 1

Introduction

The pioneering work of Grill and co-workers in 2007 can be regarded as the origin of the on-surface synthesis research field.¹ This rapidly developing field of research aims at creating new covalently bonded organic materials by chemical coupling reactions on surfaces. For this approach, the well-defined surfaces are particularly important for both the confinement of the molecular precursors in 2D and for activating chemical reactions. The on-surface synthesis approach led to the emergence of many new material classes like molecular wires, graphene nanoribbons (GNRs), macrocycles, nanographenes, and porous networks by means of various coupling reactions.²⁻⁴ Hitherto well established on-surface reaction mechanisms are Ullmann coupling, Glaser coupling, condensation, and dehydrogenation reactions.⁵⁻⁷ All these reactions aim at creating atomically precise carbon-based nanostructures. These feature promising physical properties that are strongly related to their shape and chemical functionalization.^{8,9} Ullmann-type coupling or, more generally, dehalogenative coupling is the most reliable and widespread reaction among the on-surface synthesis approaches. Thereby, haloarenes adsorbed onto metal substrates split off their halogen substituents by virtue of the reactive surface. The recombination of the activated species leads to the formation of new C-C bonds. A substantial benefit of this reaction is the control of dimensionality and topology of the polymer by virtue of the halogen substitution pattern of the molecular precursors.

The most important inspiration for the creation of tailored 2D materials by far arose from the experimental discovery of graphene in 2004, which was, until then, predicted to be thermodynamically unstable.¹⁰ Geim and Novoselov were awarded the Nobel prize in physics in 2010 for this discovery and the physical properties of graphene have been intensely investigated since.¹¹ Particularly noteworthy are its outstanding high thermal and electrical conductivity, the extremely high tensile strength, and the light absorbing properties that a single layer of graphite features.¹² Nevertheless, the zero band gap of graphene hampers most technological applications in electronics. Various attempts have

been made to overcome this problem by substitutional doping (boron or nitrogen), substrate-induced band gap opening, and quantum confinement.¹³⁻¹⁶ The most prevalent examples for confinement-induced band gap opening are GNRs, first reported by top-down approaches.^{17, 18} However, the lack of atomic control of these lithography-based GNRs limits their scope of applicability. Since Cai et al. reported on the formation of atomically precise GNRs by means of a bottom-up approach in 2010, tremendous interest has arisen in this promising class of materials.¹⁹ It is well known that atomically precise GNRs have distinct electronic properties by virtue of their width and edge structure.²⁰⁻²² Applying the bottom-up approach, the choice of molecular precursor predetermines the width and the edge structure of the synthesized GNRs, which opens up the possibility of band gap engineering by modification of the monomeric units.²³ GNRs now represent the most studied material class in the on-surface synthesis research field.

In chapter six, we report on the formation of chevron type GNRs by means of a radical deposition source (RDS). The RDS is a conventional Knudsen cell complemented with a device allowing to thermally cleave the carbon halogen bond of haloarenes before impinging on the surface. The focus of this study is on advancing the synthesis conditions of the GNRs by spatially separating dehalogenation of the molecular precursors from on-surface recombination of activated sites. In this respect, the surface confines the molecules in 2D and the catalytic activity of the substrate is only needed for the second reaction step of GNR formation, i.e. the cyclodehydrogenation (CDH) reaction. We consider this a possible way to improve future on-surface synthesis conditions of GNRs or other 1- or 2D covalent organic nanostructures as compared to conventional reaction schemes, which are in most cases restricted to reactive surfaces.

A strategy to obtain 2D carbon-based materials with non-zero bandgap is the bottom-up synthesis of covalently linked nanostructures. Therefore, planar conjugated organic precursor molecules adsorbed on defined substrates are connected *via* intermolecular coupling reactions. Accordingly, the atomic and electric structure and functionality of the formed network strongly depends on the design of the molecular precursor. There is a large variety of conceivable applications for covalent 2D nanoarchitectures like molecular electronics, photovoltaics, photo catalysis, and membranes with selective permeability.²⁴⁻²⁷ However, for most potential applications, the nanostructures need to have tunable electronic properties, high mechanical stability, precise physical dimensions with long range order, and a low defect density. The first two requirements can be

fulfilled by covalent coupling of suited monomers, while the last two requirements remain highly demanding thus far.

Chapter four and five aim at synthesizing 2D networks by a bottom-up approach connecting triply brominated precursor molecules *via* an Ullmann-type reaction on the 111-facets of the coinage metals. Despite the seeming straightforwardness of this reaction, topological defects in 2D networks are commonly observed in on-surface synthesis.²⁸⁻³¹ Our approach to tackle the problem of poor network quality is to gain a detailed insight into the thermal progression of on-surface Ullmann coupling on the two most important substrates, i.e. Au(111) and Ag(111). Onset temperatures of reactions and their kinetic progression, in particular, are a central issue of chapter five. These newly found insights could be used to advance prospective synthesis conditions.

Organometallic networks based on C-M-C bonds, usually observed on Ag(111) and Cu(111) surfaces, can be intermediates before a conversion into covalent networks at elevated temperatures becomes feasible. In contrast to covalent bonds, organometallic bonds are reversible, therefore mild annealing can help to heal defects. Hence, a promising concept to produce defect free long-range ordered covalent nanostructures would be an isotopological conversion of high quality organometallic into covalent networks. However, even after equilibration at temperatures, where C-M-C bonds become reversible, most organometallic networks still feature topological defects.^{30, 32} In chapter four, we propose a simple method that inhibits topological defects in organometallic networks on Cu(111) and drastically reduces defects on Ag(111). This is achieved by imposing steric hindrance, which reduces the C-M-C bond angle flexibility by means of an *ortho*-methyl substitution.

The one- and two-dimensional carbon-based nanoarchitectures presented in this thesis adsorbed on defined metal and metal-halide surfaces have usually spatial extensions below 100 nm. Hence, STM as local real space technique is ideally suited for resolving both the topology and bond configurations of the molecules under investigation. To gain chemical information of the surface-supported nanostructures over an extended temperature range, TP-XPS measurements were performed. These TP-XPS measurements were complemented with DFT calculations to support the experimental findings, and to explain the observed surface-dependent differences in network quality on Ag(111) versus Au(111). For a more comprehensive understanding and mechanistic insights into formation of surface-supported nanostructures, a brief overview about the

role of the substrate, adsorption and desorption, molecule-surface interactions, and the applied reaction mechanism i.e. Ullmann-type coupling is given in chapters 3.1 - 3.3. Moreover, chapter 3.4 aims at introducing the basic concepts of kinetically versus thermodynamically controlled processes. In the following chapter the experimental techniques used in this thesis will be explained in detail.

Chapter 2

Techniques to study surface-supported nanoarchitectures

On the one hand, we have the challenge to invent novel or improve existing strategies for the on-surface synthesis of atomically precise carbon-based nanoarchitectures. On the other hand, we need analytical tools that allow us to comprehensively characterize these formed structures. To achieve this, the combination of true local imaging techniques, with space-averaging surface sensitive techniques, is a frequently applied approach.^{5,33} In this respect, STM with a resolution down to the atomic scale, complemented with X-ray photoelectron spectroscopy (XPS) yielding detailed chemical information on the topmost layers, is ideally suited for a profound characterization of the surface-supported nanostructures. In the following, both techniques are introduced, while, in chapter 4-6, nanostructures and their characterization with these techniques will be presented and discussed.

2.1 Scanning tunneling microscopy

2.1.1 Overview

The family of scanning probe microscopy (SPM) encloses techniques where images are recorded by scanning over a sample by means of a tip. These images can include various information. In 1981, the STM and a few years later the atomic force microscope (AFM) were invented, and they represent the two most important techniques in the large and growing field of SPM.^{34, 35} In 1986, Gerd Binnig and Heinrich Rohrer were honored with the Nobel Prize in physics for the invention of the STM. STM and AFM both record topographic maps of a defined surface area by scanning and simultaneous maintaining

the tunneling current or force shift on the cantilever constant, respectively. The frequency shift of the cantilever is only one example of a multitude of static and dynamic interactions used for image acquisition in AFM.^{36,37} Although, the interaction mechanism of the sample and the tip are completely different for the two techniques, STM as well as AFM acquire their images by sampling over the surface. Both methods use atomically sharp tips as probe to characterize the sample of interest. In addition to the above mentioned topographic maps STM as well as AFM can be used to create nanostructures by manipulation on surfaces.^{38,39} Furthermore, mechanical properties of the surface and adsorbates which are inaccessible with STM measurements can be probed with an AFM.^{40,41} As this thesis comprises no AFM data the focus will be on STM in the following. STM is a very powerful technique that enables real-space-imaging with a spatial resolution in the sub nanometer range. The obtained images, also called topographic maps or in short topographs, can visualize the substrates down to single atoms and molecules adsorbed on the surface. Compared with other surface sensitive methods based on diffraction there is no need for translational symmetry. Therefore, only two requirements exist for the examined sample: the specimen has to be electrically conducting and flat. In the novel research field of on-surface synthesis, the STM is an inevitable technique for studying nanostructures. The milestones of recent on-surface reactions were always accompanied by STM images atomically resolving the structures, like no other technique is capable of.^{1,19,42}

2.1.2 Theoretical principle

This technique takes advantage of the quantum mechanical tunneling effect. The tunneling effect describes the possibility of a particle to “tunnel” through an energy barrier larger than its own total energy, with a certain probability. Two important examples where tunneling plays an important role in nature are: the α -decay where a helium nucleus escapes from a heavy nucleus⁴³ and the thermonuclear fusion in stars.⁴⁴ Modern solid state data storage is also based on the tunneling effect used to encode a binary value.⁴⁵

As classical physics cannot explain this phenomenon, an alternative approach has to be considered for understanding this effect. This is the point where only a quantum

mechanical attempt, treating a completely different length scale compared to classical physics, is needed to explain the tunneling effect. According to quantum mechanics, very small particles like molecules or electrons can behave like waves, proved by the interference pattern of the famous double slit experiment. In 1961 this experiment was performed with electrons for the first time by C. Jönsson.⁴⁶ In the following years it was shown that this phenomenon can be observed for larger molecules like bucky balls,⁴⁷ and recently even for functionalized oligoporphyrine molecules consisting of 2000 atoms.⁴⁸ When a metallic atomically sharp tip is brought very close ($< 1\text{nm}$) to a flat sample, the wave functions of their electrons can overlap, allowing electrons to tunnel between. Applying an external voltage between tip and sample leads to a measurable current between occupied and unoccupied states. This current is an indirect measure for the size of the gap, separating tip and sample. By changing the polarity of the applied voltage the flow direction of the electrons is reversed, meaning the electrons of the tip can tunnel into the sample or vice versa. A simple way of describing the tunneling process is obtained by assuming a one-dimensional barrier. This simplification allows to explain the basic dependencies, and can further be assumed as the best understood way in describing the phenomenon. Figure 2.1 shows a schematic sketch of a one-dimensional tunnel barrier.

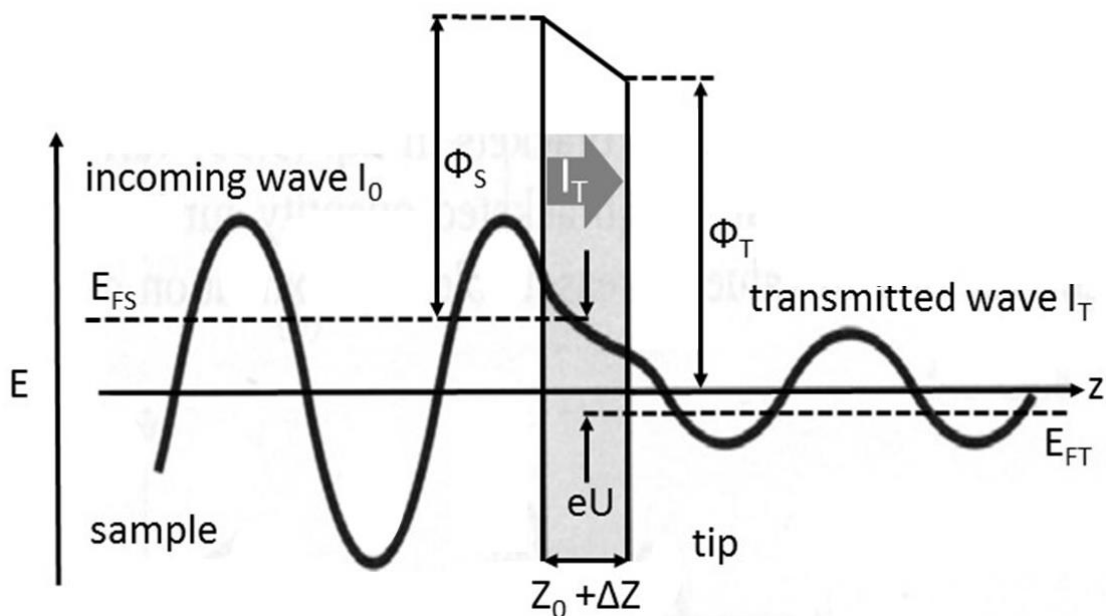


Figure 2. 1: Tunneling effect at a one-dimensional barrier including: incoming I_0 and transmitted wave I_T , Fermi level of sample E_{FS} and tip E_{FT} , potential barrier (width ΔZ and heights Φ_S Φ_T), and applied tunneling voltage U , adapted from Refs.^{49, 50}

Due to the occurrence of reflection as well as transmission of a part of the electrons, the amplitude of the transmitted wave after the barrier is reduced but not zero for barrier widths ΔZ in the Å range. The transmission (t) is defined as:

$$t = |I_T|^2 / |I_0|^2 \quad (2.1)$$

With I_T and I_0 as the amplitudes of the transmitted and incoming waves, respectively. The mean potential barrier φ for an electron with energy E can be written as:

$$\varphi = \frac{\Phi_T + \Phi_S}{2} + \frac{eU}{2} - E = \Phi + \frac{eU}{2} - E \quad (2.2)$$

In this simple model Φ is the average work function of tip and sample, while eU defines the energy range of electrons that can contribute to the tunneling current. This energy range is defined by E_{FT} and E_{FS} . The probability for tunneling of an electron through a trapezoid shaped barrier is given by the following expression:⁵⁰

$$T(E, U, \Phi, z_0 + \Delta z) = \exp\left(-2\sqrt{\frac{2m}{\hbar^2}} \sqrt{\Phi + \frac{eU}{2} - E} (z_0 + \Delta z)\right) \quad (2.3)$$

With m as the rest mass of the electron, \hbar as the reduced Planck constant and U as the applied voltage. Within the potential barrier the wave function decays exponentially. The decay constant (α) is defined as:

$$\alpha^2 = \frac{2m}{\hbar^2} \varphi \quad (2.4)$$

With the assumption of small voltages ($|U| \ll \Phi$) and small electron energies ($E \approx E_F = 0$), equation 2.3 can now be rewritten only with α including φ and the width of the tunneling barrier $z = z_0 + \Delta z$:⁵⁰

$$\begin{aligned} I_T &= I_0 e^{(-2\alpha z)} \\ I(\Delta z) &= I(Z_0) e^{(-2\alpha \Delta z)} \end{aligned} \quad (2.5)$$

Obviously, the tunneling current strongly varies with tip-sample distance. Assuming $\Phi = 5\text{eV}$, which lies close to the work function of Cu(111),⁵⁰ leads to α values of about 23 nm^{-1} . Hence, increasing the tip-sample distance by 1 \AA , leads to a decrease of the tunneling current by approximately one order of magnitude.^{50, 51} The above discussed exponential decay of the tunneling current with increasing the barrier width according to equation 2.5 makes the STM extremely sensitive to variations in the tip-sample distance. This relationship is the reason for the high vertical resolution of the STM. However, the tip-sample distance is not the only factor contributing to the tunneling current. Additionally, the applied voltage, the work functions of the materials, and the local density of states (LDOS) near the Fermi level affect the measured current. The LDOS is essential for the contrast in STM. For instance, two structures with equal geometric height can have different apparent heights in STM images, due to variations in their LDOS. Hence, every point in a topographic map is a convolution of electronic and geometric properties. Conventionally, brighter colors in an STM image correspond to higher appearing structures. The STM data presented in this thesis was used to characterize formation of one- and two-dimensional molecular structures on surfaces. However, the focus lay on the lateral extension of the nanostructures. Therefore, the precise details of contrast formation and the exact height of the adsorbed structures was not the main interest for characterizing the nanostructures. The following two sections aim at introducing the basic experimental setups of the two STMs used in this thesis as well as the preparation of samples and tips, respectively.

2.1.3 Experimental setup UHV-STM

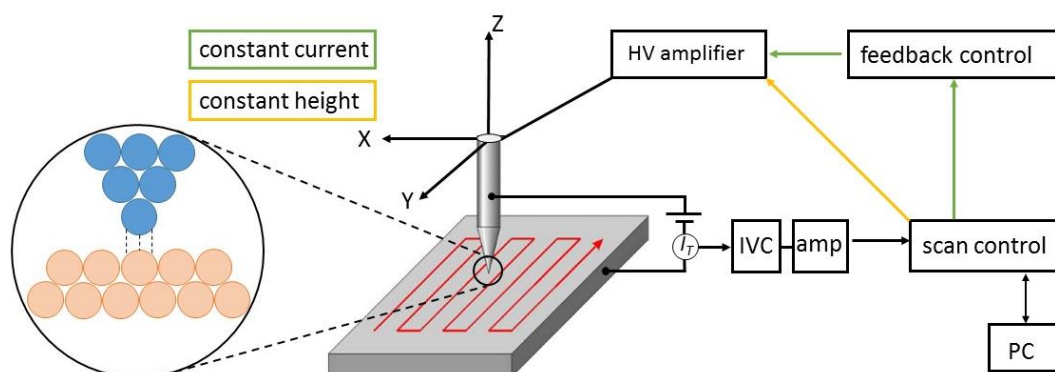


Figure 2. 2: Principle of a STM operating in constant height (-) or constant current (-) mode. The main components are a current voltage converter (IVC), a high voltage (HV) amplifier, a scan control, a feedback control, and a personal computer (PC).

STM measurements can be performed in two different modes: namely the constant current-, and constant height-mode. Applying the constant current mode, the different z -positions, for maintaining the current constant, yield the images. This is in contrast to the constant height mode, where the tip only moves in a parallel plane. Hence, variations in tunneling current between tip and sample are recorded and form the image. Data presented in this work was exclusively acquired using the constant current mode, whereby the feedback loop aims to keep the current at a preset value. Therefore, the height adjustment from the feedback loop is recorded. Differences in the z -position are displayed by a color scale. The constant height mode enables fast scanning as no adjustments of the tip are required. However, the risk of crashing a tip is significantly higher for this operation mode. Therefore, only samples with very low topography variations can be measured applying the constant height mode. Changes in the z -position as well as the scanning movement (x , y) are accomplished with piezoelectric actuators. These are also used for coarse and fine approach. The scanning movement (x , y , z), with sub nanometer accuracy, is realized with a piezo tube, whereas a multilayer piezo is used for approaching the tip to the surface, by means of the stick slip mechanism. Calibration of the scanner in the x - and y -direction was done by atomically resolving single crystal surfaces, whereas z calibration was done by scanning over several step edges with known height and taking the mean value. Gwyddion 5.0 was used for data processing and

visualization. Images were in most cases levelled, mean value filtered, and the color range was optimized for the regions of interest.

To reduce noise during STM-measurements a multistage damping system is used. The whole chamber is resting on an optical table and can be isolated from external vibrations by a pneumatic damping. As the UHV-chamber also comprises moving parts generating noise, like the turbomolecular pump, the STM has to be decoupled from the rest of the system. This is done by spring suspension of the STM. Advantageously, all mechanical pumps can be turned off to minimize noise. Moreover, a symmetric arrangement of magnets damps by the induction of eddy currents. Nevertheless, some low-frequency vibrations will remain, therefore the eigenfrequency of the scanning unit should be as high as possible.⁵¹ Commonly this is achieved by designing a small and stiff scanning unit. Furthermore, the tip as well as the sample need to be securely fixed to avoid the stimulation of oscillations. In summary, acquiring overview as well as atomically resolved high resolution STM images was appropriate to characterize the systems under investigation.

2.1.4 Sample and tip preparation in UHV

The base pressure of the UHV systems for STM experiments was around 2×10^{-10} mbar, avoiding contamination of the (111) single crystals (Au, Ag, Cu) in the typical time range of our experiments. This was achieved by the combination of a fore pump (oil free), a turbomolecular pump, an ion pump, and bakeout of the whole UHV chamber at temperatures $> 100^\circ\text{C}$ for at least 2 days.

Additionally, a load lock with a magnetic linear rotary transfer enabled inserting new tips and samples without the need of venting the main UHV chamber. Newly inserted tips and samples can be stored in the carousel or directly transferred to the heater. Furthermore, the load lock was equipped with a Knudsen cell, enabling the deposition of molecules on the surface, and a leak valve filled with iodine. The Knudsen cells used were all home built after Gutzler et al.,⁵² but with small modifications to match the requirements of the respective port. All UHV-chambers are equipped with quadrupole mass analyzers that may be needed for a leak test, or to identify contaminants. The ion gun used for sample preparation was a Specs IQE 11/35 together with a Specs IS 2000 A

control unit, while the tip sputtering was done with a home built system. Pressure measurement was done with an ionization gauge in combination with a Granville-Phillips Series 307 controller. The UHV components briefly mentioned here were principally similar for the XPS measurements, differing only due to special demands of the synchrotron and end station. Therefore, they will not be considered again in chapter 2.2.8. Cleaning of the crystals was performed by cycles of Ar⁺ sputtering and annealing to 500°C. The tungsten tips were prepared by a two-step electrochemical etching protocol in KOH solution. In the first step, a tungsten wire ($\varnothing = 0,5$ mm) is dipped into KOH solution and a AC voltage is applied until the forming tip loses contact to the etchant. The second step, monitored with a light microscope, only treats the apex by short DC voltage pulses, etching only the part wetted by the solution inside a small platinum loop. This procedure worked reliably, yielding high quality tips. As tungsten oxidizes under ambient conditions, the tips have to be prepared in the UHV chamber before measuring. The oxide was removed either thermally by e-beam annealing, taking advantage of the high volatility of WO₂,⁴⁹ or by Ar⁺ sputtering. Therefore, an acceleration voltage of 1.5 kV and a counter voltage of 150 V at the tip was used to remove the oxide layer and sharpening the tip.⁵³ Sputtering of the tips worked more reliably than heating, additionally allowing to resharpen blunt tips after mechanical contact with the substrate, in many cases. The next section aims to give a brief view on the possibilities and limitations of STM experiments.

2.1.5 Benefits and limitations of STM

A main advantage of STM measurements is that non-periodic structures like irregular networks, impurities, step edges, randomly adsorbed or reacted molecules, can be probed locally with atomic resolution. This feature was exploited in chapter four where the pore dimensionality of organometallic networks was comparatively examined on copper and silver surfaces. Also, for the elucidation of surface reconstructions, the STM as a truly local technique is perfectly suited, as the discovery of the herringbone reconstruction on the Au(111) surface has demonstrated.^{54, 55} As no lenses are used, problems due to aberration are excluded that can occur in light- and electron microscopes. Additionally,

the electrons in STM have comparatively small energies of a few eV, smaller than typical energies of chemical bonds, therefore allowing a non-destructive imaging of the sample.⁵¹ STM has a wide range of application as it is possible to measure in UHV as well as under ambient conditions. For the latter the experimental setup can be quite simple, further increasing the number of possible users. The temperature range for UHV STM measurements beginning close to absolute zero to more than 1000 K makes this technique extremely versatile to different branches of surface science. Recently Ochs et al. developed an immersion-STM for long term measurements in solution that allows to gain insights into kinetics and thermodynamics of supramolecular self-assembly up to 100°C.⁵⁶ The possibility of so called video or fast STM measurements is an important improvement for the direct monitoring of reactions proceeding on surfaces first reported by Ludwig et al. in 1992 with at least 20 frames s⁻¹.⁵⁷ A recent video STM study demonstrated the possibility of monitoring an up to that point unknown diffusion pathway of a fully CO covered Ru(0001) surface.⁵⁸ Additionally, Scanning Tunneling Spectroscopy (STS), can be performed with an STM, by placing the tip stably above the surface while measuring the current as a function of applied bias voltage. This technique provides information on the local electronic structure of the sample with a high spatial resolution. But, as for this technique the feedback loop has to be turned off in most cases, it is necessary to have a very stable tunneling junction, which is usually achieved by cooling with liquid helium. Furthermore, the STM tip can be used to laterally manipulate single atoms or molecules adsorbed on surfaces.^{59, 60} The STM also stimulates interdisciplinary research, as for instance the liaison between surface science and organic chemistry⁶¹ demonstrated by numerous collaborations.^{30, 62} This is just a small excerpt of advantages and possibilities of STM measurements, but also some of the limitations have to be mentioned here.

When performing UHV-STM measurements one always has to keep in mind that only the vacuum tails of the surface wave functions are probed lacking chemical information. Hence, in many cases additional analytical techniques, providing subsurface and chemically specific information are needed.⁵¹ Additionally, the convolution of topographic and electronic information can lead to nontrivial interpretation of STM images. Examples for this are chemisorbed atomic oxygen on a Pt(111) surface occurring as 30-40 pm deep depressions,⁶³ or organometallic and covalent networks appearing as

depressions in STM images of chapter four (cf., Figures 4.1 (b), (c), 4.2 (d), and 4.5 (a)) and five (cf., Figures 5.8 (e) and (f)), respectively.

Furthermore, STM measurements are not suitable for determining lattice constants with high precision, as piezo creep and thermal drift are never ruled out completely. The small sample area probed, normally not reaching a square micron, is often not sufficient to provide average information of the sample of interest. To overcome this problem, it is common practice to take several images of different areas. But this can be accompanied by tedious statistical analysis, like the evaluation of pore geometry in chapter four. Moreover, it is advantageous to employ complementary space averaging techniques like LEED or XPS to support the STM data. Finally, noise can cause difficulties during measuring originating from multiple sources like: mechanical noise from pumps, oscillation of the building or any other moving part, but also electronic noise from electronic control units.

All images presented in this theses were recorded with home built UHV STMs. Compared to ambient STMs, there are two major advantages of working under UHV-conditions. First, it is not necessary to dissolve the molecules, which can lead to difficulties in determining the influence of the solvent on the self-assembly. For instance, the choice of solvent and the used concentration of the molecule have shown to induce formation of different polymorphs.^{64, 65} Second, the possibility to work on reactive surfaces, i.e. catalytically active substrates, is essential for most of the existing on-surface synthesis approaches. Even though some limitations exist for STM measurements, it is still by far the most suitable technique to study surface-supported nanoarchitectures with atomic precision.

2.2 X-ray Photoelectron Spectroscopy

2.2.1 Overview

Photoemission spectroscopy (PES) techniques measure the kinetic energy of electrons ejected from a solid as a direct result of impinging photons. Depending on the wavelength of the light, they can be classified into ultraviolet photoelectron spectroscopy (UPS), X-ray photoelectron spectroscopy (XPS) and hard X-ray photoelectron spectroscopy (HAXPES) with increasing energy of the photons respectively. UPS is used to probe the most weakly bound electrons of a sample, i.e. the valence electrons, to obtain information on the valence band structure with high resolution. XPS and HAXPES both probe core level electrons of the sample. In the case of HAXPES, the photoelectrons have a large kinetic energy enabling to gain information of deeper laying atoms. A special, more sophisticated technique is the angle resolved photoelectron spectroscopy (ARPES), which enables band mapping. In the following only XPS will be discussed in more detail, for the other above mentioned techniques the interested reader is referred to these sources.^{66, 67}

As STM provides virtually no chemical information, another complementary tool is additionally required to facilitate a profound characterization of the sample. XPS is a surface sensitive and element specific technique that gains information by probing core level electrons with X-rays. In addition to the chemical composition of the surface, electronic changes in the adsorbates and substrates can also be directly monitored by XPS due to small binding energy shifts. Variations in the valence electron distribution are usually related to changes caused by breaking or forming new bonds. This enables monitoring of chemical reactions taking place on surfaces. In chapter five a series of XPS-measurements allows us to track the important reaction steps in surface-assisted Ullmann coupling. The next sections aim to introduce some basic concepts necessary for understanding the XPS results presented in this thesis.

When electromagnetic radiation interacts with matter various effects can occur: coherent or incoherent scattering of photons, pair or triplet production, generation of a photoelectron and, very rarely, photodisintegration. XPS measurements rely on the photoelectric effect, for which Albert Einstein set the theoretical background in 1905⁶⁸ and was awarded the Nobel price in 1921. On the basis of this effect Kai M. Siegbahn

developed the technique called electron spectroscopy for chemical analysis (ESCA) in 1957,⁶⁹ now better known as X-ray photoelectron spectroscopy, for which he was honored with the Nobel Prize in 1981.⁷⁰

2.2.2 Theoretical principle

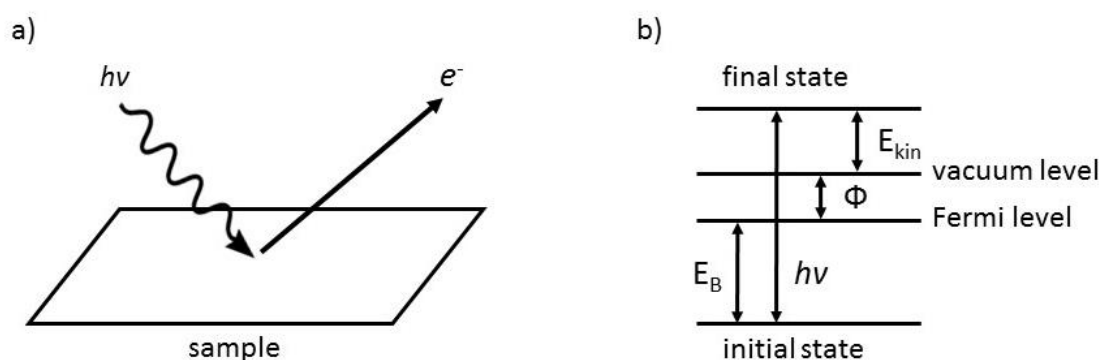


Figure 2. 3: Scheme of the photoemission process a) and energy level diagram b) according to equation 2.6. Adapted from Ref. ⁷¹

The photoelectric effect describes the emission of an electron absorbing a photon, with the whole energy transferred to one electron. Thus the core hole is filled by another electron, resulting in the emission of an Auger electron or characteristic X-rays. The energy of the photon ($h\nu$) must be larger than the sum of binding energy (E_B), with respect to the Fermi level, and the work function (Φ) of the surface to eject the electron. The work function is the minimum energy required to remove an electron from the crystal to vacuum, in other words, it corresponds to the energy difference from the Fermi level to the vacuum level.

$$E_B = h\nu - (\Phi + E_{kin}) \quad (2.6)$$

According to equation 2.6 the E_B can be calculated by subtracting the work function and the measured kinetic energy (E_{kin}) from the photon energy used for excitation. As the

energy of the emitted electrons is measured in the spectrometer, it is common to equalize the Fermi level of sample and analyzer by an electrical connection. Consequently, solely the work function of the spectrometer is required to calculate E_B . The E_{kin} of photoelectrons is most commonly measured with a concentric hemispherical analyzer (CHA). This device allows to disperse the electrons depending on their kinetic energy, by applying a potential difference (ΔV) between outer and inner hemispheres. Hence, only electrons with a defined pass energy can reach the detector slits at a given ΔV . As it is necessary to include electrons with different E_{kin} to acquire a spectrum, a potential difference is used to retard the electrons to the respective pass energy. XP-spectra are recorded by varying the retarding field at a constant pass energy. Conventionally, the photoelectron intensity is plotted as a function of E_B , which can be calculated from the measured E_{kin} after equation 2.6. It is noteworthy that the resolution of the analyzer is given by $\Delta E/E$, where E is the pass energy.⁷² Accordingly, small pass energies of 5 – 25eV are used to obtain high energy resolution XP-spectra, while for survey spectra higher pass energies between 100 – 200eV are used. This is done since the signal intensity will decrease with decreasing pass energies.⁷²

The binding energies of core level electrons are a tabulated,⁷³ well known material property. Therefore, the kinetic energy offset caused by the analyzer can be obtained by using a reference sample. Reference samples used for the binding energy calibration in this thesis were clean single crystal facets.

Accordingly, the chemical composition of the surface can be obtained by comparing the peak areas of the different elements, i.e. of the examined core levels. Unfortunately, the peak intensity is influenced by differences in the photoionization cross section. The photoionization cross section is a core-level specific value additionally depending on the photon energy. Therefore, the photoionization cross section states the probability for the photoionization of different orbitals and elements at a given energy of the photon. Furthermore, the intensity of the peak can also be reduced as a consequence of generally losses, where a part of the energy of the escaping electron is transferred to another electron, leading to a satellite at higher binding energies with respect to the central peak. For this reason, the intensity of the main peak is reduced, with the magnitude depending on the probability for the satellite formation. Consequently, data analysis can be complicated, often only resulting in semi-quantitative information on the chemical composition of the surface. For the XPS measurements in this thesis the stoichiometric

compositions of the organic compounds were pre-defined by the choice of molecule. Hence, only relative variations of different elements or the loss of intensity due to thermal desorption was tracked. In the following, some important features of XP spectra like spin orbit splitting, chemical shifts, and the origin of the surface sensitivity, will be discussed in more detail.

2.2.3 Surface sensitivity

Even though X-rays can penetrate several microns into the crystal, only photoelectrons created up to a certain depth contribute to the measured signal in XPS measurements. Thus, the average distance an electron can travel through a solid is of paramount importance for the information depth. A commonly used quantity is the inelastic mean free path (IMFP) describing the average distance between two inelastic scattering events of an electron. The sensitivity to the topmost surface layers directly results from the small mean free path of photoelectrons in solids, within a certain energy range of the electrons.

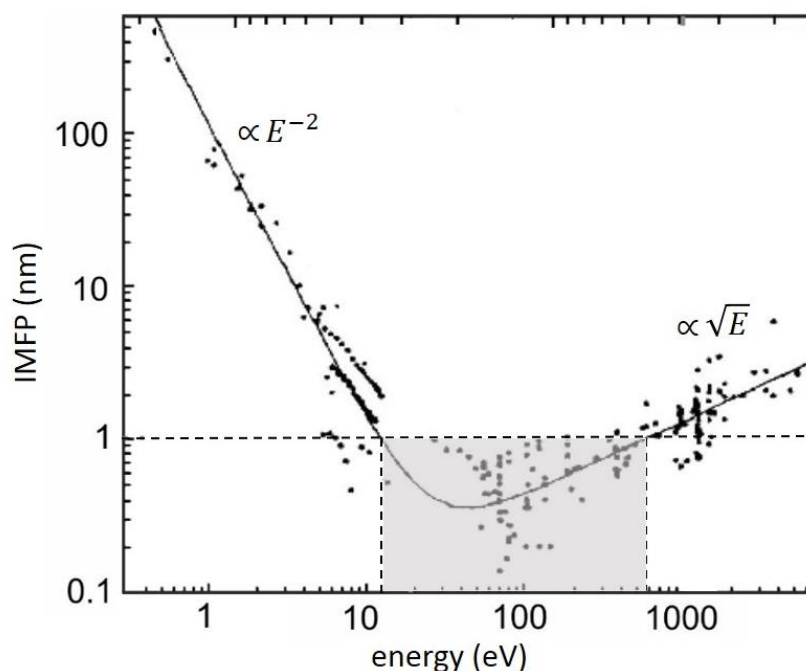


Figure 2.4: The “universal curve” of the IMFP of electrons in metals after Refs. ^{50, 74}

Figure 2.4 shows the IMFP of electrons in various metals depending on their kinetic energy, worked out by compiling of a multitude of experimental data.⁷⁴ The fitted curve is, of course, only an approximation which can vary up to a factor of 5 for different metals.⁵⁰ The basic shape of the curve can be divided into three parts. First, a linear decrease of the IMFP of electrons occurs between 0 and 10 eV, followed by a transition area with an inflection point from decreasing to increasing the IMFP (10-80 eV), and finally a linear increase of the IMFP for (>80 eV). Electrons with low kinetic energies mainly interact by exciting electron hole pairs. Thus the curve falls with approximately E^{-2} as the probability of an energy loss, due to an inelastic scattering event, is proportional to the product of available occupied- and unoccupied-states. Excitation of plasmons and ionization of core levels sets in with increasing kinetic energy of the electrons, reducing the IMFP of electrons. Further increase of the energy of the electrons enhances the IMFP of the electrons and can be approximated by $E^{1/2}$ with energies exceeding 80 eV. That is because of the crude assumption that the inelastic scattering cross section is proportional to the interaction time of passing electrons.⁵⁰

The hatched area depicts the energy range of electrons that would facilitate the highest surface sensitivity. This low IMFP of electrons is the reason for the high surface sensitivity of different techniques, like low energy electron diffraction (LEED) or high resolution electron energy loss spectroscopy (HREELS), that use electrons with kinetic energies in the range of the highlighted energy range.

2.2.4 Characteristics of XP spectra

Conventionally, XP-spectra are acquired by plotting the binding energies of core level electrons against the intensity (number of electrons at a certain energy). The main feature a spectrum consists of are sharp photoelectron peaks, resulting from the well-defined binding energies, of inner shell electrons. Figure 2.5 shows a survey spectrum of an Au(111) film, acquired directly after sample preparation.

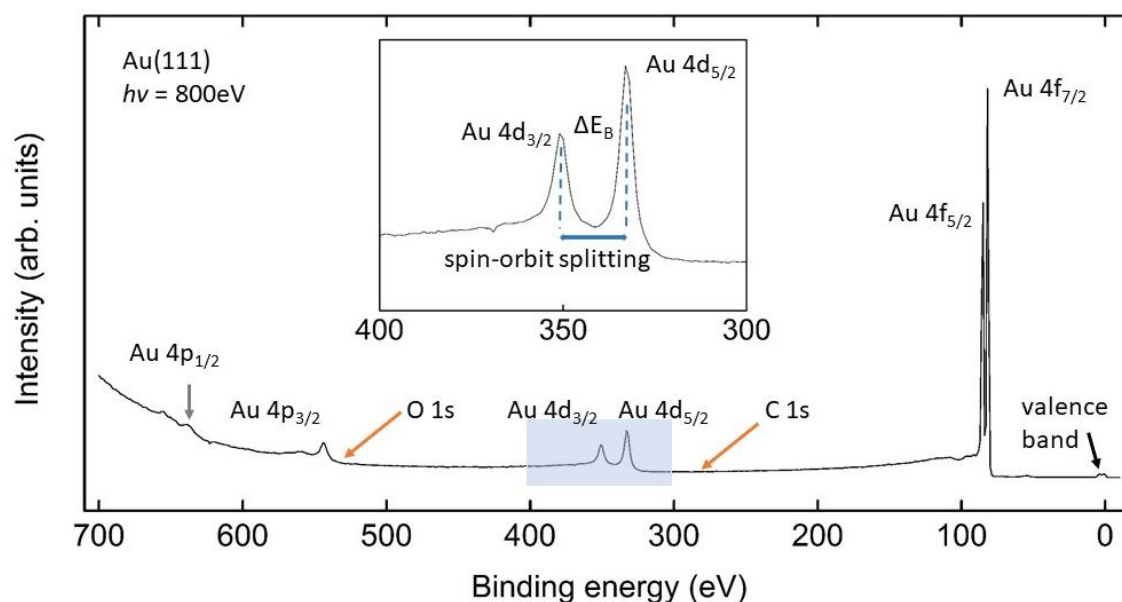


Figure 2. 5: XP survey spectrum of a clean Au (111) surface recorded at the UE56/2-PGM-2 end station at Bessy II with a photon energy of 800 eV.

This survey spectrum shows the characteristic peaks of gold, as well as the valence band near the Fermi level. Moreover, the increasing background at the high E_B side is nicely visible. The reason for this is that a fraction of the emitted electrons loses part of their E_{Kin} by inelastic scattering events, hence appear at the high E_B side. Important evidence for the cleanliness of the surface is the absence of C 1s and O 1s peaks that would be expected at approximately 284 eV and 532 eV respectively.⁷³ Noticeably, the Au 4d, 4p and 4f peaks split into two well separated lines. This phenomenon is called spin orbit splitting and will be explained later. The spectrum illustrates different intensities of the gold peaks, owing to differing cross sections of the probed core levels at the used photon energy. All peaks of the spectrum are superimposed over a background comprised of inelastically scattered electrons and secondary electrons.

Further regularly observed features of XP-spectra are Auger peaks, plasmon loss peaks and shake-up satellites. An Auger electron is generated through a three-electron process: starting with the creation of a core hole after photon absorption, continuing with the filling of the hole by a higher energy electron, ending with the emission of an Auger electron with a defined energy. Conventionally, the Auger transitions are termed according to the involved electron shells. Hence, a KLM-Auger transition describes a

hole in the K-shell filled by an electron of the L-shell and the resulting emission of an electron from the M-shell. The kinetic energy of the Auger electron only depends on the energy differences of the binding energies of the involved core level orbital transitions, but not on the photon energy used in the experiment. Hence, they can easily be distinguished by varying the photon energy. Plasmon loss peaks occur when a part of the energy of an emitted photoelectron induces a collective oscillation of the free electrons. This leads to an apparent increase of the binding energy.⁷⁵ Whereas shake-up features in a spectrum are observed when an outgoing photoelectron excites a valence electron, leading to a satellite peak at higher E_B than the main line. This is often observed for the C 1s orbital in aromatic systems where a $\pi \rightarrow \pi^*$ transition is excited or for transition metal ions.⁷²

2.2.5 Spin-orbit splitting

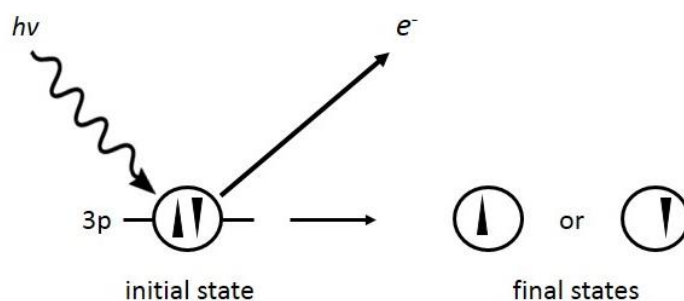


Figure 2.6: Schematic illustration of the initial state before- and final states after photoemission for the 3d subshell. Adapted from Ref.⁷²

Photoemission peaks of the p, d and f core levels ($l \neq 0$) are split into two separate lines. This is caused by spin-orbit coupling effects in the final state.⁷² Relative motion of the electron with respect to the nucleus result in a magnetic momentum parallel to the orbital angular momentum vector. The interaction of this orbital angular momentum with the intrinsic magnetic momentum (spin) of the electron is the reason for the occurrence of two discrete energy levels for the same core level. As the spin can be only oriented parallel or antiparallel to the angular momentum, exactly two energy sub levels can be observed, leading to a spin orbit doublet in the spectrum. Splitting of the peaks is only

observed for non-zero orbital angular momentum. Hence, s levels show no spin-orbit splitting and result in a single peaks (cf., C 1s in Figure 5.5 and Appendix Figures B6 and B7). The following table summarizes the decisive quantum numbers and explains the different intensity ratios of the spin orbit doublets that can be observed, after Refs.^{71,72}

	l	$j = l \pm s$	$2j + 1$ intensity ratio
s	0	1/2	-
p	1	1/2, 3/2	1/2
d	2	3/2, 5/2	2/3
f	3	5/2, 7/2	3/4

Table 2.1: Spin-orbit splitting with: l = orbital quantum number, j = total angular momentum and s = spin quantum number

Apparent from the table the total angular momentum for the two states amounts to $j_+ = l + \frac{1}{2}$ or $j_- = l - \frac{1}{2}$ for the spin quantum number $s = \frac{1}{2}$. The intensity ratio of the spin orbit doublet is determined by the multiplicity, i.e. the number of degenerated states being $2j_+ + 1$.

$$(2j_- + 1) / (2j_+ + 1) = 2l / (2l + 2) \quad (2.7)$$

This leads to intensity ratios of 1:2, 2:3, and 3:4 for the p, d, and f orbitals, respectively. Within one spin orbit doublet the peak with the higher intensity and higher j value is always located at lower binding energies. The ΔE_B , separating a spin-orbit doublet (identical n, l) increases with increasing atomic number Z due to stronger interaction of the electrons with the nucleus. Increasing n while maintaining l constant at a given Z leads to a reduction of ΔE_B , for similar reasons.⁷⁵ This can intuitively be understood by considering mean nucleus-electron distances of the orbitals and their decreasing interaction in the following order $f < d < p$. This trend, i.e. increasing ΔE_B for $f \rightarrow d \rightarrow p$, is nicely visible in the survey spectrum of gold depicted in Figure 2.5.

Especially for systems with strongly overlapping peaks, the fixed intensity ratio together with the known ΔE_B can be used as a constraint. This facilitates data fitting of complex XP peaks, like Hofmann et al. showed for different oxidation states of Ta 4f $_{5/2,7/2}$.⁷⁶ For monitoring the dehalogenation reaction in this thesis, the Br 3d orbital was used because the large magnitude of spin orbit splitting leads to a complete separation of the doublet peak. Additionally, the doublet peaks feature a large chemical shift, hence all four components are fully separated. The Br 3d data presented in chapter five (cf., Figure 5.1) was fitted by fixing ΔE_B and the intensity ratio of 2:3. This has shown to work very reliably.

2.2.6 FWHM of XPS peaks

The following section aims to explain how the full-width at half-maximum (FWHM) of an XPS peak is influenced by the instrument and the probed core level. Factors contributing to the actual line width (ΔE_{tot}) are: the monochromaticity of the X-rays used for excitation (ΔE_x), the natural line width of the probed orbital (ΔE_n) and the resolution of the analyzer (ΔE_a). The only factor not depending on the instrument is the natural line width that is related to the lifetime of the core hole τ . Based on Heisenberg's uncertainty relationship, the ΔE_n can be calculated after the following equation.⁷⁵

$$\Delta E_n = h/\tau \quad (2.8)$$

Hence, typical life time broadening lies below one eV with lifetimes between 0.1 – 100 fs.⁵⁰ Lifetimes of core holes increase from the inner to the outer shell orbitals. Accordingly, the natural line width of an element decreases in the following order $s > p > d > f$. This effect can clearly be observed in the survey scan shown in Figure 2.5, where the FWHM of the peaks increases with increasing binding energy. The probability for filling up a core hole increases for heavier atoms due to the higher number of electrons. Hence, the line width of a given orbital also increases with increasing atomic number Z . An approximation for the peak width including instrumental broadening as well as intrinsic broadening is given by:⁷⁵

$$\Delta E_{tot} = (\Delta E_n^2 + \Delta E_x^2 + \Delta E_a^2)^{1/2} \quad (2.9)$$

Obviously, the only way to improve the resolution, i.e. to reduce the FWHM of peaks in a spectrum, is to decrease ΔE_x and ΔE_a , for example by using of a monochromator or a lower pass energy for the analyzer.⁷⁷ Other features possibly contributing to the actual line width are satellites, due to vibrational broadening or shake-up satellites.⁷⁵ As these features lie only on the high binding energy side of the core level, an asymmetry is introduced.

2.2.7 Chemical shifts

The E_B of a specific core level does not only depend on the probed element. This is caused by differences in the chemical environment of the probed orbital, what is referred to as chemical shift. In the following only initial state effects are considered, while final state effects are neglected (Koopmann's theorem).⁷⁸ Thus only the ground state before emission of a photoelectron is taken into account, and processes like relaxation occurring during photoemission are not considered. This simplification is valid because final state effects in many cases have a similar magnitude for a distinct atom in different oxidation states. Therefore, interpretation of changing binding energies solely due to initial state effects is valid.⁷²

Chemical shifts of core levels occur even though they are not directly involved in chemical bonding. This is due to the fact, that the distribution and density of all electrons are affected by the valence electron distribution. Considering the electronegativity after Pauling usually aids in qualitatively understanding the shift. Highly electronegative elements reduce the electron density of their bonding partner, resulting in a partial positively charged atom with increased negative background. Hence, the binding energy of an atom, connected to a highly electronegative element, shifts to higher values. In this thesis, chemical shifts are of particular interest because they enable us to monitor reactions taking place on the surfaces. In the C 1s XP-spectra presented in chapter five, carbon bound (C-C) could be easily discriminated from halogen bound carbon (C-Br) at higher binding energies. This can already be explained with the Pauling electronegativity values of 2.5 and 2.8 for C and Br, respectively.⁷⁹ After thermally induced C-Br bond

scission the molecules form organometallic networks on Ag(111). The C 1s peak features a characteristic low BE shoulder arising from the carbon atoms directly binding to the metal. A more pronounced chemical shift is observable when monitoring the Br 3d core level, depicted in 2.7.

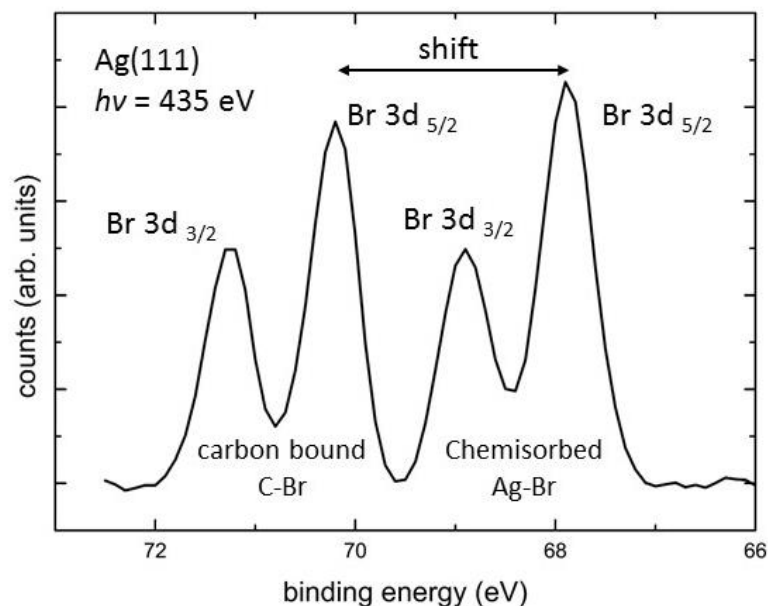


Figure 2. 7: chemical shift of the Br 3d core level doublet measured with a photon energy of 435 eV on a Ag(111) surface

The bromine bound to the molecule (carbon bound), exhibits a strong shift of approximately 2.5 eV to higher binding energies as compared to the chemisorbed species. This can be explained by assuming that the metal substrate acts as electron donator. Therefore, the valence electron density of the chemisorbed Br species increases, as also reflected in a lower electric potential of the Br 3d core level. Consequently, the electrostatic attraction at the nucleus is reduced. Hence, this chemical shift leads to a peak at lower binding energies. This shift enabled us to comparatively track the progression of the dehalogenation on gold and silver surfaces in chapter five. Many open databases can be found, listing binding energy values depending on their bonding partners, possibly helping data interpretation.^{73, 80}

2.2.8 Synchrotron-based XPS

All the above explained XPS theory is valid for both lab source and synchrotron radiation. This section aims to highlight some special features and possibilities of XPS experiments performed at a 3rd generation synchrotron. The basic concept of all synchrotron light sources is that charged particles moving at relativistic velocities are forced to change their path by a magnetic field, leading to the emission of electromagnetic radiation. Commonly, synchrotrons produce light featuring a very high intensity, natural collimation, and high degree of polarization. This can be summarized in a single quantity called brilliance, which will be addressed in detail below. In first generation synchrotrons, radiation was solely a side product of machines constructed to smash nuclei apart with high energy electrons, in contrast to 2nd generation synchrotrons that were built in order to produce light, but are restricted to bending magnets. Therefore, the so-produced light has a significantly lower brilliance as compared to modern 3rd generation facilities that use insertion devices and have brilliances of at least 10^{18} photons/s/mrad²/mm²/0.1%BW.⁸¹

In the beginning, a brief description of how modern synchrotron facilities generate light is given. After that some possibilities exclusively available at a synchrotron light source are discussed. This is followed by an explanation, how the TP-XPS measurements were performed at the undulator beamline UE56/2-PGM-2 at Bessy II.

Figure 2.8 shows the five most important components a 3rd generation synchrotron consists of: 1 electron source, 2 booster ring, 3 storage ring, 4 radio frequency supply, and 5 insertion devices.

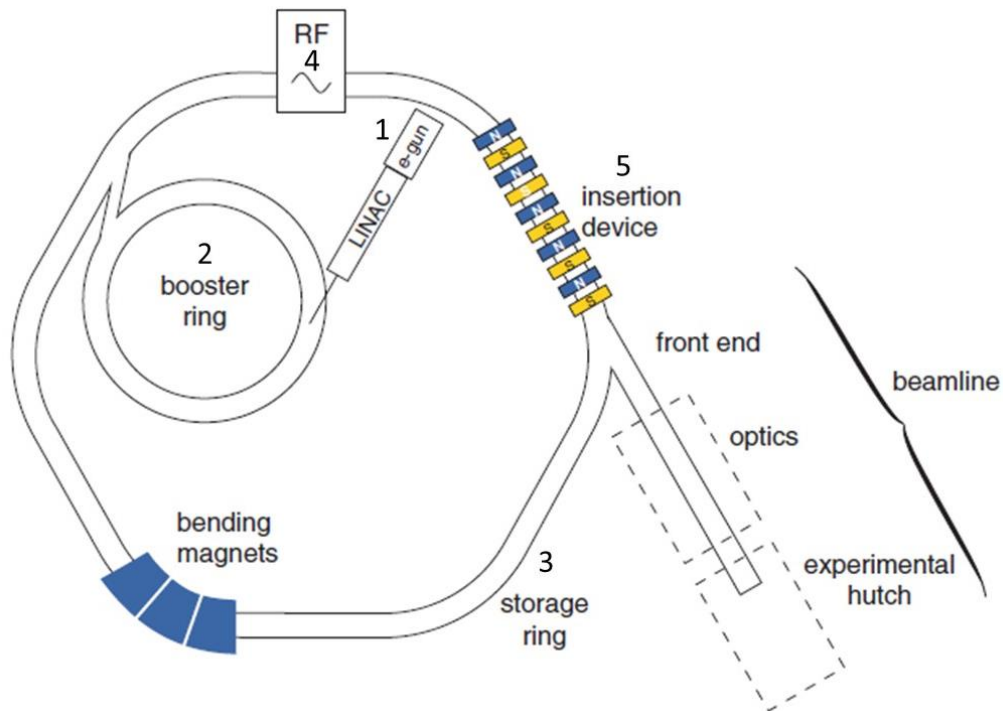


Figure 2. 8: Scheme of a modern synchrotron light source.⁸²

The scheme in Figure 2.8 is reduced to the minimum of components required in order to briefly explain the operation principle. Additionally, the devices and pumps for maintaining the UHV are neglected. Furthermore, the proportions of the different components depicted in the above scheme is not to scale, as for instance storage ring circumferences of a couple of hundred meters are normal for modern synchrotron facilities.

In the beginning, electrons are continuously emitted from an e-gun by a hot filament and accelerated in the linear accelerator (LINAC) to kinetic energies of approximately 100 MeV. Subsequently, the electrons are injected into the booster ring, where they are further accelerated to energies in the GeV range. From the booster ring the electrons are transferred to the storage ring. As loss of electrons is inevitable in the storage ring, the lost electrons have to be replenished in order to keep the specified storage ring current constant. Modern synchrotrons use the so called top up method, where the storage ring is continuously topped up by small injections of electrons maintaining the ring current constant. This has major advantages for stable operation, as temperature fluctuations of X-ray optical components due to variations in the photon flux are significantly smaller.⁸² In the storage ring the electrons have kinetic energies in the GeV range that correspond

to highly relativistic velocities. To keep the electrons on the path of the ring, dipole magnets are used to change the direction. Focusing of the electrons is done with quadrupole magnets, whereas sextupole magnets are used to compensate chromatic aberrations caused by the quadrupole.⁸² When charged particles are accelerated electromagnetic radiation is emitted tangentially to the directional movement of the particles. Synchrotron light is generated by deflection of electrons with highly relativistic velocities. By the emission of light the kinetic energy of the electrons is reduced. In the dawn of synchrotrons, bending magnets were used to generate the synchrotron light. In order to increase the number of photons generated, modern synchrotron radiation sources use insertion devices. Insertion devices consist of several dipole magnets with alternating N and S poles, where the electrons are forced into multiple bends. Therefore, insertion devices produce a higher photon flux, as synchrotron radiation is generated at every bend. A precise arrangement of dipole magnets forces the electrons on a sinus path, thereby emitting radiation in the mean flight direction of the electrons. The insertion devices can be divided into undulators and wigglers, but their basic operating principle is the same. If the light cones interfere with each other it is an undulator, if not it is a wiggler. For a detailed description of the insertion devices the interested reader is referred to literature.⁸² The photons can leave the storage ring through openings and enter the end station by passing the beam line. As mentioned above, the electrons reduce their kinetic energy by emission of synchrotron radiation. A radio frequency supply replenishes just the right amount of energy every time they pass. The light generated by a synchrotron is usually classified by the flux or the brilliance. If an unfocused beam is used, it is sufficient to characterize the beam by the flux, which is the number of photons within a certain band width (BW) passing through a defined area per second. Considering also spatial and angular dependence, the beam is described by the brilliance.⁸²

$$brilliance = \frac{photons}{time[s] \text{ solid angle}[mrad^2] \text{ unit source area}[mm^2] \text{ BW}[0,1]} \quad (2.10)$$

Hence, the brilliance is the flux per unit source area per solid angle. The brilliance can be regarded as a concentration of photons fulfilling the above mentioned temporal-, angular-, spatial-, and energetic conditions. A 3rd generation synchrotron undulator has brilliances in the range of 10^{20} photons/s/mrad²/mm²/0.1%BW.⁸³ Synchrotron light sources have several advantages as compared to laboratory X-ray sources: several orders of magnitude

higher intensities of the photons, tunability of the photon energy, linear polarization of the electromagnetic radiation in the orbit plane, a much higher brilliance, and the possibility of time resolved studies by using short pulses. The energy of the photons can be tuned from the near infrared to hard x rays. Hence, it is possible to optimize the photon energy with respect to the highest cross-section for the respective core level. Moreover, the surface sensitivity can be enhanced. This is done by adjusting the photon energy in order to obtain E_{kin} values where the IMFP has a minimum. As opposed to (HAXPES), where the probing depth can be maximized, by virtue of the increasing IMFP of photoelectrons with high energies (2-10 keV). Hence, it is possible to study buried layers or interfaces inaccessible with conventional XPS measurements.⁸⁴ Furthermore, the tunability of the photon energies in combination with the linear polarization can be used to perform near edge absorption fine structure (NEXAFS) measurements. This technique reveals information on electronic and structural properties of the adsorbates. For the field of on-surface synthesis this can be particularly important, as the orientation of molecular entities as phenyl rings with respect to the surface can be probed with NEXAFS measurements.⁶² This is done by varying the X-ray incidence angle, and measuring angle dependent changes in the resonance intensity of a specific chemical group.⁸⁵ The high photon flux available allows to acquire high resolution XP-spectra in less than one minute, opening up the possibility of performing so called TP-XPS studies. However, the high photon flux can be detrimental if the investigated structures are susceptible to radiation damage. The next section aims to shortly introduce TP-XPS measurements and mention some characteristics of the UE56/2-PGM-2 end station.

TP-XPS, sometimes also called “Fast-XPS”, is a variant of XPS which is performed while varying the temperature. This is done by choosing a core level and continuously acquiring the XP spectra of the same energy range while heating the sample with a constant ramp. The acquired data is therefore extended into temperature space, which has to be included into the graphs. Conventionally, the binding energy is plotted against the temperature, and the peaks are looked at from a bird’s eye view, whereas the intensities are displayed by a color code. This kind of spectra are rich in information, but for details on the peak shape or small shoulders the individual spectra have to be considered. Regardless, TP-XPS measurements proved to be an invaluable tool to follow chemical reactions on surfaces in real time. Furthermore, TP-XPS measurements have proven to be suitable for

the investigation of various systems.⁸⁶⁻⁸⁹ To date TP-XPS measurements are restricted to synchrotron facilities as the required photon flux is not available using lab sources.

2.2.9 Benefits and limitations of XPS

A key advantage of XPS is that all elements with a mass exceeding two atomic units can be detected, which makes this technique applicable to a multitude of systems from different research fields. For that reason XPS related studies sum up to more than 9000 papers published per year.⁹⁰ In addition to the information what elements are present on the surface, also details on their chemical environment i.e. bonds and oxidation states of the atoms are gained from chemical shifts. In the last years TP-XPS (also referred to as Fast-XPS) measurements, where a core level is probed at varying temperatures, showed the possibility to monitor chemical changes taking place on surfaces over extended temperature ranges.^{86-88, 91, 92} Reversible and irreversible temperature dependent processes on surfaces can be directly monitored with TP-XPS measurements. In contrast to STM imaging, where usually only irreversible processes are observed after thermal treatment. In section 2.2.8 some characteristics of the TP-XPS experiments of this work were highlighted. XPS measurements can feature relatively high energy resolution of < 0.2 eV, but increasing the resolution is always accompanied by a loss of intensity.⁷⁵ The sensitivity of XP-spectra to the topmost layers is a crucial benefit when studying adsorbed nanostructures, which can be additionally enhanced by geometric optimizations. This can be achieved by varying the detection angles of electrons, with respect to the surface, reaching the analyzer. Reducing the emission angle from $90^\circ \rightarrow 0^\circ$ increases the path length of the electrons travelling inside the solid. Hence, the surface sensitivity can be enhanced by using small emission angles.

Nevertheless, there are also some limitations when performing XPS measurements, often requiring a complementary technique for a comprehensive characterization of the sample of interest. A drawback in comparison to STM measurements where one gains information of every measured site is that your XPS data is averaged over hundreds of square microns, which is much bigger than the size of the nanostructures. Consequently, the signal is a convolution of every object illuminated by the X-rays, hampering interpretation if various on-surface reactions take place. Further, defects that are always

present in bottom up fabricated two dimensional covalent nanostructures thus far, are normally not detected with XPS. Moreover, mostly conducting samples are measured in XPS measurements to avoid charging effects which complicate the data by shifting of the peaks. The often mentioned advantage as a nondestructive method is not always valid, especially for organic compounds, beam damages are frequently observed.^{93, 94} Another limitation is the high costs generated by XPS measurements, because UHV conditions are required and the whole equipment is very expensive, which is especially valid for synchrotron based studies. Finally, data collection can be slow, depending on the cross sections, the concentrations of the elements, and the photon flux of the X-ray source. In many cases the combination of STM and XPS allows a thorough characterization, which is a benefit owing to their complementary nature.^{33, 95, 96}

Chapter 3

Bottom-up synthesis of carbon-based nanoarchitectures

There are two fundamentally different approaches for the creation of one atom thick nanostructures. On the one hand, there is the bottom-up synthesis method, where self-organization of adsorbed molecular building blocks or a surface-supported intermolecular coupling reaction, forms the structure. These self-assembly of molecules can be stabilized by various weak intermolecular forces or undergo chemical reactions and form strong organometallic or covalent bonds. On the other hand, there is the top-down fabrication method where material is removed from the source material to obtain the desired structure. The intensely studied GNRs represent a material class frequently synthesized with top-down as well as bottom-up approaches, both having benefits and limitations.^{18, 19, 97, 98} There are nanostructures where the mechanism of formation is controversially discussed. An example is the fullerene molecule, with the majority of publications postulating a bottom-up mechanism, where graphene dissociates in small C₂ clusters which subsequently coalesce to form buckyballs.^{99, 100} But also studies exist that postulate a top-down approach where graphene is directly transformed into fullerene.¹⁰¹ In the following, only the bottom-up approach will be considered, as exclusively this approach was used in this thesis. The bottom-up fabrication bears some decisive advantages in comparison to the top-down method. By employing the bottom-up approach it is possible to synthesize nanoarchitectures with atomic precision, which is virtually inaccessible for the top-down approach. Another benefit of the bottom-up approach is the possibility of gaining insight into fundamental chemical reaction mechanisms on surfaces. Furthermore, the bottom-up approach is extremely versatile, with unlimited possibilities concerning the design and functionalization of nanostructures. In addition, the reaction conditions for bottom-up synthesized nanostructures are often mild, in comparison with the harsh reaction conditions most top-down methods need for cutting the source material.¹⁰² Ullmann-type coupling reactions are by far the most frequently studied reactions in the on-surface synthesis community.

As this coupling mechanism was also subject of this thesis, some important aspects of this reaction will be discussed in section 3.2. A brief description of the new research field of “on-surface synthesis” is outlined in the following. On-surface synthesis describes a chemical approach where organic nanostructures are formed by assembling and covalent coupling of molecular precursors adsorbed on surfaces. The surface confines the molecular building blocks and supports or even drives their covalent coupling.¹⁰³ Some definitions also include intramolecular reactions, without any intermolecular coupling reactions.¹⁰⁴ Commonly, the reactions are performed in UHV. This bottom-up approach allows fabricating tailored nanoarchitectures with promising properties. Even though, this research field emerged only about one decade ago, many breakthroughs have been reported. Examples are atomically precise GNRs, nanographenes, molecular chains, porous covalent networks, metal coordination frameworks, etc. that have been synthesized by this highly versatile method.¹⁰⁴⁻¹⁰⁷ The structures formed by the on-surface synthesis approach feature several benefits. First, the obtained covalent structures have a high thermal and mechanical stability. Second, they can allow efficient electron transport, which makes the structures interesting for various electronic applications. Finally, synthesis of novel molecular species, not accessible with conventional solution chemistry, is possible. As the nanoarchitectures are formed under UHV conditions, they are chemically pure and can be investigated by surface science characterization techniques. For further examples and benefits of the on-surface synthesis approach the interested reader is referred to literature.²

All nanostructures presented in this work were fabricated on atomically flat metal or iodine passivated metal surfaces. These surfaces play a crucial role for the bottom-up synthesis of nanostructures, therefore some important aspects will be addressed in the following.

3.1 The role of the surface

The surface of every material is of paramount importance, because the surface always interacts with its environment first. For simplicity in the following the term surface is always synonymously treated as a single crystal surface. Wolfgang Pauli said once: “*God made the bulk; the surfaces were invented by the devil*”. In the bulk of a crystal every

atom or molecule is surrounded by its neighbors having a defined coordination. Hence, the combination of lattice vectors together with the basis defines the bulk of our crystal. For cutting a crystal into two pieces the free energy cost for creation of the new surface has to be overcome, i.e. the work to break the bonds inside the crystal perpendicular to the cleavage plane. Therefore, the translational symmetry perpendicular to the surface is broken and the atoms have to rearrange and modify their new bonding environment to minimize their energy. This can strongly affect the physical properties of the surface compared to the bulk, like insulating materials can become conducting on the surface, known as topological insulators.¹⁰⁸ All surfaces display a more or less strong relaxation of the surface layers in comparison to the bulk, i.e. an increased or reduced layer spacing. Additionally, the in plane structure of the surface can be altered as well, known as a reconstruction. Reconstructions are routinely observed in STM measurements, whereas diffraction techniques are needed to prove relaxations. Prominent examples are the herringbone $22 \times \sqrt{3}$ reconstruction of the Au(111) surface or the 7×7 reconstruction of the Si(111) surface.^{54, 109}

The perfect crystal with each facet consisting of only one terrace exists solely in theory. This holds true for both natural occurring crystals as well as for crystals grown in the lab. In reality there is a large variety of defects which can be found when analyzing a crystal. The most frequently observed defects in STM measurements are line defects separating terraces from each other. But many other defects can be observed like, such as point defects, dislocations, interstitials, and vacancies, just to mention some. A special case are vicinal surfaces, where the crystal is cut with a small deviation with respect to a low index surface. The resulting crystal exhibits a high density of atomic steps. Vicinal surfaces are of particular interest as they can feature a high catalytic activity, or they can be used as a template for one-dimensional structures.^{110, 111} In our case the interaction of the surface with the molecules is particularly important. For the bottom-up synthesis of one- or two-dimensional nanostructures, the surface plays a crucial role as the molecules have to adsorb and stay on the surface during synthesis. Diffusion and coupling barriers of SSRs are important factors for ordered structure formation, which is the goal in most cases. Reactions can be classified into diffusion-limited and coupling-limited. Therefore, coupling and diffusion rates are compared: for a coupling-limited process the rate of coupling is smaller than the rate of diffusion, while for a diffusion-limited process the diffusion rate is slower than the coupling rate.¹¹² The recombination of Cyclohexa-*m*-

phenylene radicals was found to be diffusion-limited on Cu(111), coupling limited on Ag(111), and somewhere in between on Au(111).¹¹³ Results were fragmented polyphenylene structures on Cu(111) contrary to dense packed networks on Ag(111). This emphasizes that diffusion-limited processes must be avoided to obtain covalent densely packed high quality networks.¹¹³⁻¹¹⁵ When intermolecular coupling reactions are desired, the catalytic activity of the metal surfaces is particularly important. As all results presented in this work were obtained on coinage metals (Au, Ag, Cu) (111)-facets or iodine covered Au(111) and Ag(111) surfaces, the following section will not consider other surfaces. For the most prominent and reliable on-surface reaction, the so called Ullmann-type coupling which will be treated in the next section, the choice of surface can strongly affect both the temperature window where the reaction takes place and the quality of the nanostructures.^{29, 30, 116}

3.2 On-surface Ullmann coupling

F. Ullmann et al. discovered in 1904 that heating of iodobenzene in solution with copper powder acting as a catalyst, leads to a high yield of biphenyl.¹¹⁷ For many years this reaction was restricted to solution chemistry until in 1992 it was transferred to a Cu(111) crystal under UHV conditions. Whereby, iodobenzene dehalogenates already at 175 K, but approximately 375 K are required to form biphenyl, at low coverages.¹¹⁸ A couple of years later, tunneling electrons released by the tip with an energy of 1.5 eV were used to trigger cleavage of the carbon iodine (C-I) bonds.¹¹⁹ Apart from thermally induced activation and activation by electrons, photons with energies exceeding 4.4 eV also showed the capability to cleave C-Br bonds on insulating surfaces.¹²⁰ In 2007, the first covalent network was synthesized on Au(111) by Grill et al. by connecting brominated porphyrins *via* an Ullmann-type reaction.¹ Therefore, halogenated precursor molecules were thermally activated on-surface and the coupling proceeded at predefined connection points. The possibility of controlling the topology of the formed structures by the halogen substitution pattern of the molecule makes on-surface Ullmann coupling a versatile method to produce tailored nanoarchitectures. For instance, molecules substituted with one, two, three or more halogens can lead to dimers,¹¹⁸ one-dimensional structures (wires and ribbons),^{19, 121-123} or 2D networks,^{29, 124} respectively. On the more inert Au(111)

surface (compared to Cu(111)), the reaction could be brought back to ambient conditions. Thereby a tri(4-bromophenyl)benzene precursor formed dimers, whereas a 1,3,5-Tri(4-iodophenyl)benzene precursor formed networks.^{125, 126} However, these examples of ambient on-surface Ullmann coupling reactions represent only a small niche. The fundamental reaction steps of surface-assisted Ullmann coupling are activation and coupling, respectively. In the first step, adsorbed molecules get activated, whereby the surface catalytically promotes the homolytic cleavage of the carbon-halogen (C-X) bond. This is followed by coupling of the activated sites, i.e. the recombination of the surface stabilized radicals (SSRs). Hence, the second step in on-surface Ullmann coupling concludes the reaction by the formation of covalent C-C bonds. Despite the seeming straightforwardness of the reaction, there are examples where it was not possible to synthesize the desired covalent nanostructure. For instance steric repulsion, hindering covalent coupling or unwanted side reactions, can hinder the bottom-up synthesis of the intended nanoarchitectures.^{30, 116} Therefore, Figure 3.1 aims to emphasize that more requirements exist to form a defined covalent nanostructure from a not yet explored molecular precursor by surface-assisted Ullmann coupling.

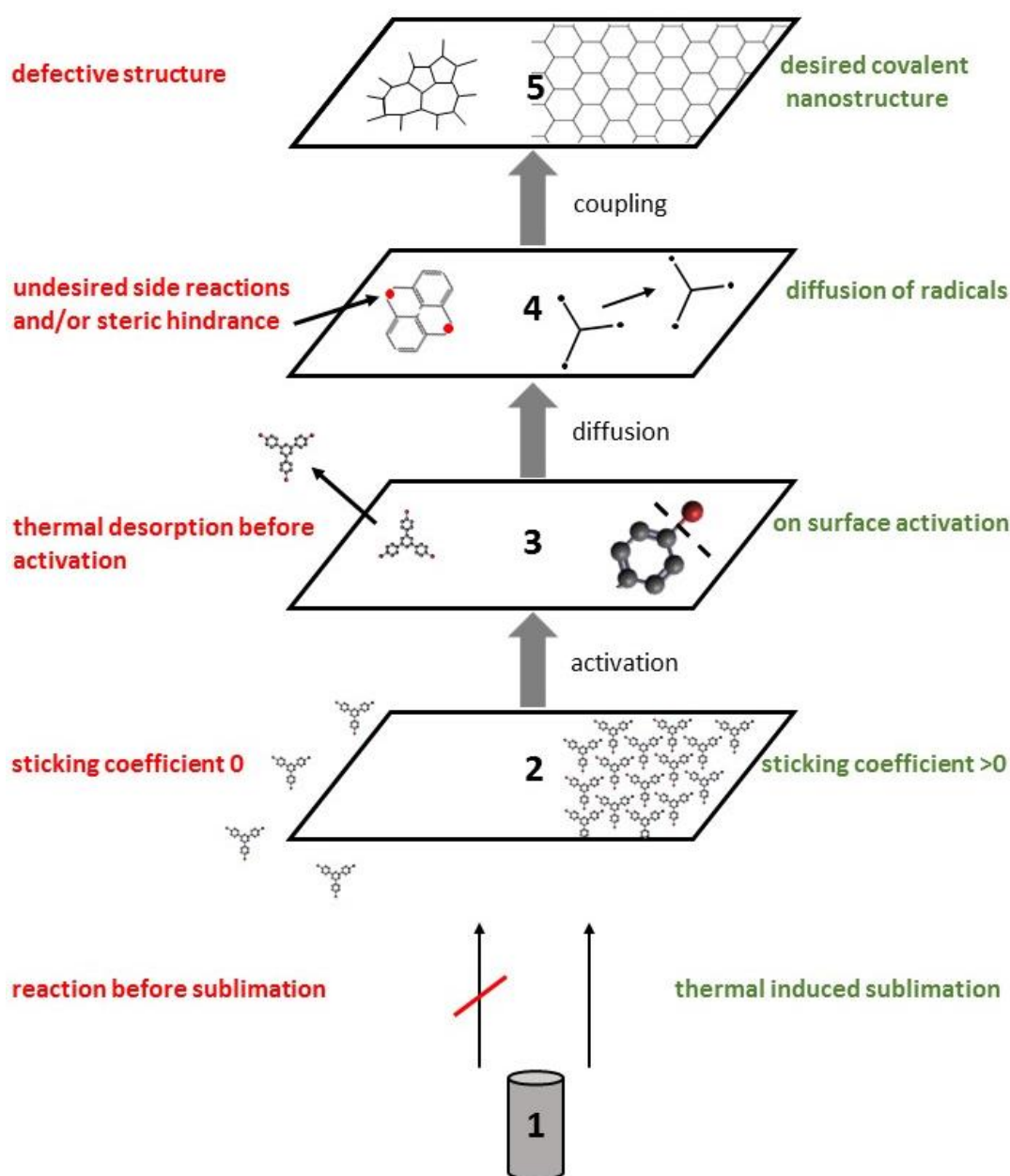


Figure 3. 1: Elementary reaction steps of on-surface Ullmann coupling from a halogenated aromatic precursor (1) to the desired covalent nanostructure (5) on Au(111) without organometallic intermediate structure.

Surface-supported Ullmann coupling, as used to fabricate atomically precise nanostructures on catalytically active surfaces, involves multiple steps. All five steps as shown on the right hand side of Figure 3.1 must be feasible in order to accomplish an on-surface synthesis of the intended nanoarchitecture. This emphasizes that multiple factors can hinder the synthesis of the desired covalent structure. First, the molecules have to be

sublimable and have a sticking coefficient > 0 , to enable further chemistry on the surface. The next requirement is that the molecules can be activated by annealing before the energy barrier required for thermal desorption of the intact or partly dehalogenated molecular precursor is overcome. For instance in chapter six a temperature ramp to 200°C led to a thermal desorption of DITTP molecules from an iodinated Ag(111) surface, precluding further on-surface chemistry. Additionally, the SSRs need enough energy to diffuse over the surface in order to enable intermolecular coupling reactions. Unintended side reactions can occur, but they are only rarely observed. An example of detrimental side reactions, leading to uncontrolled polymerization into amorphous structures, is C-H activation proceeding on Cu(111) already at temperatures below 200°C.³⁰ Finally, if no steric repulsion hinders coupling, the covalent bonds can be formed, resulting in the favored nanostructure. Nevertheless, most synthesized 2D nanoarchitectures contain topological defects, like five- or seven membered rings as commonly found in networks derived from 1,3,5-tris(*p*-bromophenyl)benzene (TBB/2).^{29-31, 127} When studying Ullmann-type coupling of TBB precursors on Au(111) (cf., chapter five), each on-surface reaction step has to be triggered by further increasing the temperature. This is in contrast to the more reactive copper and silver surfaces, where network formation directly upon room temperature deposition is frequently observed.¹²⁸ The directly formed intermediate structures are connected by carbon-metal-carbon (C-M-C) linkages, i.e. organometallic bonds. Thereby two molecules are connected *via* a surface adatom. On Ag(111) and Cu(111) surfaces organometallic bonds are commonly observed, whereas on Au (111) they are only rarely found.^{116, 129-132} It is often possible to convert these organometallic into covalent bonds through thermally induced demetalation.^{32, 133} However, exceptions are reported where side groups induce steric repulsion, hindering covalent bond formation.^{30, 116} The following section aims to point out some differences of the halogen functionalization (F, Cl, Br, I) as well as surfaces of choice and give some examples, without the intention of giving a complete overview.

The first reaction step in surface-assisted Ullmann coupling is a homolytic splitting of the carbon halogen bond, upon which the split off halogens become chemisorbed. The cleavage of the halogen results in an unpaired electron at the molecule. Experimental^{29, 134} as well as theoretical¹³⁵ works underpin that the catalytic activity of coinage metals for breaking the carbon halogen bond increases in the following order Au \rightarrow Ag \rightarrow Cu. The theoretical basis was established by Hammer and Norsov via the study of dissociation

energies of H₂ on gold, copper, nickel, and platinum surfaces. They proposed that the nobleness is related to two factors: the degree of filling of antibonding orbitals upon adsorption and their spatial extent (orbital overlap).¹³⁶

The choice of halogen (F, Cl, Br, I) substituent for the desired on-surface Ullmann reaction also strongly influences the reaction pathway in several ways. Depending on the halogen substituent, the carbon halogen (C-X) bond strength varies substantially, which will be addressed later. Furthermore, their different atomic weights of 19, 35.5, 80, and 127 u for F, Cl, Br, and I, respectively affect the sublimation temperature of precursors with the same organic backbone, but different halogens. Specifically, the magnitude of intermolecular forces like van der Waals interactions and halogen bonds depend on the choice of halogen, and therefore determines the sublimation temperature. For larger molecules, this can lead to premature reactions inside the crucible before sublimation sets in. As the halogens in most cases chemisorb after activation, they can influence the formation of the resulting structures. The chemisorbed halogens can inhibit diffusion of radicals by blocking surface sites hindering covalent coupling.¹¹³ Another detrimental effect of halogens can be the passivation of active sites of network rims, preventing further growth.¹³⁷ For small molecules, the problem of halogen poisoning can even be enhanced when a fraction of the activated molecular precursors thermally desorbs. Deposition of 1,3-diiodobenzene on Cu(111), for example leads to covalent trimers adsorbed atop a closed iodine layer, because a fraction of the radicals desorbs before recombining with another.¹³⁸ One possible way of reducing the impact of chemisorbed halogens was outlined by Stöhr et al. *via* annealing in 10⁻⁷ mbar H₂.¹³⁹ Thereby the Br 3p peak vanished from the XP-spectrum. Recently, a molecular beam of atomic hydrogen showed the possibility of removing the halogens already at room temperature.¹⁴⁰ Finally, the above mentioned different C-X bond strengths lead to different energies required for activation. Bond dissociation energies increase in the following order I-C → Br-C → Cl-C → F-C, showing that the bond strength decreases with increasing the atomic number of the halogen. The bond dissociation barriers are also strongly influenced by the substrate. For instance RT deposition of 1,3,5-tris(4-bromophenyl) benzene (TBB) leads to self-assembly of intact monomers on Au(111), to a partially cleavage of the C-Br bond on Ag(111) and to a complete dehalogenation on Cu(111).^{29, 127} Notably, the energy required for breaking a C-C bond is smaller than for breaking the F-C bond, which presumably leads to a decomposition of the carbon skeleton before activation.^{141, 142}

Hence, fluorinated precursors are precluded for Ullmann-type coupling reactions. The catalytic activity of the substrates reduce the C-X bond strength, i.e. facilitates the C-X bond cleavage. Despite, the aforementioned differences in surface reactivity of the coinage metals and differences in the C-X bond strengths, each adsorbate/adsorbent system has to be regarded individually. Particularly, the height of halogen over the surface influences the magnitude of interaction. Therefore, the catalytic activity of the surface acting on the C-X bond can vary, rendering exact predictions on activation temperatures very challenging. For instance, C-Br bonds from 2,2',10,10'-tetrabromo-9,9'-bianthracene dissociate at different temperatures on Au(111), based on different heights of the halogen with respect to the surface.¹⁴³ The combination of used halogen and surface, together with the organic skeleton and the adsorption site, determines the onset temperature of dehalogenation.

Using molecules substituted with different halogens, leading to distinct C-X bond strengths i.e. distinct activation barriers for breaking the C-X bond, opens up the possibility of achieving a selective dehalogenation. For thermal activation this leads to different temperatures for splitting the C-X bond. Hence, the activation of the respective halogenated sites follows a defined order known as hierarchical polymerization.^{28, 42, 144} However, a recent study showed that hierarchical polymerization is also possible for an exclusively brominated molecule. This was achieved by linking the bromine atoms with two non-equivalent carbon atoms.¹⁴³

The topology of the resulting nanostructures can be predefined by the choice of organic precursor, representing an essential advantage of this type of on-surface reaction. In addition to the choice of molecule, the choice of substrate can also influence the topology and or quality of the nanostructures. An example for this is the 10,10'-dibromo-9,9'-bianthracene (DBBA) molecular precursor resulting in GNRs on Cu(111) as opposed to nanographenes on Cu(110), for annealing to 250°C.¹⁴⁵ On Au(111) and Ag(111), deposition and subsequent annealing of DBBA to 400°C and 350°C respectively, leads to the formation of GNRs.^{19, 146} Influences on the quality of organometallic networks on Ag(111) and Cu(111) surfaces will further underpin the importance of the substrate in chapter four.

GNRs represent a special case of on-surface Ullmann-type reactions as a second reaction step has to be introduced to obtain the desired structure. In the first reaction step, a classical Ullmann coupling reaction generates a linear covalent polymer. By further

increasing the temperature the CDH reaction transforms the polymer into GNRs.¹⁹ In chapter six, a novel strategy for the formation of polymer chains and GNRs, by means of a RDS, is outlined.

In conclusion, on-surface Ullmann-type coupling is a well-studied approach, suitable to a multitude of systems synthesizing a large variety of 2D nanostructures. However, the elementary reaction steps and processes involved in Ullmann-type couplings are still not entirely understood.

3.3 Molecule-surface interactions

In this chapter only solid-gas interfaces will be discussed, i.e. the interactions between atoms or molecules in the gas phase and a solid surface. The reason for this is that all results presented in this work were obtained from UHV experiments, where the molecules originate from a gas phase before adsorbing. A single molecule from the gas phase impinging on a solid surface has two principal possibilities: it can be reflected, or adsorbed on the surface. The proportion of the number of adsorbed molecules to the total number of molecules impinging the surface is expressed in the sticking coefficient. Factors influencing this coefficient are the temperature and the actual coverage of the surface, i.e. the amount of available adsorption sites. As a rule of thumb, the sticking coefficient decreases with increasing surface temperature or coverage. For the adsorption process an activation barrier can exist that needs to be overcome, commonly observed for dissociative chemisorption.^{147, 148} Additionally, the arriving particles need to dispose their kinetic energy to avoid desorbing again immediately. This can be realized by exciting surface phonons and or plasmons by the particle. Also the exact site of the impact plays a role, as the atomic and electronic structure varies across the surface.¹⁴⁸

Depending on the strength of interaction between molecule and substrate, we can discriminate between chemisorption and physisorption. If the interaction is strong, i.e. chemical bonds are formed between substrate and adsorbate, we call it chemisorption. Therefore, the orientation of the molecule's electronic orbitals with respect to the surface need to have a certain alignment. An observable consequence of the strong forces exerted through bond formation between surface and adsorbate is the lifting of the herringbone reconstruction when chemisorbing a monolayer of iodine on Au(111), commonly

observed in this thesis. In contrast, upon physisorption the interactions are very weak as they arise mainly due to van der Waals forces. Hence, the electronic structure of the adsorbate is hardly modified upon physisorption. The attractive potential holding a physisorbed particle on a surface is due to mutually induced dipole moments in the bonding partners.¹⁴⁸ Physisorption is often a preliminary stage of a stronger chemisorption. Hence, the physisorbed state can be regarded as a local energy minimum that can be transitioned to the chemisorbed global energy minimum. A recent publication showed the transition from a physisorbed to chemisorbed state by overcoming a measurable energy barrier with a carbon monoxide functionalized AFM tip.¹⁴⁹ Again the surface plays a crucial role for adsorption processes. This is nicely shown by comparing the adsorption of a pentacene molecule on Au(111), Ag(111), and Cu(111) surfaces, respectively. Pentacene molecules are physisorbed on Au(111), weakly chemisorbed on Ag(111) and strongly chemisorbed on Cu(111), underpinning the strong influence of the substrate.¹⁵⁰ A molecule chemisorbed on a surface has binding energies of a couple of eV.⁵⁰ This explains why a pure thermal removal of impurities is often not possible. The binding energy of physisorbed molecules usually lies between 10 – 100 meV explaining why physisorbed molecules often need low temperatures to stay adsorbed.¹⁴⁸ These differences in adsorption energies is also reflected in the adsorption height of 2 – 3 Å compared to 3 – 4 Å for chemisorbed and physisorbed molecules, respectively.^{50, 148} Nevertheless, the transition between physisorption and chemisorption is not sharp, accordingly they cannot be always clearly separated. Especially for large molecules, the interplay of strong (chemical) and weak (van der Waals) interactions *via* specific functional groups can lead to complex adsorption scenarios.⁷⁷ The different places, i.e. adsorption sites, a molecule can occupy are noteworthy. The most important adsorption sites on the (111) facets of the coinage metals are: three-fold hollow sites, two-fold bridge sites, and six-fold top sites. For a small atom or molecule adsorbed above one of these sites the lateral forces acting on the molecule are canceled out. In chapter four, the templating effect of the substrate will be demonstrated by comparing organometallic networks derived from the 1,3,5-tris(4-bromo-3,5-dimethylphenyl)benzene (MTBB/1) precursor on copper and silver surfaces. The observed differences in network quality can be explained by calculating adsorption energies for the different adsorption sites on the Ag(111) and Cu(111) surfaces. Desorption of halogens occurs during the on-surface reactions presented in chapter five and six. Therefore, desorption will briefly be discussed in the next paragraph.

A solid surface exposed to a gas atmosphere at constant temperature is in equilibrium i.e. the adsorption and desorption rates are equal. In chapter six iodine monolayers were generated on Au(111) and Ag(111) surfaces. Therefore, the samples were exposed to a defined iodine atmosphere built up with a leak valve. After closing the leak valve the equilibrium between adsorption and desorption vanishes, but the iodine remains on the surface. In the simplest case, thermal desorption sets in when the energy of the adsorbed particle exceeds the adsorption energy.¹⁴⁸

A relatively simple method based on desorption from an adsorbate-covered surface is the temperature programmed desorption (TPD). This technique is used to measure adsorption energies. TPD experiments are carried out by incrementally heating of the substrate and synchronously measuring the number of desorbing molecules or atoms. This is typically performed with a linear temperature ramp while counting the desorbing particles with a mass spectrometer. Different desorption temperatures can be associated with different adsorption energies of the respective adsorbate. These differences originate from non-equivalent adsorption sites. In some systems one can discriminate between particles originating from: multilayers, monolayer terraces, step edges, kinks or vacancies with increasing the desorption temperature, i.e. the adsorption energy, respectively. Especially the peak of the monolayer terrace can be broad because of the above mentioned different adsorption sites. But desorption kinetics also influences the peak shape. Measurements at different heating rates can help to quantify the kinetic influence. Additionally, coverage can also influence the adsorption energy. From TPD experiments one can also gain insights into the desorption mechanism. For instance, associative desorption of bromine during formation of GNRs on Au(111) was tracked by TPD measurements.¹⁵¹ In summary, this straightforward technique offers insights into the desorption process, over a defined temperature range, within reasonable time frames.

TP-XPS measurements, as discussed in section 2.2.8, can also be used to study thermally induced desorption. Therefore, the intensity loss of a specific core level can be associated with a loss of material due to desorption. For instance, thermal desorption of bromine, i.e. an intensity loss of the Br 3d core level, at elevated temperatures was monitored by TP-XPS measurements (cf., Figure 5.1). Also a possible loss of carbon, i.e. desorption of molecules, with increasing temperature was tracked by TP-XPS measurements of the C 1s core level in chapter five. A drawback of TP-XPS compared to TPD measurements is

that no information on the desorbing species is obtained. Nevertheless, the TP-XPS measurements in chapter five were ideally suited to follow both temperature induced on-surface reactions and loss of material, synchronously. In the following pages a brief introduction of thermodynamically as well as kinetically controlled processes will be presented.

3.4 Thermodynamically versus kinetically controlled processes

In chapter five the activation step of surface-assisted Ullmann coupling, i.e. the debromination of TBB, is comparatively studied on Ag(111) and Au(111) surfaces by TP-XPS measurements of the Br 3d core level. Debromination progresses vastly differently with increasing temperature on these two surfaces. On Ag(111) the activation can be modeled by first-order reaction kinetics, contrary to the Au(111) surface where thermodynamic control can explain the observed behavior. Therefore, the following section aims to explain the characteristics of thermodynamically compared to kinetically controlled reactions, and introduces the concepts used for modeling the experimental data.

In chemistry it is common to distinguish between thermodynamically and kinetically controlled reactions. As it is in most cases impossible to predict reaction kinetics based on thermodynamic theory, the reactions of interest have to be studied experimentally. With the knowledge gained by these experiments it becomes feasible to predict the kinetics of similar reactions.¹⁵² Generally, a thermodynamically controlled reaction proceeds in order to gain maximum amount of energy, i.e. the pathway with the largest negative reaction energy.¹⁵³ Hence a thermodynamically controlled reaction aims to find the global free energy minimum, contrary to kinetically controlled processes which take the route of the lowest activation energy (energy barrier). Furthermore, the back reaction from the product to the reactant has to be possible with reasonable rates for a thermodynamically controlled reaction, whereas for a kinetically governed process no or very slow back reactions may occur.¹⁵² In Figure 3.2 the reactant (R) can either form product B by a kinetically governed process or a follow the thermodynamically controlled reaction forming product A.

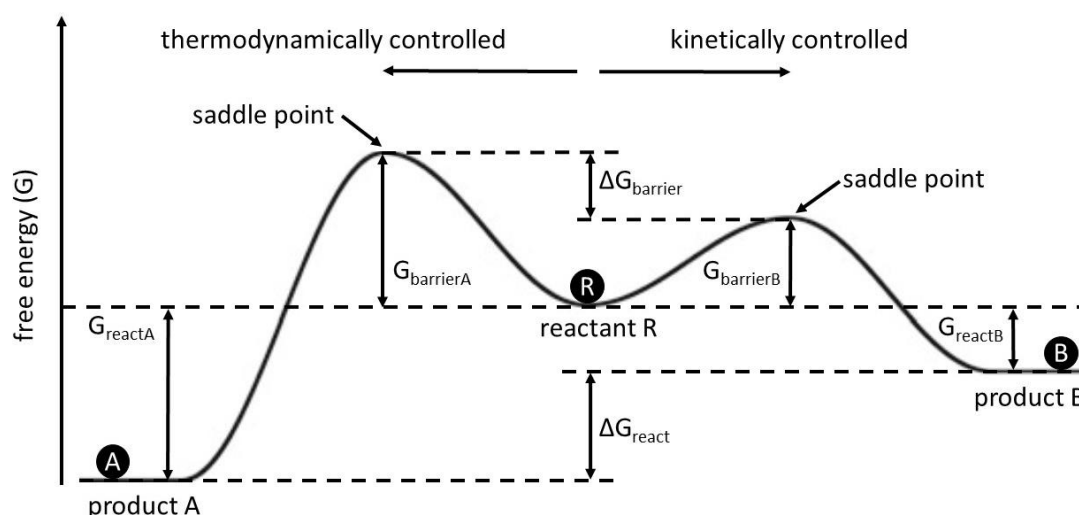


Figure 3. 2: Free energy landscape of a thermodynamically- versus a kinetically controlled process, forming product A or product B from the reactant, respectively. Adapted from Refs.^{152, 153}

The reactant is located in a local free energy minimum, enclosed by the saddle points on the free energy surface. The heights represent the activation energy barriers for product A and B respectively. As G_{barrier} is smaller for B, a kinetically controlled process will proceed in this direction, resulting in a local energy minimum. To maximize the energy difference between R and the possible products A and B, a thermodynamically governed process follows the reaction in order to minimize the free energy, leading to formation of A. In addition to these general trends mentioned above, the magnitude of $\Delta G_{\text{barrier}}$ and ΔG_{react} influences the pathway a reaction prefers. For example, large values of $\Delta G_{\text{barrier}}$ lead to kinetic controlled processes as one of the products is formed more likely, and no equilibrium between possible products is established. Moreover, kinetically driven processes become more likely with increasing ΔG_{react} , leading to large reaction rate differences of competing reactions. Consequently, once the reaction barrier is overcome, the reaction is practically completed. Contrarily, for small $\Delta G_{\text{barrier}}$ values of the two competitive processes the magnitude of ΔG_{react} determines the equilibrium position and the process is thermodynamically controlled.¹⁵²

The free energy landscape depicted in Figure 3.2 intends to discriminate between kinetically and thermodynamically controlled processes, in a simple model system. In reality the situation is usually more complex, as the global free energy minimum of a system needs to be defined and the reaction pathway is usually more sophisticated, i.e.

multiple steps are required to get to the final product.¹⁵³ Additionally a pure thermodynamically as well as a pure kinetically controlled process does not exist, since every thermodynamically controlled reaction needs an infinite time to equilibrate, and every kinetically controlled reaction undergoes some equilibration before all reactants are consumed.

A thermodynamically controlled process implies that forth and back reaction, i.e. dehalogenation and halogenation, are in dynamic equilibrium. Therefore, the Gibbs free energy (G) is of paramount importance. In a completely reversible process, G is the maximum amount of work that may be done by a system at constant pressure and temperature. The Gibbs free energy was defined by Josiah Williard Gibbs in order to find out whether a process proceeds spontaneously at fixed pressure and temperature.

$$G = H - TS \quad (3.1)$$

The Gibbs free energy is defined as the enthalpy (H) minus the product of entropy (S) and temperature (T). The equilibrium of a system (constant pressure and temperature) is found when the Gibbs free energy is at a minimum. This can be achieved either by a small negative value for the enthalpy or a large positive value for the entropy term TS . G describes a competition between entropy and energy, with the temperature acting as the factor determining their relative weight.¹⁵⁴ Hence, at low temperatures, the entropic term is small like for liquids and solids with a high attractive potential between their molecules/atoms. Increasing the temperature can lead to a situation where energy and entropy contribute in a comparable magnitude, like for the coexistence of a liquid (low energy, low entropy) and a vapour phase (high energy, high entropy) at phase equilibrium conditions. Further increase of the temperature leads to the dominance of the TS term of the Gibbs free energy. Therefore, high entropy states, like the vapour phase become thermodynamically favorable. The above mentioned trends are also influenced by the pressure, nevertheless the correlation of increasing the entropy term with increasing the temperature persists. Especially the temperature for the liquid to vapour phase transition depends on the pressure. A prominent example is the shifting boiling point of water owing to altitude induced pressure changes on Earth. Often ΔG is used to express the change in free energy between reactants and products. A reaction is called exergonic if ΔG is

negative, i.e. the reaction releases energy, in contrast to endergonic reactions that absorb energy ($\Delta G > 0$).

$$\Delta G = \Delta H - T\Delta S \quad (3.2)$$

For a chemical reaction with the products having a smaller free energy than the educts, the reaction proceeds in the direction of the products and vice versa. Generally, reactions with negative ΔG proceed spontaneously, as opposed to processes with a positive ΔG that need an additional energy input to occur. Nevertheless, the spontaneity of a reaction does not allow predictions on the reaction rate. An example for this is the solid-solid phase transition from diamond to graphite, that has a negative ΔG at standard conditions, however the ultra slow reaction kinetics hinders its occurrence. This shows that the fact whether a reaction is thermodynamically advantageous does not allow conclusions on the reaction rate. The reason for this is the fact that ΔG is obtained by comparing initial and final states of a reaction, but does not contain activation barriers that may exist. In order to determine reaction rates for a thermodynamically governed process, the Gibbs free energy of activation ΔG^* is necessary.

$$\Delta G^* = \Delta H^* - T\Delta S^* \quad (3.3)$$

For this purpose the transition state theory (TST), i.e. the assumption that a reaction from one local minimum to another is separated by a saddle point on the free energy surface is essential. TST can be used to qualitatively understand how a reaction proceeds and for calculating of the activation enthalpy ΔH^* and entropy ΔS^* . Considering a reaction without intermediate state (only one transition state), the rate constant (ν) between two states at a given temperature can be calculated with the Eyring equation.¹⁵³

$$\begin{aligned} \nu &= \frac{k_B T}{h} e^{-\frac{\Delta G^*}{k_B T}} \\ \nu &= \frac{k_B T}{h} e^{\frac{\Delta S^*}{k_B}} e^{-\frac{\Delta H^*}{k_B T}} \end{aligned} \quad (3.4)$$

With h as Planck's constant and k_B as Boltzmann's constant ν can now be determined after equation 3.4. In the following the different descriptions that were used to model the dehalogenation on Au(111) and Ag(111) surfaces are briefly outlined.

The dehalogenation of TBB was modelled as a reversible process on Au(111), implying that the formed radical can recombine with the bromine. Direct evidence for the recombination process is given by STM images in Figure 5.8 (f), clearly showing reformed C-Br bonds after annealing to 250°C. Therefore, the debromination can be considered as a thermodynamically controlled process with an equilibrium between dehalogenation and halogenation. The 3-fold brominated molecule can be modeled by a four level system, depending on the number of bromine atoms remaining at the molecule ($C_{24}H_{15}Br_3$, $C_{24}H_{15}Br_2$, $C_{24}H_{15}Br$, $C_{24}H_{15}$). Accordingly, at a given temperature, ΔS and ΔH are the only free parameters (assuming equal ΔS and ΔH values for each debromination step). By means of the partition function of the four level system, the total probability of dehalogenation (P_{dehal}) can be calculated. P_{dehal} is dependent on the temperature and was experimentally tracked with TP-XPS measurements. In chapter five the experimental data was fitted and the experimentally deduced values for ΔS and ΔH were compared to theoretical values.

The debromination as an isolated reaction step is exothermic on Ag(111), and additionally accompanied by translational entropy gain arising from the dissociated bromine. Together the reaction is also exergonic. Since the C-Br cleavage is exergonic on Ag(111), debromination of TBB molecules can be modeled by a kinetic approach. Hence, only the activation barrier hinders the dehalogenated state to occur already at low temperatures. Once the activation barrier is overcome the molecules will remain dehalogenated. This enables the evaluation of rate constants (ν) with an Arrhenius relation.

$$\nu = A \exp[-E_{barrier}/k_B T] \quad (3.5)$$

The rate constant directly depends on the energy barrier ($E_{barrier}$), and the temperature T . A is a pre-exponential factor derived from collision theory with the unit s^{-1} . In a simplistic picture A can be regarded as the attempt frequency which, together with the reaction probability $\exp[-E_{barrier}/k_B T]$, yields the reaction rate. To a first

approximation A can be viewed as the frequency of the C-Br stretch vibration. For the calculation in chapter five A was fixed and ν values were evaluated for the temperature window of interest.

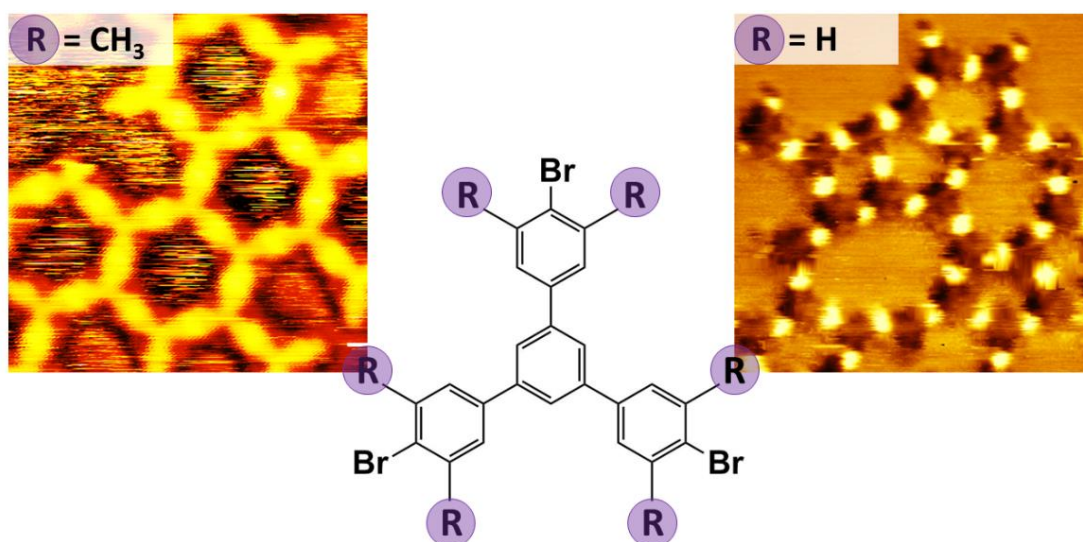
This section aimed to discriminate between thermodynamically as well as kinetically controlled processes in on-surface reactions. In chapter five these concepts will be used to model the TP-XPS derived findings on the debromination on Au(111) and Ag(111), respectively. The experimental results are presented, discussed, and examples what kind of experiments could be conducted in future research are pointed out in the following.

Chapter 4

On-surface synthesis of two-dimensional organometallic networks

– reducing topological defects by imposing steric hindrance

In this chapter, organometallic networks derived by on-surface Ullmann coupling of 1,3,5-tris(4-bromo-3,5-dimethylphenyl)benzene (**1**) molecules are investigated under UHV conditions. In contrast to the thoroughly studied 1,3,5-tris(*p*-bromophenyl)benzene precursor (**2**), this precursor is substituted with bulky side groups that reduce the bond angle flexibility of the C-M-C angle after dehalogenative coupling reactions. Organometallic networks derived from both molecules are comparatively studied by STM on Cu(111) and Ag(111) surfaces. The experimental findings are underpinned by evaluation of bond angle dependent energy variations, and by studying the different adsorption geometries on Cu(111) versus Ag(111) by DFT.*



* The results this chapter is based on were published as: Massimo Fritton, Katrin Otte, Jonas Björk, Pronay Kumar Biswas, Wolfgang M. Heckl, Michael Schmittel, and Markus Lackinger. **The influence of *ortho*-methyl substitution in organometallic self-assembly – a comparative study on Cu(111) versus Ag(111)**. Chem. Commun. 54 (2018), 9745-9748. Reproduced by permission of The Royal Society of Chemistry. Copyright 2018 by the Royal Society of Chemistry.

I performed all STM experiments, the corresponding data analysis and interpretation, and prepared the manuscript under supervision of Prof. Lackinger. Bond angle dependent energy variations were calculated by Dr. Katrin Otte (Leibniz-Rechenzentrum). DFT calculations of different adsorption geometries were done by Prof. Jonas Björk (Linköping University). The molecules were synthesized in the group of Prof. Schmittel (Siegen University).

4.1 Abstract

Metal surface-induced dehalogenation of precursors is known to initiate self-assembly of organometallic networks, where tectons are connected *via* carbon-metal-carbon (C-M-C) bonds. Even though reversibility of the C-M-C bonds facilitates structural equilibration, defects associated with highly bent organometallic linkages are still commonly observed. By introducing a steric hindrance to reduce the C-M-C bond angle flexibility, we find well ordered organometallic networks of an *ortho*-methyl substituted 1,3,5-tris(*p*-bromophenyl)benzene analogue on Cu(111) after room-temperature (RT) deposition and on Ag(111) after annealing.

4.2 Introduction

Ullmann-type dehalogenative couplings are the most abundantly employed reactions in on-surface synthesis.⁵ Thereby surface-stabilized radicals are generated by the surface-assisted dissociation of carbon-halogen bonds (Cl, Br, I) from precursors. Yet, instead of direct covalent coupling, organometallic intermediates based on C-M-C linkages are

always observed on copper and silver,^{132, 155-157} and occasionally on gold surfaces.^{116, 158} In these intermediates structural equilibration can be promoted by mild annealing, thereby confirming bond reversibility of the organometallic linkages. Highly ordered organometallic networks can thus be formed with a topology controlled by the precursor's halogen substitution pattern. These networks finally serve as templates for the thermally activated isostructural conversion into similarly ordered covalent networks.^{28, 144, 159, 160} Meanwhile, however, organometallic self-assembly itself represents a promising arena for the fabrication of nanostructures with a fairly high stability.

On surfaces the C-M-C linkages assume mostly straight alignments, but frequently observed topological defects indicate a remarkable bond angle flexibility. For instance, the three-fold 1,3,5-tris(*p*-bromophenyl)benzene precursor (**2**, cf., Figure 4.1 (b)) would ideally afford a honeycomb network, but tetragonal, pentagonal, and heptagonal pores are abundant.¹⁶¹

To improve the initial structural quality of organometallic networks we propose to exploit the steric hindrance introduced by bulky side groups at the *ortho*-positions. The underlying idea is to increase the energetic cost of angled C-M-C linkages to impose a strong bias for the exclusive formation of straight linkages. This strategy is tested in the self-assembly of 1,3,5-tris(4-bromo-3,5-dimethylphenyl)benzene (**1**, cf., Fig 4.1 (a) and (c) and Appendix A for synthesis) on Cu(111) and Ag(111) surfaces. Both surfaces differ in temperature thresholds for dehalogenation as well as molecular adsorption energies and organometallic bond strength. Comparative experiments under identical conditions (e.g. deposition and heating rates) were carried out for the non-methylated analogue **2**.

4.3 Results and Discussion

Samples were prepared under ultra-high vacuum conditions and *in-situ* characterized by STM. Upon RT deposition of **1** onto Cu(111) molecules form fully reticulated networks as depicted in Figure 4.1 (a) and (c). The measured center-to-center distance of (1.6±0.1) nm unambiguously indicates C-Cu-C linkages as corroborated by the scaled overlay. Yet, the normally observed pronounced STM contrast of the organometallic Cu atoms is merged into a combined feature with the four *ortho*-methyl groups. A striking observation

is the absence of topological defects. Even though the network exhibits other defects, such as missing molecules or incomplete pores, both molecular positions and orientations strictly obey the ideal honeycomb network.

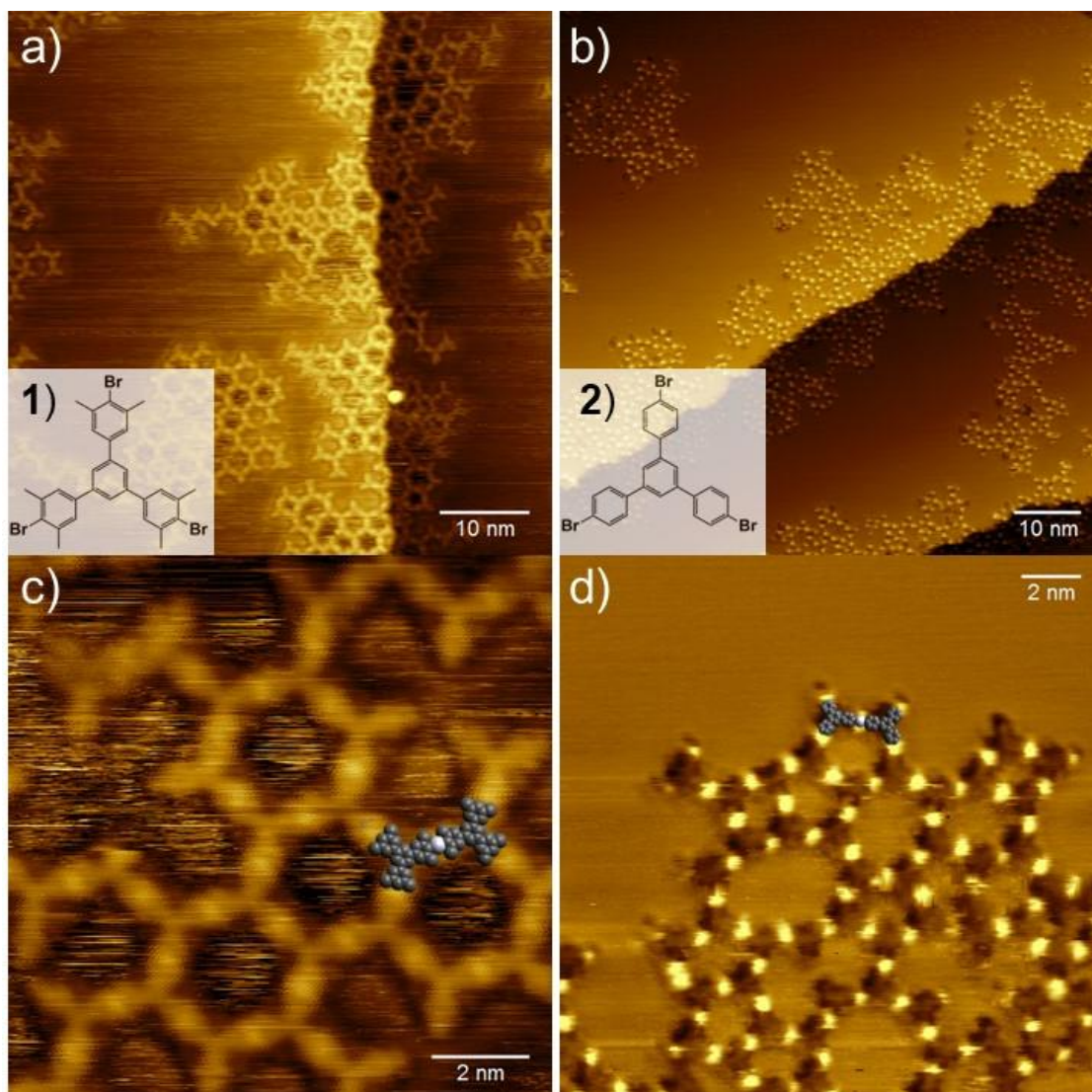


Figure 4. 1: STM images of organometallic networks on Cu(111) acquired after RT deposition: (a) **1**, (b) **2** overview STM images; (c) **1**, (d) **2** close-up images; The inserts show the respective molecular structures;

Attempts to further heal out these defects and increase the network's compactness by mild annealing at 100 °C did not result in notable differences. Only molecules trapped within pores as frequently seen after RT deposition were no longer observed (cf., Appendix Figure A.1). To further assess the influence of the *ortho*-methyl substituents, comparative complementary experiments were carried out with the unsubstituted analogue **2**. The corresponding STM images in Figure 4.1 (b) and (d) obtained on

Cu(111) after RT deposition display a similar intermolecular distance of (1.6 ± 0.1) nm, confirming the anticipated formation of organometallic networks.¹⁶² The occasionally observed inverted contrast (molecules appear dark/low) emphasizes the organometallic copper atoms (bright protrusions). Consistent with previous studies, the networks are entirely irregular with tetragonal up to decagonal pores and only approximately 20% hexagonal pores.¹⁶¹ Formation of these irregular pores is obviously associated with bending of the C-Cu-C linkages, but additional flexibility in the network may arise from bending the C-C-M or the covalent phenyl-phenyl bonds.¹⁶³ The organometallic networks obtained directly after RT deposition of both molecular precursors (cf., Figure 4.1) were identically heated to 150°C. Subsequently acquired STM images are presented in Figure 4.2.

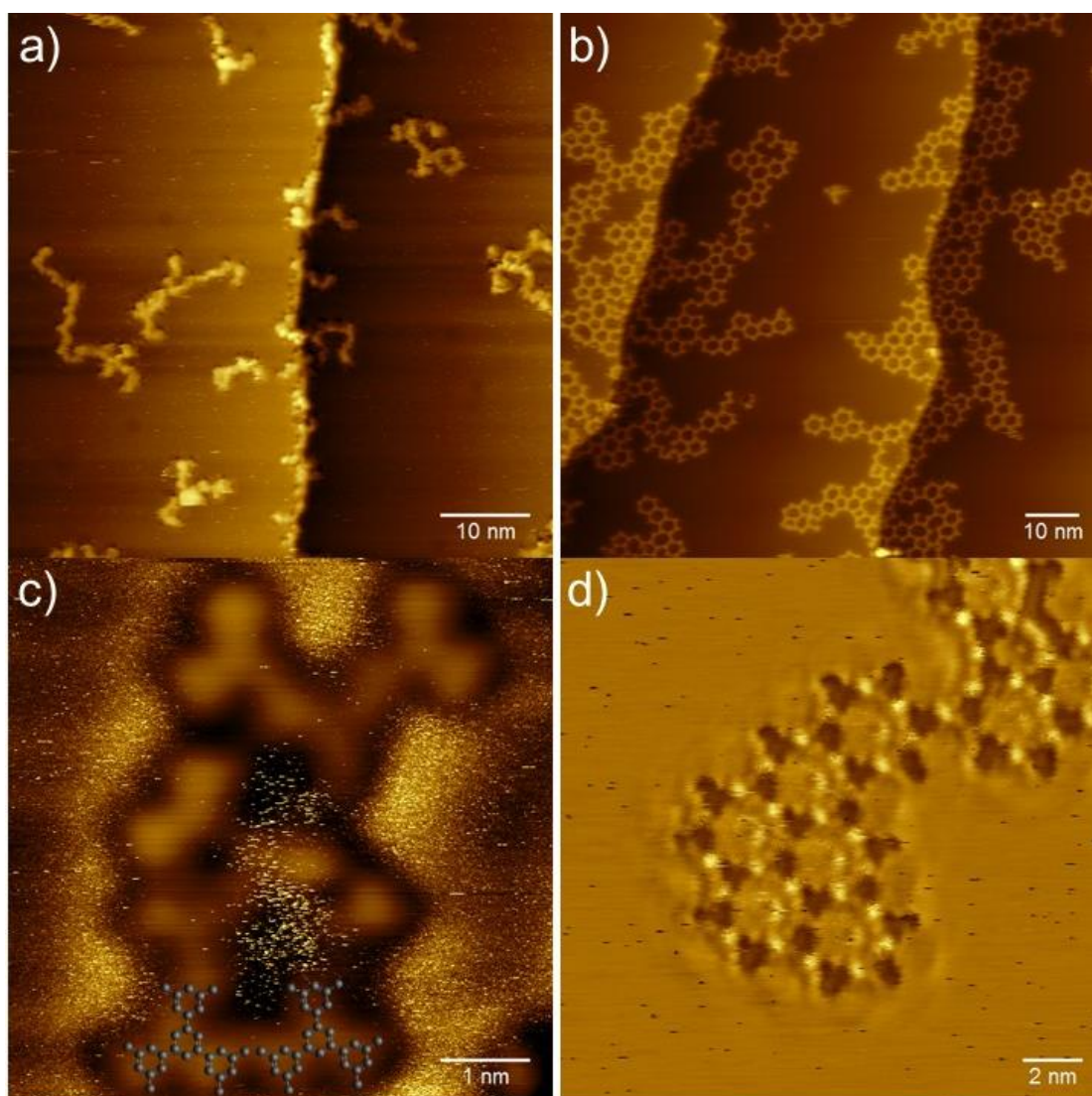


Figure 4. 2: STM images on Cu(111) acquired after RT deposition and annealing to 150°C: (a) **1**, (b) **2** overview STM images; (c) **1**, (d) **2** close-up images;

Higher annealing of **1** at 150 °C resulted in disordered structures as demonstrated in representative STM images shown in Figure 4.2 (a) and (c). Single molecular entities can still be identified by means of their three-fold footprint. Overlays suggest covalent interlinking, yet without site selectivity, at unfunctionalized positions (cf., Figure 4.2 (c)). It is noteworthy that at these temperatures C-H activation can already occur on copper surfaces.¹⁶⁴ For precursor **2** the quality of the organometallic networks on Cu(111) could be improved by heating to 150 °C as demonstrated by the STM image in Figure 4.2 (b) and (d) predominantly showing hexagonal pores. The statistical analysis of pore geometries presented in Figure 4.3 substantiates this preference.

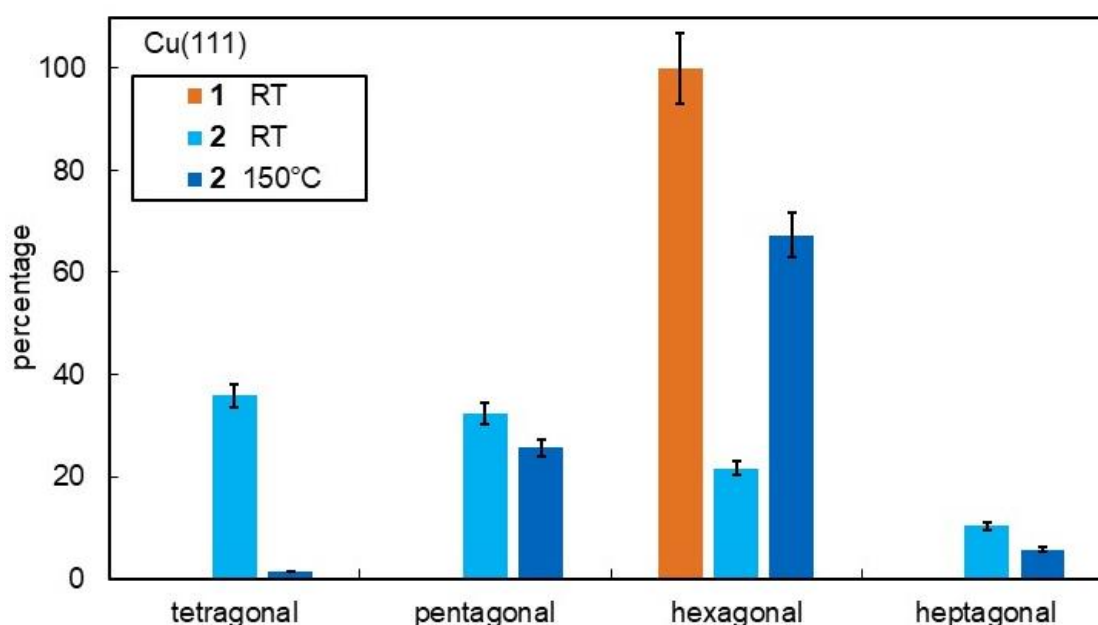


Figure 4. 3: Histograms of observed pore geometries for **1** and **2** on Cu(111) after RT deposition and after annealing. For **2** at RT the occasionally observed octagonal to decagonal pores were added to the heptagonal pores.

Such findings suggest both a reversibility of the C-Cu-C linkage and a preference for straight organometallic links. Still, both the overview images in Figure 4.1 (a) and (b) and the histograms in Figure 4.3 consistently unveil an inferior network quality as compared to **1**. Moreover, heating of **2** at 150 °C did not induce any C-H activation as observed for **1**. This marked difference between **1** and **2** at higher surface temperatures suggests an enhanced reactivity of the *ortho*-methyl substituents. However, upon annealing of **2** at 150 °C first organometallic linkages were converted into covalent bonds (cf., Figure 4.2 (b) right upper corner), thereby ceasing structural equilibration.

Similar experiments were also conducted on Ag(111), the prototypical surface for organometallic self-assembly.^{156, 159} STM data acquired for both precursors **1** and **2** are summarized in Figure 4.4. After RT deposition, fully reticulated networks are observed for **1**, indicating a full debromination also on this less reactive surface.

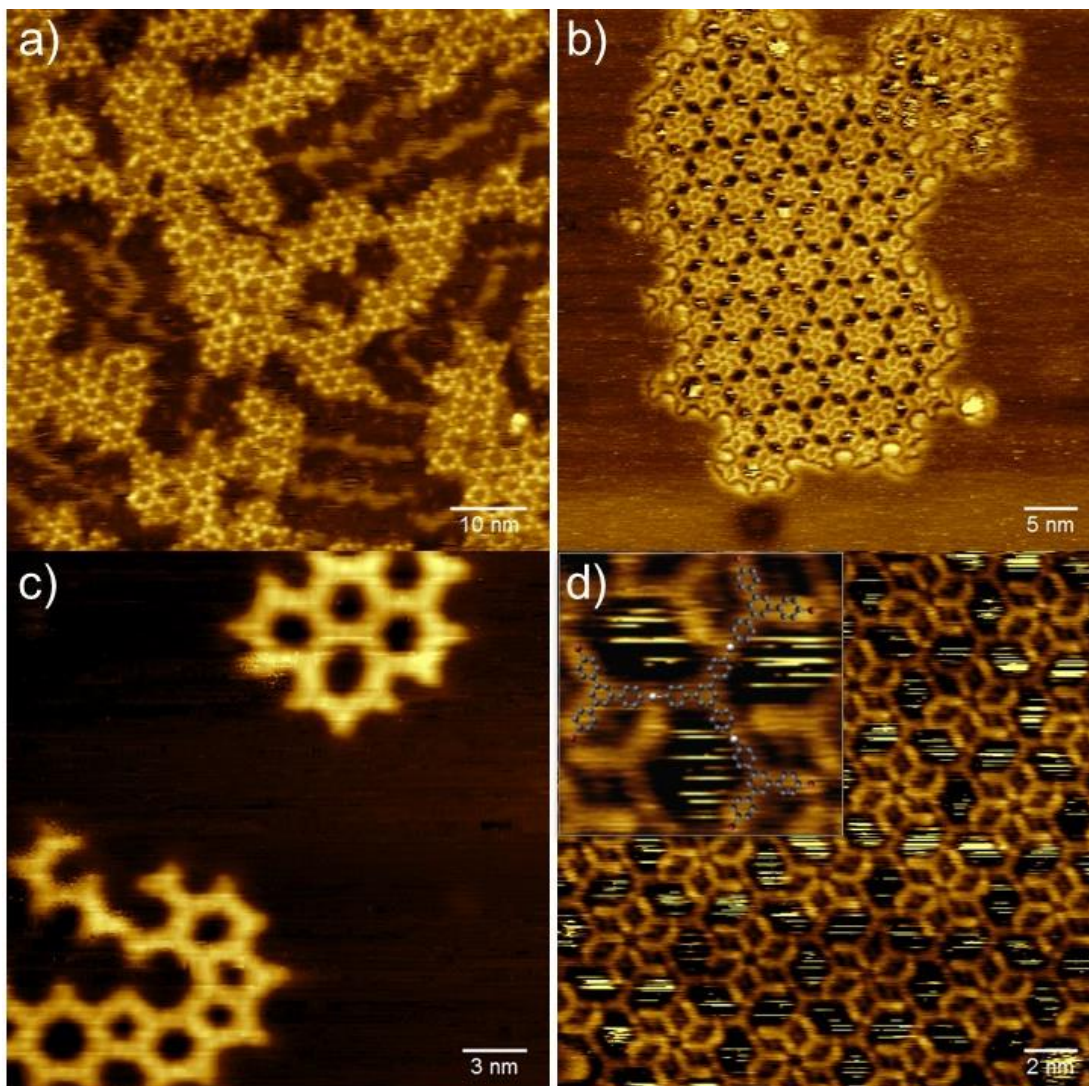


Figure 4. 4: STM images on Ag(111) acquired after RT deposition: (a) **1**, (b) **2** overview STM images; (c) **1**, (d) **2** close-up images; The insert in (d) highlights the basic motif of this highly ordered structure, i.e. the three-fold symmetric organometallic tetramer with scaled molecular overlay.

Even though many hexagonal pores are formed, the pentagonal and heptagonal pores exemplary shown in Figure 4.4 (c) still account for almost 30% of all pores (cf., Figure 4.6). Albeit tetragonal or octagonal pores were not observed, the overall structural quality of **1** on Ag(111) remains lower than that on Cu(111) directly after RT deposition. The

topology and quality of the organometallic networks on Ag(111) remained unaltered after annealing at 100 °C (cf., Appendix A), but annealing to 150 °C resulted in structural equilibration and healing of defects, without any indication of covalent bond formation.

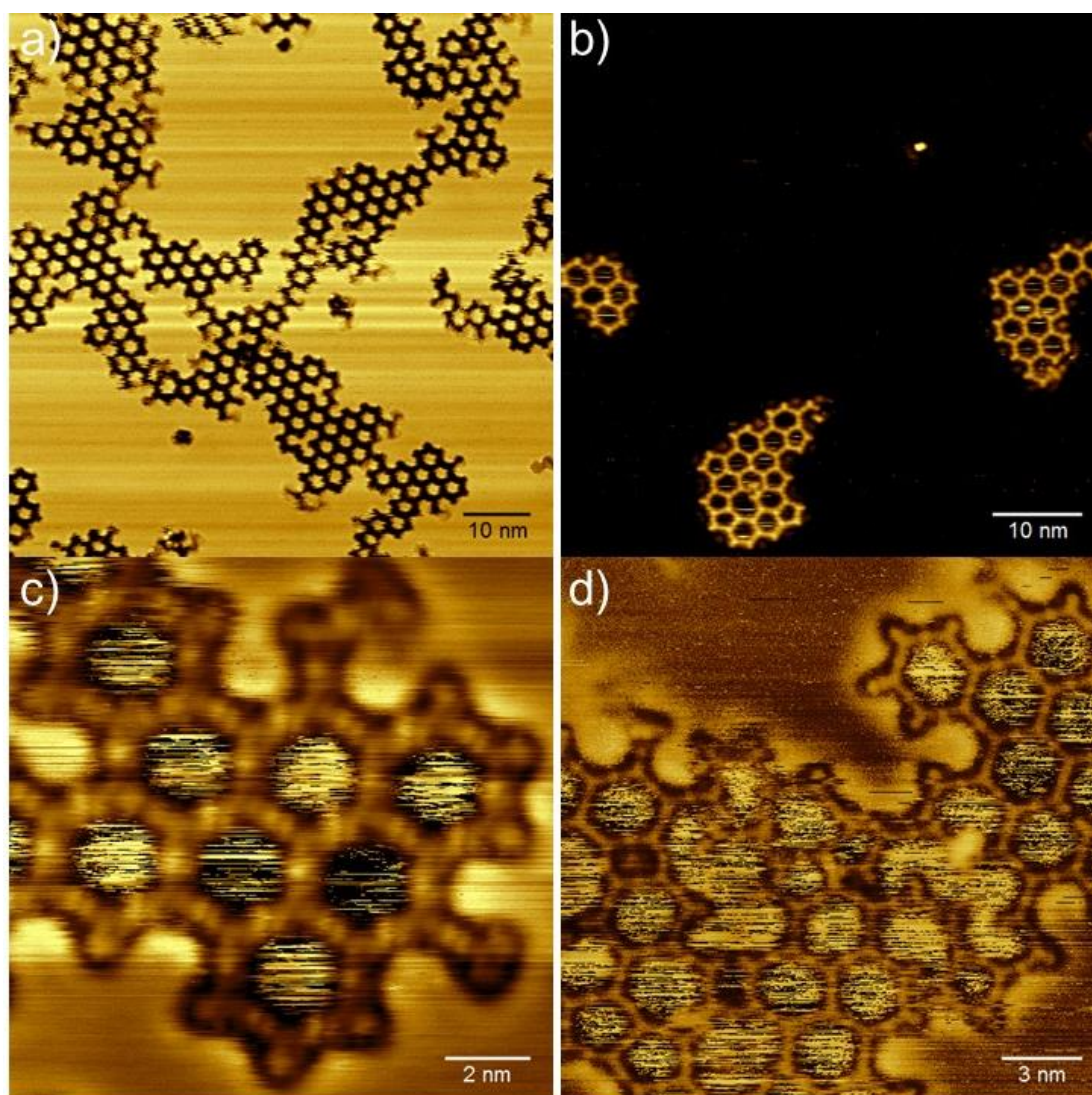


Figure 4. 5: STM images of organometallic networks on Ag(111) acquired after RT deposition and annealing to 150°C: (a) **1**, (b) **2** overview STM images; (c) **1**, (d) **2** close-up images;

The resultant highly ordered organometallic networks shown in Figure 4.5 (a) and (c) exhibit nearly 100% hexagonal pores (cf., Figure 4.6). Pentagonal pores account for less than 5% and were observed exclusively at domain boundaries. For comparison analogous experiments were conducted with precursor **2** on Ag(111). STM data acquired directly after RT deposition and after annealing to 150 °C are depicted in Figures 4.4 (b), (d) and 4.5 (b), (d). Even after annealing, 25% of all pores still remained non-hexagonal.

Interestingly, the RT image shows the previously reported, highly ordered flower structure.¹⁶² Its basic motif is a three-fold organometallic tetramer that is still brominated at its termini (cf., insert in Figure 4.4 (d) with scaled molecular overlay). These remaining bromine substituents either form halogen-halogen bonds or interact with the organometallic Ag atoms as recently proposed.¹⁶⁵ Full debromination of **1** versus partial debromination of **2** upon RT deposition appears counterintuitive, given that the methyl substitution should increase the Br adsorption height, and consequently the debromination barrier. However, the temperature used for sublimation of **1** is approximately 80 °C higher than that for **2**. Accordingly, these results indicate a so far unexplored, but important role of the arriving molecule's thermal energy for initial dehalogenation. Full debromination of **2** on Ag(111) is achieved upon annealing to 150 °C. The concomitant structural equilibration results in highly ordered hexagonal organometallic networks, yet with still higher defect densities than for **1**. Additionally, STM imaging suggests a clear separation of highly ordered (cf., Figure 4.5 (c), top right) and more defective regions (bottom left).

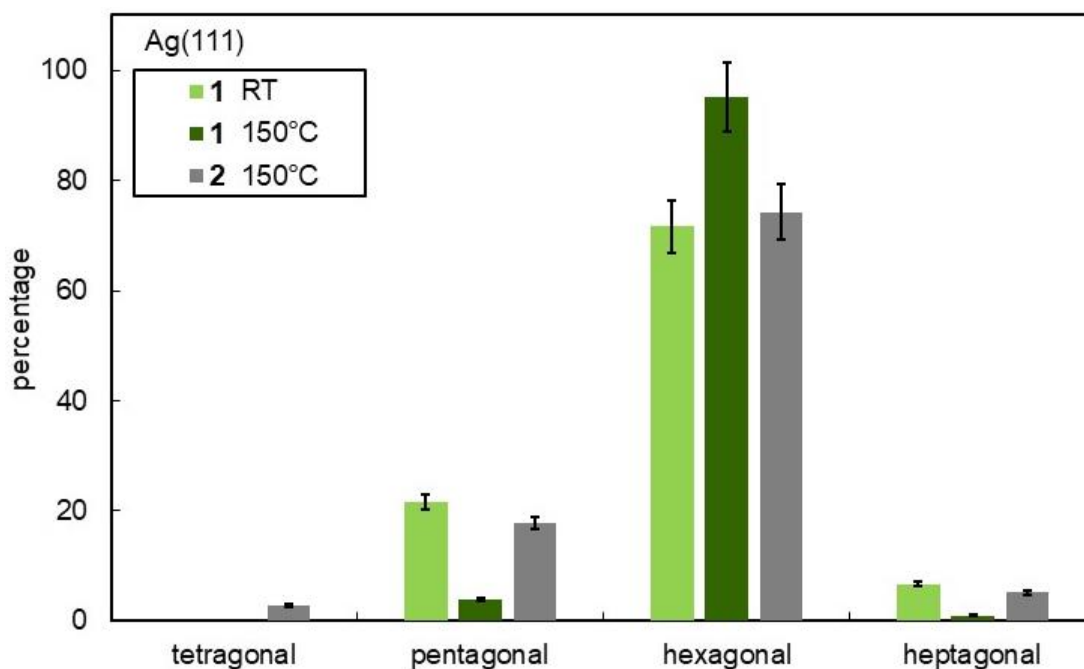


Figure 4. 6: Histograms of observed pore geometries for **1** and **2** on Ag(111) after RT deposition and after annealing.

Within the scope of our work we compared the unsubstituted precursor **2** with its *ortho*-methyl substituted analogue **1** on two different surfaces, both directly after RT deposition

and after annealing. The statistical analysis presented in Figures 4.3 and 4.6 indicate a higher structural quality of organometallic networks derived from the methylated precursor **1** in all cases. According to our working hypothesis, the origin lies in the steric hindrance imposed by the methyl substitution, giving rise to an energy cost for a deviation of the organometallic bond angle from the straight geometry. To estimate the magnitude of this effect, DFT simulations were performed on the simplified model system shown as insert in Figure 4.7 (cf., Appendix A for details).

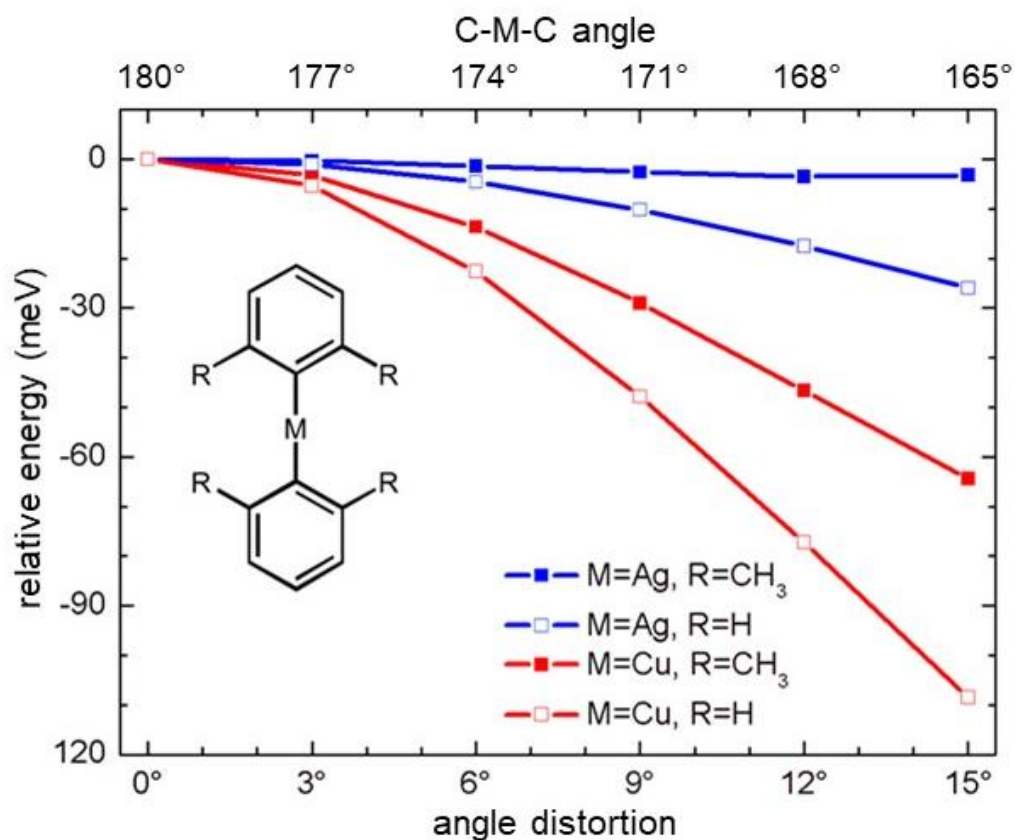


Figure 4. 7: DFT-derived energies for metal-linked phenyls as a function of angle deviation from a straight geometry with a 180° C-M-C bond angle. Energies were calculated for 3° increments, and the lines serve as a guide to the eye.

Energies were evaluated for C-M-C bond angles fixed between 180° to 165°, i.e. for 0° to 15° angle deviation from a straight geometry. The surface influence was mimicked by enforcing co-planarity between the two phenyl rings. Relative energies with respect to the straight geometry are depicted in Figure 4.7. Interestingly, straight linkages do not represent the energetic optimum. Significant deviations from a straight geometry were

earlier reported for C-M-C bonds based on X-ray diffraction data,^{166, 167} and corroborated later by DFT.¹⁶⁸

For the model systems (R = H) presented in Figure 4.7 the energy is lowered by 108 meV and 26.0 meV for a bond angle deviation of 15° at Cu and Ag, respectively. Methyl substitution reduces the energy differences to 3.0 meV (Ag) and 64 meV (Cu), clearly indicating an energetic cost due to steric hindrance. This methyl-related cost is smaller for C-Ag-C than for C-Cu-C linkages owing to the larger C-M bond lengths (0.223 nm versus 0.202 nm for straight linkages), resulting in a lower steric hindrance of the former. Interestingly, for Ag the contributions from steric hindrance and intrinsic properties of the organometallic linkages seem to mutually cancel each other, resulting in a negligible dependence of the energy on bond angle in the studied range. It is worth mentioning that pentagonal and heptagonal pores require bond angle deviations of 12.0° and 8.6°, respectively, in each organometallic linkage, provided that the entire distortion is localized there.

Even though this semi-quantitative assessment can provide a rationale for the improved structural quality in the organometallic networks derived from **1** as compared to **2**, it additionally gives rise to new questions. Based on these DFT results the formation of pentagonal pores should be energetically more favorable than that of hexagonal pores, even more so for Cu than for Ag. Yet, hexagonal pores facilitate energetically favorable crystalline structures with translational symmetry. Based on our experimental finding that pentagonal and heptagonal pores were present on Ag(111), but absent on Cu(111) after RT deposition of **1**, we propose a decisive additional surface influence. To support this hypothesis, the adsorption of **1** (with all bromine substituents replaced by metal atoms) was further studied by DFT (cf., Figure 4.8 and 4.9). On Cu(111), the most stable adsorption geometry is highly symmetric with the molecule centred above a three-fold hollow site and aligned with the surface's high symmetry directions (cf., Figure 4.8 (j)). Moreover, the 180° rotated, but otherwise equivalent adsorption geometry corresponds to the second most stable structure with a small energy difference of +0.10 eV (cf., Figure 4.8 (a)). The distinct energetic preference of these two adsorption geometries underpins a directing influence of the Cu(111) surface toward the honeycomb structure. Moreover, the highly irregular networks observed after RT deposition of **2** onto Cu(111) (cf., Figure 4.1 (b) and (d)) indicate a decisive influence of the *ortho*-methyl substituents.

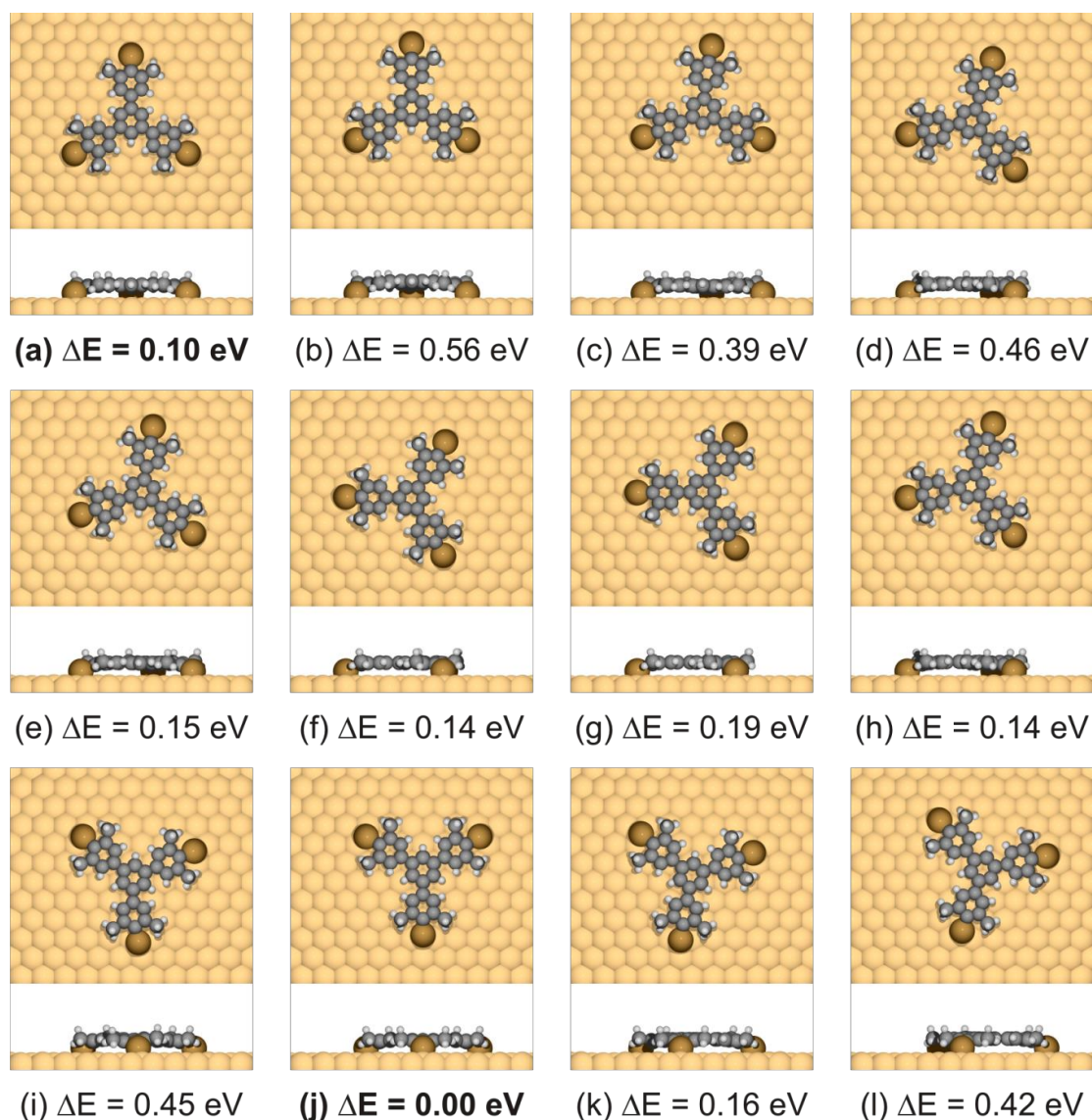


Figure 4. 8: Top- and side views of DFT-optimized geometries of 1 on Cu(111). All bromine substituents were replaced by Cu atoms to conform to the organometallic networks. The relative energies with respect to the most stable structure shown in (j) are given directly underneath each structure. The most stable adsorption geometry is highly symmetric: The molecule is centered above a three-fold hollow site and the mirror planes of surface and molecule are aligned. Note that the second most stable structure in (a) corresponds to the most stable structure with a 180° (or 60°) rotated molecule. These two structures are identical with respect to the topmost copper layer, but are different from the second copper layer on.

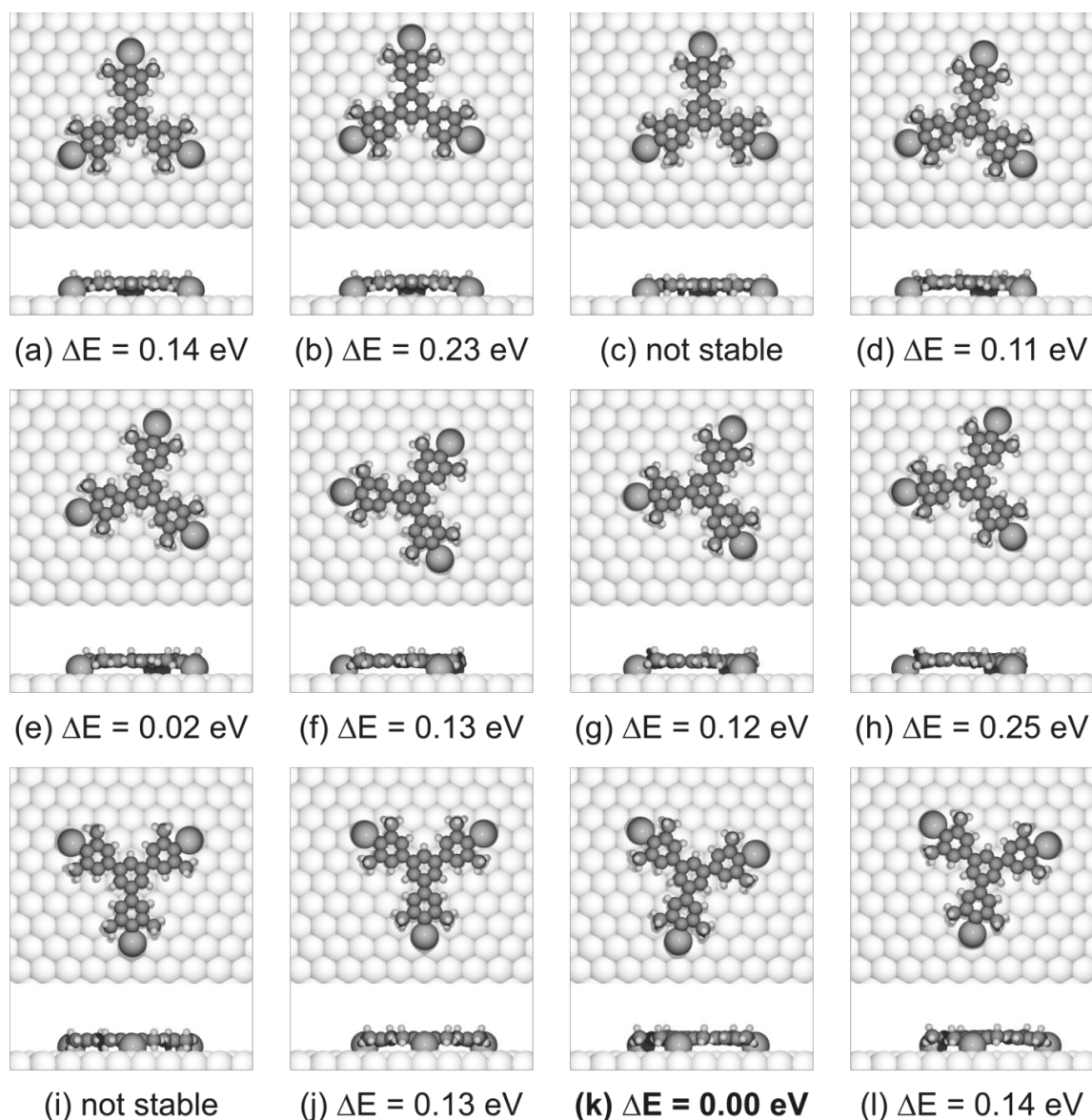


Figure 4. 9: Top- and side views of DFT-optimized geometries of 1 on Ag(111). All bromine substituents were replaced by Ag atoms to conform to the organometallic networks. The relative energies with respect to the most stable structure shown in (k) are given directly underneath each structure. The most stable adsorption geometry on Ag(111) is less symmetric than that on Cu(111): The molecule is still centered above a three-fold hollow site, but the mirror planes of surface and molecule are not aligned anymore. This gives rise to two energetically equivalent adsorption geometries with a clockwise and counterclockwise rotational angle of $\sim 12^\circ$ between the mirror planes of surface and molecule. For the two unstable adsorption geometries in (c) and (i) only the respective starting geometries are shown.

In contrast, on Ag(111) the most stable adsorption geometry was found for the peripheral Ag atoms above three-fold hollow sites, resulting in a rotation of approximately $\pm 12^\circ$ of the molecule with respect to the surface (cf., Figure 4.9). The energetic equivalence of these two mirror symmetric adsorption geometries on Ag(111) as well as the comparatively small energy differences between structures with slightly rotated molecules indicate an overall less pronounced azimuthal alignment of the molecules on Ag(111).

The *ortho*-methyl groups of **1** do not only increase the energy of non-straight linkages in organometallic networks, but also impose an insurmountable energy barrier for covalent aryl-aryl coupling. In the corresponding covalently linked biphenyl, the large steric hindrance results in orthogonal phenyl rings with a substantial rotational barrier, where a reduction of the dihedral angle to 60° would result in an energy increase of ~ 1.65 eV.¹⁶⁹ Even though covalent aryl-aryl coupling cannot be expected for **1**, it is nevertheless of interest to explore further chemical and structural changes upon annealing at higher temperatures. Distinct differences were observed between Cu(111) and Ag(111): on the former surface, irregular covalent aggregates were observed already at 150°C , whereas annealing at 200°C on the latter surface just resulted in desorption of the molecules. These differences can tentatively be explained by the well-known differences in adsorption strength on both surfaces.¹⁷⁰ At sufficiently high temperatures the organometallic linkages are dissociated, resulting in decomposition of the organometallic networks into individual molecular moieties, presumably as surface-stabilized radicals. On Ag(111) the respective adsorption energy is not sufficient to stabilize the molecules until they can interact, inevitably resulting in desorption. In contrast, on Cu(111) the individual molecular moieties remain stably adsorbed on the surface. Consequently, the activated molecules have the opportunity for covalent cross-linking at sterically accessible sites with a conceivable amount of C-H activation at the methyl substituents.¹³ The resulting larger covalent aggregates remain stably adsorbed on Cu(111).

4.4 Conclusion

In summary, we have demonstrated that reducing the bond angle flexibility of organometallic C-M-C linkages by introducing steric hindrance through *ortho*-methyl

substitution represents a viable strategy to improve the structural quality in organometallic self-assembly both on Cu(111) and on Ag(111). This is particularly evident on Cu(111), where for the non-substituted analogue **2** highly defective organometallic networks are kinetically trapped after RT deposition. Interestingly, pentagonal and heptagonal pores were also observed on Ag(111) even for the methyl-substituted precursor **1**. DFT calculations indicate an energetic cost for deviations of the organometallic linkages from a straight geometry due to the *ortho*-methyl groups. Nevertheless, bent C-Cu-C linkages still remain energetically more favorable, albeit to a lesser extent than for the unsubstituted case. Consequently, the observation of mostly hexagonal pores on Cu(111) after RT deposition and on Ag(111) after additional annealing is attributed to an alignment effect due to the underlying surfaces, resulting in an energetic preference for distinct molecular orientations as further corroborated by DFT simulations. These findings highlight once more the importance of symmetry matching between molecules, networks, and surfaces for the growth of highly regular networks. Future research will address the combination of improved organometallic self-assembly with possibilities for an isostructural conversion into covalent networks.

4.5 Experimental details

All experiments were carried out under ultra-high vacuum conditions with a base pressure below 3×10^{-10} mbar. Cu(111) and Ag(111) single crystal surfaces were prepared by cycles of Ne⁺ sputtering at 2.0 keV and radiative annealing to 500 °C. Prior to deposition of 1,3,5-tris(4-bromo-3,5-dimethylphenyl)benzene (**1**) or 1,3,5-tris(*p*-bromophenyl)benzene (**2**), the cleanliness and appropriateness of terrace sizes were verified by large scale STM images. **1** was synthesized as further described below, **2** was purchased from Sigma-Aldrich with a purity of 97%. Both molecules were deposited from home-built Knudsen cells, using the integrated quartz crystal microbalance as rate monitor.⁵² A crucible temperature of 200 °C was used for sublimation of **1** and of 120 °C for **2**, respectively. All thermal sample treatments were carried out with the same heater, using identical heating and cooling rates of 1.0 °C min⁻¹ and dwell times of 0.5 h at the target temperature to facilitate direct comparability.

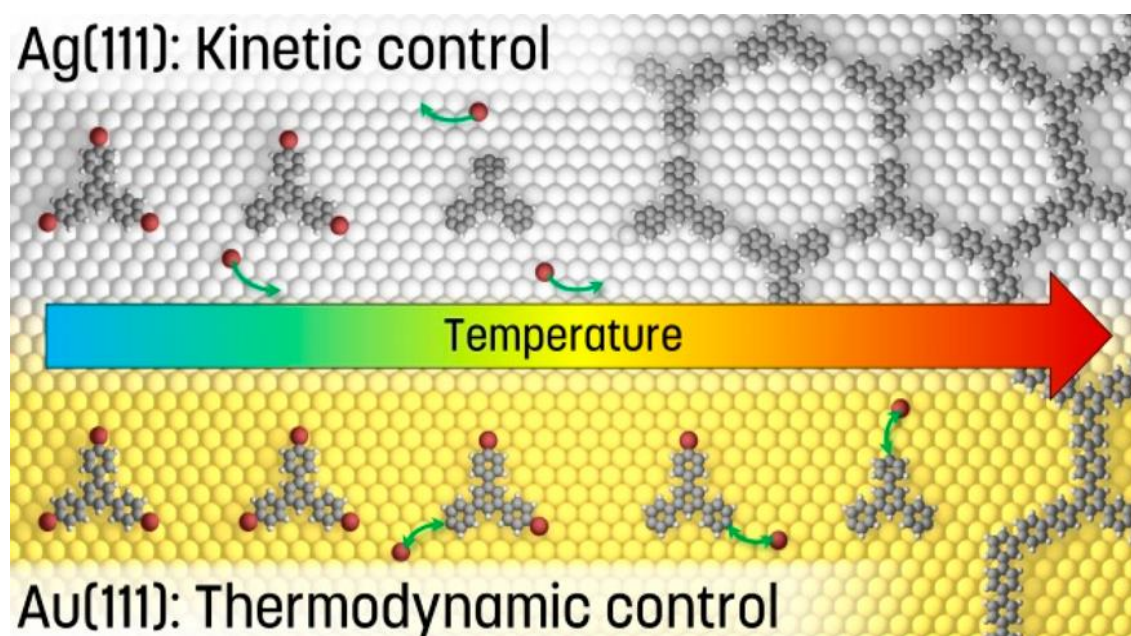
STM data were acquired at room temperature with a home-built instrument operated by a SPM 100 controller from RHK. Images were levelled and mean value filtered using the Gwyddion software. The pore geometry distributions were statistically analyzed for each molecule on both surfaces after RT deposition and after annealing to 150 °C, except for **2** on Ag(111) at RT and **1** on Cu(111) after annealing, where non-porous self-assembled and irregular covalent structures were observed, respectively. For each case at least 200 pores were evaluated and \sqrt{N} was used for the error bars.

Chapter 5

On-surface synthesis of two-dimensional polyphenylene networks

– thermodynamics versus kinetics in surface-assisted Ullmann coupling on Au(111) and Ag(111)

Dehalogenative C-C coupling of 1,3,5-tris(4-bromophenyl)benzene, yielding 2D porous frameworks on Au(111) and Ag(111) surfaces, is studied with STM and TP-XPS. Particular focus is put on the reaction progression with increasing temperature. This is directly assessable from chemical changes accompanied with each reaction step. The experimental findings are underpinned by DFT calculations. Interestingly, a thermodynamic model is needed to model the experimentally observed dehalogenation on Au(111), whereas first order reaction kinetics allow a description of the dehalogenation on Ag(111).



* The results this chapter is based on were published as: Massimo Fritton, David A. Duncan, Peter S. Deimel, Atena Rastgoo-Lahrood, Francesco Allegretti, Johannes V. Barth, Wolfgang. M. Heckl, Jonas Björk, and Markus Lackinger. **The role of kinetics versus thermodynamics in surface-assisted Ullmann coupling on gold and silver surfaces.** *J. Am. Chem. Soc.* 141, 12 (2019), 4824-4832. Reproduced with permission of The American Chemical Society. Copyright 2019 by The American Chemical Society.

I performed all STM experiments, analyzed and interpreted the corresponding data, and prepared the manuskript under supervision of Prof. Lackinger. DFT calculations were provided by Prof. Jonas Björk (Linköping University). The measurements at the synchrotron were done in collaboration with other co-authors.

5.1 Abstract

Surface-assisted Ullmann coupling is the workhorse of on-surface synthesis. Despite its obvious relevance, many fundamental and mechanistic aspects remain elusive. To shed light on individual reaction steps and their progression with temperature TP-XPS experiments are performed for a prototypical model system. The activation of the coupling by initial dehalogenation is tracked by monitoring Br 3d core levels, whereas the C 1s signature is used to follow the emergence of metastable organometallic intermediates and their conversion to the final covalent products upon heating in real time. The employed 1,3,5-tris(4-bromophenyl) benzene precursor is comparatively studied on Ag(111) versus Au(111), whereby intermolecular bonds and network topologies are additionally characterized by STM. Besides the well comprehended differences in activation temperatures for debromination, the thermal progression shows marked differences between the two surfaces. Debromination proceeds rapidly on Ag(111), but is relatively gradual on Au(111). While on Ag(111) debromination is well explained by first-order reaction kinetics, thermodynamics prevail on Au(111), underpinned by a close agreement between experimentally deduced and DFT calculated reaction enthalpies. Thermodynamically controlled debromination on Au(111) over a large temperature range implies an unexpectedly long lifetime of surface-stabilized radicals prior to covalent coupling, as corroborated by TP-XPS of C 1s core levels. These

insights are anticipated to play an important role regarding our ability to rationally synthesize atomically precise low-dimensional covalent nanostructures on surfaces

5.2 Introduction

On-surface synthesis provides unique synthetic routes to lowdimensional extended covalent nanostructures that are inaccessible by conventional wet-chemistry.^{7, 27, 96, 171-173} Thereby, the judicious choice of coupling reaction is a particularly sensible aspect, and knowledge from solution chemistry is in many cases not directly transferable to surface chemistry due to distinct surface influences. A growing number of coupling reactions, such as homocoupling of terminal alkynes,^{133, 174, 175} C-H activation,^{164, 176-178} decarboxylative coupling,¹⁷⁹ and various implementations of dehalogenative coupling,^{1, 180, 181} have been successfully adapted to surfaces. Nevertheless, dehalogenative aryl-aryl coupling, commonly referred to as surface-assisted Ullmann coupling, remains the most successful, and arguably the most predictable and controllable on-surface reaction.^{1, 42, 182} The formed C-C bonds bestow the resulting networks high stability and are invaluable for π -conjugation.^{144, 183}

Despite the great success of surface-assisted Ullmann coupling, the still limited structural quality, for example, topological defects in 2D networks, as well as restricted length and regularity of 1D wires and ribbons, represents a serious obstacle for applications of these materials. The key for improving the structural quality and unveiling the origins of defect formation is an atomistic understanding of the elementary processes involved. Hence, experiments aiming at exploring mechanisms and kinetics of elementary reaction steps are highly relevant for a heuristic and systematic optimization of reaction parameters, nonetheless for a thorough understanding in the field. Furthermore, our current knowledge is lacking a thermodynamic understanding of the coupling chemistry. In this context, the present study sheds light on the thermal progression of crucial elementary steps of surface-assisted Ullmann coupling, dehalogenation as well as formation and conversion of organometallic intermediates. Understanding their kinetics and thermodynamics provides an important foundation for rationally optimizing reaction parameters. With regard to dehalogenation, differences in activation temperatures between the typically used Cu, Ag, and Au surfaces are well documented,^{5, 62, 113} and

reflect the reactivity sequence with Cu and Au being most and least reactive, respectively. Yet, the dehalogenation and coupling characteristics during commonly applied heating treatments and their relation to kinetics and thermodynamics remain largely unexplored, despite their obvious relevance for on-surface synthesis.

To elucidate these important aspects, we present a combined study of dehalogenation and coupling on the most important Au(111) and Ag(111) surfaces. The vast majority of reported experiments has been carried out on these two surfaces, because they are sufficiently reactive to induce dehalogenation at moderate temperatures,^{1, 19, 32, 62} whereas more reactive copper surfaces could already have detrimental side-effects such as molecular decomposition.¹²⁴ Moreover, the observation of dramatically different structural qualities of covalent networks obtained on these two surfaces from analogous molecular precursors further prompts comparative studies.^{28, 31, 32} Two important differences are already well documented: (1) dehalogenation temperatures are generally lower on Ag(111) as compared to Au(111); and (2) metastable organometallic intermediates with molecules linked by C-M-C bonds prevail on Ag(111),^{32, 160, 161} while interfering only occasionally on Au(111).^{158, 184}

Because of its high-resolution capability, STM is the most important structure characterization tool in on-surface synthesis. For monitoring the reaction kinetics, however, its limited temporal resolution and chemical sensitivity urge for complementary techniques. Hence, we employ TP-XPS, where XP spectra of specific core levels are continuously acquired during sample heating at constant rate. The great potential of this technique for on-surface synthesis was recently demonstrated by a mechanistic study of the coupling kinetics of 1,4-dibromobenzene on Cu(110)^{91, 92} and by monitoring the onsurface synthesis of graphene nanoribbons.^{88, 146, 184, 185}

We have chosen 1,3,5-tris(*p*-bromophenyl)benzene (TBB, Figure 5.4 (a)) as a relatively simple and thoroughly studied model compound.^{161, 125, 127, 162, 186} According to previous studies on TBB and comparable analogues, debromination should proceed around room temperature on Ag(111),³² whereas heating to 420 – 470 K is required on Au(111).^{28, 31}

TP-XPS experiments were carried out for Br 3d and C 1s core levels to assess both the debromination and the evolution of organometallic intermediates, respectively. A relatively large chemical shift of Br 3d allows one to safely discriminate molecule-bound from dissociated and subsequently adsorbed bromine,^{32, 124} whereas on Ag(111) a pronounced shoulder in the C 1s peak allows for monitoring the emergence and

conversion of organometallic intermediates.¹¹⁶ The interpretation of the TP-XPS data is complemented and guided by accompanying STM experiments and DFT calculations.

5.3 Results and Discussion

For the TP-XPS experiments, the TBB precursor was deposited *in-situ* onto clean surfaces either at room temperature (Au(111)) or at ~ 100 K (Ag(111)) to suppress initial debromination as verified by XPS. The TP-XPS results for Br 3d core levels are shown in Figure 5.1.

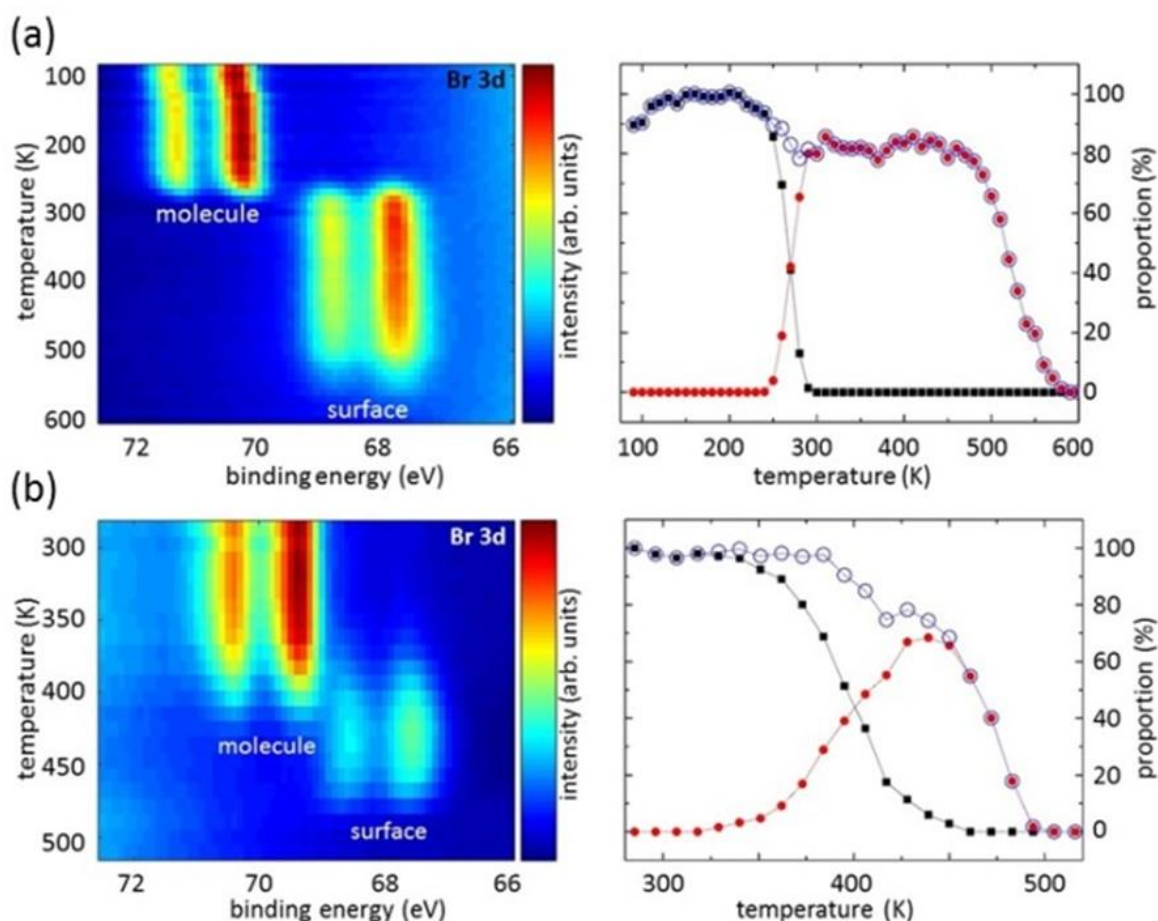


Figure 5. 1: Br 3d TP-XPS data of TBB on (a) Ag(111) versus (b) Au(111). The graphs on the right-hand side depict the relative intensities of molecule-bound (black ■) versus surface-bound (red ●) bromine as obtained from fitting the individual spectra. The blue ○ correspond to the sum of both species, that is, the total amount of bromine.

Directly after deposition, spin-orbit doublets were observed on both surfaces, corresponding to a single chemical bromine species. Br $3d_{3/2}$ binding energies (BE) of 70.4 eV on Au(111) and 71.4 eV on Ag(111) indicate organo-halide species,^{157, 184} confirming the expected adsorption of fully intact TBB precursors. On Au(111) the integrity of the precursors after room temperature deposition was also corroborated by STM, where the self-assembled halogen-bonded structure of fully brominated TBB precursors shown in Figure 5.8 (d) was found. Upon heating, a second doublet emerges with a significant chemical shift to lower Br $3d_{3/2}$ BE of 68.7 eV for Ag(111) and 68.6 eV for Au(111), indicating chemisorbed bromine as debromination product.¹⁸⁷ For a more quantitative view, the respective intensities of molecule-bound and surface-bound bromine were deduced from fits of the individual spectra and are shown on the right hand side of Figure 5.1 (see the Appendix Figure B8 for a combined plot of Ag(111) and Au(111) data for direct comparison). The sum of both species represents the total amount of bromine on the sample. Despite the overall similar behavior, marked differences between Ag(111) and Au(111) become evident: First, the onset temperature of debromination on Ag(111) (~250 K) is significantly lower than that on Au(111) (~325 K). Second, the temperature progression is vastly different: debromination proceeds much more rapidly on Ag(111) in a relatively small temperature window between 250 and 290 K, whereas on Au(111) the debromination proceeds rather gradually, extending over a more than 3-fold wider temperature range from 325 to 460 K.

At higher temperatures, that is, 450 K on Ag(111) and 390 K on Au(111), bromine desorption sets in and is completed at 580 and 500 K on Ag(111) and Au(111), respectively. The higher desorption temperature on Ag(111) is consistent with the larger DFT-derived bromine adsorption energy of 2.83 eV as compared to 2.26 eV on Au(111), respectively.¹⁸⁸ Interestingly, on Au(111), surface-bound bromine already starts desorbing before completion of the debromination.

The lower debromination temperature on Ag(111) is in accord with previous experimental studies,³² and underpinned by DFT calculations of reaction barriers, reporting considerably lower dehalogenation barriers on Ag(111) as compared to Au(111).¹³⁵ A significant disparity in reaction barriers explains the differences in the observed onset temperatures; however, the origin of the differences in the temperature progression still remains unclear: Why does the debromination proceed relatively rapidly on Ag(111) and so gradually on Au(111)? Yet, understanding these differences is of

paramount importance, as dehalogenation is thought to be the ratedetermining step for the global C-C coupling.

DFT calculations of the metal surface-assisted dehalogenation unveil a further important difference: debromination as an isolated reaction step is exothermic on Ag(111), but endothermic on Au(111) with calculated reaction energies of -0.15 eV¹⁸⁹ and $+0.25$ eV for bromobenzene, respectively (cf., Appendix Figure B12). These values are slightly larger than previously reported values¹³⁵ due to higher numerical accuracy and a slightly different density functional in this study and ref¹⁸⁹. Hence, debromination on Ag(111) is both exothermic, and with an additional entropy gain (*vide infra*) exergonic, with its thermodynamic equilibrium shifted far to the debrominated side already at room temperature. Accordingly, its temperature progression is adequately described by chemical kinetics. The debromination kinetics was modeled based on an Arrhenius law for the temperature-dependence of the rate constant ν with ΔE corresponding to the debromination barrier:

$$\nu = \nu_0 \cdot e^{-\frac{\Delta E}{k_B \cdot T}} \quad (5.1)$$

In the TP-XPS experiments the temperature was linearly increased with time:

$$T(t) = T_0 + \alpha \cdot t \quad (5.2)$$

where a rate of $\alpha = 0.15 \text{ K} \cdot \text{s}^{-1}$ was applied in all experiments, resulting in:

$$dT = \alpha \cdot dt \quad (5.3)$$

$N(t)/N(T)$ denote the amount of still brominated sites as a function of time and temperature, respectively. The reaction rate was modeled assuming first-order reaction kinetics. Accordingly, in a time increment dt the change of the amount of brominated sites dN is given by:

$$dN = -\nu(T) \cdot N(t) \cdot dt \quad (5.4)$$

For direct comparability with the experiment, it is more convenient to express the amount of brominated sites $N(T)$ as a function of temperature T :

$$dN = -v \cdot N(t) \cdot dt = -v \cdot N(T) \cdot \frac{dT}{\alpha} = -\frac{v_0 \cdot e^{-\frac{\Delta E}{k_B T}}}{\alpha} \cdot N(T) \cdot dT \quad (5.5)$$

Since α is a given experimental parameter, the only free parameters are the debromination barrier ΔE and the pre-exponential factor v_0 . The temperature progression of the debromination, i.e. $N(T)$, was determined numerically based on finite temperature increments ΔT by first calculating the change $\Delta N(T, \Delta T)$:

$$\Delta N(T, \Delta T) = -\frac{v_0 \cdot e^{-\frac{\Delta E}{k_B T}}}{\alpha} \cdot N(T) \cdot \Delta T \quad (5.6)$$

This change was then used to calculate the remaining number of brominated sites at an increased temperature of $T + \Delta T$ according to:

$$N(T + \Delta T) = N(T) + \Delta N(T, \Delta T) = N(T) - \frac{v_0 \cdot e^{-\frac{\Delta E}{k_B T}}}{\alpha} \cdot N(T) \cdot \Delta T \quad (5.7)$$

For the numerical calculation a temperature increment of $\Delta T = 0.30$ K was chosen, i.e. sufficiently small to ensure convergence. Note that in this approach all debromination events even on the same molecule are treated as independent.

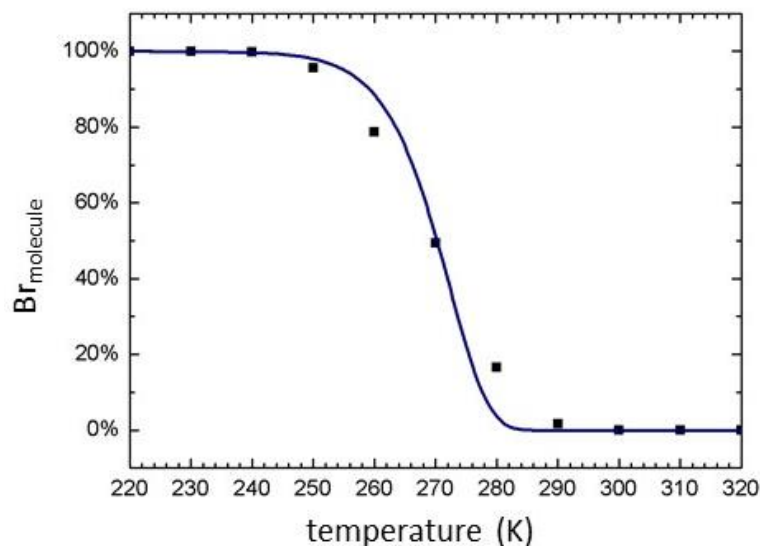


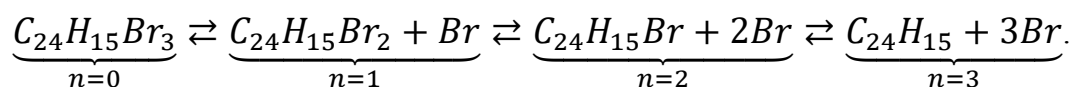
Figure 5. 2: Kinetic model applied to Ag(111). Black filled squares represent data from the Br 3d TP-XPS experiment shown in 5.1 (a). The blue curve represents a fit according to the kinetic model described above, using a DFT calculated reaction barrier of $\Delta E = 0.98$ eV.¹⁸⁹ The amount of molecule-bound bromine ($\text{Br}_{\text{molecule}}$) was normalized by $(\text{Br}_{\text{molecule}} + \text{Br}_{\text{surface}})$, i.e. the total amount of bromine detected by XPS. A least square fit yielded a pre-exponential factor of $\nu_0 = 3.25 \times 10^{16} \text{s}^{-1}$.

The excellent match between experimental and simulated data shown in Figure 5.2 indicates that the debromination on Ag(111) can be adequately described by first-order reaction kinetics. However, the same kinetic model fails to explain the experimentally observed debromination on Au(111) (cf., Appendix Figure B13).

A potential explanation for the gradual debromination on Au(111) is offered by the inhomogeneity of the surface due to its chevron reconstruction,⁵⁴ possibly resulting in a broader distribution of reaction barriers. Even though such reactivity differences for the hcp versus fcc stacked regions exist, the effect was reported to be rather small for hydrogen and fluorine atoms, with adsorption energies varying by merely ~ 50 meV between the two regions.¹⁹⁰ On the other hand, this spatial inhomogeneity finds expression in the XPS data. The fwhm of the Br 3d peaks of the surface-bound species is significantly broader on Au(111) (0.67 eV) than on Ag(111) (0.53 eV) (cf., Appendix Figure B5).

To estimate the effect of the spatial inhomogeneity on the debromination barriers, we performed DFT calculations of the reaction for the established bromobenzene model system (cf., Appendix Figure B12) using the climbing image nudged elastic band method.^{191, 192} Because full account of the $\sqrt{3}\times 22$ herringbone reconstruction is too computationally expensive, an ideal bulk terminated Au(111) surface (fcc-stacked) was compared to a stacking-fault terminated Au(111) surface (hcp-stacked). DFT-derived debromination barriers are 1.12 eV for the fcc and 1.10 eV for the hcp termination, respectively. Again, the small difference from previously reported results¹³⁵ is due to adapted DFT parameters (*vide supra*). However, the minute difference between fcc- and hcp-stacked Au(111) of only 0.02 eV is below the numerical accuracy of our calculations, and is also too small to explain the large temperature spread of the debromination.

An explanatory alternative is offered by a thermodynamic description of the debromination on Au(111), that is, postulating equilibrium between dehalogenation and halogenation. The TBB molecule ($C_{24}H_{15}Br_3$) is 3-fold brominated; thus its debromination is appropriately modeled by a four-level system, considering fully brominated, and single, double, and triple (fully) debrominated states:



For simplicity, but also to restrict the number of fit parameters, we approximate that the enthalpy and entropy changes are similar for each debromination step. Accordingly, with respect to the free energy of the fully brominated TBB molecule (G_0), the relative free energies for the single (ΔG_1), double (ΔG_2), and triple (ΔG_3) debrominated states are given by

$$\Delta G_n = G_n - G_0 = n \cdot (\Delta H - T\Delta S) \quad (5.8)$$

at a given temperature T , where ΔH and ΔS are the enthalpy and entropy differences for dissociation of any bromine substituent from either the intact or already partly debrominated TBB molecule. Hence, the proposed four-level system features only the two free parameters ΔH and ΔS . The probability P_n of having a state with n number of bromine atoms removed per molecule is then given by

$$P_n = \frac{\exp\left(-\frac{\Delta G_n}{k_B \cdot T}\right)}{Z} = \frac{\exp\left(-n \cdot \frac{\Delta H}{k_B \cdot T} + n \cdot \frac{\Delta S}{k_B}\right)}{Z} \quad (5.9),$$

with Z being the partition function of the four-level system. By considering the probability P_n of each state n and its respective degree of debromination $\frac{n}{3}$, the total probability of dehalogenation P_{dehal} is given by

$$P_{dehal} = \sum_{n=0}^3 \frac{n}{3} P_n = \frac{1}{3} P_1 + \frac{2}{3} P_2 + P_3 \quad (5.10).$$

The dependence of P_{dehal} on surface temperature is directly experimentally accessible from the TP-XPS experiments as the ratio of the Br 3d intensities of surface-bound to the total amount of bromine. Experimental data along with a fit based on equation 5.10 are shown in Figure 5.3, providing an excellent match with $\Delta H = +0.54$ eV ($52 \frac{\text{kJ}}{\text{mol}}$) and $\Delta S = +1.35 \frac{\text{meV}}{\text{K}}$ ($130 \frac{\text{J}}{\text{mol} \cdot \text{K}}$).

To assess the plausibility of the proposed thermodynamic model, it is instructive to compare the experimentally deduced enthalpy and entropy values to theoretical estimates. The experimental enthalpy difference $\Delta H = +0.54$ eV for removing one bromine atom is significantly larger than the DFT-derived value of +0.25 eV for bromobenzene (cf., Appendix Figure B12). Accordingly, we performed DFT calculations for the actual TBB molecule on Au(111), and the corresponding DFT-optimized structures before and after full debromination are shown in Figure 5.4. For TBB, the calculated reaction energy for full debromination amounts to +1.19 eV.

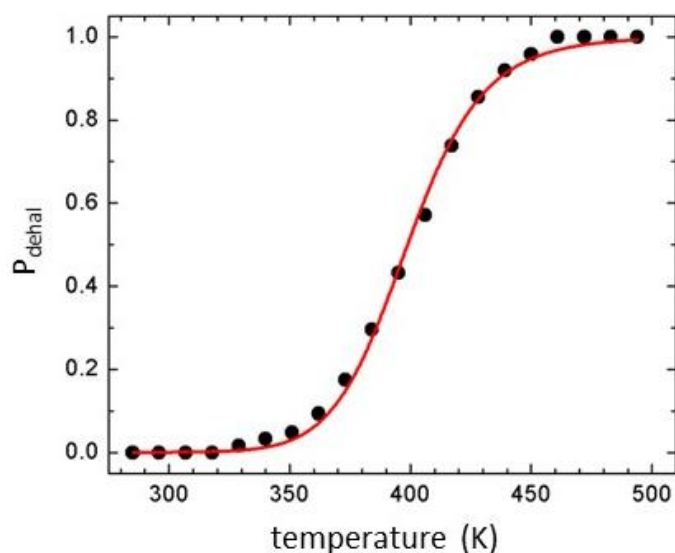


Figure 5. 3: Probability of the dehalogenated state P_{dehal} on Au(111) as a function of surface temperature. The experimental values (●) were derived from Br 3d TP-XPS data, and are well fitted by equation 5.10 (red line), that is, by assuming thermodynamical equilibrium at the respective temperatures (see text).

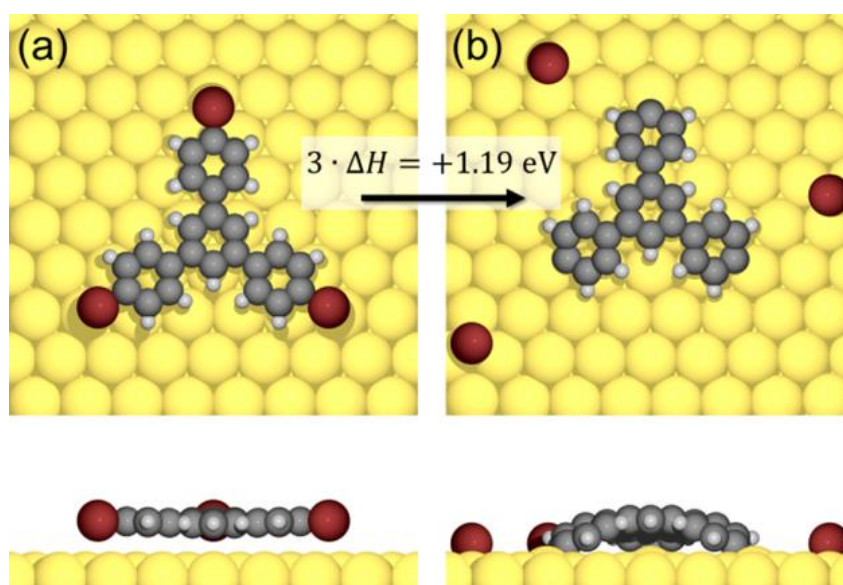


Figure 5. 4: Top- and side-views of DFT-optimized structures of (a) fully brominated TBB on Au(111) and (b) after dissociation and chemisorption of all three bromine substituents. The total energy difference of +1.19 eV corresponds to $3 \cdot \Delta H$. The adsorption energy of split-off bromine on Au(111) was evaluated in separate calculations to mimic a final state where the bromine atoms are isolated from the molecule, and the chemisorbed bromines are shown here for illustrative purposes.

Because this value corresponds to the reaction energy for removal of all three bromine substituents, we obtain an average theoretical value of $\Delta H = +0.40$ eV per debromination, in close agreement with the experiment. Additional DFT calculations of the reaction enthalpies of each individual debromination step result in similar values for the first, second, and third debromination, within the numerical accuracy of our calculations (cf., Appendix figure B10). This corroborates the appropriateness of the previously made assumption, and indicates weak conformational or electronic cross-talk between the reactive sites of TBB. The deviations between bromobenzene and TBB are attributed to the final state geometries: the resulting benzene radical binds to the Au(111) surface with an almost upright geometry (cf., Appendix Figure B12), whereas the TBB-derived surface-stabilized triradical is pinned down at its periphery, hence adsorbs mainly flat on the surface (cf., Figure 5.4 (b)). This gives rise to a delicate balance of optimizing the C-Au bonding at the same time as reducing the energy cost of molecular deformation and Pauli repulsion, resulting in an overall less favorable C-Au bond geometry in the triradical as compared to the benzene radical.

With regard to the reaction entropy, ΔS , a dominating gain can be expected from the translation entropy of the dissociated bromine. Theoretical estimates based on the Sackur-Tetrode equation for two translational degrees of freedom result in $\Delta S = 0.86 \dots 1.25 \frac{\text{meV}}{\text{K}} (82.9 \dots 121 \frac{\text{J}}{\text{mol}\cdot\text{K}})$ for assuming surface areas of $1 \dots 100 \text{ nm}^2$ for each dissociated bromine. Even though an accurate quantitative agreement is not achieved for ΔS , the range of theoretical values is reasonably close to the experimental value. Additional smaller contributions arise from reaction-related changes in molecular translational, rotational, and vibrational entropy due to differing aggregate sizes or symmetry as well as immobilization of larger aggregates, which may account for the discrepancies.

In summary, the consistency between experimentally and theoretically derived ΔH and ΔS values corroborates a thermodynamically controlled debromination on Au(111). Yet, the absence of kinetic limitations in the relevant temperature range is a prerequisite. Indeed, employing the same first-order kinetic model as for Ag(111), with a DFT-calculated reaction barrier of 1.12 eV on Au(111) (*vide supra*) and a similar pre-exponential factor as obtained from fitting the Ag(111) data, results in full debromination already at around 320 K (cf., Appendix Figure B13). A thermodynamically controlled debromination on Au(111) bears far-reaching implications, as it inherently implies

equilibrium between forth and back reaction, that is, (re)halogenation must similarly be possible. In the present case, this indicates that dehalogenated sites (surface-stabilized radicals) must be available, hence sizable covalent coupling that would deplete the dehalogenated sites by C-C bond formation must not occur immediately. Even though substantial C-C coupling is ruled out in the relevant temperature regime based on C 1s TP-XPS data (*vide infra*), the formation of few covalent links between molecules cannot be excluded. Thereby the concentration of available debrominated sites is reduced. According to Le Chatelier's principle, the equilibrium becomes shifted to the product site, giving rise to an apparent enhancement of the debromination rate. Nonetheless, C 1s TP-XPS data indicate a comparatively small influence. Hence, these experiments suggest a surprisingly long lifetime of the surface-stabilized radicals, and recapturing freely diffusing bromine atoms is more likely than covalent coupling between molecules within the debromination temperature window. Indeed, we find direct evidence for halogenation in the STM measurements, which clearly show bromine-terminated sites at the periphery of covalent networks as in Figure 5.8 (f) even after annealing to 525 K. Moreover, mostly self-assembled structures of intact, fully brominated TBB molecules were observed by STM for a sample that was briefly annealed to 473 K and immediately cooled (cf., Appendix Figure B3).

A second series of TP-XPS experiments were performed, aimed to study the emergence and conversion of the organometallic intermediates, well-known for Ag(111), into covalent products by monitoring C 1s core levels. Results for both surfaces are shown in Figure 5.5.

On Ag(111), C 1s can exhibit two shoulders at high and low BE, originating from still bromine-substituted (C-Br) and organometallic carbon atoms (C-Ag), respectively.¹¹⁶ Specifically, for TBB, 1 in 8 carbon atoms can directly bind to bromine or silver atoms, resulting in small, but safely detectable shoulders (cf., Appendix Figure B7). The graph on the right-hand side of Figure 5.5 (a) shows the intensity of both the C-Br and the C-Ag shoulders as a function of surface temperature (see the Appendix Figure B9 for a combined plot of Ag(111) and Au(111) data for direct comparison).

In the debromination temperature window between 250 K and 290 K, the C-Br and C-Ag components are anticorrelated. This indicates a direct conversion of C-Br into C-Ag by the immediate bond formation with silver atoms at the freshly debrominated sites. The nearly complete conversion of all brominated sites into organometallic linkages is also

apparent in the STM image shown in Figure 5.8 (a) by the formation of reticulated networks.

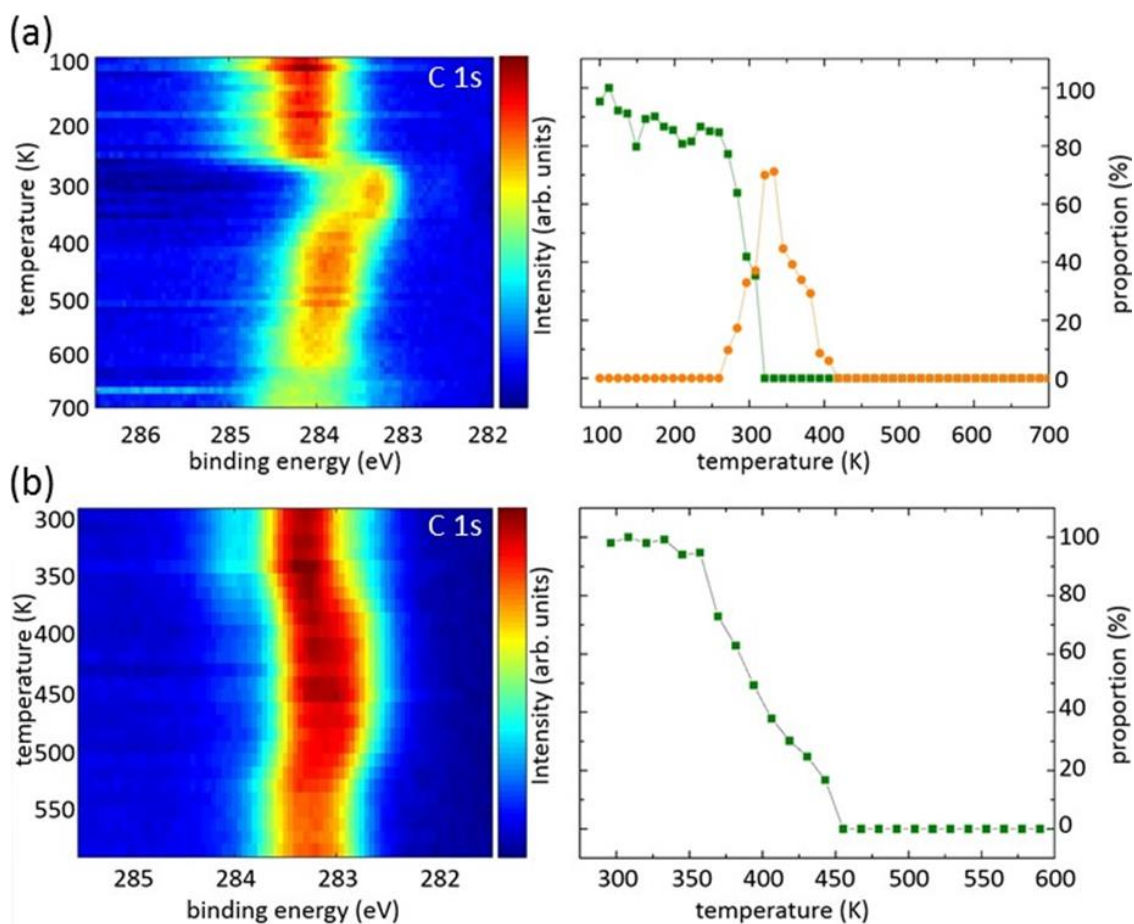


Figure 5. 5: C 1s TP-XPS data of TBB on (a) Ag(111) and (b) Au(111). The graphs on the right-hand side depict the relative intensities of C-Br (green ■) versus C-Ag (orange ●) as obtained from fits of the individual spectra.

Organometallic C-Ag-C linkages can be recognized by the enlarged center-to-center distance between molecules of 1.6 nm as compared to 1.3 nm for covalent links, but also by a bright feature at the bond center, commonly attributed to a signature of the organometallic silver atom.³² In addition to the low BE shoulder, emergence of organometallic intermediates is also accompanied by an integral peak shift of C 1s to lower BE.⁹² On Ag(111) the rapid shift of C 1s by 0.8 eV at ~250 K coincides with the debromination onset (cf. Figure 5.6 (a)). Its origin is discussed controversially, and local work function changes due to the chemisorption of negatively charged bromine have been

proposed.¹⁹³ In this instance, a correlation between the magnitude of the C 1s shift and the amount of chemisorbed bromine would be expected.

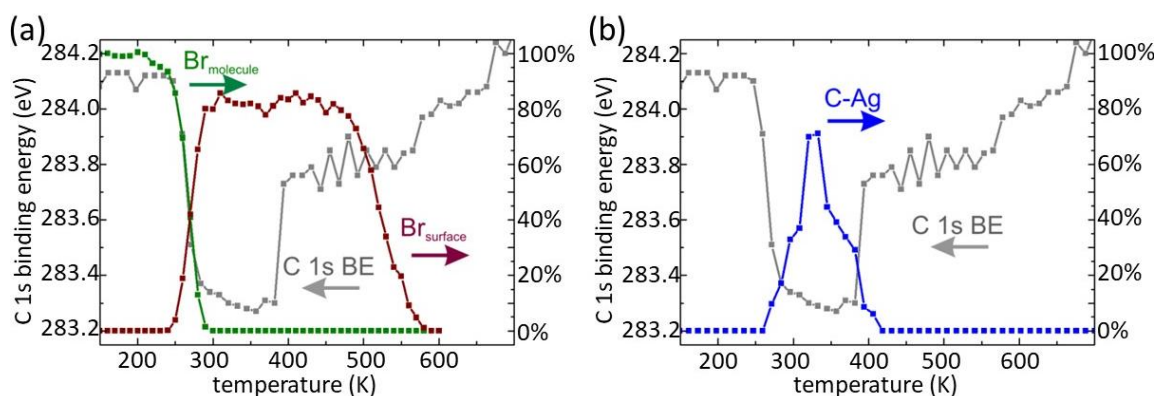


Figure 5. 6: Integral peak shifts of C 1s on Ag(111) vs. surface temperature shown alongside with the intensities of (a) molecule-bound (Br_{molecule} , green curve) and surface-bound (Br_{surface} , red curve) bromine as derived from Br 3d data and (b) the amount of organometallic carbon atoms (C-Ag, blue curve) as derived from C 1s data.

However, here the magnitude of the C 1s shift exhibits a better correspondence with the C-Ag intensity rather than with the amount of surface-bound bromine (cf., Figure 5.6 (b)), suggesting a causal correlation of the C 1s shift with the organometallic linkages. Obviously, the onset of the C 1s shift coincides with both the decrease of Br_{molecule} (or alternatively the increase of Br_{surface}) (cf., Figure 5.6 (a)) and the emergence of C-Ag (cf., Figure 5.6 (b)). Yet, around 390 K the C 1s shift mostly recedes, even though the intensity of Br_{surface} still remains constant up to 500 K. The recession of the C 1s shift, however, exhibits a strong correlation with the decreasing C-Ag intensity due to the conversion of organometallic into covalent bonds. These combined plots indicate a direct correlation between the C 1s peak shift and the presence of organometallic carbon (C-Ag).

Upon further annealing, the C-Ag intensity reaches its maximum at around 330 K and decreases to zero at about 420 K. Again, this 90 K temperature spread indicates a rather gradual conversion of organometallic into covalent linkages. Accordingly, the coexistence of organometallic and covalent interlinks is routinely observed in STM, and a representative example is shown in Figure 5.8 (b) along with the overlaid molecular model. Interestingly, the already covalent *p*-quaterphenyl edges of the network appear

with larger height in the STM contrast. This is presumably related to their electronic conjugation, affecting both local density of states and tunneling current. Once the conversion is completed, the covalent networks remain stable up to a temperature of ~ 650 K, where significant C 1s intensity losses indicate decomposition and desorption.

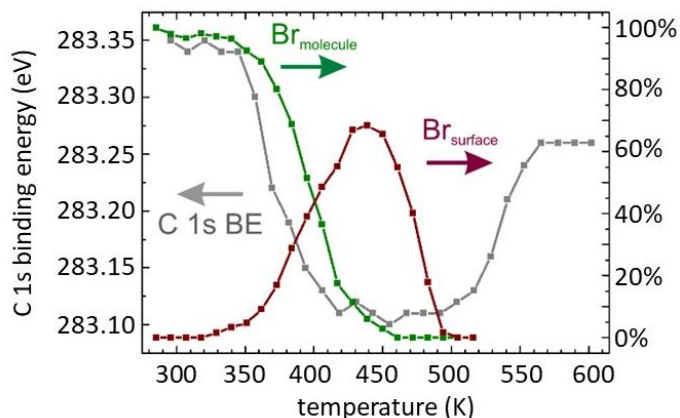


Figure 5. 7: Integral peak shifts of C 1s on Au(111) vs. surface temperature shown alongside with the intensity of molecule-bound ($\text{Br}_{\text{molecule}}$, green curve) and surface-bound ($\text{Br}_{\text{surface}}$, red curve) bromine as derived from Br 3d data.

The C 1s TP-XPS data on Au(111) presented in Figure 5.5 (b) do not display such a pronounced and rapid shift as for Ag(111). Yet, a smaller integral peak shift of ~ 0.25 eV to lower BE with a more gradual temperature progression is similarly observed. Analogous to Ag(111), the onset of the C 1s shift coincides with the debromination as directly monitored by Br 3d in Figure 5.7. Interestingly, the C 1s shift on Au(111) persists up to fairly high temperatures of 560 K, even though the intensity of $\text{Br}_{\text{surface}}$ starts to decrease around 450 K due to thermal desorption of bromine. Again, a correlation of the observed C 1s shift with the amount of surface-bound bromine can be excluded as bromine is already fully desorbed at 500 K.

In analogy to Ag(111), a possible explanation for the C 1s shift on Au(111) is given by the formation of C-Au bonds upon debromination. These organometallic bonds do not necessarily have to be formed with gold adatoms, but could also comprise direct bonds with gold surface atoms as illustrated in Figure 5.4 (b) and experimentally observed for dangling phenyl groups at the periphery of covalent networks (cf., Figure 5.8 (f) and the Appendix Figure B2). In this case, the debrominated molecules would not form organometallic networks. Yet, a pronounced organometallic low BE shoulder in C 1s as

observed on Ag(111) cannot be expected for C-Au due to a smaller chemical core level shift.¹³⁵ This is in accord with our studies on a pyrene derivative on Au(111), where solely a C 1s shift, but no C-Au related low BE shoulder, was observed, even though the presence of organometallic linkages was unambiguously confirmed by STM.¹¹⁶

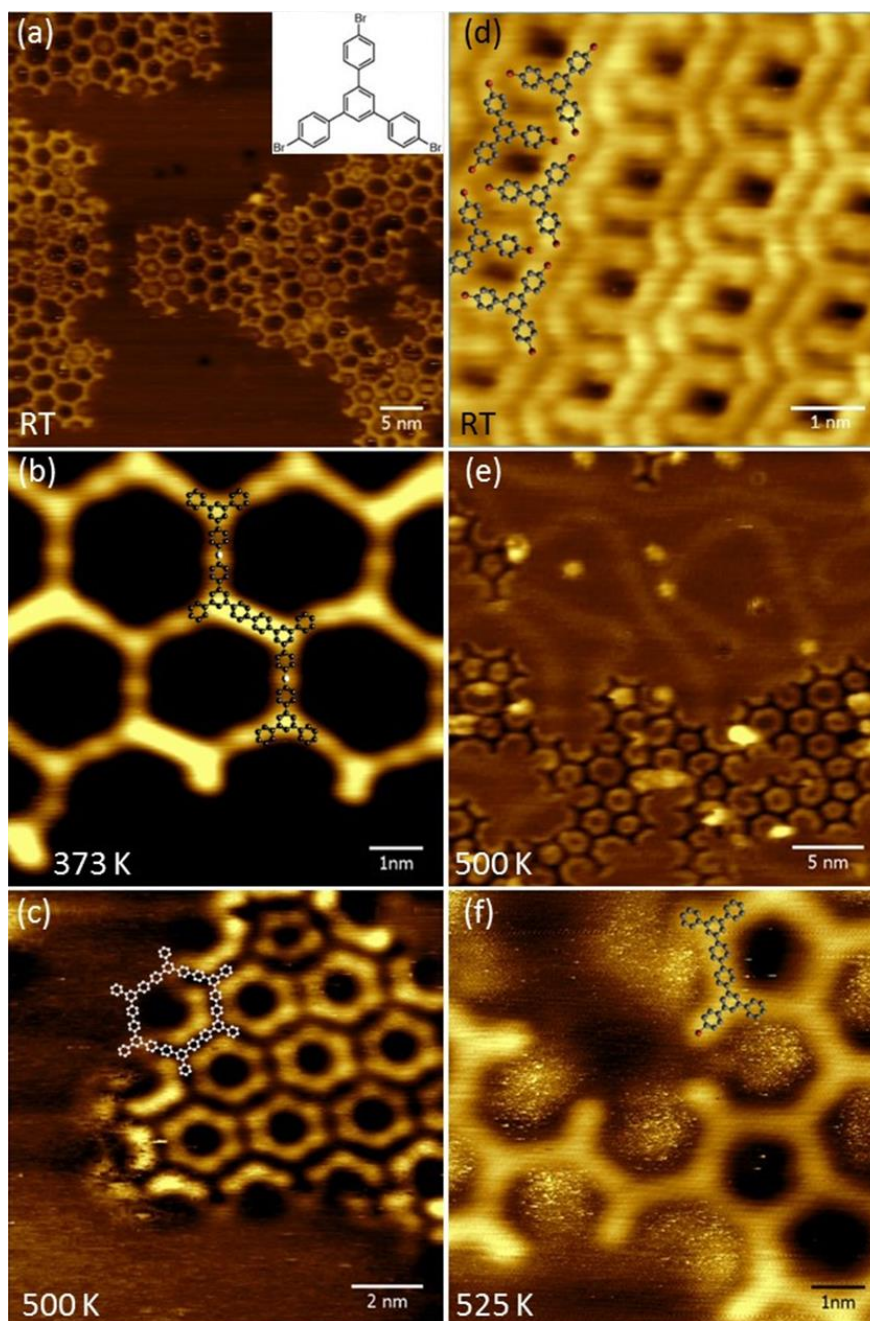


Figure 5. 8: STM images showing (a) organometallic networks on Ag(111) and (b) the coexistence of organometallic and covalent links on the same surface after annealing to 375 K; (c) completely covalent networks on Ag(111) after annealing to 500 K with inverted contrast; (d) self-assembly of intact TBB molecules on Au(111) after room temperature deposition as well as (e) and (f) covalent networks obtained on Au(111) after overnight annealing to 500 K and annealing to 525 K, respectively. The overlay highlights both a brominated and debrominated phenyl ring at the periphery. Tunneling parameters: (a) 0.75 V, 29.9 pA; (b) 1.53 V, 30.6 pA; (c) 1.39 V, 31.7 pA; (d) 1.01 V, 39.7 pA; (e) 2.11 V, 37.4 pA; (f) 0.88 V, 41.6 pA.

Attributing the C 1s shift on Au(111) also to organometallic bonds implies that the observed recession at around 550 K is related to a decreasing amount of C-Au bonds by the eventual formation of covalent intermolecular bonds. The hypothesis that TBB derived surface-stabilized radicals do not immediately form covalent bonds after debromination is in accord with and confirms the precondition for the proposed thermodynamic model for Au(111).

After a sample that was annealed above 500 K was cooled to room temperature again, STM and XPS consistently indicated the absence of organometallic bonds: STM exclusively showed covalent networks with a molecule center-to-center distance of 1.3 nm as exemplified in Figure 5.8 (e) and (f). Also, the C 1s BE of 283.3 eV as measured at a temperature of 550 K at the end of the TP-XPS run remained unchanged after being cooled to room temperature, indicating the absence of further chemical changes. Hence, metastable organometallic networks based on C-Au-C linkages either are not formed for aryl-aryl coupling on Au(111) or are directly converted into the covalent products.

Interestingly, the surface-stabilized radicals persist even after complete desorption of bromine, prompting the question of what inhibits covalent coupling. As a possible explanation, we propose kinetic limitations that can only be overcome at sufficiently high temperatures. Covalent coupling of the surface-stabilized triradicals requires both their lateral diffusion and their rotation to obtain an appropriate mutual position and orientation. According to DFT simulations, the associated energy barriers are surprisingly high, even exceeding 1 eV (cf., Appendix Figure B11). Moreover, for the TBB-derived triradical, these simulations indicate for both diffusion and rotation the sequential breaking of the phenyl-Au bonds one at a time. This mechanism should similarly give rise to a relatively high barrier for the actual coupling, where both involved phenyl groups initially bond to the same Au-atom and then have to simultaneously break their surface bonds in order to form the new C-C bond. Yet, these processes are crucially dependent on the intramolecular mechanics of the surface-stabilized radicals, and hence on the molecular structure of the precursor.

5.4 Conclusion

TP-XPS provided unique insights into the thermal progression of elementary reaction steps of Ullmann-type coupling on Au(111) versus Ag(111) as summarized in Figure 5.9. While onset temperatures for debromination and bromine desorption from both surfaces are consistent with previous experimental findings and DFT calculations, striking differences were found for the principles underlying the reaction scenario. On Ag(111) the rapid progression of the dehalogenation is well explained by first-order reaction kinetics. The use of the experimental heating rate and a DFT-derived reaction barrier results in an excellent match between model and experimental data. In contrast, the same kinetic model fails to explain the gradual debromination as a function of temperature on Au(111). Consequently, a thermodynamic model is put forward, where the dehalogenation probability is captured by a four-level system. Fitting the experimental data yielded values for both the reaction energy ΔH and entropy ΔS of an individual debromination step consistent with theoretical values as obtained from DFT calculations and statistical mechanics, respectively.

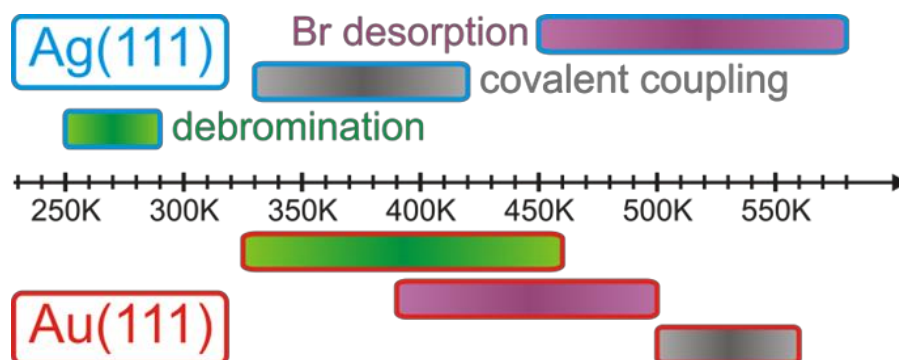


Figure 5. 9: Schematic overview and comparison of the temperature ranges for debromination (green), covalent coupling (grey), and thermal desorption of bromine (violet) on Ag(111) (top) versus Au(111) (bottom) as deduced from both Br 3d and C 1s TP-XPS data.

An important outlook of this study is the generalizability of kinetic control on Ag(111) versus thermodynamic control on Au(111) also for other polyaromatic precursors. On Ag(111), debromination is expected to always be exothermic due to the strong interactions of both surface-stabilized radicals and chemisorbed bromine with the surface.

In combination with the entropy gain, the debrominated state is thermodynamically favored already at room temperature on Ag(111); hence debromination should remain kinetically controlled also for other brominated precursors. To judge the impact of the reaction barrier, the first-order kinetic model was evaluated for a variation of reaction barriers (cf., Appendix Figure B14). Accordingly, a 20% increase shifts the temperature for full dehalogenation to approximately 345 K. In reverse, the modest variation of reported experimental debromination temperatures on Ag(111) suggests fairly uniform debromination barriers.

Similarly, the scope of the thermodynamic model was evaluated by variation of both reaction enthalpies and entropies (cf., Appendix Figures B15 and B16). For a 20% increase of the endothermic reaction enthalpy, the temperature for full debromination is considerably up-shifted above 600 K. Such high temperatures compromise the applicability of the thermodynamic model, as bromine is fully desorbed, and sizable C-C coupling is also expected. Decreasing the reaction entropy has generally an effect similar to that of increasing the reaction enthalpy. A comparison of our DFT results on bromobenzene and TBB illustrates the significant influence of final state geometries, that is, the bonding of surface-stabilized radicals to Au(111), on the reaction enthalpy. Consequently, significant reaction enthalpy variations are conceivable for different precursors and might account for the relatively large range of reported reaction temperatures on Au(111). On the other hand, the largest contribution to the reaction entropy originates from the translational entropy of the split off bromine. So in principle, the reaction entropy can additionally depend on coverage for a given molecule, but we anticipate a comparatively weak effect.

The thermodynamic approach proposed for Au(111) implies that the surface-stabilized radicals do not immediately form intermolecular covalent bonds after the debromination, but have an unexpectedly long lifetime on the surface. This hypothesis is further corroborated by TP-XPS data: while the onset of an integral peak shift of C 1s is correlated with the debromination, persistence of this shift even after complete desorption of the surface-bound bromine at around 500 K clearly indicates a different origin. In analogy to the results on Ag(111), this C 1s shift is attributed to the formation of C-Au bonds. Accordingly, recession of the C 1s shift at 550 K indicates that covalent coupling only takes place later at significantly higher surface temperatures, a surprising result that

can be reasoned by relatively high diffusion, rotation, and coupling barriers. The main findings that debromination on Au(111) is reversible as long as bromine remains present on the surface and that covalent coupling does not occur immediately after debromination, suggest a profound influence of reaction parameters such as heating rate, duration, and final temperature on the polymerization progress and structural quality of covalent nanostructures on Au(111) in accord with previous experimental findings.²⁸

On Ag(111), the C1 s TP-XPS experiments provided further insights into the temperature evolution of the well-known organometallic intermediate. The results bear important implications for applying organometallic self-assembly to improve the structural quality of covalent networks.^{28, 144, 159, 160} TP-XPS clearly indicates that the conversion of organometallic into covalent bonds already sets in before the debromination is completed. The associated irreversibility of intermolecular covalent bonds definitively hampers full equilibration of the organometallic networks. In this respect, further predictive *ab-initio* studies hold the potential to identify precursors that feature both low dehalogenation temperatures and high conversion temperatures as promising candidates for further advancement of organometallic self-assembly. Progress in this direction is a key ingredient toward the on-surface synthesis of highly regular and extended covalent 2D materials.

5.5 Experimental details

STM

Sample preparation and characterization was carried out in ultra-high vacuum at a base pressure below 3×10^{-10} mbar. Ag(111) and Au(111) single crystal surfaces were prepared by cycles of Ne⁺ sputtering at 500 eV and electron-beam annealing at 500 °C for 10 min. 1,3,5-tris(*p*-bromophenyl)benzene (TBB) was purchased from Sigma Aldrich with a purity of > 97%. Prior to deposition of TBB, the cleanliness and appropriateness of terrace sizes of the surfaces was verified by large scale STM imaging. TBB was deposited from a home-built Knudsen Cell with an integrated quartz crystal microbalance at a crucible temperature of 140 °C for 15 min.

STM images were acquired in the constant current mode at room temperature with a home-built beetle type STM operated by a SPM 100 controller from RHK. Electrochemically etched tungsten tips were used and *in-situ* conditioned by electron beam annealing or sputtering. Stated bias voltages are referred to the sample. STM images were processed by leveling and mean value filtering using the Gwyddion software.

TP-XPS

TP-XPS experiments were conducted at the undulator beamline UE56/2-PGM-2 at Bessy II at the Helmholtz-Zentrum Berlin utilizing a custom built UHV chamber as a temporary end station. This chamber operated at a base pressure around 5×10^{-11} mbar and is equipped with a Phoibos 100 CCD hemispherical electron analyzer. The analyzer was mounted 83° from the incident direction of the photon beam. The analyzer could be rotated around the axis defined by the incident beam, so that it was either in-plane with the linear-horizontal or the linear-vertical polarization of the undulator light. Linear-horizontal light was used for all experiments. For the Ag(111) sample, the thermocouple (K-type) was put in thermal contact with the sample by spot welding the two thermocouple wires to the thick Ta wire that held the sample in place on the sample holder. For the Au(111) sample, the thermocouple was put in thermal contact with the sample by pushing it against the surface with a metal clip. In both cases, the sample temperature, i.e. heating rate, was controlled by a custom built PID controller, which could maintain a constant heating rate to an accuracy of $\sim 0.01 \text{ K s}^{-1}$. Samples were prepared analogously to the STM experiments. Prior to deposition, the surface cleanliness was checked by XPS taking both survey spectra and scans of the C 1s and O 1s regions. Low energy electron diffraction (LEED) was used to gauge the crystalline quality of the samples prior to molecular deposition. Due to the significant beam damage caused to molecular overlayers by low energy electrons, LEED was not taken of the molecular overlayer.

TP-XPS experiments were carried out at low molecular coverages (approximately 30% w.r.t. the covalent honeycomb structure) in order to avoid additional influences known for higher coverages. TP-XP spectra were acquired in independent experimental runs for

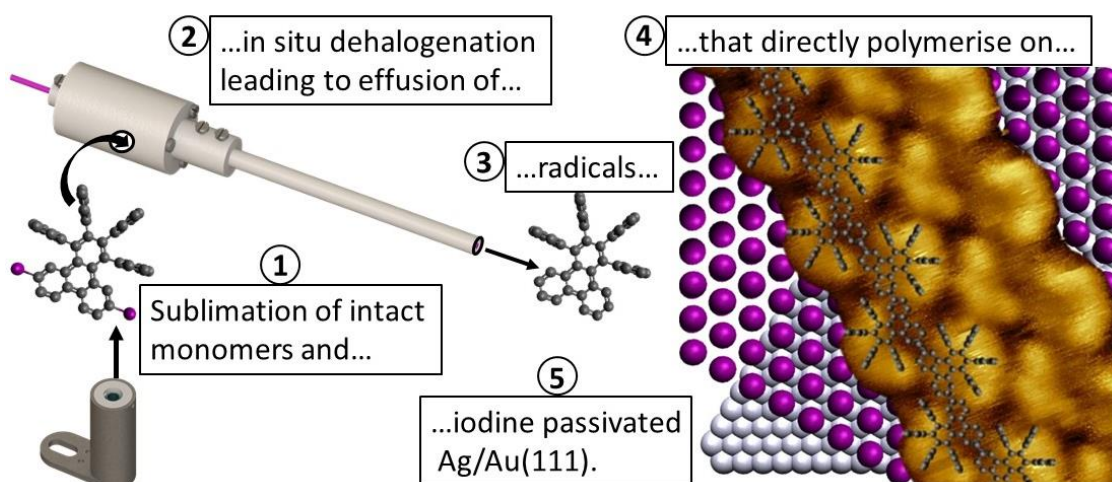
the Br 3d and C 1s core levels at photon energies of 190 eV and 435 eV, respectively, to optimize the photoionization cross-section. Identical deposition parameters were used in all experiments. A similar coverage was confirmed by C 1s XPS for Au(111), whereas for Ag(111) the coverage was about 30% lower for the C 1s as compared to the Br 3d TP-XPS experiment. Yet, under these experimental conditions coverage dependent effects are not known, hence a direct comparison of the C 1s and Br 3d TP-XPS data remains feasible. For the TP-XPS data acquisition samples were heated at a constant rate of 0.15 K s^{-1} . Each individual XP spectrum was acquired in approximately 70 s, i.e. represents an average over a temperature range of approximately 10 K. To minimize radiation damage (i.e. the X-ray or secondary electron-induced dissociation of C-Br bonds), samples were continuously moved during the TP-XPS data acquisition. Moreover, both the X-ray entrance and exit slits of the monochromator were minimized to further prevent radiation damage, and by the same token to improve X-ray monochromaticity. The complete absence of the surface-bound bromine species in the Br 3d TP-XPS for temperatures below the onset of thermal debromination indicates a negligible influence of radiation damage. Before and after the TP-XPS measurements individual spectra of all core levels were acquired for validation.

For the quantitative analysis of the Br 3d and the C 1s species as summarized in Figure 5.1 and Figure 5.4 of the main manuscript, Voigt line shapes and linear backgrounds were used. For evaluation of the C 1s integral peak shifts presented in Figure 5.6 and Figure 5.7 peak maxima were used.

Chapter 6

On-surface synthesis of chevron-type graphene nanoribbons *via* direct deposition of radicals

In this chapter, we present an unconventional reaction pathway for the synthesis of atomically precise chevron-type GNRs, by means of a radical deposition source (RDS). By geometric design of the RDS, the 6,11-Diiodo-1,2,3,4-tetraphenyltriphenylene (DITTP) precursor is forced to undergo multiple deflections on hot alumina surfaces, before impinging on the surface. Thereby, the halogen-substituents are split-off from the molecular precursor by virtue of the heated ceramic walls. Hence, direct deposition of radicals onto the iodine passivated Ag(111) and Au(111) surfaces was feasible. STM measurements were performed to prove the functionality of the RDS by following the on-surface reaction pathway from the polymer chain, to the final products, that are GNRs.*



*I performed the main part of the STM experiments and all data analysis. The STM image in Figure 6.7 (a) was acquired by Dr. Matthias Lischka.

6.1 Introduction

In the following the principle and first tests with a RDS will be discussed. The basic idea is to alleviate the need of the reactive metal substrates required for the rate limiting step of surface-assisted Ullmann coupling (assuming molecules with low diffusion barriers), i.e. the dehalogenation step. This is particularly promising for the synthesis of polymers on insulating surfaces. The RDS can be used to directly deposit activated molecules (radicals) onto the surface. To achieve this, the RDS thermally cleaves the C-X bond of the halogenated precursors, thereby generating a radical which can adsorb on the surface of interest. First motivating aspects, underscoring benefits and possibilities of a RDS, are given. Thereupon, the operation principle of the RDS is explained. In the end the first results obtained by deposition of an activated molecule *via* the RDS are presented and discussed.

Bottom-up synthesis of one- and two-dimensional covalent nanostructures *via* Ullmann-type coupling is a prevalent approach in the on-surface synthesis community. The vast majority of on-surface Ullmann-type reactions are performed on close-packed coinage metal surfaces, as the metal substrates reduce the activation barrier for the homolytic bond scission of the haloarenes and confine the molecules in 2D.^{5, 32, 194, 195}

Our new approach proposes a RDS, combining a Knudsen cell with a device for activation of the molecular precursors. Accordingly, the surface of interest can be directly exposed to radicals. Hence, the catalytic aid of the substrate is not needed anymore for activation of the molecules. This can open up the possibility to synthesize covalent nanoarchitectures also on insulating surfaces. For measuring electrical properties of adsorbates an insulating adsorbent is favorable, as no charge carriers of the surface influence the measurement.

With decreasing reactivity of the surfaces the temperatures needed for activation of adsorbed molecules increases. Higher activation temperatures can be detrimental. The reason for this is that topologically defective structures are usually energetically unfavorable compared to ideal structures. Therefore, formation energies for defects have to be surmounted to trigger the emergence of topological defects. Schlögl et al. calculated defect formation energies for pentagonal and heptagonal pores by DFT, referring to the energetically favored 6-membered ring.¹⁶³ Accordingly, the formation energies for five- and seven-membered rings, could already be overcome at room-temperature for the

molecules under investigation. If the formation energies for topological defects are sufficiently high, defect formation could be reduced or even avoided. A possible way to increase defect formation energies is to use more rigid molecular precursors. The use of a RDS could be beneficial, as the activation step is not triggered thermally on the surface like in conventional on-surface Ullmann-type reaction schemes. Therefore, covalent coupling could occur at temperatures below the activation threshold for formation of topological defects.

Thermal desorption of molecular precursors can also limit further on-surface chemistry. For instance, annealing of 6,11-Diiodo-1,2,3,4-tetraphenyltriphenylene (DITTP) monomers adsorbed on an iodinated Ag(111) surface leads to desorption of monomers before activation (cf., Appendix Figure C1). For this specific system the use of the RDS was inevitable to achieve covalent coupling. This example demonstrates that an RDS may enable the formation of nanostructures, inaccessible by a conventional on-surface synthesis approach. Also, thermally instable materials, that would melt or decompose at the activation temperatures, could be used as substrates. Another benefit of performing the activation spatially separated is that unwanted on-surface side reactions may be excluded. Furthermore, the activated molecules could in principle be directly deposited onto the respective nanostructured surface for building the electric device. Hence, no transfer of the nanostructure would be necessary. This would be advantageous as transfer to other surfaces is often intricate, time-consuming, material-consuming, and the harsh conditions can damage the fragile nanoarchitectures.¹⁹⁶ For instance the transfer of GNRs from Au(111) films on mica onto a SiO₂ surface includes multiple steps.¹⁹⁷ First, spin-coating of poly-methyl methacrylate (PMMA) onto the GNR adsorbed on Au(111) and a subsequent annealing step is conducted, followed by a delamination in concentrated hydrofluoric acid to remove the mica. Further, the Au is removed by an etchant. After rinsing, the GNR/PMMA film is drawn onto the target substrate and the PMMA is removed with acetone.¹⁹⁷

Finally, the overall time for the synthesis could be reduced, as no temperature program for activation and eventually no transfer are needed. For basic research experiments time plays a minor role, but in case of industrial production the synthesis time is a major cost factor. In the following part the basic operation principle of the RDS will be elucidated.

6.2 Basic principle of the RDS

In this section the main components of the RDS will be introduced and their respective functions will be explained. However, the focus is on elucidation of the operation principle. Therefore, the dimensions of the components as well as details on every used material will not be given.

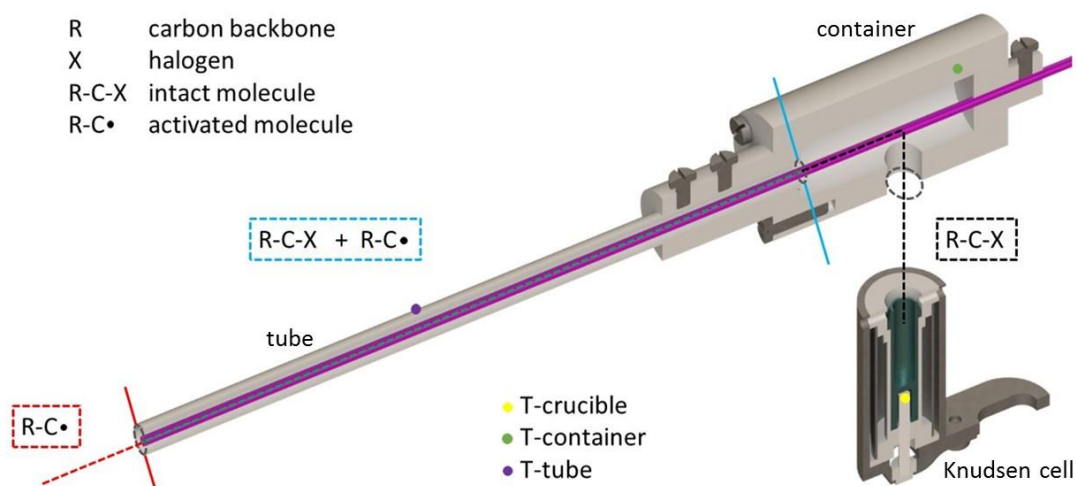


Figure 6. 1: Cross section of the RDS, consisting of a Knudsen cell, a container, and a tube. The black dashed line corresponds to areas, where intact monomers occur, the blue dashed line to a coexistence-region of intact-, partially activated-, and fully activated monomers, and the red dashed line to a region of fully activated monomers. The yellow, green, and purple points indicate the position of the thermocouples for tracking the temperature of the crucible, the container, and the tube respectively. For the sake of simplicity, feedthroughs, filaments, thermocouples, and the vacuum components surrounding the RDS are not included.

To reach the surface, a molecule has to follow the path of the dashed line, and the color indicates the progression of the activation. In reality, the molecules cannot follow the direct path of the dashed line, since the actual path has to include multiple deflections at the walls of container and tube. The molybdenum crucible can be filled with the molecules of choice. A sufficiently high crucible temperature can be selected to induce a thermal sublimation of molecules. In order to maximize the amount of molecules entering

the container, the crucible is positioned very close (< 10 mm) to the entrance hole of the container. The Knudsen cell allows to dose a precise amount of molecules into the container. A molecule inside the container has two possible ways to leave the container: it can exit where it entered, or it can be transferred into the tube. The latter path is desired for our purpose. The area ratio of exit and entrance should be a valid approximation for determining the proportion of molecules taking the desired path. This approach does not consider the different length of the cylindrical entrance and exit paths. Accordingly, about 43% of the molecules, that entered the container, should exit the RDS at the desired end of the tube. To avoid stable adsorption of molecules on the walls of the container, this part can be separately heated to a temperature above the sublimation temperature. Defined heating of the container is achieved with a resistance heater. Therefore, a tungsten wire ($\varnothing = 0.3$ mm) is wrapped around the container and the temperature is measured inside the walls of the container with a K-type thermocouple, while a 6-fold ceramic capillary with a threaded tantalum wire is centered inside the ceramic tube to facilitate a defined and homogenous heating. The temperature is also measured with a K-type thermocouple at the outer walls approximately in the middle of the tube. Therefore, the actual temperature at the inner walls of the ceramic tube will be higher than the measured. The activation of the molecules, representing the decisive process of the RDS, happens at the inner walls of the tube. Hence, the temperature needs to be sufficiently high to trigger C-X bond cleavage during contact with the wall. This bond fission can be regarded as a mainly temperature driven process, as the ceramic wall of the tube has a negligible catalytic activity. In the end, a completely dehalogenated molecule exits the RDS through the front hole of the tube. The angle characteristics of the effusion of the radicals remains elusive, as it is unknown at which part of the tube the average molecule has its last contact to the ceramic walls. Nevertheless, to increase the amount of molecules impinging on the surface, the distance between the RDS and the surface has to be minimized. But the radiative heat load on the surface also increases with decreasing distance. Therefore, a distance of approximately 15 cm was selected as a reasonable compromise.

6.3 Graphene nanoribbons

Single-layer carbon strips, better known as GNRs, represent a material class intensely investigated in the last years. Especially, the combination of high-current-carrying capability and mobility (like graphene) and the possibility of band gap engineering, solely by their design, make GNRs a promising material class. GNRs were first synthesized by top-down approaches. Typically, in these approaches the GNRs are cut out of graphene by using various lithographic methods^{17, 18, 198, 199} or by unzipping of carbon nanotubes.^{97, 200} The major drawback of top-down synthesized GNRs is the lack of control at the atomic level. This is a result of the harsh reaction conditions of lithography-based manufacturing.²⁰¹ Furthermore, GNRs synthesized with top-down methods usually have large imprecise widths, rarely below 5 nm.²⁰² Bottom-up synthesis in solution can also be used to produce GNRs.^{203, 204} Solution based approaches appear especially suitable for synthesizing narrow (0.5 nm) or long (>200 nm) GNRs.^{205, 206} In 2010, the first atomically precise GNRs were presented by employing an on-surface bottom-up approach in the pioneering work by Cai et al.¹⁹ Since then, a multitude of different GNRs were synthesized by this approach. The versatility of the GNRs obtainable by this approach relies on the large number of possible molecular precursors available for the synthesis. They are all based on the same reaction scheme. First, a polymer chain is formed by an Ullmann-type coupling of haloarenes at moderate temperatures (< 200°C), followed by a CDH reaction at higher temperature (> 350°C) leading to the GNRs. Ullmann-type on-surface reactions were covered in chapter 3.2. As the name explains, CDH processes form new aromatic rings by an intra- or intermolecular oxidative C-C coupling. First, the C-H bonds have to be cleaved to induce covalent coupling. Usually CDH processes are temperature-driven and catalyzed by the substrates.¹⁰⁴ CDH reactions and Ullmann-type coupling reactions both rely on a metal surface-catalyzed activation of the molecular tectons, followed by their covalent coupling. The main difference is that C-X bonds are weaker than C-H bonds, explaining the higher temperatures required for CDH reactions. Here we present a novel way for the bottom up synthesis of GNRs where the activation step is spatially separated from the coupling- and CDH step. This bears two decisive advantages compared to conventional synthesis of GNRs: Defect formation during activation through unwanted on-surface side reactions is excluded, and no catalytic aid of the substrate for C-X bond cleavage is required. As a model precursor DITTP (cf.,

Figure 6.2) is chosen. This molecule is known to form chevron type GNRs by a bottom up approach involving dehalogenation, step growth polymerization, and CDH reactions on Au(111) respectively.²⁰¹ Conventionally, all these steps are carried out with molecules adsorbed on low index metal (Au, Ag, Cu) surfaces and the reaction steps are successively activated by increasing the temperature.²⁰⁷⁻²⁰⁹ In the next section, experiments performed with this molecular precursor on iodine passivated Ag(111) and Au(111) substrates with the RDS are presented.

6.4 Results and Discussion

The activated DITTP precursor was deposited onto iodinated Ag(111) and Au(111) surfaces *via* the RDS. Iodinated surfaces were used to reduce both the catalytic activity of the metal substrates and the interaction strength of substrate and nanostructures. Iodination was done in the load lock *via* a leak valve for 10 minutes at a iodine pressure of 1×10^{-6} mBar and 1×10^{-7} mBar for Au(111) and Ag(111), respectively. The freshly iodinated surfaces were brought to the main chamber and heated to 200°C for 15 minutes. This mild annealing yielded high quality iodine-terminated surfaces, as routinely observed with the STM. Before every experiment, large scale images as well as atomically resolved images of the iodine atoms were acquired. First results were obtained on an iodinated Ag(111) surface. Therefore, DITTP was sublimated at 200°C and the container was kept at temperatures above 200°C. For activation of the DITTP molecules inside the tube a temperature of 390°C turned out to be convenient. In order to reach 390°C at the tube, the tube heating element introduced a sufficiently high heat load to the container therefore no additional heating of the container was necessary. A deposition time of 90 minutes and the above mentioned parameters were used for all experiments with the RDS presented in the following. Directly after room temperature deposition with the RDS, polymeric chains were observed by STM on the iodinated Ag(111) surface (cf., Figure 6.2).

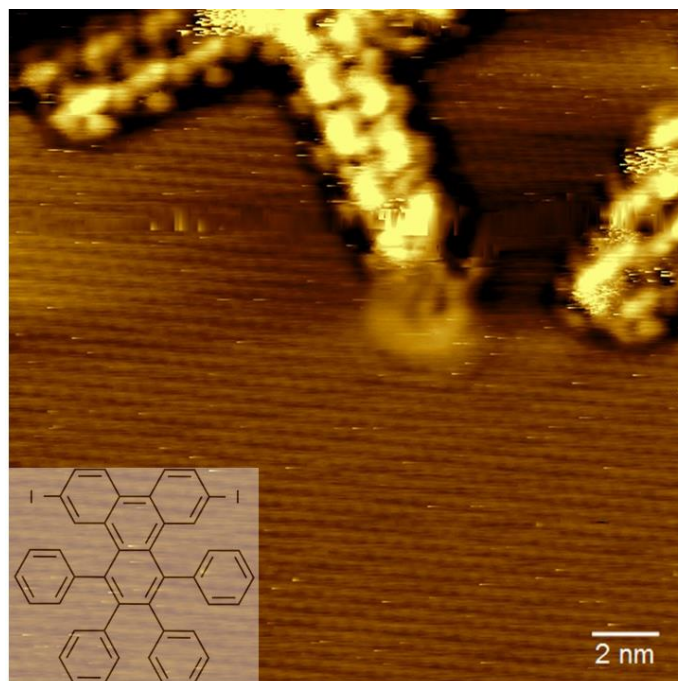


Figure 6. 2: STM image of DITTP-derived polymers on iodinated Ag(111), acquired after room-temperature deposition with the RDS. The inset shows the chemical structure of DITTP. The polymers are adsorbed on a closed iodine monolayer.

The polymers can be identified by their periodicity of approximately 1.7 nm consistent with previous literature values.^{19, 201} The typical crescent-shaped structures, that arise from the four tilted phenyl rings, corroborate the proposed molecular arrangement. Moreover, a close packed hexagonal structure is visible at the background of Figure 6.2 that corresponds to the known $\sqrt{3} \times \sqrt{3}$ R30° iodine superstructure on Ag(111).^{62, 210, 211} Nevertheless, the polymer chains are relatively short, and imaging of the structures is intricate. To allow the polymers to diffuse over the surface and to facilitate a image acquisition the sample is annealed to 200°C, at which temperature the $\sqrt{3} \times \sqrt{3}$ R30° iodine superstructure on Ag(111) is known to remain intact.²¹¹ Further deiodination of intact molecules is not expected by a thermal treatment at 200°C on the non-reactive iodine passivated surface.

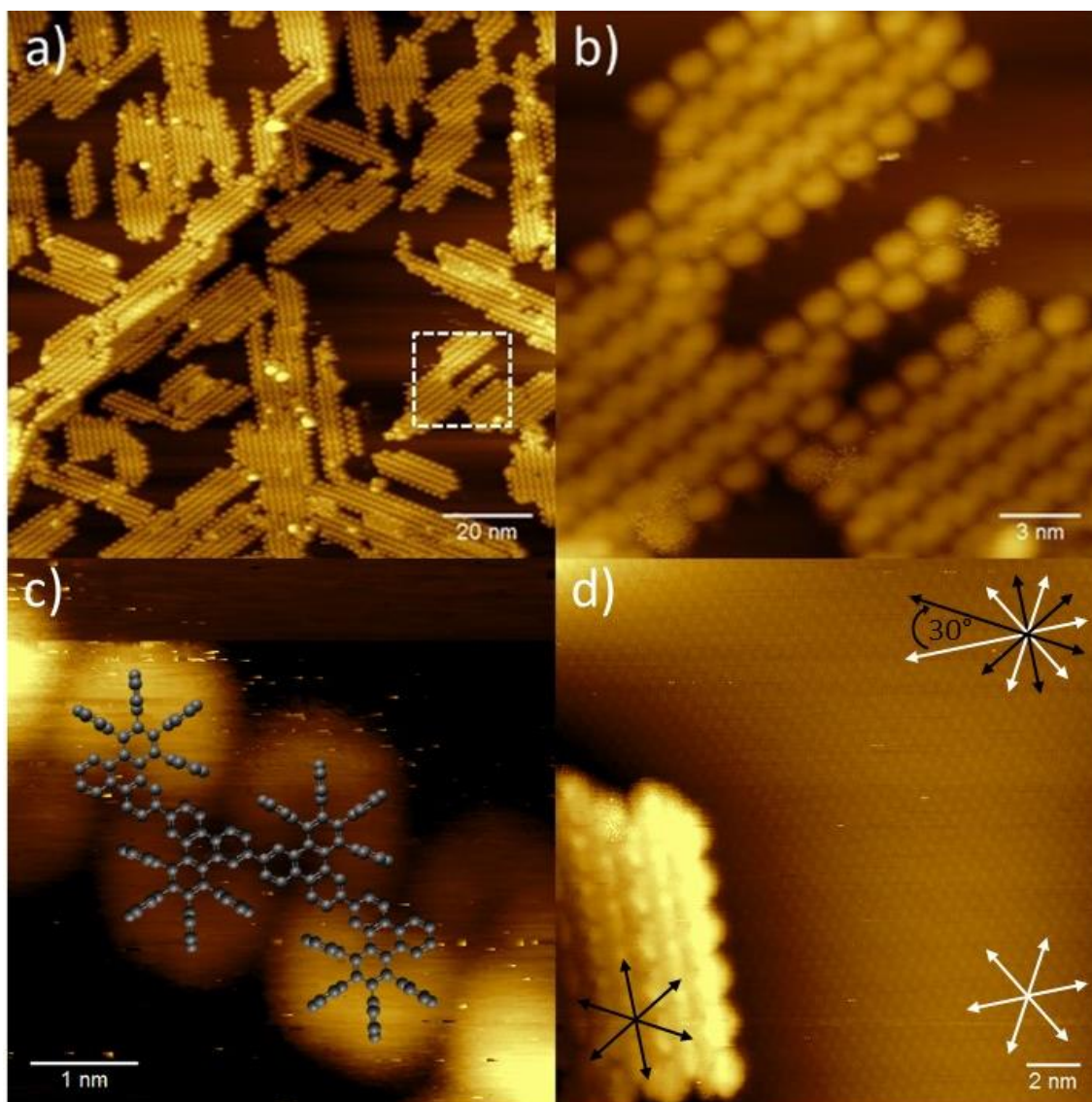


Figure 6. 3: STM image of DITTP-derived polymers on iodinated Ag(111), acquired after annealing to 200°C: (a) Overview STM image showing self-assembled domains of the polymer; (b) close-up image of the area highlighted by the white dashed square; (c) Close-up image with a scaled molecular overlay of the polymer; (d) STM image simultaneously showing the iodine $\sqrt{3} \times \sqrt{3}$ R30° superstructure and the adsorbed polymer. The black arrows depict the orientations adopted by the polymers and the white arrows the high symmetry directions of the iodine monolayer.

The STM images in Figure 6.3 (a) and (b) clearly show the aggregation of one-dimensional polymers into domains of parallel aligned chains. Most polymers exhibit a length between 10 and 50 nm, but individual polymers can be found up to lengths of 100 nm. The high resolution STM image in Figure 6.3 (c) with a scaled molecular overlay

illustrates the exact orientation in the polymeric chains. In Figure 6.3 (d), the chemisorbed iodine monolayer and the polymer adsorbed are both visible. Obviously the domains are not randomly oriented. The white arrows indicate the three high symmetry directions of the densely packed iodine monolayer, while the black arrows display the three polymer orientations of the overview STM image in Figure 6.3 (a). In the top right corner of Figure 6.3 (d), the directions of the polymer and the iodine $\sqrt{3} \times \sqrt{3}$ R30° superstructure are centered above each other. Accordingly, the polymers are tilted by 30° with respect to the high symmetry directions of the close packed iodine. The growth direction of the polymers and the high symmetry directions of Ag(111) are both rotated by 30° with respect to the iodine unit cell. Therefore, the polymer islands are oriented along the high symmetry directions of the (111) surface of the silver crystal. All polymers depicted in Figure 6.3 (a)-(d) follow the same directions, marked in (d). The chevron type polymer favors a stacking, where the adjacent crescents are shifted by a half polymeric repeat distance. Furthermore, the tilted phenyl rings at the rim of a domain appear different from interior ones.

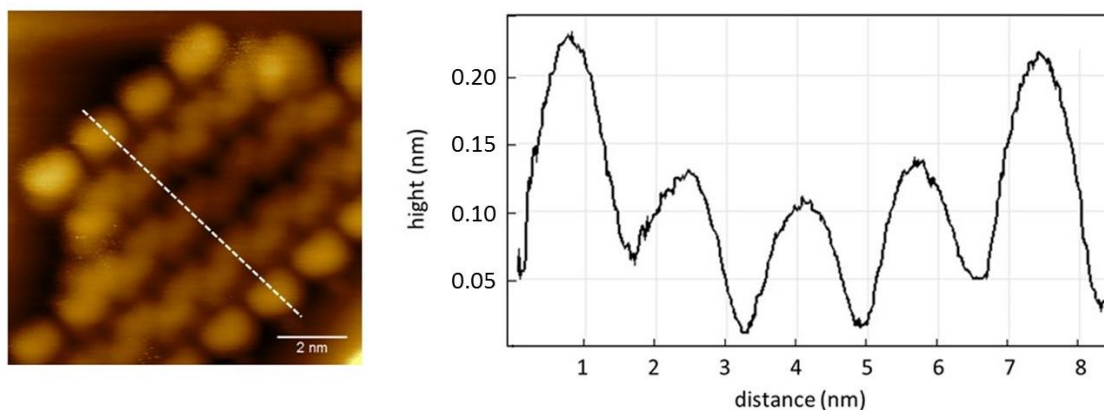


Figure 6. 4: High-resolution STM image of DITTP-derived polymers on iodinated Ag(111), acquired after annealing to 200°C. The white dashed line indicates the path of the line-profile depicted on the right.

This can tentatively be explained by π - π interactions of non-planar phenyl rings of neighboring polymers which point towards each other. Aromatic-aromatic interactions are a type of non-covalent attractive interaction occurring between conjugated π -electron clouds. They are known to influence self-assembly pattern.²¹² This attractive force stabilizes the self-assembly of the one-dimensional polymer and determines the

configuration of the phenyl rings. Accordingly, the phenyl rings inside a domain are exposed to additional interactions that are absent at the rim. Hence, the rims of the domains appear different in STM images. This can clearly be seen in the STM images of Figure 6.3 (b) and 6.4, where the four tilted phenyls of one monomeric unit at the boundary of a domain appear as a single bright feature, in contrast to the phenyl rings between adjacent polymers appearing as continuously corrugated structures. These differences are also reflected in the corresponding line-profile depicted on the right side of Figure 6.4. The line profile runs across four polymer chains, corresponding to the four local height minima indicating the position of the polymer chain. Obviously, the phenyl rings at the rim of the domains appear approximately 0.1 nm higher in the STM images compared to the inner phenyl rings. The reason for this is that the phenyl rings terminating an island can point upwards as explained above. In the next step the sample was annealed to 400°C.

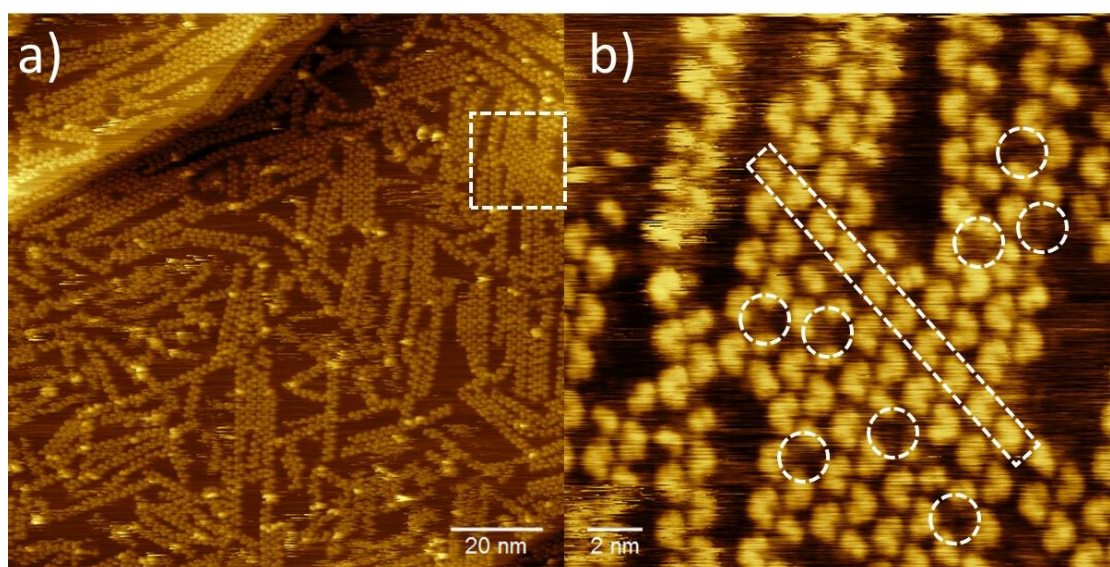


Figure 6. 5: STM image of DITTP-derived polymers on Ag(111), acquired after annealing to 400°C: (a) overview STM image showing the polymer; (b) close-up image of the area highlighted by the white dashed square.

After a thermal treatment to 400°C the polymer is still clearly discernible in STM images. But the polymers are not anymore aggregated into dense packed islands like before, and are also oriented in multiple different directions. Annealing to 400°C leads to thermal desorption of a fraction of the iodine atoms. STM gives no evidence of remaining adsorbed iodine, but a TPD study suggests remaining iodine up to more than 500°C.²¹¹

The absence of densely packed polymer islands, in addition to the different appearance of the polymer in STM topographs, indicates that the polymer is now directly adsorbed on the bare metal surface. This has a strong impact on the adsorbed polymer. The polymer is now interacting strongly with the metal surface, in contrast to the polymers adsorbed on the passivating iodine monolayer displayed in Figure 6.3. Notably, the polymer is oriented differently on the bare metal as compared to the close packed island on top of the chemisorbed iodine monolayer. Therefore, some rearrangements of the polymers must have occurred during annealing to 400°C. But the different appearance in STM images of polymers adsorbed on Ag(111) as compared to polymers adsorbed on I-Ag(111) can also originate from decoupling induced contrast changes. Additionally, some slightly bent polymers can be found. A possible explanation for this different adsorption behavior of the polymers depending on the substrate (I-Ag(111) versus Ag(111)) can be given by considering the strength of polymer-surface interactions. The adsorption strength planarizing the polymer will be stronger on the metal. Therefore, the four tilted phenyl rings will also be attracted more strongly by the Ag(111) surface. As a result, the strength of the π - π interactions among adjacent polymers is reduced. This is also reflected in the average center to center distance of two adjacent polymers. On the I-Ag(111) surface, the average spacing between polymers is approximately 1.25 nm compared to 1.75 nm on the bare metal, underscoring the strong impact of the substrate. This less dense aggregation also leads to an apparent increase of the surface coverage with respect to the densely packed structures observed after annealing to 200°C. Nevertheless, adjacent polymers still favor a defined stacking with the tilted phenyl rings shifted by a half repeat distance, indicated by the dashed rectangle in 6.5 (b). Moreover, polymers are frequently observed where the entire crescent or parts of it are not visible in the STM images. Examples are displayed by the dashed circles in Figure 6.5 (b). This could be due to first CDH reactions, forcing the respective phenyl rings into the same plane. Also, diffusion barriers for the polymer adsorbed on the metal could be higher than that on top of the iodine layer, further hindering aggregation in densely packed structures with a defined epitaxial relation to the substrate. As a temperature of 400°C did not trigger a sizeable CDH reaction, the sample was further heated to 500°C.

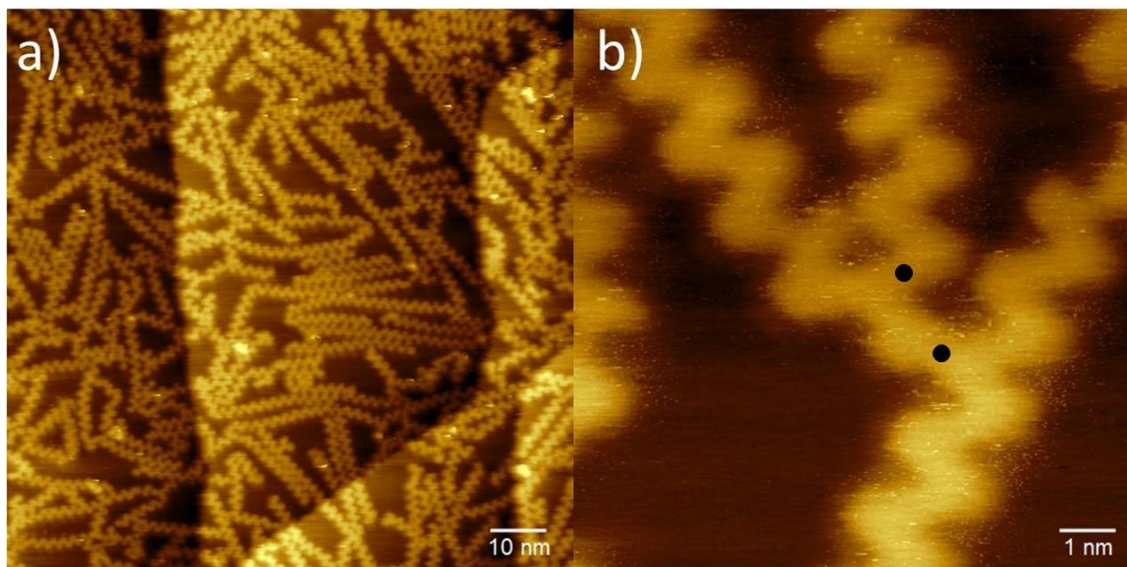


Figure 6. 6: STM images of DITTP-derived GNRs on Ag(111), acquired after annealing to 500°C: (a) overview STM image; (b) close-up image of fused GNR. Black points indicate positions of threefold junctions.

Upon further annealing to 500°C chevron-type GNRs emerge. They can clearly be distinguished from the polymer by their appearance in STM images. This is a direct result of the CDH reaction forcing the formerly tilted phenyl rings in a plane. Planarization also changes the electron charge distribution along the polymer, further affecting the STM images. The GNRs appear with a uniform apparent height of 0.18 nm over the surface, compared to the polymers with an apparent height up to 0.24 nm. These values are in agreement with previous literature values of polymers and GNRs on Au(111).^{19, 201} However, the apparent height of the polymer strongly varies with the exact position. For instance, the longitudinal axis appears lower than the tilted phenyl rings at the rim.

Furthermore, the synthesized GNRs do not show a preferred adsorption orientation on the Ag(111) surface. Even their overall shape deviates frequently from a perfect straight-lined shape. Moreover, connection points are commonly observed where two GNRs are fused together (cf., black points in Figure 6.6 (b)). Thus, threefold junctions are generated. A possible explanation for this is the high temperature of 500°C used for the synthesis of the GNRs on the Ag(111) surface. This can lead to unspecific C-H activation favoring coupling reactions of adjoining GNRs. However, the detailed understanding of the fusion reactions on an atomically level remains elusive. A better understanding of the mechanisms favoring the threefold junctions would be desirable, to make it possible to

minimize their emergence by adjusting the reaction conditions or to maximize their occurrence, in order to create reticulated structures from the GNRs. Cai et al. triggered the formation of an atomically precise threefold GNR junction by adding triply halogenated precursor molecules.¹⁹ Recently, nanoporous graphene was synthesized by dehydrogenative cross coupling of adjacent GNRs.²¹³ This example shows that the GNRs do not necessarily have to be the final product of the synthesis. However, the focus of our study was on proving the feasibility of directly depositing radicals *via* the RDS with DITTP as a model compound. Additional experiments were performed to underscore the functionality of the RDS. Therefore, the DITTP molecules were deposited on iodinated Ag(111) *via* a conventional Knudsen cell. Furthermore, the RDS was used to deposit the radicals directly on the Ag(111) surface. The results are depicted in Figure 6.7 (a) and (b).

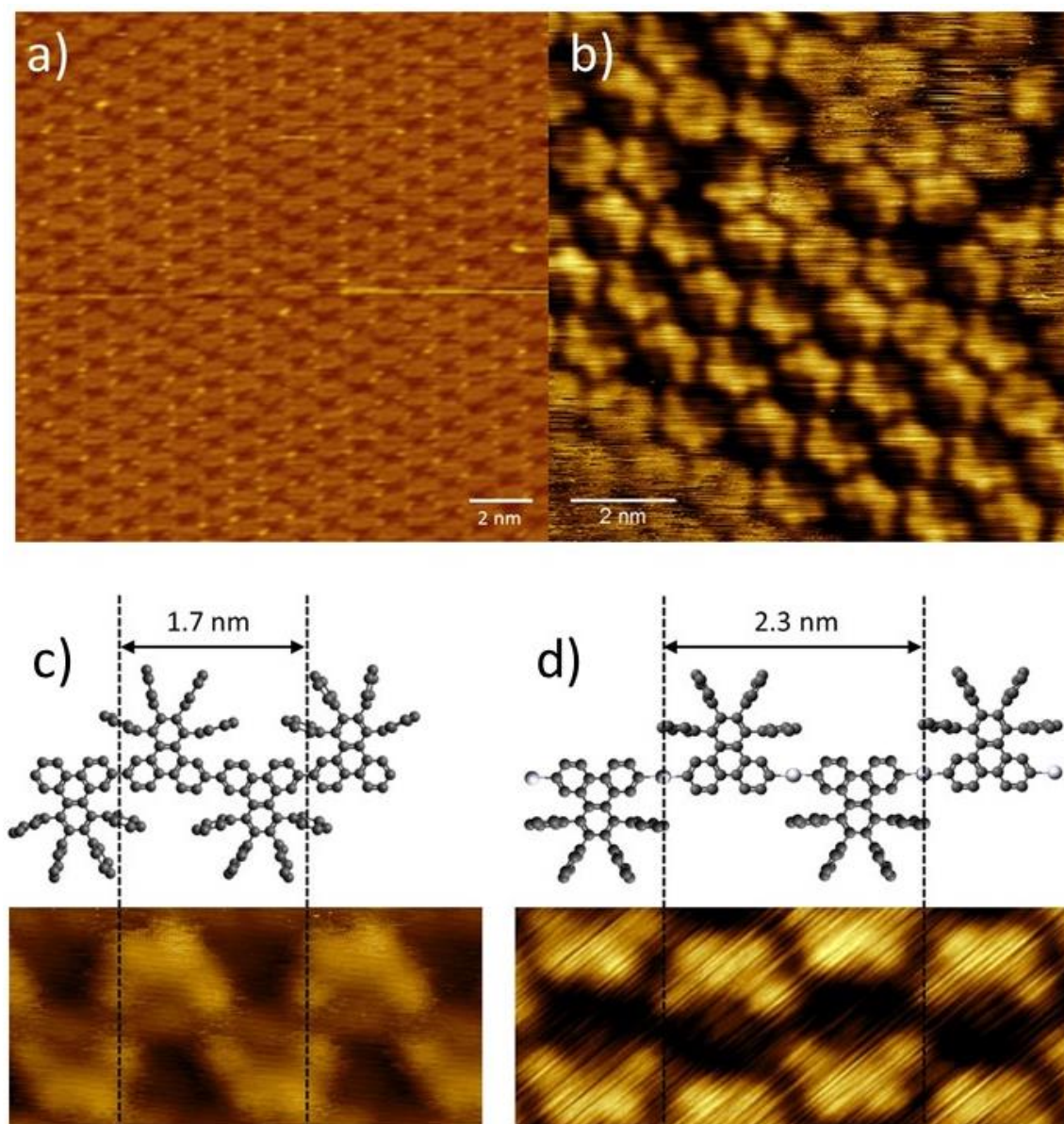


Figure 6. 7: STM images of DITTP (a) on iodinated Ag(111) deposited with a Knudsen cell, (b) on Ag(111) deposited with the RDS. The close-up in (c) shows the covalent polymer obtained by deposition with the RDS on iodinated Ag(111), while (d) shows an organometallic structure obtained with the RDS on Ag(111). The molecular overlays in (c) and (d) illustrate the different repeat distances.

Deposition of DITTP with a conventional Knudsen cell onto iodine terminated Ag(111) results in self-assembled structures shown in Figure 6.7 (a). The obtained self-assembly resembles the structures obtained by Bronner et al. with the brominated analogue on Au(111).²⁰¹ Mild annealing to 200°C, led to a thermal desorption of the molecules, whereupon the $\sqrt{3} \times \sqrt{3}$ R30° iodine superstructure becomes visible again in STM images

(cf., Appendix Figure C1). The same temperature treatment, after deposition with the RDS, resulted in dense packed polymer islands. This is a further proof of the functionality of the RDS. Direct deposition on Ag(111) *via* the RDS lead to the formation of linear organometallic chains. This is corroborated by the increased periodicity of the organometallic structure of 2.3 nm as compared to the 1.7 nm periodicity of the covalent polymer. Organometallic C-Ag-C linkages are known to increase the center to center distance between the carbon atoms approximately 0.3 nm with respect to the covalent C-C bond.^{29, 32} As two C-Ag-C linkages are present in each repeat unit of the chains, the increased distance of 0.6 nm is in good agreement with the expected values. Interestingly, it was not possible to convert the organometallic structures into a covalent polymer by a temperature induced demetalation. The sample was annealed to 200°C, whereupon only the bare Ag(111) surface was visible. One possible explanation for this is that the temperature required for breaking the C-Ag bonds already exceeds the energy for thermally desorbing the molecular species before covalent coupling sets in. Hence, the iodine layer, as well as the use of the RDS is a prerequisite for obtaining chevron-type GNRs from the DITTP precursor on Ag(111). This emphasizes the benefits of performing experiments with a RDS on surfaces that are not reactive enough for conventional Ullmann-type coupling. Nevertheless, from 10,10'-dibromo-9,9'-bianthracene molecules organometallic chains can be formed and transformed into covalent chains and armchair GNRs on Ag(111), consecutively.¹⁴⁶ Cai et al. were able to synthesize chevron type GNRs from 6,11-Dibromo-1,2,3,4-tetraphenyltriphenylene that has the same organic backbone like the DITTP molecule used in this study.¹⁹ The only difference is that instead of iodine, bromine is used as substituent. In the following, experiments on iodinated Au(111) will be presented.

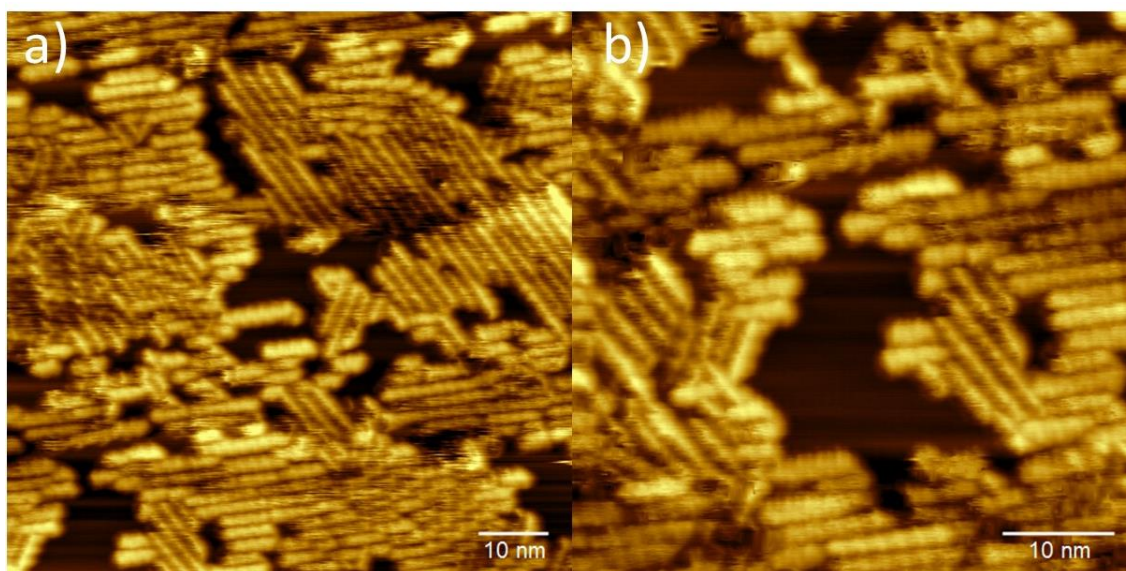


Figure 6. 8: STM images of DITTP-derived polymers on iodinated Au(111), acquired after annealing to 200°C: (a) Overview STM image showing self-assembled domains of the polymer; (b) close-up of the bottom left area of a).

Identical preparation protocols were used for the iodinated Au(111) and Ag(111) surfaces. Directly after room temperature deposition onto the iodinated Au(111) surface, STM imaging was not possible. Therefore, the sample was annealed to 200°C. This temperature was selected for the same reasons as on the I-Ag(111) surface, and to allow a direct comparison after an identical temperature ramp on both substrates. After the annealing, aggregated covalent polymers with lengths of 5-30 nm are present on the surface, significantly shorter than on iodine terminated Ag(111). The polymers also show preferred orientations on the surface, but less regular than on I-Ag(111). Again there are three preferred orientations, but this time it was not possible to acquire images resolving the orientation with respect to the substrate. Nevertheless, iodine monolayers on Au(111) are also known to form the $\sqrt{3} \times \sqrt{3}$ R30° superstructure.^{214, 215} Au(111) and Ag(111) both crystalize in the fcc structure and they have very similar lattice parameters of 407.82 pm and 408.53 pm, respectively.²¹⁶ Therefore, it is likely that the polymers are again aligned parallel to the high symmetry directions of the unreconstructed Au(111) surface. The actual coverage is higher compared to previous experiments on I-Ag(111). This can be explained by the less dense aggregation of the polymers, assuming deposition of equivalent amounts and similar sticking coefficient. Adjacent polymers have an average distance of 1.9 nm which is significantly higher compared to 1.25 nm on the iodinated

Ag(111) surface. These distances were found to be identical also for lower coverages on both surfaces. The overall appearance of the polymers adsorbed on I-Au(111) is different in STM images. To further corroborate this, additional STM images of polymers on both iodinated surfaces, acquired with the same tip and tunneling parameters, would be needed. The adjacent polymers can be clearly distinguished, but no internal resolution of the molecular entities is achieved. A reason for this could be the lower adsorption strength of the surface, acting on the polymer, compared to the iodinated Ag(111) surface. Additionally, the larger distance of the polymers will reduce stabilizing forces of adjacent polymers by π -stacking. This leads to a less stable self-assembly. Hence, the polymers could have some motional freedom, hampering submolecular resolution. In the next step the sample was annealed to 400°C.

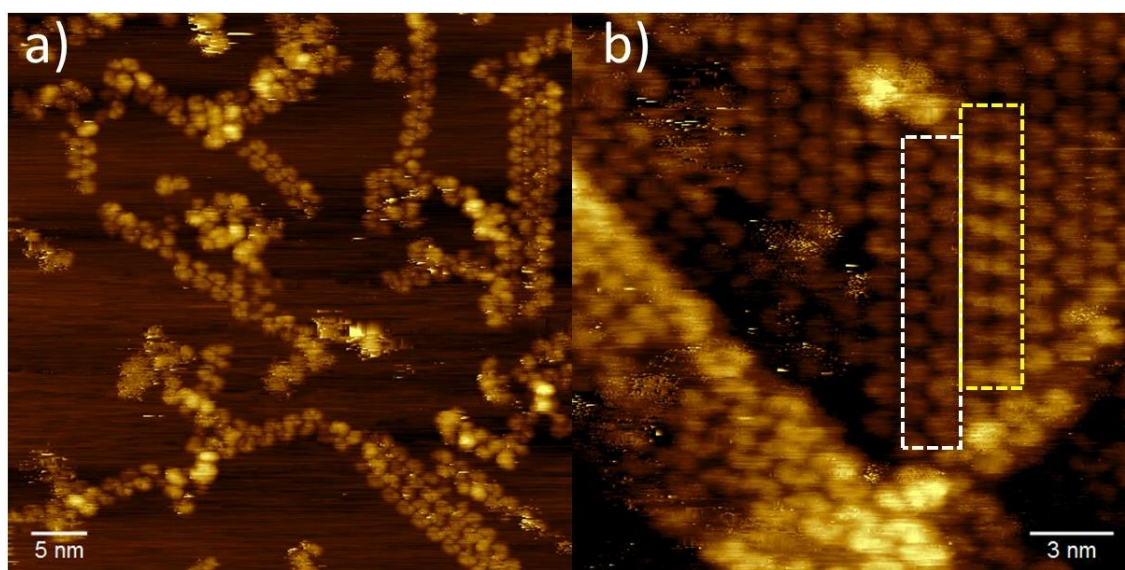


Figure 6. 9: STM image of DITTP-derived polymers on Au(111), acquired after annealing to 400°C: (a) Overview STM image showing the polymer and (b) image of parallel aligned polymer chains.

Upon further annealing to 400°C the covalent polymer is now adsorbed on the Au(111) surface. The adsorption strength will be higher for the polymers adsorbed on the metal surface as compared to polymers adsorbed onto an iodine monolayer. This will also influence the contrast in STM images. The molecular entities along the polymer chain are now discernible again. Especially the tilted phenyl rings can be recognized by their typical crescent-like shape. Even though no evidence for adsorbed iodine was obtained from STM measurements, the absence of the herringbone reconstruction indicates

remaining chemisorbed iodine. A possible explanation for this could be that it is normally not possible to image iodine at submonolayer coverage with the STM at RT, due to the high mobility of iodine. In addition, preferred adsorption of the iodine in between the polymer and the metal substrate could provide an alternative explanation why the iodine remains invisible in STM. Like on Ag(111), the preferred orientation of the polymers disappeared after annealing to 400°C. Adjacent polymer chains can be orientated with the crescents shifted in the growth direction of the polymer (highlighted by the white dashed rectangle), or in a less dense configuration (highlighted by the yellow dashed rectangle). In the latter configuration the polymers adopt a mirrored configuration. No indications for nascent CDH reaction were found. Therefore the sample was further annealed to 500°C.

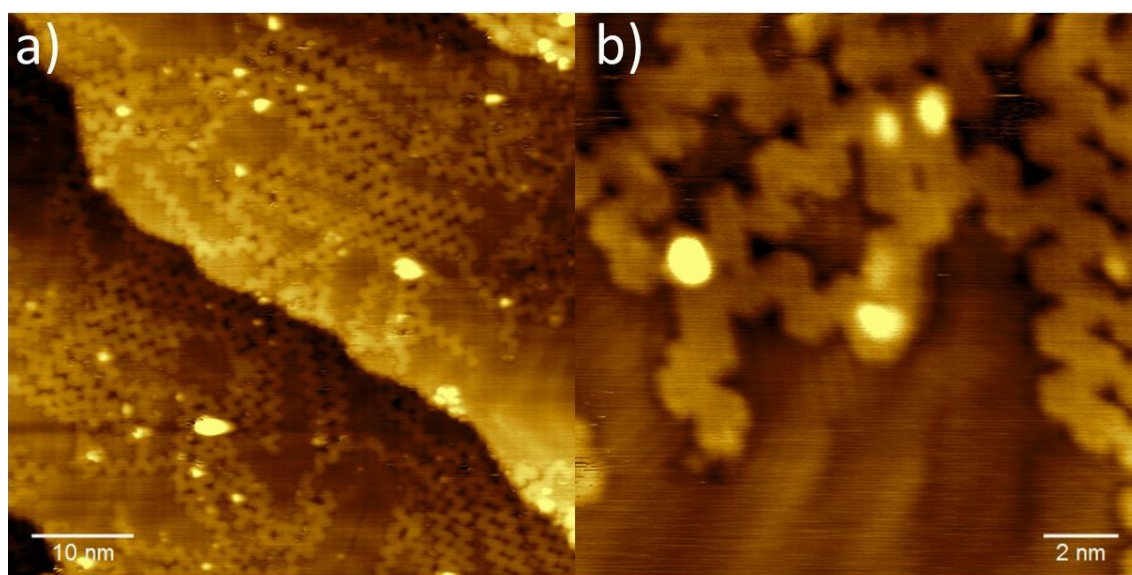


Figure 6. 10: STM image of DITTP-derived chevron type GNRs on Au(111), acquired after annealing to 500°C: (a) Overview STM image showing the spatial distribution of GNRs; (b) close-up image featuring fused GNRs.

Like on Ag(111), the chevron type GNRs can again unambiguously be identified by their characteristic appearance in STM images. The main differences to the polymer are the absence of the dark appearing line at the center, the uniform height, and the defined edge structure of the atomically precise GNRs. In the overview image of Figure 6.10 (a) the herringbone reconstruction is discernable again, indicating desorption of iodine to a great extent. Again connecting points are frequently present, where two GNRs are fused together. But this time also parallel aligned GNRs can be fused together, as shown on the

right hand side of Figure 6.10 (b). Actually, all structures observed in the close up image of Figure 6.10 (b) are fused together. After annealing to 400°C no CDH reactions were observed with STM, whereas after annealing to 500°C a complete CDH process was observed and adjoining GNRs were fused together. To examine if the desired intramolecular CDH reaction can be separated from intermolecular fusion of GNRs, another experiment with an intermediate annealing temperature of 450°C was performed.

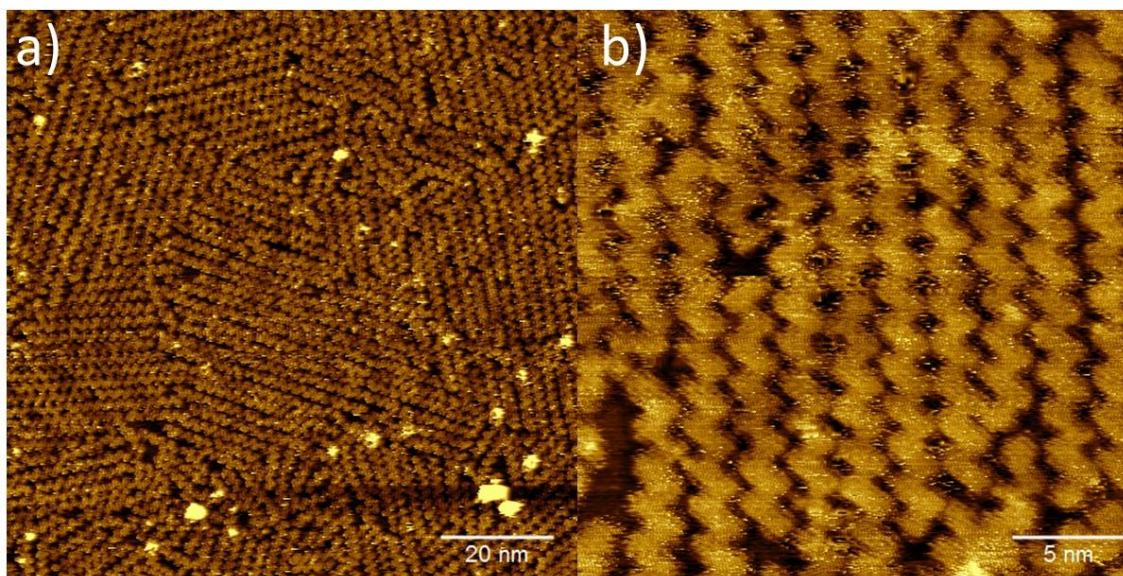


Figure 6. 11: STM image of DITTP-derived chevron type GNRs on Au(111), acquired after annealing to 450°C: (a) Overview STM image showing the spatial distribution of the GNRs; (b) close-up image GNRs.

In the overview STM image of Figure 6.11 (a) chevron type GNRs adsorbed on an Au(111) surface are depicted. The actual coverage of approximately one monolayer is higher as compared to previous experiments. The crucible had to be refilled with molecules just before this experiment, this possibly being the reason for the variation in coverage. The surface is covered with different domains that consist of parallel oriented GNRs. One of these domains is depicted in the close-up image of Figure 6.11 (b). Obviously, the GNRs are not fused together as observed after annealing to 500°C. Hence, the temperature treatment to 450°C is sufficient to produce fully cyclized chevron type GNRs, but not enough to trigger unspecific C-H activation reactions. This demonstrates how the fine variation of reaction conditions (here temperature) can help inhibiting unwanted side reactions. Contrary to the Ag(111) surface, where the use of the RDS and the passivating iodine monolayer is a prerequisite to synthesize GNRs from the DITTP

monomer, on Au(111) chevron-type GNRs can be obtained conventionally by deposition of the intact molecular precursor and a heating to 450°C. This demonstrates that the absence of an organometallic intermediate structure can be advantageous. In the next chapter the results obtained with the RDS on iodinated Ag(111) and Au(111) surfaces are concluded. Furthermore, a brief outlook concerning future experiments is given.

6.5 Conclusion and Outlook

In summary, the functionality of the RDS could be validated by experiments on iodine passivated Ag(111) and Au(111) surfaces. The RDS allowed us to dose radicals directly onto the substrates, therefore no catalytic aid of the surface was necessary for covalent coupling into the polymer. Nevertheless, the substrate is still needed as a template to form the polymer. In the applied reaction scheme only the second reaction step, i.e. the CDH reaction, requires the catalytic aid of the reactive metal substrates to eventually obtain GNRs. This is a decisive advantage compared to conventional on-surface synthesis approaches for GNRs, where both reaction steps (Ullmann-type coupling and CDH reaction) require reactive substrates. Many dehydrogenation reactions are endothermic on the coinage metal surfaces.^{114, 217} Nevertheless, they occur spontaneously. This is commonly explained by associative desorption of H₂ into the vacuum and the related entropy gain.¹⁵³ Although Ag(111) is known to be more reactive than Au(111), the temperatures required to induce the CDH reaction were similar in our study.

Directly after RT deposition with the RDS, exclusively on the I-Ag(111) surface, polymer chains could be observed by STM. On I-Ag(111) and I-Au(111), annealing to 200°C lead to parallel aligned polymer chains. Whereas, after annealing to 400°C in both cases, polymers directly adsorbed onto the metal substrates were found. Further annealing to 500°C triggered a full CDH reaction on both substrates, leading to atomically precise chevron-type GNRs. Bronner et al. obtained chevron type GNRs on Au(111) from the same molecular precursor already slightly above 350°C.²⁰¹ This is approximately 100 K lower than the temperatures required to obtain GNRs in our experiments. In our study, as well as in the above mentioned study, coadsorbed iodine can influence the reaction. However, the origin of the chemisorbed iodine is different. In our study the iodine is remaining from the previously deposited monolayer, whereas the iodine in the study of

Bronner et al. originates from the iodinated precursor molecule. Therefore, the amount of chemisorbed iodine will definitely be higher in our study. DFT calculations suggest a preferred adsorption of bromine underneath the phenyl rings of polyanthrylene on Au(111).¹⁵¹ Assuming a similar adsorption behavior of iodine, i.e. iodine between the polymer and the respective metal substrate, could explain the observed differences. This would also explain why the remaining iodine is not observable using STM. Hence, the higher temperatures required in our study, could be related to the removal of iodine atoms attached to the polymer. In other words, the iodine atoms could inhibit the CDH reaction by blocking reaction sites. Furthermore, the electronic coupling between polymer and metal substrate is reduced if iodine is adsorbed underneath the phenyl rings. Bronner et al. also performed TPD experiments revealing an associative desorption of HBr preferred over desorption of Br₂.¹⁵¹ Assuming associative desorption of HI from the Ag(111) and Au(111) surfaces could explain the high temperatures required for the synthesis of GNRs. The hydrogen source for the associative desorption is the CDH step, releasing atomic hydrogen. On Au(111) we never observed the coexistence of already cyclodehydrogenated parts and tilted phenyl rings. An explanation for this could be the following: once the CDH reaction starts to release molecular hydrogen, the associative desorption of HI becomes favorable. Desorption of HI liberates the tilted phenyl rings and allows them to dehydrogenate and couple covalently to form the GNRs. Once the reaction starts, it accelerates itself by providing more atomic hydrogen. This can explain the observed “narrow” temperature windows for the CDH reactions on Au(111) ($400 < T_{CDH} < 450$) and Ag(111) ($400 \leq T_{CDH} < 500$). To further determine the temperatures for the CDH reactions, more STM experiments after different thermal treatments would be required. We propose coadsorbed iodine as the limiting factor for synthesis of GNRs on both surfaces. This could also explain the marked temperature differences for the synthesis of chevron type GNRs mentioned above. The supply of atomic hydrogen to enable associative desorption of HI already at lower temperatures would be a possible way to remove the adsorbed halogens, as proposed by several studies.^{139, 140, 151} Hence, GNR formation should occur already at lower temperatures, as no coadsorbed iodine would hamper CDH reactions.

To date, only STM measurements were used to characterize the executed experiments with the RDS. Hence, only irreversible processes after the respective thermal treatment

are monitored at RT. This makes the experiments time consuming, and the progression of the reactions remains elusive. For the investigated systems, measurements that acquire temperature dependent, *in-situ* real time information would complement the STM data. In the present case TP-XPS or TPD measurements would be suitable to follow the reaction progression. Both techniques enable tracking the desorption of iodine. TPD could, additionally, help to clarify in which chemical state the iodine (AgI, HI, I₂, I) desorbs. High resolution TP-XPS measurements that allow to discriminate between C[C₂H] and C[C₃] would enable monitoring of the temperature window of the CDH reaction. However, C 1s core level shifts induced by dehydrogenation reactions are usually smaller than 0.5 eV, therefore, only accessible by synchrotron-based XPS measurements.¹⁰⁴ Hence, TPD measurements that allow direct tracking of the hydrogen species, are more suitable for following dehydrogenation reactions.²¹⁸

The RDS could also be beneficial for the synthesis of covalent networks. Since chemisorbed halogens as well as high activation temperatures can reduce the quality of 2D covalent networks,²⁸ the use of an RDS could help to reduce topological defects. Particularly on Au(111) surfaces, where the radicals usually directly form irreversible covalent bonds, the use of the RDS could bear decisive advantages. Further experiments with the RDS on more inert surfaces like HOPG, SiC, SiO₂, or h-BN would be desirable to march in the direction of possible applications.

Chapter 7

Conclusion and Outlook

In the present work, one- and two-dimensional organic nanoarchitectures were *in-situ* synthesized and investigated by means of UHV-based surface science techniques. Particular emphasis was placed on the formation of atomically precise organometallic and covalent nanostructures on the (111)-facets of the coinage metals and iodine-passivated Au(111) and Ag(111) surfaces employing a bottom-up approach. As a local real-space technique, STM was used to identify both the topology and different types of chemical bonds that stabilize the molecular assemblies. TP-XPS measurements were performed to follow temperature-driven on-surface chemical reactions that ultimately couple the monomers. For a better understanding of surface-dependent differences in network quality, dehalogenation and coupling temperatures, DFT calculations were performed. The results of this thesis are briefly summarized and put into perspective in the following pages.

Chapters four and five were concerned with organometallic and covalent networks obtained by on-surface Ullmann-type coupling of triply halogenated aromatic precursor molecules on the (111)-facets of the coinage metals. In chapter four, the influence of an *ortho*-methyl substitution on organometallic self-assembly was evaluated by STM and DFT calculations, with respect to the unsubstituted analogue. Therefore, organometallic networks derived from MTBB (**1**) and TBB (**2**) were comparatively studied on Ag(111) and Cu(111) surfaces. The underlying idea was that the steric hindrance exerted by the bulky methyl groups of **1** reduce the C-M-C bond angle flexibility, resulting in networks that exhibit less topological defects. After surface catalyzed dehalogenation, both molecules formed networks with tectons connected *via* C-M-C bonds. STM images in Figures 4.1 and 4.5 clearly indicate that networks obtained from **1** have a higher regularity as compared to the non-methylated compound on both surfaces. To quantify these differences, a statistical analysis of the pore geometries was performed, exclusively including closed pores. On Cu(111), only about 20% of the pores adapted the ideal

hexagonal conformation after RT deposition of **2**, contrary to compound **1**, which exclusively formed hexagonal pores. As dehalogenation of compound **2** was not completed on Ag(111) after RT deposition, the networks derived from both precursors were compared after annealing to 150°C. Again, the network quality obtained from **1** was higher compared to the networks derived from the unsubstituted analogue, but this time about 5% of the pores formed by **1** were non-hexagonal after annealing to 150°C. To estimate the impact of steric hindrance, bond angle dependent energies were evaluated by DFT calculations. Therefore, the C-M-C bond angles were fixed between 180° to 165° with increments of 3° and energies were calculated with respect to the straight geometry (180°). Against our expectations, the 180° C-M-C bond angle (straight linkage) was not the energetic optimum. In all cases the C-M-C bond angle of 165° was energetically favored. Nevertheless, on both surfaces hexagonal pores derived from **1** were energetically preferred over hexagonal pores built up from compound **2**. This could explain the differences between the two compounds, but according to the DFT results, pentagonal pores formed by **1** should be energetically preferred over hexagonal pores, particularly on Cu(111). Yet, the reason for the higher network quality of **1** on Cu(111) remained elusive. Therefore, adsorption of **1** (with all Br replaced by Cu/Ag) was studied by DFT on both surfaces. On Cu(111) the energetic optimum was found for the molecule centered above a three-fold fcc hollow site and aligned with the surface high symmetry directions. On Ag(111), two mirror symmetric adsorption geometries are energetically preferred with a rotation of $\pm 12^\circ$ with respect to the surface. This, together with small energy differences between slightly rotated structures, explains the lower quality of organometallic networks derived from **1** on Ag(111). It also exemplifies the strong influence of the substrate on the synthesized nanostructures. Covalent aryl-aryl coupling was not possible for **1** due to the strong steric repulsion of its *ortho*-methyl groups. This study doubtlessly demonstrated the possibility of improving the quality of organometallic networks by deliberately introducing steric hindrance that favors the ideal bonding configuration. In future research, tailored systems that form highly regular organometallic networks that can be isostructurally transformed into covalent networks could be promising candidates for the synthesis of highly regular 2D polymers.

However, **2** is known to afford covalent networks by moderate annealing on the (111) facets of the coinage metals. In chapter five, **2** was used to comparatively study surface-assisted Ullmann coupling on Au(111) and Ag(111), respectively. Particular emphasis

was put on the progression of the on-surface reactions with increasing temperature. The reaction progression was tracked with TP-XPS measurements, whereas STM was used to characterize intermolecular bonds and network topologies. Additionally, DFT calculations were performed to compare experimentally derived reaction enthalpies with theoretical values. TP-XPS-derived onset temperatures for dehalogenation were, as anticipated, lower for the silver surface, but interestingly the progression of dehalogenation was also vastly different. On Ag(111), the dehalogenation proceeded rapidly within a narrow temperature window of approximately 40 K, and was well described by first order reaction kinetics. Using the experimental heating rate and DFT-derived values for the reaction barriers lead to a decent match for the model. In contrast, dehalogenation on Au(111) was more gradual over an extended temperature range of more than 130 K. However, on Au(111), kinetic models fail to explain the dehalogenation over the large temperature range. Hence, a thermodynamic model is proposed to explain the gradual debromination on Au(111). Here, ΔH and ΔS values derived from the model for each debromination step were compared with theoretical values obtained by DFT and statistical mechanics. Assuming a thermodynamic equilibrium at the respective temperatures, theoretical and experimental values are consistent on Au(111). Dehalogenation as an isolated reaction step is exothermic on Ag(111) and endothermic on Au(111). The dehalogenated state is favorable already at low temperatures on Ag(111), but kinetically hindered. That implies that once the halogen is split off, the molecule is not likely to recombine with bromine. However, on Au(111), the dehalogenated state is energetically not favorable, meaning that after C-X bond scission, it is likely that the radical recombines with the bromine. Hence, debromination remains reversible on Au(111) as long as bromine is present on the surface. Covalent coupling on Au(111) is initiated at approximately 500 K and is completed at 560 K, implying an unexpectedly long lifetime of the SSRs. Possible explanations for this could be high diffusion, rotation and coupling barriers that need to be overcome to form covalent bonds. This is in contrast to the Ag(111) surface, where dehalogenation and subsequent formation of organometallic networks can be observed directly after RT deposition of **2**. Upon further annealing, these networks can be transformed into covalent networks by demetallation. This study demonstrates that even frequently applied coupling reactions like on-surface Ullmann-type coupling are far from being entirely understood. Particularly little is known about the reaction kinetics, as most studies only analyze structures of the final products. Therefore, this work elucidates how surface-assisted

Ullmann coupling proceeds on the two most relevant surfaces, i.e. Au(111) and Ag(111), and demonstrates how the choice of substrate can influence the reaction progression with temperature. The thermodynamic description of the dehalogenation on Au(111), as well as the kinetic description on Ag(111), should also apply to similar systems. This knowledge could be used to improve or adapt the temperature programs that drive the on-surface reactions. Future TP-XPS experiments with different heating rates would be beneficial to unveil more details of the kinetic progression, e.g. the pre-exponential factor. Moreover, the implementation of isothermal segments would be insightful, as the fixed temperature simplifies modelling because the rate constants remain constant. Furthermore, the reaction progression of a molecule known to dehalogenate hierarchically would be instructive. In the end, it would be insightful to perform experiments on Au(111) with different amounts of codeposited Ag atoms, in order to investigate if experimental evidence for a transition from thermodynamic to kinetic control can be observed. All these experiments should be closely interlinked with theoretical studies to further improve the consistency between experiments and theory.

A proof-of-concept study is presented in chapter six, where atomically precise chevron type GNRs are synthesized by means of a RDS. The RDS was used for dehalogenation of the molecular precursor before adsorbing on the surface, in other words, the direct deposition of radicals on the substrate was demonstrated. Hence, the catalytic activity of the substrate, typically required for the dehalogenation step of on-surface Ullmann-type coupling, became redundant. As substrates, iodine passivated Ag(111) and Au(111) were used to eliminate the catalytic activity exerted by the metals. DITTP was used as a prototypical model system to validate the functionality of the RDS. It is known that on Au(111), DITTP forms polymer chains by an Ullmann-type coupling at moderate temperatures which can be directly converted into GNRs *via* CDH reactions at elevated temperatures. Synthesized nanostructures were characterized by STM. On iodine passivated Ag(111) DITTP-derived linear polymers were directly observed after RT deposition with the RDS. After mild annealing to 200°C, densely packed aggregates of linear polymers adsorbed appear on both iodine-passivated Ag(111) and Au(111) surfaces. Deposition of DITTP molecules with a conventional Knudsen cell onto iodinated Ag(111) and subsequent annealing to 200°C lead to a pristine iodine terminated surface, due to thermal desorption of intact monomers. This is a direct proof of the

functionality of the RDS, since exclusively direct deposition of radicals onto I-Ag(111) enables further on-surface chemistry. On both surfaces, it was possible to convert the polymers into GNRs by a CDH reaction at elevated temperatures. According to our current understanding of the reaction, annealing first leads to a thermal desorption of iodine. Then the CDH reactions proceed on the bare metal surfaces.

Future experiments performed on more inert surfaces like HOPG, SiC, or h-BN to further reduce the impact of the substrate on the adsorbed nanoarchitectures could be of particular interest. As 2D covalent structures often feature high defect densities, formation of networks by means of the RDS could be promising for the reduction of topological defects. Due to the spatially separated dehalogenation by means of the RDS, low temperature synthesis is feasible for molecules with low diffusion and coupling barriers. If this system additionally features decisive defect formation energies, that cannot be overcome at the low coupling temperature, topological defects could be eliminated.

The question of whether the RDS also allows cleaving C-Br or even C-Cl bonds would also be worth exploring. This would decrease sublimation temperatures of precursors compared to iodine substituted analogue molecules and so the risk of premature reactions inside the crucible could be reduced. Additionally, bromine is better suited for the organic synthesis of molecular precursors. Furthermore, a mass spectrometer could be used to fine-tune the parameters for a direct deposition of radicals, of so far unknown molecules, in real-time. For instance, the minimum tube temperature, necessary to induce a complete dehalogenation of the molecular precursor, could be selected for upcoming experiments. This would be much less time-consuming than acquiring STM images after several experiments with different tube temperatures.

To conclude, the experiments presented in this thesis extend the knowledge of the temperature-driven progression of surface-assisted Ullmann coupling on the two most important surfaces, Au(111) and Ag(111). Additionally, the relevance of both small modifications of the molecular precursor and the choice of substrate for the bottom-up synthesis of nanoarchitectures is stressed. In particular, the combination of surface sensitive experimental techniques such as STM and (TP-)XPS complemented by DFT-calculations facilitates a thorough characterization of the system under investigation with ample possibilities to decipher mechanistic aspects.

Appendix A

Supplementary information for chapter 4

Details of DFT simulations:

DFT simulations for isolated aggregates were performed using the Gaussian 16 software.²¹⁹ Therefore the '6-31+G* + LANL2DZ' mixed basis set was employed and created through the use of the 'genECP' keyword. 6-31+G* was applied to both C and H, while LANL2DZ was used to model the transition metals Ag and Cu.

Constraints were added with the 'addGIC' keyword. To assess the dependence of the total energy on the bond angle, it was necessary to freeze the C-M-C bond angle for selected values (between 180° and 165°) as well as to fix selected dihedral angles in order to impose co-planarity of the two phenyl rings in the aggregate. Apart from that, relaxation within geometry optimization was allowed.

Adsorption geometries of the debrominated and metal-terminated compound **1** were studied by periodic DFT calculations using the VASP code,²²⁰ with the projector-augmented wave method to describe ion-core interactions, and with plane waves expanded to a kinetic energy cutoff of 400 eV. The van der Waals density functional describes exchange-correlation effects,²²¹ with the version by Hamada denoted as rev-vdWDF2²²² which has been shown to describe adsorption of molecules on coinage metals accurately.²²³ The Ag(111) and Cu(111) surfaces were modeled by four layered slabs. Furthermore, p(8x8) and p(9x9) surface unit cells were used for the calculations on Ag(111) and Cu(111), respectively, together with a 2x2 k-point sampling for both surfaces. All structures were geometrically optimized until the residual forces on all atoms (except the two bottom layers of the respective slab which were kept fixed) were smaller than 0.01 eV Å⁻¹.

Additional STM data:

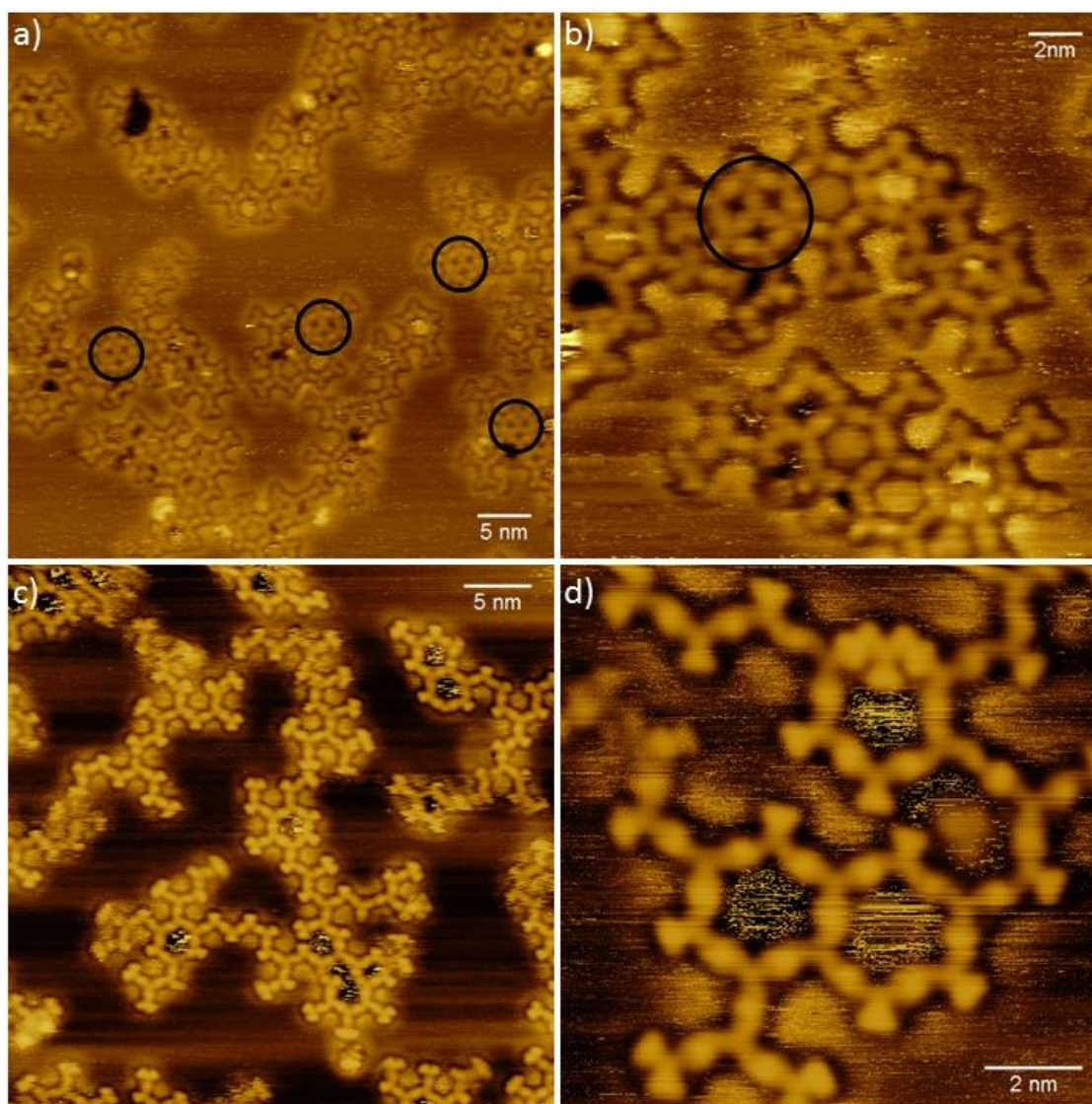


Figure A 1: STM images of organometallic networks acquired directly after (a) / (b) RT deposition of **1** onto Cu(111) and (c) / (d) after subsequent annealing to 100 °C. Additional molecules trapped inside pores (examples marked by black circles) were frequently observed after RT deposition, but could not be found anymore after annealing to 100 °C.

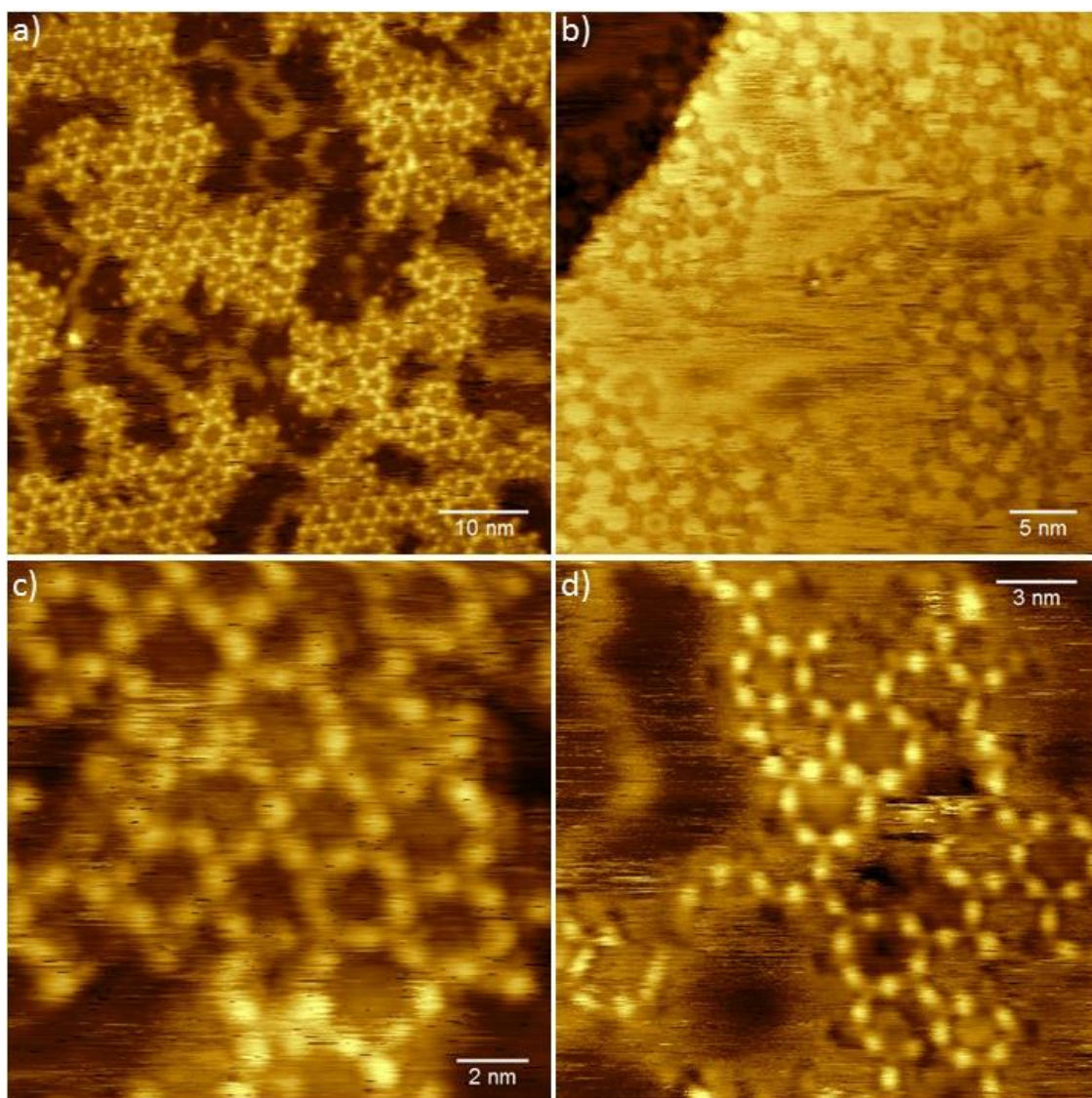


Figure A 2: STM images of organometallic networks on Ag(111) acquired after RT deposition of **1** (a) and (c), and after annealing to 100°C (b), and (d).

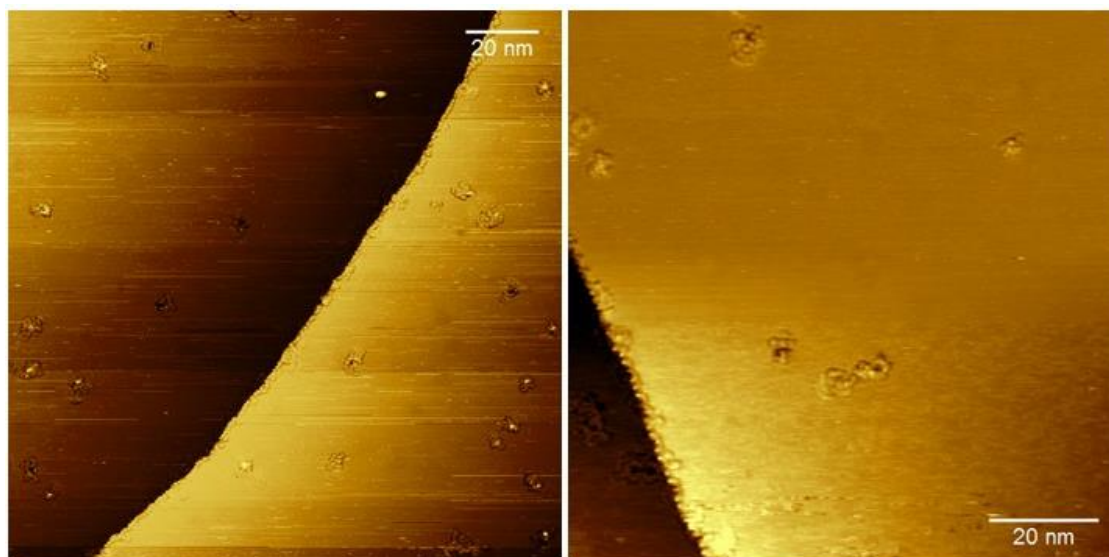
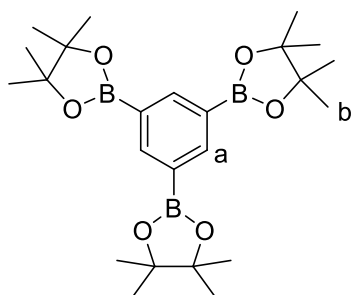


Figure A 3: STM images acquired after RT deposition of **1** onto Ag(111) and subsequent annealing to 200 °C. Most molecules desorbed from Ag(111) at higher annealing temperatures, in contrast to Cu(111), where covalent cross-linking was already observed at 150 °C.

Synthesis details:

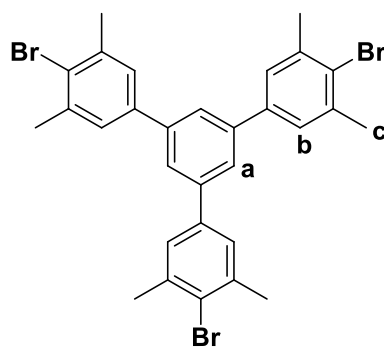
Synthesis details of **1**

1,3,5-Tris(4,4,5,5-tetramethyl-1,3,2-dioxaborolan-2-yl)benzene (**3**)²²⁴



1,3,5-Tribromobenzene (93.0 mg, 0.295 mmol), bis(pinacolato)diboron (300 mg, 1.18 mmol), potassium acetate (434 mg, 4.43 mmol) and palladium acetate (10.0 mg, 44.0 μ mol) were combined in 15 mL of dry distilled DMF under inert atmosphere. This mixture was heated at 70 °C for 24 h maintaining inert conditions. After evaporating the solvent under vacuum, the residue was extracted with dichloromethane. The organic layer was dried over anhydrous Na_2SO_4 . The crude product was purified by column chromatography over SiO_2 (silica gel) using 5% ethyl acetate in hexane as eluent (88 mg, 65%). ^1H NMR (CDCl_3 , 400 MHz, 298 K): δ = 1.33 (s, 36H, b-H), 8.36 (s, 3H, a-H) ppm.

1,3,5-Tris(4-bromo-3,5-dimethylphenyl)benzene (**1**)



Compound **3** (80.0 mg, 0.175 mmol) and 2-bromo-5-iodo-1,3-dimethylbenzene (546 mg, 1.76 mmol) were dissolved in 25 mL of THF, 15 mL of MeOH and 10 mL of water as a solvent mixture. The solution was deoxygenated for 30 min by purging with a continuous flow of N₂ gas. Then Pd(PPh₃)₄ (30.3 mg, 26.3 μmol) was added and again N₂ gas was bubbled through the solution for 10 min. After stirring the reaction mixture at 65 °C for 36 h, the organic solvents were evaporated and the aqueous part was extracted with dichloromethane. The organic layer was separated and dried over anhydrous Na₂SO₄. Column chromatography was performed over SiO₂ (silica gel) using pentane (*R_f* = 0.4) as eluent to furnish the product as pure colorless solid (60 mg, 55%). Mp > 250 °C; ¹H NMR (CDCl₃, 400 MHz, 298 K): δ = 2.51 (s, 18H, c-H), 7.37 (s, 6H, b-H), 7.67 (s, 3H, a-H) ppm; ¹³C NMR (CDCl₃, 100 MHz, 298 K): δ = 24.2, 125.0, 127.2, 127.3, 138.9, 139.6, 141.7 ppm; IR (KBr): ν 429, 510, 533, 570, 646, 692, 710, 734, 783, 857, 870, 883, 904, 951, 1017, 1029, 1108, 1200, 1300, 1379, 1406, 1435, 1469, 1511, 1576, 1600, 1687, 2851, 2919, 2953, 3026 cm⁻¹. Elemental Analysis: Calcd. for C₃₀H₂₇Br₃: C, 57.44; H, 4.34. Found: C, 57.26; H, 4.16.

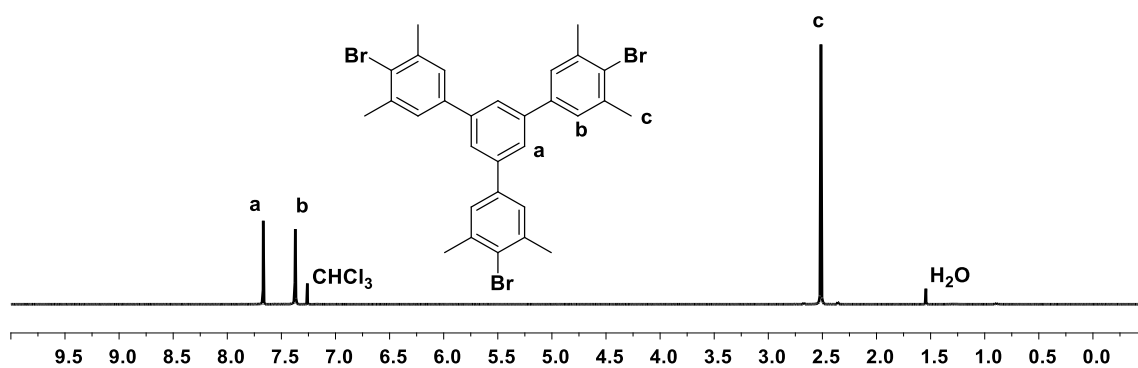


Figure A 4: ^1H NMR of compound **1** in CDCl_3 (400 MHz, 298 K).

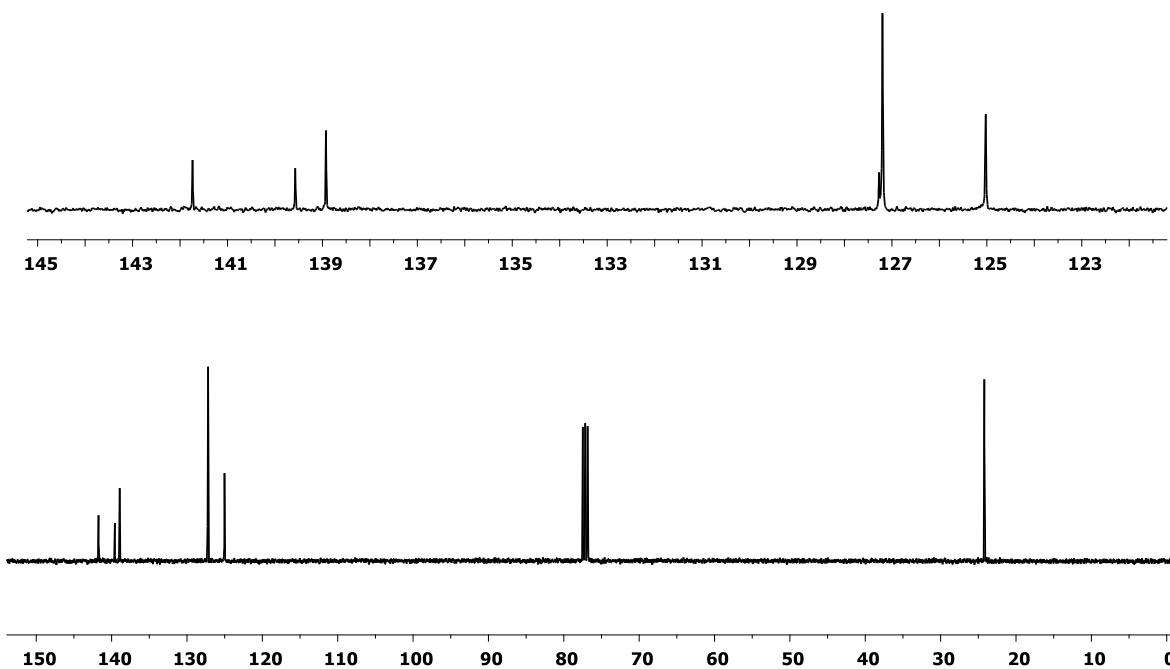


Figure A 5: ^{13}C NMR of compound **1** in CDCl_3 (100 MHz, 298 K).

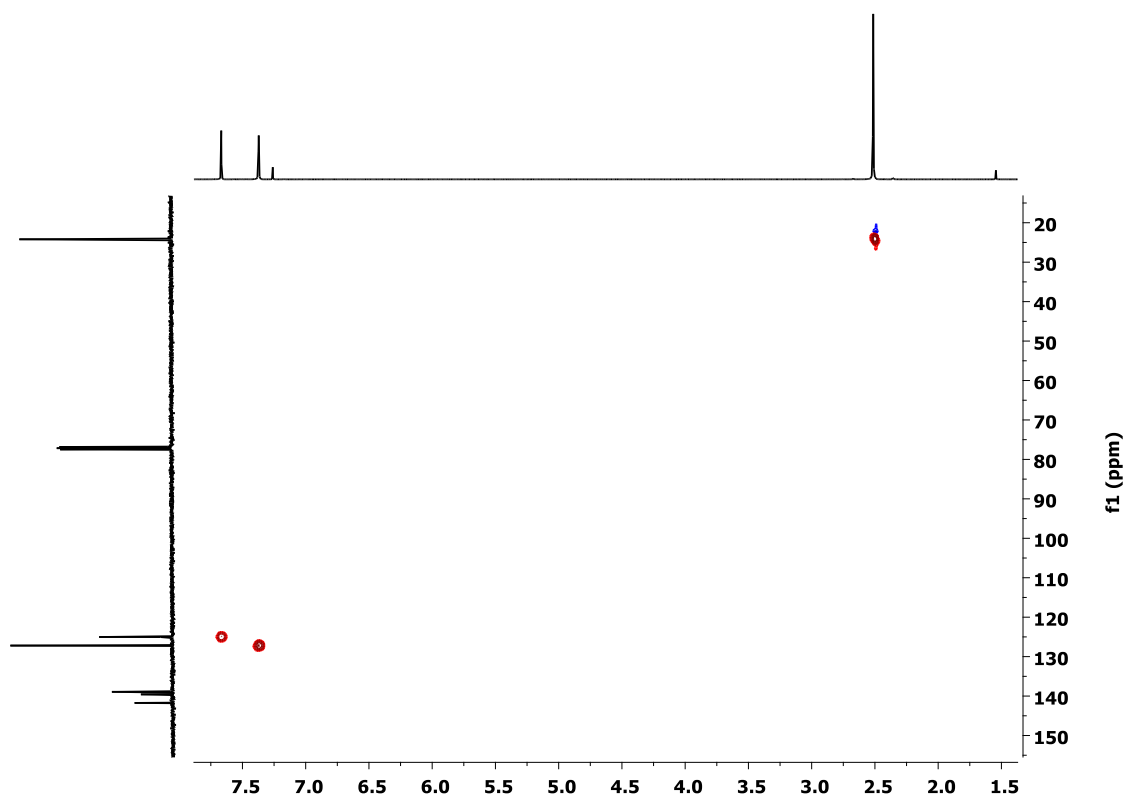


Figure A 6: ^1H - ^{13}C HSQC NMR of compound **1** in CDCl_3 (100 MHz, 298 K).

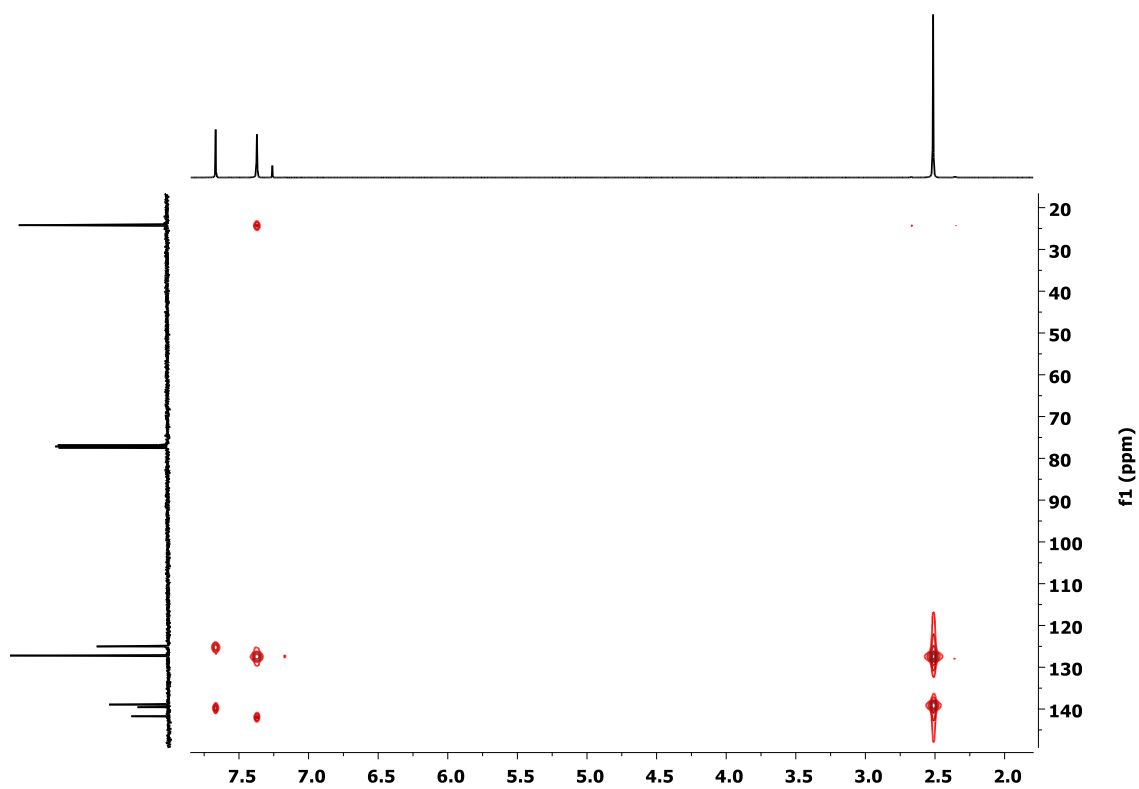


Figure A 7: ^1H - ^{13}C HMBC NMR of compound **1** in CDCl_3 (100 MHz, 298 K).

Appendix B

Supplementary information for chapter 5

Computational Details:

Periodic DFT calculations were performed with the VASP code,²²⁰ using the projector-augmented wave method to describe ion-core interactions,²²⁵ and with planewaves expanded to a kinetic energy cutoff of 400 eV. The van der Waals density functional²²¹ described exchange-correlation effects, with the version by Hamada denoted as rev-vdWDF2²²² which has been shown to describe adsorption of molecules on coinage metals accurately.²²³ The Au(111) surface was modelled as four layer slab. Furthermore, in the calculations of the TBB debromination we used a $p(8 \times 8)$ surface unit cell together with a 3×3 k -point sampling for the adsorption of the intact TBB molecule, a $p(7 \times 7)$ surface unit cell together with a 6×6 k -point sampling for the adsorption of fully or partly dehalogenated TBB molecules (surface-stabilized radicals), and a $p(5 \times 5)$ surface unit cell together with a 8×8 k -point sampling for the adsorption of a single bromine atom. These settings ensure a numerical convergence of all reported values within 50 meV.

For calculations of the reaction pathway of bromobenzene dehalogenation on Au(111) a $p(5 \times 5)$ surface unit cell together with a 6×6 k -point sampling was used, while for calculations of the diffusion of fully dehalogenated TBB molecules (surface-stabilized triradicals) a $p(7 \times 7)$ unit cell with a 3×3 k -point sampling was used. Transition states were found using a combination of the climbing image nudged elastic band¹⁹² (CI-NEB) and Dimer²²⁶ methods, where CI-NEB was used to obtain an initial guess of a transition state to be refined by the Dimer method. All structures (local minima as well as transition states) were geometrically optimized until the residual forces on all atoms (except the two bottom layers of the Au(111) slab which were kept fixed) were smaller than $0.01 \text{ eV } \text{\AA}^{-1}$.

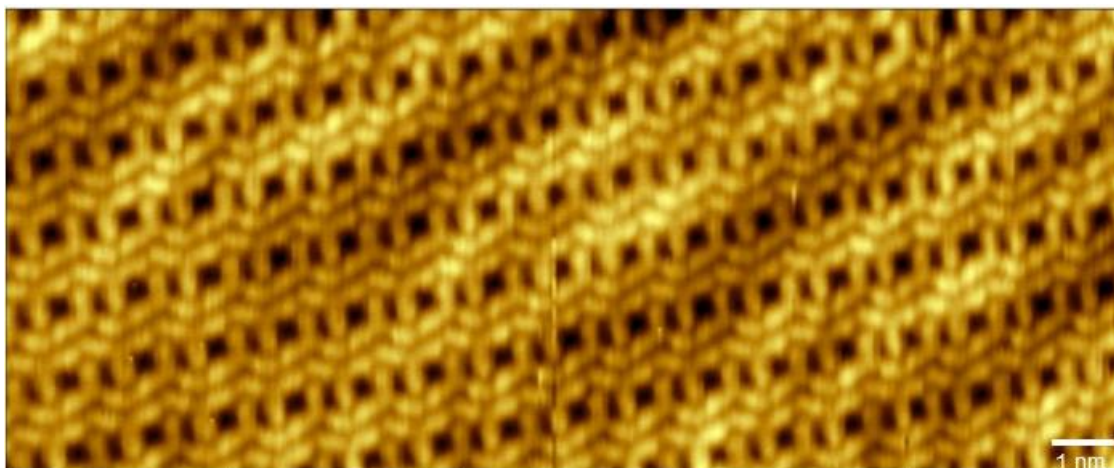
Additional STM data:

Figure B 1: STM topograph of the self-assembled structure of intact TBB molecules on Au(111) observed after room temperature deposition. The soliton walls of the Au(111) herringbone reconstructions are still visible as bright lines in the apparent height, hence corroborating the continued existence of the surface reconstruction.

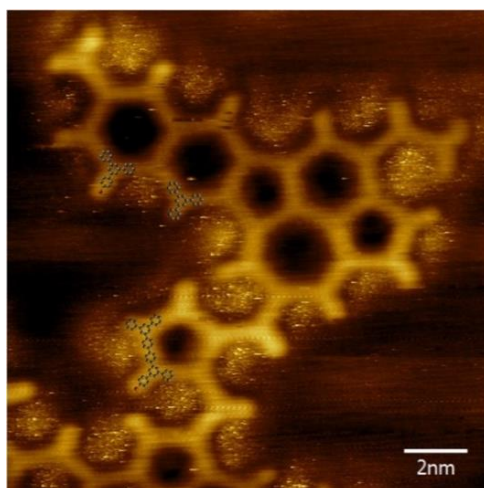


Figure B 2: STM topograph of a fully covalent network derived from TBB precursors on Au(111) after overnight annealing to 525 K. The dangling phenyl groups at the periphery appear with two different lengths: longer phenyl groups are bromine substituted, whereas shorter appearing phenyl groups are debrominated and form organometallic bonds with Au surface atoms as illustrated by the overlays.

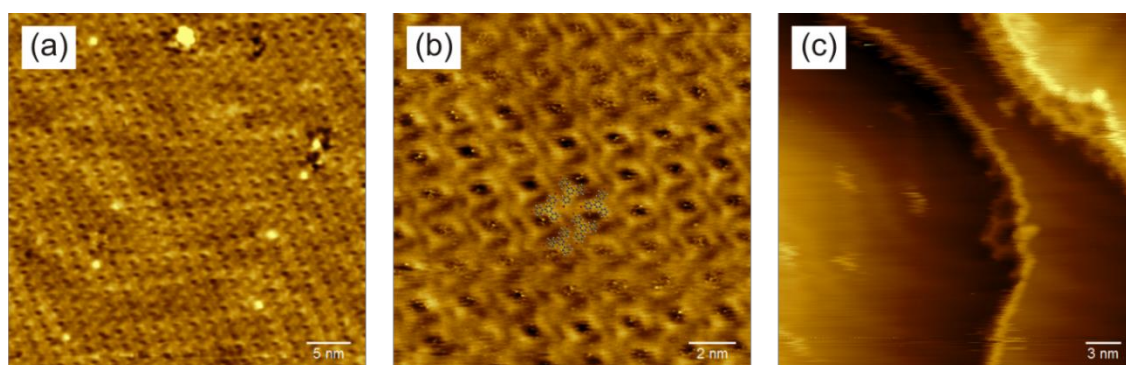


Figure B 3: STM topographs acquired at room temperature after deposition of TBB precursors onto Au(111) at room temperature and subsequent annealing to 473 K with a heating rate comparable to the TP-XPS experiments. To promote a swift cool down the hot sample was directly transferred from the heater to the sample storage carousel. (a) / (b) self-assembled structures comprised of intact TBB molecule as similarly found for room temperature deposition (see Figs. S1 and 5(d) main manuscript); (c) covalent aggregates as occasionally observed at step-edges; These results indicate the absence of sizable C-C coupling at 473 K in accord with C 1s TP-XPS data.

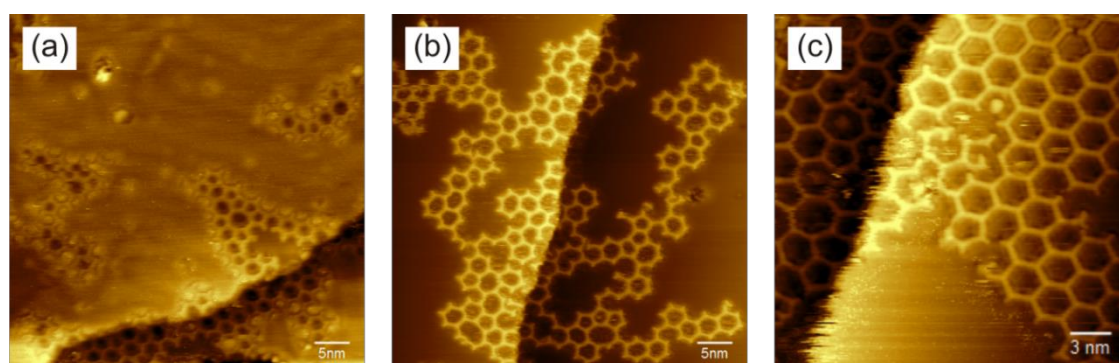


Figure B 4: Overview STM images of fully covalent networks derived from TBB precursors on (a) Au(111) and (b) / (c) Ag(111). The covalent networks depicted in (a) and (b) exhibit relatively high proportions of non-hexagonal pores, whereas the covalent network shown in (c) is predominantly composed of hexagonal pores. The higher structural quality in (c) was achieved by carefully heating and cooling the sample with a low rate of 2 K min^{-1} in order to exploit structural equilibration processes in the organometallic phase, followed by an isotopological conversion of the organometallic into similarly ordered covalent networks.³²

Additional XPS results:

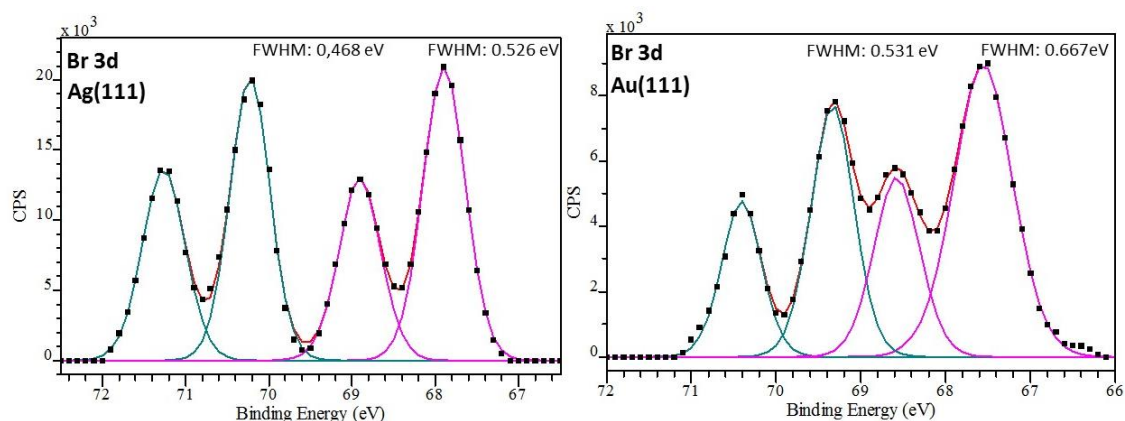


Figure B 5: XP spectra of Br 3d core levels on Ag(111) (left) and Au(111) (right). These spectra represent cases, where the debromination was approximately 50% completed. Spin-orbit doublets corresponding to molecule-bound (green curves) and surface-bound (pink curves) bromine are observed at higher and lower binding energies, respectively. Both spectra were taken from the Br 3d TP-XPS experiment presented in the main manuscript. Raw data are represented by black filled squares, green and pink lines correspond to fits of molecule-bound and surface-bound bromine, respectively. Red lines indicate the sum of all fitted components. For the fits Voigt line-shapes and Shirley backgrounds were used. In all cases, the FWHM was used as fit parameter, resulting values are stated next to the respective peaks. Both the molecule-bound and surface-bound bromine species exhibit a larger FWHM on Au(111). This is attributed to inhomogeneous broadening due to different adsorption sites on the herringbone reconstruction.

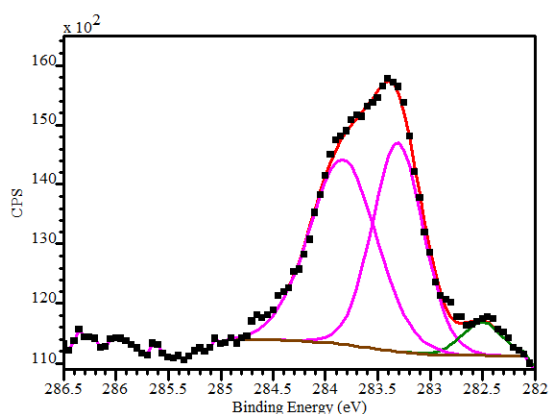


Figure B 6: XP spectrum of C 1s core levels on Ag (111) showing the main peaks of the organic backbone (pink curves) as well as a pronounced organometallic shoulder at lower binding energy (green curve). This spectrum was taken from the C 1s TP-XPS experiment presented in the main manuscript. Raw data are represented by black filled squares, the purple lines correspond to fits of the carbon main components of the organic backbone, the green line corresponds to fits of the organometallic carbon directly bound to Ag (C-Ag). The red line indicates the sum of all fitted components. For the fit Doniach Sunjic line-shapes and a Shirley background were used.

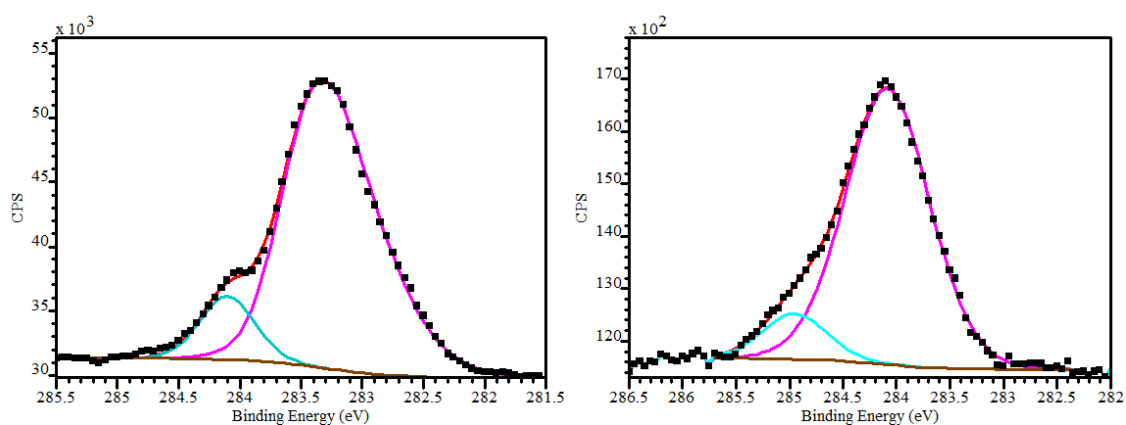


Figure B 7: XP spectra of C 1s core levels on Ag(111) (left) and Au(111) (right) showing the main peak of the organic backbone (pink curves) as well as a pronounced shoulder of bromine-substituted carbons (C-Br) at higher binding energy (light blue / green curves). These spectra were taken from the C 1s TP-XPS experiment presented in the main manuscript. Raw data are represented by black filled squares, the purple lines correspond to fits of the carbon main component of the organic backbone, the light blue lines correspond to fits of the still bromine-substituted carbon. The red lines indicate the sum of all fitted components. For the fits Doniach Sunjic line-shapes and Shirley backgrounds were used.

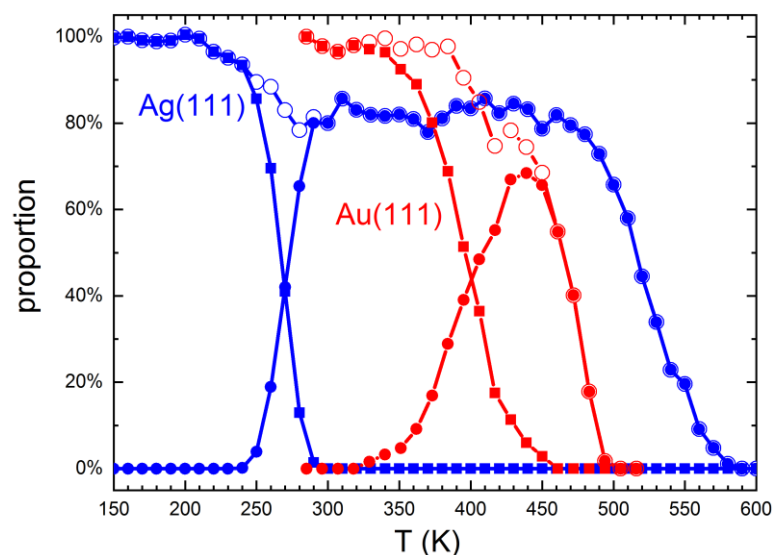


Figure B 8: Summarized Br 3d intensities from both TP-XPS experiments showing the relative intensities of molecule-bound (filled squares) vs. surface-bound (filled circles) bromine, both for Ag(111) (blue) and Au(111) (red), respectively. Open circles correspond to the sum of both bromine species, i.e. the total amount of bromine. This figure compiles data of Figs. 1(a) and (b) of the main manuscript to facilitate direct comparability.

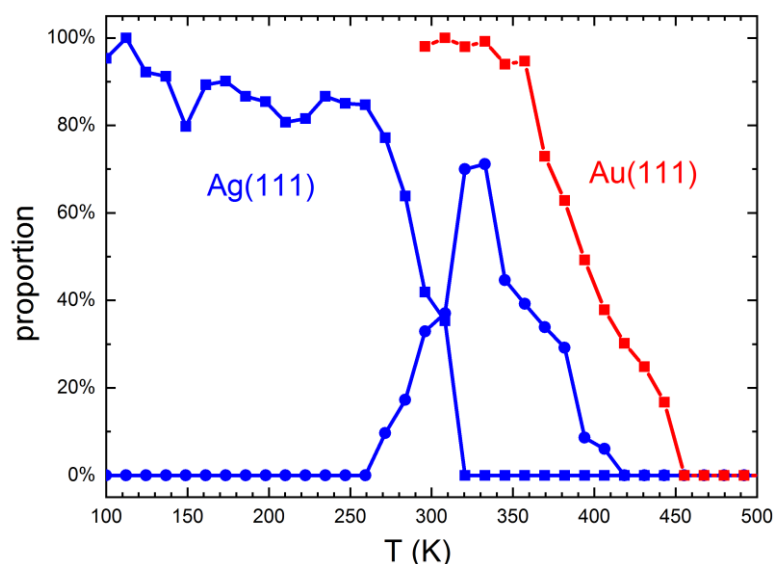


Figure B 9: Summarized C 1s intensities from both TP-XPS experiments showing the relative intensities of bromine-substituted carbon (C-Br, filled squares) and organometallic carbon (C-Ag, filled circles, only for Ag(111)) both for Ag(111) (blue) and Au(111) (red), respectively. This figure compiles data of Figs. 4(a) and (b) of the manuscript to facilitate direct comparability.

DFT calculations of debromination enthalpies on Au(111):

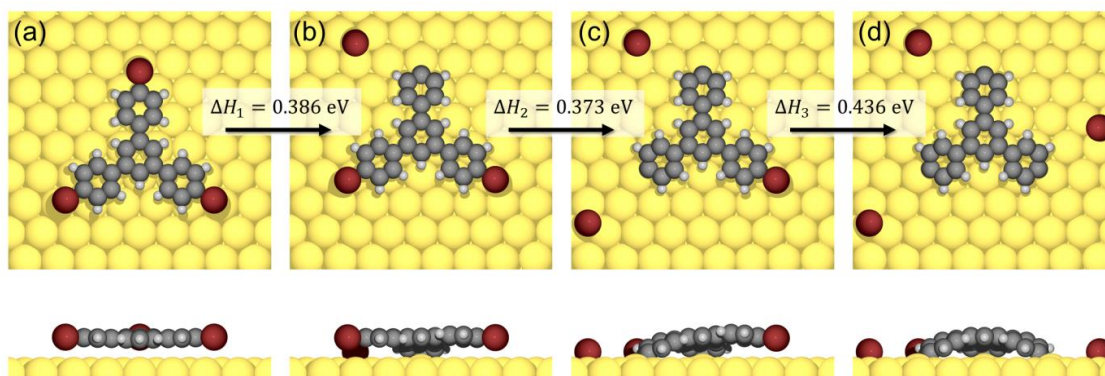


Figure B 10: DFT calculations of the reaction enthalpies for each individual debromination step of TBB on Au(111), resulting in $\Delta H_1 = 0.386 \text{ eV}$, $\Delta H_2 = 0.373 \text{ eV}$, and $\Delta H_3 = 0.436 \text{ eV}$ for the first, second, and third debromination, respectively. These values are similar within the stated numerical accuracy of 50 meV, hence justifying the simplifying assumption of similar reaction enthalpies for each debromination step for the thermodynamic model.

DFT calculations of diffusion barriers:

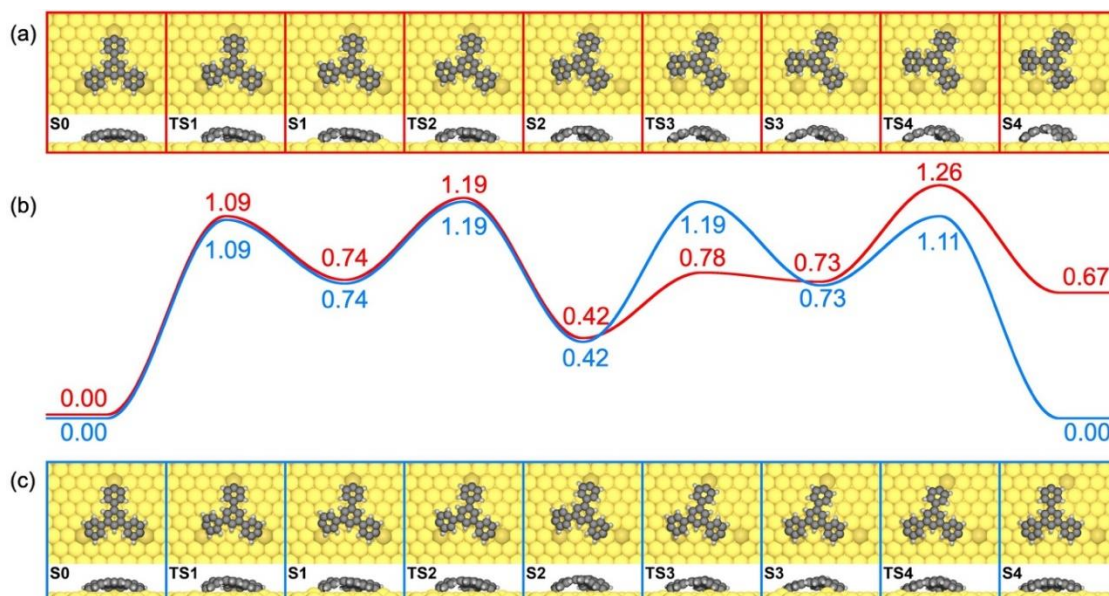


Figure B 11: DFT calculations of the diffusion of the fully dehalogenated TBB molecule (surface-stabilized triradical) on Au(111), with top and side views of local energy minima (S0, S1, ...) and transition states (TS1, TS2, ...) for (a) rotation and (c) migration. The three Au surface atoms to which the molecule initially binds to in S0 are rendered darker in the top views to make it easier to follow the paths. (b) Corresponding energy profiles with rotation in red and migration in blue. The two first steps (S0 to S2) are identical for both diffusion modes. For the rotation, only the first half of a complete 120° rotation between two equivalent states is shown, as the second half is identical to the first half by mirror symmetry (with respect to the outermost surface layer). All energy values are stated in eV.

DFT calculations of debromination barriers on Au(111):

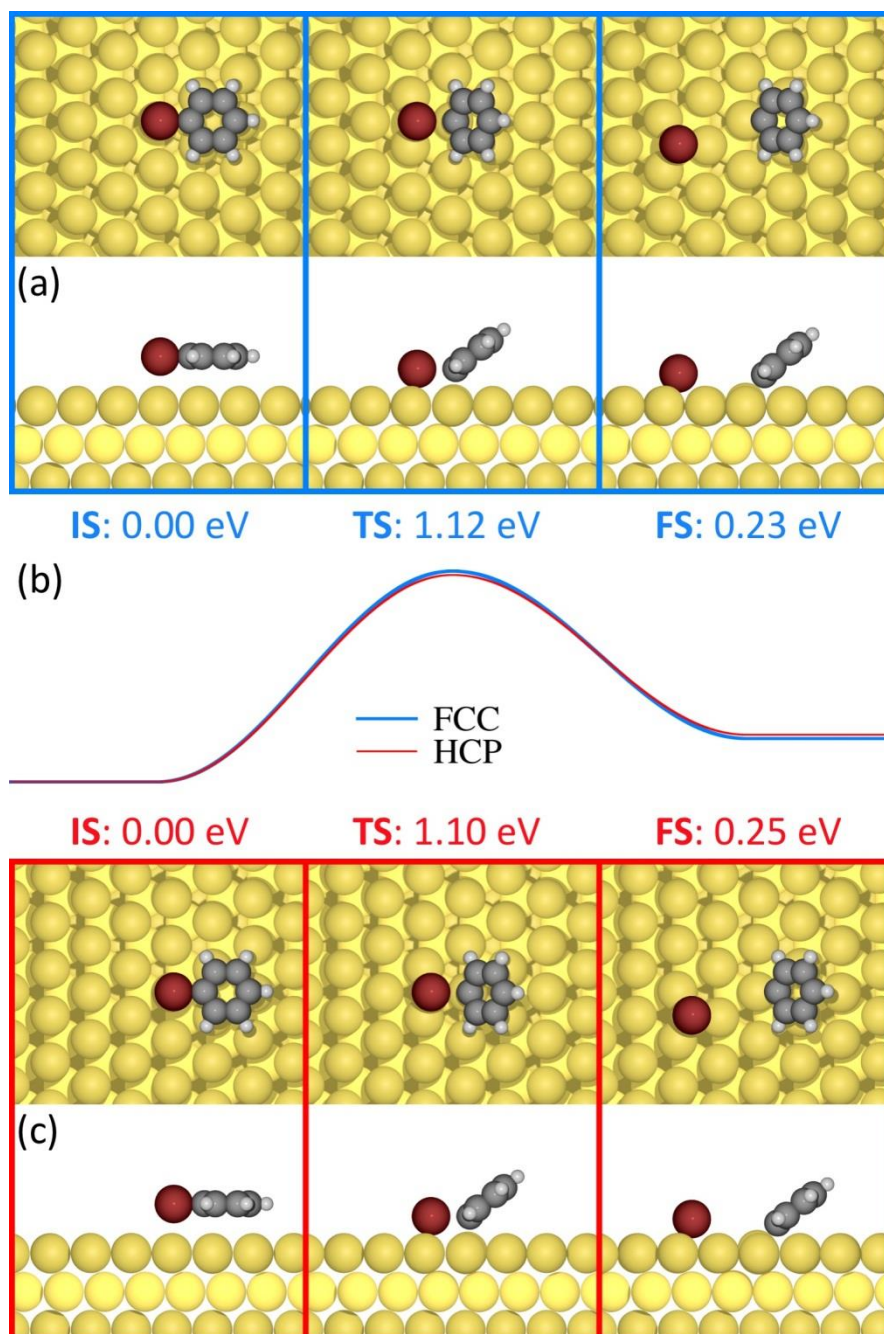


Figure B 12: DFT calculations of the debromination of bromobenzene on Au(111) with top and side views of initial state (IS), transition state (TS), and final state (FS). The stated energies are given with respect to IS. (a) FCC-terminated Au(111) and (c) HCP-terminated Au(111) surfaces, respectively. (b) Corresponding energy profiles showing almost similar activation and reaction energies for both FCC- and HCP-terminated Au(111), respectively.

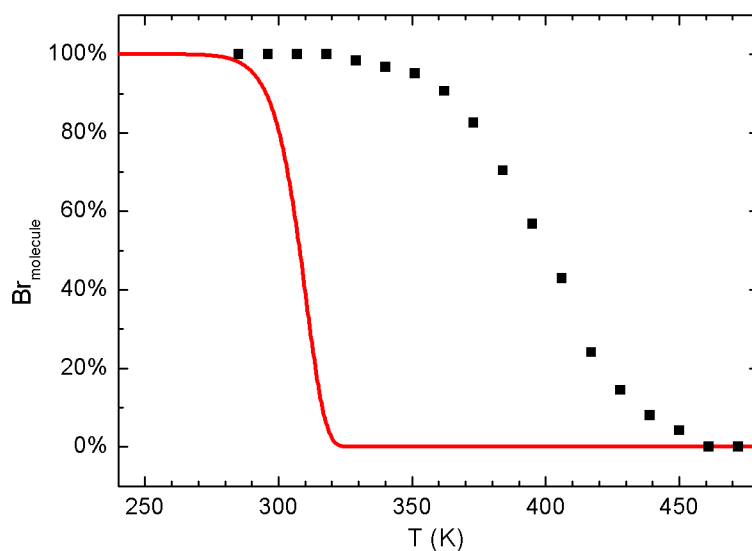
Kinetic model applied to Au(111) data:

Figure B 13: Kinetic model applied to Au(111). Black filled squares represent data from the Br 3d TP-XPS experiment shown in the main manuscript. Here the amount of molecule-bound bromine ($\text{Br}_{\text{molecule}}$) was normalized by $(\text{Br}_{\text{molecule}} + \text{Br}_{\text{surface}})$, i.e. the total amount of bromine detected by XPS. The red curve represents the outcome of the kinetic model using a pre-exponential factor of $\nu_0 = 3.25 \times 10^{16} \text{s}^{-1}$ as obtained from fitting the Ag(111) data (cf. Figure 5.2) and using a DFT calculated reaction barrier of $\Delta E = 1.12 \text{ eV}$ (cf. Figure B12). Based on reaction kinetics, debromination should be already completed at $\sim 320 \text{ K}$, corroborating the need for a thermodynamic model as described in the main manuscript.

Kinetic model for variation of the reaction barrier:

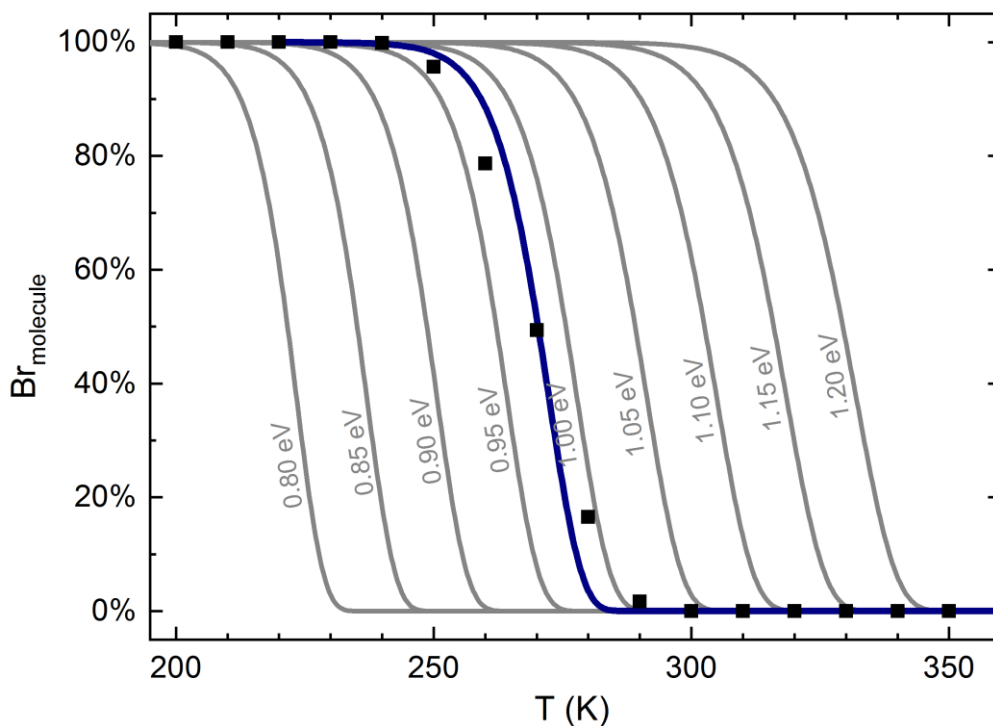


Figure B 14: Kinetic model evaluated for variable reaction barriers in the range of $\Delta E = (0.80 \dots 1.20) \text{ eV}$ in increments of 0.05 eV . The black squares and blue line represent experimental data and the corresponding fit ($\Delta E = 0.98 \text{ eV}$) on Ag(111) as presented in Figure 5.2. A similar pre-exponential factor of $\nu_0 = 3.25 \times 10^{16} \text{ s}^{-1}$ as for the Ag(111) fit was used for all curves. For a 50 % increase of the reaction barrier ΔE from 0.80 eV to 1.20 eV the temperature for full debromination varies from approximately 230 K to 345 K.

Thermodynamic model for variation of the reaction enthalpy:

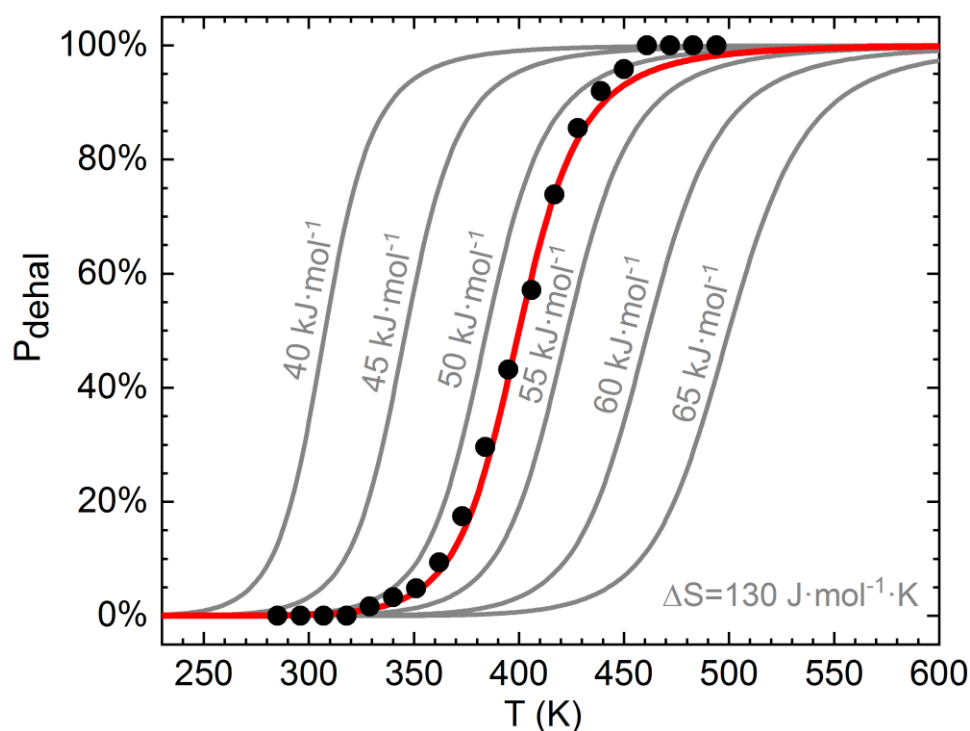


Figure B 15: Thermodynamic model evaluated for variable reaction enthalpies in the range of $\Delta H = (40 \dots 65) \frac{\text{kJ}}{\text{mol}}$ in increments of $5.0 \frac{\text{kJ}}{\text{mol}}$. The black filled circles and red line represent experimental data and corresponding fit ($\Delta H = 52.0 \frac{\text{kJ}}{\text{mol}}$) on Au(111) as presented in Figure 5.3 of the main manuscript. A similar reaction entropy of $\Delta S = 130 \frac{\text{J}}{\text{mol}\cdot\text{K}}$ as for the Au(111) fit was used for all curves.

Thermodynamic model for variation of the reaction entropy:

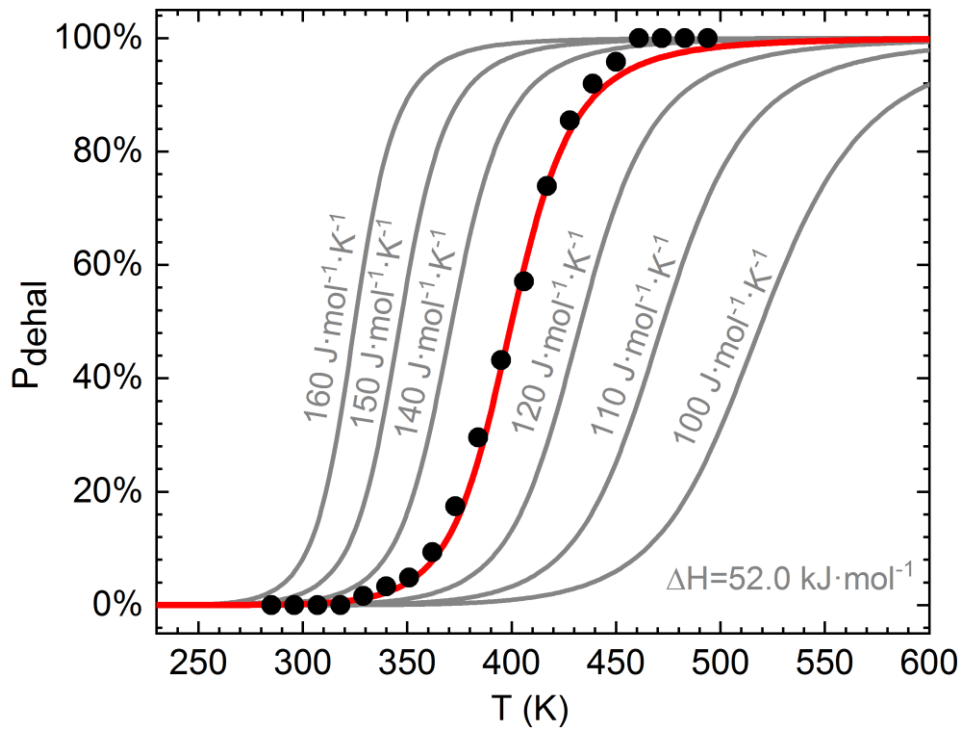


Figure B 16: Thermodynamic model evaluated for variable reaction entropies in the range of $\Delta S = (100 \dots 160) \frac{J}{mol \cdot K}$ in increments of $10 \frac{J}{mol \cdot K}$. The black filled circles and red line represent experimental data and the corresponding fit ($\Delta S = 130 \frac{J}{mol \cdot K}$) for Au(111) as presented in Figure 5.3 of the main manuscript. A similar reaction enthalpy of $\Delta H = 52.0 \frac{kJ}{mol}$ as for the Au(111) fit was used for all curves.

Appendix C

Supplementary information for chapter 6

Additional STM data:

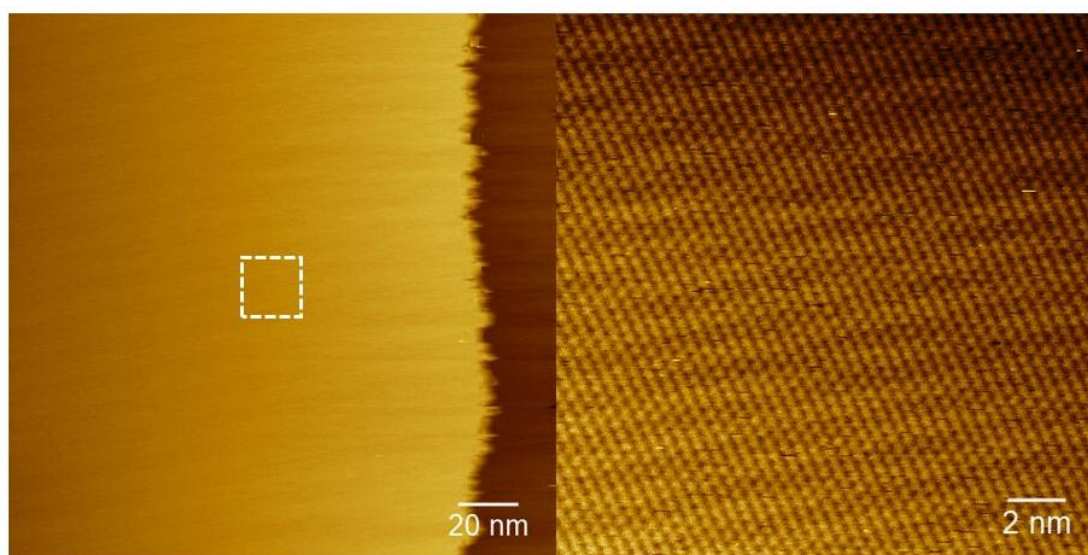


Figure C 1: STM images acquired after Deposition of DITTP with a conventional Knudsen cell onto iodine terminated Ag(111) and subsequent annealing to 200°C. leads to a pristine I-Ag(111) surface.

List of Abbreviations

1D	one-dimensional
2D	two-dimensional
AFM	atomic force microscopy
ARPES	angle resolved photoelectron spectroscopy
BW	band width
C-C	carbon bound
CDH	cyclodehydrogenation
CHA	concentric hemispherical analyzer
CI-NEB	climbing image nudged elastic band
C-M-C	carbon-metal-carbon
DBBA	10,10'-dibromo-9,9'-bianthracene
DFT	density functional theory
DITTP	6,11-Diiodo-1,2,3,4-tetraphenyltriphenylene
ESCA	electron spectroscopy for chemical analysis
FWHM	full-width at half-maximum
GNRs	graphene nanoribbons
HAXPES	hard X-ray photoelectron spectroscopy
h-BN	hexagonal boron nitride
HOPG	highly oriented pyrolytic graphite
HREELS	high resolution electron energy loss spectroscopy
HV	high voltage
IMFP	inelastic mean free path

IVC	current voltage converter
LDOS	local density of states
LEED	low energy electron diffraction
LINAC	linear accelerator
MTBB/1	1,3,5-tris(4-bromo-3,5-dimethylphenyl)benzene
NEXAFS	near edge X-ray absorption fine structure
PC	personal computer
PES	photoemission spectroscopy
PMMA	poly-methyl methacrylate
RDS	radical deposition source
RT	room temperature
SPM	scanning probe microscopy
SSRs	surface stabilized radicals
STM	scanning tunneling microscopy
STS	scanning tunneling spectroscopy
TBB/2	1,3,5-tris(<i>p</i> -bromophenyl)benzene
TPD	temperature programmed desorption
TP-XPS	temperature programmed X-ray photoelectron spectroscopy
TST	transition state theory
UHV	ultra-high vacuum
UPS	ultraviolet photoelectron spectroscopy
X	halogen
XPS	X-ray photoelectron spectroscopy

List of Figures

Figure 2. 1: Tunneling effect at a one dimensional barrier.....	7
Figure 2. 2: Operating principle of a STM	10
Figure 2. 3: Scheme of the photoemission process.....	16
Figure 2. 4: The “universal curve” of the IMFP of electrons in metals.....	18
Figure 2. 5: XP survey spectrum of a clean Au (111) surface.....	20
Figure 2. 6: Initial state before- and final states after photoemission	21
Figure 2. 7: Chemical shift of the Br 3d core level doublet.....	25
Figure 2. 8: Scheme of a modern synchrotron light source	27
Figure 3. 1: Reaction steps of on-surface Ullmann coupling.....	38
Figure 3. 2: Free energy landscape of thermodynamically- versus kinetically controlled processes	46
Figure 4. 1: STM images of 1 and 2 on Cu(111) acquired after RT deposition	54
Figure 4. 2: STM images of 1 and 2 on Cu(111) acquired after RT deposition and annealing to 150°C.....	55
Figure 4. 3: Histograms of observed pore geometries for 1 and 2 on Cu(111) after RT deposition and after annealing.....	56
Figure 4. 4: STM images of 1 and 2 on Ag(111) acquired after RT deposition.....	57
Figure 4. 5: STM images of 1 and 2 on Ag(111) acquired after RT deposition and annealing to 150°C.....	58
Figure 4. 6: Histograms of observed pore geometries for 1 and 2 on Ag(111) after RT deposition and after annealing.	59
Figure 4. 7: DFT-derived energies of metal-linked phenyls as a function of angle deviation.....	60
Figure 4. 8: Top- and side views of DFT-optimized geometries of 1 on Cu(111)	62
Figure 4. 9: Top- and side views of DFT-optimized geometries of 1 on Ag(111).....	63

Figure 5. 1: Br 3d TP-XPS data of TBB on Ag(111) and Au(111).....	71
Figure 5. 2: Kinetic model for debromination of TBB on Ag(111).	75
Figure 5. 3: Thermodynamic model for debromination of TBB on Au(111).....	78
Figure 5. 4: Top- and side-views of DFT-optimized structures of fully brominated TBB on Au(111) and after dissociation of all three bromine substituents.	78
Figure 5. 5: C 1s TP-XPS data of TBB on Ag(111) and Au(111).....	81
Figure 5. 6: Integral peak shifts of C 1s on Ag(111) vs. surface temperature shown alongside with the intensity of molecule-bound and surface-bound bromine	82
Figure 5. 7: Integral peak shifts of C 1s on Au(111) vs. surface temperature shown alongside with the intensity of molecule-bound and surface-bound bromine.	83
Figure 5. 8: STM images of TBB on Ag(111) and Au(111), acquired after RT deposition and after annealing.....	85
Figure 5. 9: Schematic overview of the temperature ranges for debromination, covalent coupling, and thermal desorption of bromine on Ag(111) and Au(111).....	87
Figure 6. 1: Cross section of the RDS.....	96
Figure 6. 2: STM image of DITTP-derived polymers on iodinated Ag(111), acquired after room-temperature deposition with the RDS.....	100
Figure 6. 3: STM image of DITTP-derived polymers on iodinated Ag(111), acquired after annealing to 200°C	101
Figure 6. 4: STM image and line-profile of DITTP-derived polymers on iodinated Ag(111), acquired after annealing to 200°C.....	102
Figure 6. 5: STM image of DITTP-derived polymers on Ag(111), acquired after annealing to 400°C.....	103
Figure 6. 6: STM images of DITTP-derived GNRs on Ag(111), acquired after annealing to 500°C	105
Figure 6. 7: STM images of DITTP on iodinated Ag(111) deposited with a Knudsen cell versus deposition <i>via</i> the RDS.....	107
Figure 6. 8: STM images of DITTP-derived polymers on iodinated Au(111), acquired after annealing to 200°C.	109
Figure 6. 9: STM image of DITTP-derived polymers on Au(111), acquired after annealing to 400°C.....	110

Figure 6. 10: STM image of DITTP-derived chevron type GNRs on Au(111), acquired after annealing to 500°C.	111
Figure 6. 11: STM image of DITTP-derived chevron type GNRs on Au(111), acquired after annealing to 450°C.	112
Figure A 1: STM images of 1 on Cu(111) acquired after RT deposition and after annealing to 100 °C.....	124
Figure A 2: STM images of 1 on Ag(111) acquired after RT deposition and after annealing to 100°C.....	125
Figure A 3: STM images of 1 on Ag(111) acquired after RT deposition and subsequent annealing to 200 °C.....	126
Figure A 4: ¹ H NMR of compound 1 in CDCl ₃ (400 MHz, 298 K).....	128
Figure A 5: ¹³ C NMR of compound 1 in CDCl ₃ (100 MHz, 298 K).....	128
Figure A 6: ¹ H- ¹³ C HSQC NMR of compound 1 in CDCl ₃ (100 MHz, 298 K).....	129
Figure A 7: ¹ H- ¹³ C HMBC NMR of compound 1 in CDCl ₃ (100 MHz, 298 K).....	129
Figure B 1: STM image of self-assembled TBB molecules on Au(111).....	132
Figure B 2: STM image of TBB on Au(111) after overnight annealing to 525 K..	132
Figure B 3: STM images of TBB on Au(111) at RT and after annealing to 473 K	133
Figure B 4: STM images of covalent networks derived from TBB on Au(111) and Ag(111).....	133
Figure B 5: XP spectra of Br 3d core levels on Ag(111) and Au(111).	134
Figure B 6: XP spectrum of C 1s core levels on Ag (111) showing the organometallic low BE shoulder.....	135
Figure B 7: XP spectra of C 1s core levels of intact TBB on Ag(111) and Au(111)	135
Figure B 8: Summarized Br 3d intensities from both TP-XPS experiments.....	136
Figure B 9: Summarized C 1s intensities from both TP-XPS experiments.....	136
Figure B 10: DFT calculations of the reaction enthalpies for each individual debromination step of TBB on Au(111).....	137
Figure B 11: DFT calculations of the diffusion of the fully dehalogenated TBB molecule on Au(111).....	138
Figure B 12: DFT calculations of the debromination of bromobenzene on Au(111)..	139
Figure B 13: Kinetic model applied to Au(111).	140

Figure B 14: Kinetic model evaluated for variable reaction barriers.....	141
Figure B 15: Thermodynamic model evaluated for variable reaction enthalpies	142
Figure B 16: Thermodynamic model evaluated for variable reaction entropies.....	143
Figure C 1: STM images acquired after Deposition of DITTP with a Knudsen cell onto iodine terminated Ag(111) and subsequent annealing to 200°C	145

References

1. Grill, L.; Dyer, M.; Laffrentz, L.; Persson, M.; Peters, M. V.; Hecht, S., Nano-architectures by covalent assembly of molecular building blocks. *Nat. Nano.* **2007**, *2* (11), 687-91.
2. Gourdon, A., *On-Surface Synthesis - Proceedings of the International Workshop On-Surface Synthesis, Les Houches 25-30 May 2014*. Springer International Publishing, 2016.
3. Clair, S.; de Oteyza, D. G., Controlling a Chemical Coupling Reaction on a Surface: Tools and Strategies for On-Surface Synthesis. *Chem. Rev.* **2019**, *119* (7), 4717-4776.
4. De Oteyza, D. G.; Rogero, C., *On-Surface Synthesis II - Proceedings of the International Workshop On-Surface Synthesis, San Sebastián, 27-30 June 2016*. Springer International Publishing, 2018.
5. Lackinger, M., Surface-assisted Ullmann coupling. *Chem. Commun.* **2017**, *53* (56), 7872-7885.
6. Wang, T.; Lv, H.; Feng, L.; Tao, Z.; Huang, J.; Fan, Q.; Wu, X.; Zhu, J., Unravelling the Mechanism of Glaser Coupling Reaction on Ag(111) and Cu(111) Surfaces: a Case for Halogen Substituted Terminal Alkyne. *J. Phys. Chem. C* **2018**, *122* (26), 14537-14545.
7. Lackinger, M., On-surface polymerization - a versatile synthetic route to two-dimensional polymers. *Polym. Int.* **2015**, *64* (9), 1073-1078.
8. Tan, Y.-Z.; Yang, B.; Parvez, K.; Narita, A.; Osella, S.; Beljonne, D.; Feng, X.; Müllen, K., Atomically precise edge chlorination of nanographenes and its application in graphene nanoribbons. *Nat. Commun.* **2013**, *4* (1), 2646.
9. Segawa, Y.; Ito, H.; Itami, K., Structurally uniform and atomically precise carbon nanostructures. *Nat. Rev. Mater.* **2016**, *1* (1), 15002.
10. Novoselov, K. S.; Geim, A. K.; Morozov, S. V.; Jiang, D.; Zhang, Y.; Dubonos, S. V.; Grigorieva, I. V.; Firsov, A. A., Electric Field Effect in Atomically Thin Carbon Films. *Science* **2004**, *306* (5696), 666.
11. Novoselov, K. S., Nobel Lecture: Graphene: Materials in the Flatland. *Rev. Mod. Phys.* **2011**, *83* (3), 837-849.
12. Geim, A. K.; Novoselov, K. S., The rise of graphene. *Nat. Mater.* **2007**, *6* (3), 183-191.
13. Sahu, S.; Rout, G. C., Band gap opening in graphene: a short theoretical study. *Int. Nano Lett.* **2017**, *7* (2), 81-89.

14. Jariwala, D.; Srivastava, A.; Ajayan, P. M., Graphene Synthesis and Band Gap Opening. *J. Nanosci. Nanotechnol.* **2011**, *11* (8), 6621-6641.
15. Kawasaki, T.; Ichimura, T.; Kishimoto, H.; Akbar, A. A.; Ogawa, T.; Oshima, C., Double Atomic Layers of Graphene/Monolayer h-BN on Ni(111) Studied by Scanning Tunneling Microscopy and Scanning Tunneling Spectroscopy. *Surf. Rev. Lett.* **2002**, *09* (3-4), 1459-1464.
16. Barone, V.; Hod, O.; Scuseria, G. E., Electronic Structure and Stability of Semiconducting Graphene Nanoribbons. *Nano Lett.* **2006**, *6* (12), 2748-2754.
17. Lemme, M. C.; Bell, D. C.; Williams, J. R.; Stern, L. A.; Baugher, B. W. H.; Jarillo-Herrero, P.; Marcus, C. M., Etching of Graphene Devices with a Helium Ion Beam. *ACS Nano* **2009**, *3* (9), 2674-2676.
18. Han, M. Y.; Özyilmaz, B.; Zhang, Y.; Kim, P., Energy Band-Gap Engineering of Graphene Nanoribbons. *Phys. Rev. Lett.* **2007**, *98* (20), 206805.
19. Cai, J.; Ruffieux, P.; Jaafar, R.; Bieri, M.; Braun, T.; Blankenburg, S.; Muoth, M.; Seitsonen, A. P.; Saleh, M.; Feng, X.; Mullen, K.; Fasel, R., Atomically precise bottom-up fabrication of graphene nanoribbons. *Nature* **2010**, *466* (7305), 470-3.
20. Martini, L.; Chen, Z.; Mishra, N.; Barin, G. B.; Fantuzzi, P.; Ruffieux, P.; Fasel, R.; Feng, X.; Narita, A.; Coletti, C.; Müllen, K.; Candini, A., Structure-dependent electrical properties of graphene nanoribbon devices with graphene electrodes. *Carbon* **2019**, *146*, 36-43.
21. Chen, Y.-C.; de Oteyza, D. G.; Pedramrazi, Z.; Chen, C.; Fischer, F. R.; Crommie, M. F., Tuning the Band Gap of Graphene Nanoribbons Synthesized from Molecular Precursors. *ACS Nano* **2013**, *7* (7), 6123-6128.
22. Ruffieux, P.; Cai, J.; Plumb, N. C.; Patthey, L.; Prezzi, D.; Ferretti, A.; Molinari, E.; Feng, X.; Müllen, K.; Pignedoli, C. A.; Fasel, R., Electronic Structure of Atomically Precise Graphene Nanoribbons. *ACS Nano* **2012**, *6* (8), 6930-6935.
23. Hu, Y.; Xie, P.; De Corato, M.; Ruini, A.; Zhao, S.; Meggendorfer, F.; Straasø, L. A.; Rondin, L.; Simon, P.; Li, J.; Finley, J. J.; Hansen, M. R.; Lauret, J.-S.; Molinari, E.; Feng, X.; Barth, J. V.; Palma, C.-A.; Prezzi, D.; Müllen, K.; Narita, A., Bandgap Engineering of Graphene Nanoribbons by Control over Structural Distortion. *J. Am. Chem. Soc.* **2018**, *140* (25), 7803-7809.
24. Perepichka, D. F.; Rosei, F., Extending Polymer Conjugation into the Second Dimension. *Science* **2009**, *323* (5911), 216.
25. Colson, J. W.; Dichtel, W. R., Rationally synthesized two-dimensional polymers. *Nat. Chem.* **2013**, *5* (6), 453-465.
26. Sakamoto, J.; van Heijst, J.; Lukin, O.; Schlüter, A. D., Two-Dimensional Polymers: Just a Dream of Synthetic Chemists? *Angew. Chem. Int. Ed.* **2009**, *48* (6), 1030-1069.

27. Shen, Q.; Gao, H.-Y.; Fuchs, H., Frontiers of on-surface synthesis: From principles to applications. *Nano Today* **2017**, *13*, 77-96.
28. Eichhorn, J.; Nieckarz, D.; Ochs, O.; Samanta, D.; Schmittel, M.; Szabelski, P. J.; Lackinger, M., On-Surface Ullmann Coupling: The Influence of Kinetic Reaction Parameters on the Morphology and Quality of Covalent Networks. *ACS Nano* **2014**, *8* (8), 7880-7889.
29. Fritton, M.; Duncan, D. A.; Deimel, P. S.; Rastgoo-Lahrood, A.; Allegretti, F.; Barth, J. V.; Heckl, W. M.; Björk, J.; Lackinger, M., The Role of Kinetics versus Thermodynamics in Surface-Assisted Ullmann Coupling on Gold and Silver Surfaces. *J. Am. Chem. Soc.* **2019**, *141* (12), 4824-4832.
30. Fritton, M.; Otte, K.; Björk, J.; Biswas, P. K.; Heckl, W. M.; Schmittel, M.; Lackinger, M., The influence of ortho-methyl substitution in organometallic self-assembly – a comparative study on Cu(111) vs. Ag(111). *Chem. Commun.* **2018**, *54* (70), 9745-9748.
31. Blunt, M. O.; Russell, J. C.; Champness, N. R.; Beton, P. H., Templating molecular adsorption using a covalent organic framework. *Chem. Commun.* **2010**, *46* (38), 7157-9.
32. Eichhorn, J.; Strunskus, T.; Rastgoo-Lahrood, A.; Samanta, D.; Schmittel, M.; Lackinger, M., On-surface Ullmann polymerization via intermediate organometallic networks on Ag(111). *Chem. Commun.* **2014**, *50* (57), 7680-2.
33. Klappenberger, F., Two-dimensional functional molecular nanoarchitectures – Complementary investigations with scanning tunneling microscopy and X-ray spectroscopy. *Prog. Surf. Sci.* **2014**, *89* (1), 1-55.
34. Binnig, G.; Rohrer, H.; Gerber, C.; Weibel, E., Surface Studies by Scanning Tunneling Microscopy. *Phys. Rev. Lett.* **1982**, *49* (1), 57-61.
35. Binnig, G.; Quate, C. F.; Gerber, C., Atomic Force Microscope. *Phys. Rev. Lett.* **1986**, *56* (7), 930-933.
36. Voigtlaender, B., *Scanning Probe Microscopy*. Springer-Verlag Heidelberg: 2015.
37. Leggett, G. J., Scanning Probe Microscopy. In *Surface Analysis – The Principal Techniques*, John Wiley & Sons, 2009; pp 479-562.
38. Moresco, F.; Meyer, G.; Rieder, K.-H.; Tang, H.; Gourdon, A.; Joachim, C., Conformational Changes of Single Molecules Induced by Scanning Tunneling Microscopy Manipulation: A Route to Molecular Switching. *Phys. Rev. Lett.* **2001**, *86* (4), 672-675.
39. Moreno-Moreno, M.; Ares, P.; Moreno, C.; Zamora, F.; Gómez-Navarro, C.; Gómez-Herrero, J., AFM Manipulation of Gold Nanowires To Build Electrical Circuits. *Nano Lett.* **2019**, *19* (8), 5459-5468.

40. Neugirg, B. R.; Koebley, S. R.; Schniepp, H. C.; Fery, A., AFM-based mechanical characterization of single nanofibres. *Nanoscale* **2016**, *8* (16), 8414-8426.
41. Baker, S. R.; Banerjee, S.; Bonin, K.; Guthold, M., Determining the mechanical properties of electrospun poly- ϵ -caprolactone (PCL) nanofibers using AFM and a novel fiber anchoring technique. *Mater. Sci. Eng. C* **2016**, *59*, 203-212.
42. Laffrentz, L.; Eberhardt, V.; Dri, C.; Africh, C.; Comelli, G.; Esch, F.; Hecht, S.; Grill, L., Controlling on-surface polymerization by hierarchical and substrate-directed growth. *Nat. Chem.* **2012**, *4* (3), 215-20.
43. Gurney, R. W.; Condon, E. U., Wave Mechanics and Radioactive Disintegration. *Nature* **1928**, *122* (3073), 439-439.
44. Trixler, F., Quantum Tunnelling to the Origin and Evolution of Life. *Curr. Org. Chem.* **2013**, *17* (16), 1758-1770.
45. Wegener, H. A. R.; Lincoln, A. J.; Pao, H. C.; Connell, M. R. O.; Oleksiak, R. E.; Lawrence, H. In *The variable threshold transistor, a new electrically-alterable, non-destructive read-only storage device*, International Electron Devices Meeting, 18-20 Oct. 1967; 1967; pp 70-70.
46. Jönsson, C., Elektroneninterferenzen an mehreren künstlich hergestellten Feinspalten. *Z. Phys.* **1961**, *161* (4), 454-474.
47. Arndt, M.; Nairz, O.; Vos-Andreae, J.; Keller, C.; van der Zouw, G.; Zeilinger, A., Wave-particle duality of C60 molecules. *Nature* **1999**, *401* (6754), 680-682.
48. Fein, Y. Y.; Geyer, P.; Zwick, P.; Kiałka, F.; Pedalino, S.; Mayor, M.; Gerlich, S.; Arndt, M., Quantum superposition of molecules beyond 25 kDa. *Nat. Phys.* **2019**.
49. Chen, C. J., *Introduction to scanning tunnelling microscopy*. Oxford University Press: 1993.
50. Fauster, T.; Hammer, L.; Heinz, K.; Schneider, A., *Oberflächenphysik*. Oldenburg Wissenschaftsverlag, 2013.
51. Wiesendanger, R., *Scanning Probe Microscopy and Spectroscopy*. Cambridge University Press: 1994.
52. Gutzler, R.; Heckl, W. M.; Lackinger, M., Combination of a Knudsen effusion cell with a quartz crystal microbalance: in situ measurement of molecular evaporation rates with a fully functional deposition source. *Rev. Sci. Instrum.* **2010**, *81* (1), 015108.
53. Schmucker, S. W.; Kumar, N.; Abelson, J. R.; Daly, S. R.; Girolami, G. S.; Bischof, M. R.; Jaeger, D. L.; Reidy, R. F.; Gorman, B. P.; Alexander, J.; Ballard, J. B.; Randall, J. N.; Lyding, J. W., Field-directed sputter sharpening for tailored probe materials and atomic-scale lithography. *Nat. Commun.* **2012**, *3*, 935.

54. Barth, J. V.; Brune, H.; Ertl, G.; Behm, R. J., Scanning tunneling microscopy observations on the reconstructed Au(111) surface: Atomic structure, long-range superstructure, rotational domains, and surface defects. *Phys. Rev. B* **1990**, *42* (15), 9307-9318.
55. Wöll, C.; Chiang, S.; Wilson, R. J.; Lippel, P. H., Determination of atom positions at stacking-fault dislocations on Au(111) by scanning tunneling microscopy. *Phys. Rev. B* **1989**, *39* (11), 7988-7991.
56. Ochs, O.; Heckl, W. M.; Lackinger, M., Immersion-scanning-tunneling-microscope for long-term variable-temperature experiments at liquid-solid interfaces. *Rev. Sci. Instrum.* **2018**, *89* (5), 053707.
57. Ludwig, C.; Gompf, B.; Glatz, W.; Petersen, J.; Eisenmenger, W.; Möbus, M.; Zimmermann, U.; Karl, N., Video-STM, LEED and X-ray diffraction investigations of PTCDA on graphite. *Z. Phys. B-Condensed Matter* **1992**, *86* (3), 397-404.
58. Henß, A.-K.; Sakong, S.; Messer, P. K.; Wiechers, J.; Schuster, R.; Lamb, D. C.; Groß, A.; Wintterlin, J., Density fluctuations as door-opener for diffusion on crowded surfaces. *Science* **2019**, *363* (6428), 715-718.
59. Uchida, H.; Huang, D. H.; Yoshinobu, J.; Aono, M., Single-atom manipulation on the Si(111)7 × 7 surface by the scanning tunneling microscope (STM). *Surf. Sci.* **1993**, 287-288, 1056-1061.
60. Moresco, F., Manipulation of large molecules by low-temperature STM: model systems for molecular electronics. *Phys. Rep.* **2004**, *399* (4), 175-225.
61. Lackinger, M., Bottom-Up Fabrication of Two-Dimensional Polymers on Solid Surfaces. In *On-Surface Synthesis*, Gourdon, A., Ed. Springer International Publishing: 2016; pp 199-219.
62. Rastgoo-Lahrood, A.; Björk, J.; Lischka, M.; Eichhorn, J.; Kloft, S.; Fritton, M.; Strunskus, T.; Samanta, D.; Schmittel, M.; Heckl, W. M.; Lackinger, M., Post-Synthetic Decoupling of On-Surface-Synthesized Covalent Nanostructures from Ag(111). *Angew. Chem. Int. Ed.* **2016**, *55* (27), 7650-7654.
63. Rose, M. K.; Borg, A.; Dunphy, J. C.; Mitsui, T.; Ogletree, D. F.; Salmeron, M., Chemisorption of atomic oxygen on Pd(111) studied by STM. *Surf. Sci.* **2004**, *561* (1), 69-78.
64. Lackinger, M.; Griessl, S.; Heckl, W. M.; Hietschold, M.; Flynn, G. W., Self-Assembly of Trimesic Acid at the Liquid-Solid Interface a Study of Solvent-Induced Polymorphism. *Langmuir* **2005**, *21* (11), 4984-4988.
65. Lackinger, M.; Heckl, W. M., Carboxylic Acids: Versatile Building Blocks and Mediators for Two-Dimensional Supramolecular Self-Assembly. *Langmuir* **2009**, *25* (19), 11307-11321.

66. Hüfner, S., *Photoelectron Spectroscopy*. Springer-Verlag Berlin Heidelberg: 2003.
67. Shigemasa, S.; Akira, S., *Photoelectron Spectroscopy*. Springer-Verlag Berlin Heidelberg: 2014.
68. Einstein, A., Über einen die Erzeugung und Verwandlung des Lichtes betreffenden heuristischen Gesichtspunkt. *Ann. Phys.* **1905**, 322 (6), 132-148.
69. Nordling, C.; Sokolowski, E.; Siegbahn, K., Precision Method for Obtaining Absolute Values of Atomic Binding Energies. *Phys. Rev.* **1957**, 105 (5), 1676-1677.
70. Siegbahn, K., Nobel Lecture - Electron Spectroscopy for Atoms, Molecules and Condensed Matter. *Elsevier Publishing Company* **1981**.
71. Allegretti, F.; Deimel, P. Elemental and Chemical Analysis with X-ray Photoelectron Spectroscopy. <https://www.ph.tum.de/academics/org/labs/fopra/docs/userguide-35.en.pdf> (2019/09/28).
72. Ratner, B.; Castner, D., Electron Spectroscopy for Chemical Analysis. In *Surface Analysis – The Principal Techniques*, John Wiley & Sons, 2009; pp 47-112.
73. Briggs, D., *Handbook of X-ray Photoelectron Spectroscopy*. Perkin-Elmer Corp., Physical Electronics Division, 1981.
74. Seah, M. P.; Dench, W. A., Quantitative electron spectroscopy of surfaces: A standard data base for electron inelastic mean free paths in solids. *Surf. Interface Anal.* **1979**, 1 (1), 2-11.
75. Hofmann, S., *Auger- and X-ray Photoelectron Spectroscopy in Materials Science*. Springer-Verlag Berlin Heidelberg, 2013.
76. Hofmann, S.; Sanz, J., Quantitative Erfassung des Ionenstrahleinflusses beim Sputtering von Oxidschichten mit AES und XPS. *Fresenius Z. Anal. Chem.* **1983**, 314, :215-219.
77. Allegretti, F.; Zhang, Y.-Q. Surface Analysis with Temperature Programmed Desorption and Low-Energy Electron Diffraction. <https://www.ph.tum.de/academics/org/labs/fopra/docs/userguide-89.en.pdf> (2019/10/08).
78. Koopmans, T., Über die Zuordnung von Wellenfunktionen und Eigenwerten zu den Einzelnen Elektronen Eines Atoms. *Physica* **1934**, 1 (1), 104-113.
79. Ouellette, R. J.; Rawn, J. D., 1 - Structure of Organic Compounds. In *Principles of Organic Chemistry*, Ouellette, R. J.; Rawn, J. D., Eds. Elsevier: Boston, 2015; pp 1-32.

80. NIST X-ray Photoelectron Spectroscopy Database. <https://srdata.nist.gov/xps/Default.aspx> (2019/09/11).
81. Duke, P., *Synchrotron Radiation Production and Properties*. Oxford University Press, 2008.
82. Willmott, P., *An Introduction to Synchrotron Radiation*. Wiley, 2011.
83. Zontone, F.; Madsen, A.; Konovalov, O., Measuring The Source Brilliance at An Undulator Beamline. *AIP Conference Proceedings* **2010**, *1234* (1), 603-606.
84. Fadley, C. S., Hard X-ray Photoemission: An Overview and Future Perspective. In *Hard X-ray Photoelectron Spectroscopy (HAXPES)*, Woicik, J., Ed. Springer International Publishing, 2016; pp 1-34.
85. Stöhr, J., Principles, Techniques, and Instrumentation of NEXAFS. In *NEXAFS Spectroscopy*, Springer Berlin Heidelberg, 1992; pp 114-161.
86. Duncan, D. A.; Pfisterer, J. H. K.; Deimel, P. S.; Acres, R. G.; Fritton, M.; Feulner, P.; Barth, J. V.; Allegretti, F., Formation of a thermally stable bilayer of coadsorbed intact and deprotonated thymine exploiting the surface corrugation of rutile TiO₂(110). *Phys. Chem. Chem. Phys.* **2016**, *18* (30), 20433-20442.
87. Galeotti, G.; Di Giovannantonio, M.; Lipton-Duffin, J.; Ebrahimi, M.; Tebi, S.; Verdini, A.; Floreano, L.; Fagot-Revurat, Y.; Perepichka, D. F.; Rosei, F.; Contini, G., The role of halogens in on-surface Ullmann polymerization. *Faraday Discuss.* **2017**, *204* (0), 453-469.
88. Di Giovannantonio, M.; Deniz, O.; Urgel, J. I.; Widmer, R.; Diemel, T.; Stolz, S.; Sánchez-Sánchez, C.; Muntwiler, M.; Dumsclaff, T.; Berger, R.; Narita, A.; Feng, X.; Müllen, K.; Ruffieux, P.; Fasel, R., On-Surface Growth Dynamics of Graphene Nanoribbons: The Role of Halogen Functionalization. *ACS Nano* **2018**, *12* (1), 74-81.
89. Deimel, P. S.; Stoiber, K.; Jiang, L.; Lloyd, J. A.; Oh, S. C.; Fischer, S.; Sağlam, Ö.; Schlichting, H.; Papageorgiou, A. C.; Barth, J. V.; Allegretti, F.; Reichert, J., Bisphenol A and Diethylstilbestrol on Cu(111): On-Surface Polymerization Initiated by Hydroxy-Directed Ortho C–H Bond Activation. *J. Phys. Chem. C* **2019**, *123* (2), 1354-1361.
90. Greczynski, G.; Hultman, L., X-ray photoelectron spectroscopy: Towards reliable binding energy referencing. *Prog. Mater. Sci.* **2019**, *107*, 100591.
91. Di Giovannantonio, M.; El Garah, M.; Lipton-Duffin, J.; Meunier, V.; Cardenas, L.; Fagot Revurat, Y.; Cossaro, A.; Verdini, A.; Perepichka, D. F.; Rosei, F.; Contini, G., Insight into Organometallic Intermediate and Its Evolution to Covalent Bonding in Surface-Confined Ullmann Polymerization. *ACS Nano* **2013**, *7* (9), 8190-8198.
92. Di Giovannantonio, M.; Tomellini, M.; Lipton-Duffin, J.; Galeotti, G.; Ebrahimi, M.; Cossaro, A.; Verdini, A.; Kharche, N.; Meunier, V.; Vasseur, G.; Fagot-

- Revurat, Y.; Perepichka, D. F.; Rosei, F.; Contini, G., Mechanistic Picture and Kinetic Analysis of Surface-Confined Ullmann Polymerization. *J. Am. Chem. Soc.* **2016**, *138* (51), 16696-16702.
93. Heister, K.; Zharnikov, M.; Grunze, M.; Johansson, L. S. O.; Ulman, A., Characterization of X-ray Induced Damage in Alkanethiolate Monolayers by High-Resolution Photoelectron Spectroscopy. *Langmuir* **2001**, *17* (1), 8-11.
94. Zharnikov, M.; Grunze, M., Modification of thiol-derived self-assembling monolayers by electron and X-ray irradiation: Scientific and lithographic aspects. *J. Vac. Sci. Technol.* **2002**, *20* (5), 1793-1807.
95. Xing, S.; Zhang, Z.; Fei, X.; Zhao, W.; Zhang, R.; Lin, T.; Zhao, D.; Ju, H.; Xu, H.; Fan, J.; Zhu, J.; Ma, Y.-q.; Shi, Z., Selective on-surface covalent coupling based on metal-organic coordination template. *Nat. Commun.* **2019**, *10* (1), 70.
96. Dong, L.; Liu, P. N.; Lin, N., Surface-Activated Coupling Reactions Confined on a Surface. *Acc. Chem. Res.* **2015**, *48* (10), 2765-2774.
97. Kosynkin, D. V.; Higginbotham, A. L.; Sinitskii, A.; Lomeda, J. R.; Dimiev, A.; Price, B. K.; Tour, J. M., Longitudinal unzipping of carbon nanotubes to form graphene nanoribbons. *Nature* **2009**, *458* (7240), 872-876.
98. Corso, M.; Carbonell-Sanromà, E.; de Oteyza, D. G. In *Bottom-Up Fabrication of Atomically Precise Graphene Nanoribbons*, On-Surface Synthesis II, 2018; de Oteyza, D. G.; Rogero, C., Eds. Springer International Publishing: 2018; pp 113-152.
99. Dunk, P. W.; Kaiser, N. K.; Hendrickson, C. L.; Quinn, J. P.; Ewels, C. P.; Nakanishi, Y.; Sasaki, Y.; Shinohara, H.; Marshall, A. G.; Kroto, H. W., Closed network growth of fullerenes. *Nat. Commun.* **2012**, *3* (1), 855.
100. Irlé, S.; Zheng, G.; Wang, Z.; Morokuma, K., The C60 Formation Puzzle “Solved”: QM/MD Simulations Reveal the Shrinking Hot Giant Road of the Dynamic Fullerene Self-Assembly Mechanism. *J. Phys. Chem. B.* **2006**, *110* (30), 14531-14545.
101. Chuvilin, A.; Kaiser, U.; Bichoutskaia, E.; Besley, N. A.; Khlobystov, A. N., Direct transformation of graphene to fullerene. *Nat. Chem.* **2010**, *2* (6), 450-453.
102. Iqbal, P.; Preece, J. A.; Mendes, P. M., Nanotechnology: The “Top-Down” and “Bottom-Up” Approaches. In *Supramol. Chem.*, 2012.
103. Gourdon, A.; de Oteyza, D. G.; Zhu, J., On-Surface Synthesis. *ChemPhysChem* **2019**, *20* (18), 2249-2250.
104. Martín-Gago, J. A.; Pinaridi, A. L.; Martínez, J. I. In *On-Surface (Cyclo-)Dehydrogenation Reactions: Role of Surface Diffusion*, On-Surface Synthesis, 2016; Gourdon, A., Ed. Springer International Publishing: 2016; pp 43-83.

105. Nacci, C.; Hecht, S.; Grill, L. In *The Emergence of Covalent On-Surface Polymerization*, On-Surface Synthesis, 2016; Gourdon, A., Ed. Springer International Publishing: 2016; pp 1-21.
106. Gottfried, J. M. In *Molecular On-Surface Synthesis: Metal Complexes, Organic Molecules, and Organometallic Compounds*, On-Surface Synthesis, 2016; Gourdon, A., Ed. Springer International Publishing: 2016; pp 131-165.
107. Okawa, Y.; Mandal, S. K.; Makarova, M.; Verveniotes, E.; Aono, M. In *On-Surface Synthesis of Single Conjugated Polymer Chains for Single-Molecule Devices*, On-Surface Synthesis, 2016; Gourdon, A., Ed. Springer International Publishing: 2016; pp 167-179.
108. Moore, J. E., The birth of topological insulators. *Nature* **2010**, *464* (7286), 194-198.
109. Binnig, G.; Rohrer, H.; Gerber, C.; Weibel, E., 7×7 Reconstruction on Si(111) Resolved in Real Space. In *Scanning Tunneling Microscopy*, Neddermeyer, H., Ed. Springer Netherlands: Dordrecht, 1993; pp 36-39.
110. Li, P.; Wang, T.; Yang, Y.; Wang, Y.; Zhang, M.; Xue, Z.; Di, Z., Direct Growth of Unidirectional Graphene Nanoribbons on Vicinal Ge(001). *Phys. Status Solidi RRL*. **2019**, *0* (0), 1900398.
111. Saywell, A.; Schwarz, J.; Hecht, S.; Grill, L., Polymerization on Stepped Surfaces: Alignment of Polymers and Identification of Catalytic Sites. *Angew. Chem. Int. Ed.* **2012**, *51* (21), 5096-5100.
112. Björk, J. In *Formation Mechanisms of Covalent Nanostructures from Density Functional Theory*, On-Surface Synthesis, 2016; Gourdon, A., Ed. Springer International Publishing: 2016; pp 269-287.
113. Bieri, M.; Nguyen, M.-T.; Gröning, O.; Cai, J.; Treier, M.; Aït-Mansour, K.; Ruffieux, P.; Pignedoli, C. A.; Passerone, D.; Kastler, M.; Müllen, K.; Fasel, R., Two-Dimensional Polymer Formation on Surfaces: Insight into the Roles of Precursor Mobility and Reactivity. *J. Am. Chem. Soc.* **2010**, *132* (46), 16669-16676.
114. Björk, J., Thermodynamics of an Electrocyclic Ring-Closure Reaction on Au(111). *J. Phys. Chem. C* **2016**, *120* (38), 21716-21721.
115. Björk, J., Reaction mechanisms for on-surface synthesis of covalent nanostructures. *J. Phys. Condens. Matter* **2016**, *28* (8), 083002.
116. Lischka, M.; Fritton, M.; Eichhorn, J.; Vyas, V. S.; Strunskus, T.; Lotsch, B. V.; Björk, J.; Heckl, W. M.; Lackinger, M., On-Surface Polymerization of 1,6-Dibromo-3,8-diiodopyrene—A Comparative Study on Au(111) Versus Ag(111) by STM, XPS, and NEXAFS. *J. Phys. Chem. C* **2018**, *122* (11), 5967-5977.
117. Ullmann, F., Ueber symmetrische Biphenylderivate. *Justus Liebigs Ann. Chem.* **1904**, *332* (1-2), 38-81.

118. Xi, M.; Bent, B. E., Iodobenzene on Cu(111): formation and coupling of adsorbed phenyl groups. *Surf. Sci.* **1992**, 278 (1), 19-32.
119. Hla, S.-W.; Bartels, L.; Meyer, G.; Rieder, K.-H., Inducing All Steps of a Chemical Reaction with the Scanning Tunneling Microscope Tip: Towards Single Molecule Engineering. *Phys. Rev. Lett.* **2000**, 85 (13), 2777-2780.
120. Palma, C.-A.; Diller, K.; Berger, R.; Welle, A.; Björk, J.; Cabellos, J. L.; Mowbray, D. J.; Papageorgiou, A. C.; Ivleva, N. P.; Matich, S.; Margapoti, E.; Niessner, R.; Menges, B.; Reichert, J.; Feng, X.; Räder, H. J.; Klappenberger, F.; Rubio, A.; Müllen, K.; Barth, J. V., Photoinduced C–C Reactions on Insulators toward Photolithography of Graphene Nanoarchitectures. *J. Am. Chem. Soc.* **2014**, 136 (12), 4651-4658.
121. Zhou, X.; Bebensee, F.; Shen, Q.; Bebensee, R.; Cheng, F.; He, Y.; Su, H.; Chen, W.; Xu, G. Q.; Besenbacher, F.; Linderoth, T. R.; Wu, K., On-surface synthesis approach to preparing one-dimensional organometallic and poly-p-phenylene chains. *Mater. Chem. Front.* **2017**, 1 (1), 119-127.
122. Vasseur, G.; Fagot-Revurat, Y.; Sicot, M.; Kierren, B.; Moreau, L.; Malterre, D.; Cardenas, L.; Galeotti, G.; Lipton-Duffin, J.; Rosei, F.; Di Giovannantonio, M.; Contini, G.; Le Fèvre, P.; Bertran, F.; Liang, L.; Meunier, V.; Perepichka, D. F., Quasi one-dimensional band dispersion and surface metallization in long-range ordered polymeric wires. *Nat. Commun.* **2016**, 7 (1), 10235.
123. Cirera, B.; Zhang, Y.-Q.; Björk, J.; Klyatskaya, S.; Chen, Z.; Ruben, M.; Barth, J. V.; Klappenberger, F., Synthesis of Extended Graphdiyne Wires by Vicinal Surface Templating. *Nano Lett.* **2014**, 14 (4), 1891-1897.
124. Gutzler, R.; Cardenas, L.; Lipton-Duffin, J.; El Garah, M.; Dinca, L. E.; Szakacs, C. E.; Fu, C. Y.; Gallagher, M.; Vondracek, M.; Rybachuk, M.; Perepichka, D. F.; Rosei, F., Ullmann-type coupling of brominated tetrathienoanthracene on copper and silver. *Nanoscale* **2014**, 6 (5), 2660-2668.
125. Russell, J. C.; Blunt, M. O.; Garfitt, J. M.; Scurr, D. J.; Alexander, M.; Champness, N. R.; Beton, P. H., Dimerization of Tri(4-bromophenyl)benzene by Aryl–Aryl Coupling from Solution on a Gold Surface. *J. Am. Chem. Soc.* **2011**, 133 (12), 4220-4223.
126. Eder, G.; Smith, E. F.; Cebula, I.; Heckl, W. M.; Beton, P. H.; Lackinger, M., Solution Preparation of Two-Dimensional Covalently Linked Networks by Polymerization of 1,3,5-Tri(4-iodophenyl)benzene on Au(111). *ACS Nano* **2013**, 7 (4), 3014-3021.
127. Chen, M.; Xiao, J.; Steinrück, H.-P.; Wang, S.; Wang, W.; Lin, N.; Hieringer, W.; Gottfried, J. M., Combined Photoemission and Scanning Tunneling Microscopy Study of the Surface-Assisted Ullmann Coupling Reaction. *J. Phys. Chem. C* **2014**, 118 (13), 6820-6830.

128. Galeotti, G.; De Marchi, F.; Taerum, T.; Besteiro, L. V.; El Garah, M.; Lipton-Duffin, J.; Ebrahimi, M.; Perepichka, D. F.; Rosei, F., Surface-mediated assembly, polymerization and degradation of thiophene-based monomers. *Chem. Sci.* **2019**, *10* (19), 5167-5175.
129. Zhang, H.; Lin, H.; Sun, K.; Chen, L.; Zagranyski, Y.; Aghdassi, N.; Duhm, S.; Li, Q.; Zhong, D.; Li, Y.; Mullen, K.; Fuchs, H.; Chi, L., On-surface synthesis of rylene-type graphene nanoribbons. *J. Am. Chem. Soc.* **2015**, *137* (12), 4022-5.
130. Liu, J.; Chen, Q.; Cai, K.; Li, J.; Li, Y.; Yang, X.; Zhang, Y.; Wang, Y.; Tang, H.; Zhao, D.; Wu, K., Stepwise on-surface dissymmetric reaction to construct binodal organometallic network. *Nat. Commun.* **2019**, *10* (1), 2545.
131. Wang, C.-X.; Chen, J.-L.; Shu, C.-H.; Shi, K.-J.; Liu, P.-N., On-surface synthesis of 2D COFs on Cu(111) via the formation of thermodynamically stable organometallic networks as the template. *Phys. Chem. Chem. Phys.* **2019**, *21* (24), 13222-13229.
132. Wang, W.; Shi, X.; Wang, S.; Van Hove, M. A.; Lin, N., Single-molecule resolution of an organometallic intermediate in a surface-supported Ullmann coupling reaction. *J. Am. Chem. Soc.* **2011**, *133* (34), 13264-7.
133. Eichhorn, J.; Heckl, W. M.; Lackinger, M., On-surface polymerization of 1,4-diethynylbenzene on Cu(111). *Chem. Commun.* **2013**, *49* (28), 2900-2.
134. Pham, T. A.; Song, F.; Nguyen, M.-T.; Li, Z.; Studener, F.; Stöhr, M., Comparing Ullmann Coupling on Noble Metal Surfaces: On-Surface Polymerization of 1,3,6,8-Tetrabromopyrene on Cu(111) and Au(111). *Chem. Eur. J.* **2016**, *22* (17), 5937-5944.
135. Björk, J.; Hanke, F.; Stafstrom, S., Mechanisms of halogen-based covalent self-assembly on metal surfaces. *J. Am. Chem. Soc.* **2013**, *135* (15), 5768-75.
136. Hammer, B.; Norskov, J. K., Why gold is the noblest of all the metals. *Nature* **1995**, *376* (6537), 238-240.
137. Fan, Q.; Wang, C.; Liu, L.; Han, Y.; Zhao, J.; Zhu, J.; Kuttner, J.; Hilt, G.; Gottfried, J. M., Covalent, Organometallic, and Halogen-Bonded Nanomeshes from Tetrabromo-Terphenyl by Surface-Assisted Synthesis on Cu(111). *J. Phys. Chem. C* **2014**, *118* (24), 13018-13025.
138. Rastgoo Lahrood, A.; Björk, J.; Heckl, W. M.; Lackinger, M., 1,3-Diiodobenzene on Cu(111) – an exceptional case of on-surface Ullmann coupling. *Chem. Commun.* **2015**, *51* (68), 13301-13304.
139. Tran, B. V.; Pham, T. A.; Grunst, M.; Kivala, M.; Stöhr, M., Surface-confined [2 + 2] cycloaddition towards one-dimensional polymers featuring cyclobutadiene units. *Nanoscale* **2017**, *9* (46), 18305-18310.

140. Abyazisani, M.; MacLeod, J. M.; Lipton-Duffin, J., Cleaning up after the Party: Removing the Byproducts of On-Surface Ullmann Coupling. *ACS Nano* **2019**, *13* (8), 9270-9278.
141. McMillen, D. F.; Golden, D. M., Hydrocarbon Bond Dissociation Energies. *Annu. Rev. Phys. Chem.* **1982**, *33* (1), 493-532.
142. Blanksby, S. J.; Ellison, G. B., Bond Dissociation Energies of Organic Molecules. *Acc. Chem. Res.* **2003**, *36* (4), 255-263.
143. Merino-Díez, N.; Pérez Paz, A.; Li, J.; Vilas-Varela, M.; Lawrence, J.; Mohammed, M. S. G.; Berdonces-Layunta, A.; Barragán, A.; Pascual, J. I.; Lobo-Checa, J.; Peña, D.; de Oteyza, D. G., Hierarchy in the Halogen Activation During Surface-Promoted Ullmann Coupling. *ChemPhysChem* **2019**, *20* (18), 2305-2310.
144. Steiner, C.; Gebhardt, J.; Ammon, M.; Yang, Z.; Heidenreich, A.; Hammer, N.; Gorling, A.; Kivala, M.; Maier, S., Hierarchical on-surface synthesis and electronic structure of carbonyl-functionalized one- and two-dimensional covalent nanoarchitectures. *Nat. Commun.* **2017**, *8*, 14765.
145. Simonov, K. A.; Vinogradov, N. A.; Vinogradov, A. S.; Generalov, A. V.; Zagrebina, E. M.; Svirskiy, G. I.; Cafolla, A. A.; Carpy, T.; Cunniffe, J. P.; Taketsugu, T.; Lyalin, A.; Mårtensson, N.; Preobrajenski, A. B., From Graphene Nanoribbons on Cu(111) to Nanographene on Cu(110): Critical Role of Substrate Structure in the Bottom-Up Fabrication Strategy. *ACS Nano* **2015**, *9* (9), 8997-9011.
146. Simonov, K. A.; Generalov, A. V.; Vinogradov, A. S.; Svirskiy, G. I.; Cafolla, A. A.; McGuinness, C.; Taketsugu, T.; Lyalin, A.; Mårtensson, N.; Preobrajenski, A. B., Synthesis of armchair graphene nanoribbons from the 10,10'-dibromo-9,9'-bianthracene molecules on Ag(111): the role of organometallic intermediates. *Sci. Rep.* **2018**, *8* (1), 3506.
147. Nolan, P. D.; Wheeler, M. C.; Davis, J. E.; Mullins, C. B., Mechanisms of Initial Dissociative Chemisorption of Oxygen on Transition-Metal Surfaces. *Acc. Chem. Res.* **1998**, *31* (12), 798-804.
148. Lüth, H., *Solid Surfaces, Interfaces and Thin Films*. Springer-Verlag Berlin Heidelberg, 2015.
149. Huber, F.; Berwanger, J.; Polesya, S.; Mankovsky, S.; Ebert, H.; Giessibl, F. J., Chemical bond formation showing a transition from physisorption to chemisorption. *Science* **2019**, *366* (6462), 235-238.
150. Lu, M.-C.; Wang, R.-B.; Yang, A.; Duhm, S., Pentacene on Au(1 1 1), Ag(1 1 1) and Cu(1 1 1): From physisorption to chemisorption. *J. Phys. Condens. Matter* **2016**, *28* (9), 094005.
151. Bronner, C.; Björk, J.; Tegeder, P., Tracking and Removing Br during the On-Surface Synthesis of a Graphene Nanoribbon. *J. Phys. Chem. C* **2015**, *119* (1), 486-493.

152. Perst, H., *Organische Chemie. Grundlagen, Mechanismen, bioorganische Anwendungen*. Von M. A. Fox und J. K. Whitesell. Aus dem Amerikanischen übersetzt von E. Buchholz, F. Glauner, J. Lichtenthäler, S. Müller-Becker und K. Wolf. Spektrum Akademischer Verlag, Heidelberg. 1996; p 2849-2850.
153. Björk, J. In *Kinetic and Thermodynamic Considerations in On-Surface Synthesis*, On-Surface Synthesis II, 2018; de Oteyza, D. G.; Rogero, C., Eds. Springer International Publishing: 2018; pp 19-34.
154. Struchtrup, H., *Thermodynamics and Energy Conversion*. Springer-Verlag Berlin Heidelberg, 2014.
155. Fan, Q.; Wang, T.; Liu, L.; Zhao, J.; Zhu, J.; Gottfried, J. M., Tribromobenzene on Cu(111): Temperature-dependent formation of halogen-bonded, organometallic, and covalent nanostructures. *J. Chem. Phys.* **2015**, *142* (10), 101906.
156. Yang, Z.; Gebhardt, J.; Schaub, T. A.; Sander, T.; Schonamsgruber, J.; Soni, H.; Gorling, A.; Kivala, M.; Maier, S., Two-dimensional delocalized states in organometallic bis-acetylide networks on Ag(111). *Nanoscale* **2018**, *10* (8), 3769-3776.
157. Cardenas, L.; Gutzler, R.; Lipton-Duffin, J.; Fu, C. Y.; Brusso, J. L.; Dinca, L. E.; Vondracak, M.; Fagot-Revurat, Y.; Malterre, D.; Rosei, F.; Perepichka, D. F., Synthesis and electronic structure of a two dimensional pi-conjugated polythiophene. *Chem. Sci.* **2013**, *4* (8), 3263-3268.
158. Saywell, A.; Greń, W.; Franc, G.; Gourdon, A.; Bouju, X.; Grill, L., Manipulating the Conformation of Single Organometallic Chains on Au(111). *J. Phys. Chem. C* **2014**, *118* (3), 1719-1728.
159. Fan, Q.; Wang, T.; Dai, J.; Kuttner, J.; Hilt, G.; Gottfried, J. M.; Zhu, J., On-Surface Pseudo-High-Dilution Synthesis of Macrocycles: Principle and Mechanism. *ACS Nano* **2017**, *11* (5), 5070-5079.
160. Bieri, M.; Blankenburg, S.; Kivala, M.; Pignedoli, C. A.; Ruffieux, P.; Mullen, K.; Fasel, R., Surface-supported 2D heterotriangulene polymers. *Chem. Commun.* **2011**, *47* (37), 10239-41.
161. Gutzler, R.; Walch, H.; Eder, G.; Kloft, S.; Heckl, W. M.; Lackinger, M., Surface mediated synthesis of 2D covalent organic frameworks: 1,3,5-tris(4-bromophenyl)benzene on graphite(001), Cu(111), and Ag(110). *Chem. Commun.* **2009**, *45* (29), 4456-8.
162. Walch, H.; Gutzler, R.; Sirtl, T.; Eder, G.; Lackinger, M., Material- and Orientation-Dependent Reactivity for Heterogeneously Catalyzed Carbon–Bromine Bond Homolysis. *J. Phys. Chem. C* **2010**, *114* (29), 12604-12609.
163. Schlögl, S.; Heckl, W. M.; Lackinger, M., On-surface radical addition of triply iodinated monomers on Au(111)—the influence of monomer size and thermal post-processing. *Surf. Sci.* **2012**, *606* (13-14), 999-1004.

164. In't Veld, M.; Iavicoli, P.; Haq, S.; Amabilino, D. B.; Raval, R., Unique intermolecular reaction of simple porphyrins at a metal surface gives covalent nanostructures. *Chem. Commun.* **2008**, *44* (13), 1536-8.
165. Fan, Q.; Liu, L.; Dai, J.; Wang, T.; Ju, H.; Zhao, J.; Kuttner, J.; Hilt, G.; Gottfried, J. M.; Zhu, J., Surface Adatom Mediated Structural Transformation in Bromoarene Monolayers: Precursor Phases in Surface Ullmann Reaction. *ACS Nano* **2018**, *12* (3), 2267-2274.
166. Meyer, E. M.; Gambarotta, S.; Floriani, C.; Chiesi-Villa, A.; Guastini, C., Polynuclear aryl derivatives of Group 11 metals. Synthesis, solid state-solution structural relationship, and reactivity with phosphines. *Organometallics* **1989**, *8* (4), 1067-1079.
167. Niemeyer, M., σ -Carbon versus π -Arene Interactions in the Solid-State Structures of Trimeric and Dimeric Copper Aryls (CuAr)_n (n = 3, Ar = 2,6-Ph₂C₆H₃; n = 2, Ar = 2,6-Mes₂C₆H₃). *Organometallics* **1998**, *17* (21), 4649-4656.
168. Muñoz-Castro, A., Magnetic Response Properties of Coinage Metal Macrocycles. Insights into the Induced Magnetic Field through the Analysis of [Cu₅(Mes)₅], [Ag₄(Mes)₄], and [Au₅(Mes)₅] (Mes = 2,4,6-Me₃C₆H₂). *J. Phys. Chem. C* **2012**, *116* (32), 17197-17203.
169. Pauly, F.; Viljas, J. K.; Cuevas, J. C.; Schön, G., Density-functional study of tilt-angle and temperature-dependent conductance in biphenyl dithiol single-molecule junctions. *Phys. Rev B* **2008**, *77* (15).
170. Bürker, C.; Ferri, N.; Tkatchenko, A.; Gerlach, A.; Niederhausen, J.; Hosokai, T.; Duhm, S.; Zegenhagen, J.; Koch, N.; Schreiber, F., Exploring the bonding of large hydrocarbons on noble metals: Diindoperylene on Cu(111), Ag(111), and Au(111). *Phys. Rev B* **2013**, *87* (16).
171. Franc, G.; Gourdon, A., Covalent networks through on-surface chemistry in ultra-high vacuum: state-of-the-art and recent developments. *Phys. Chem. Chem. Phys.* **2011**, *13* (32), 14283-92.
172. Lindner, R.; Kühnle, A., On-Surface Reactions. *ChemPhysChem.* **2015**, *16* (8), 1582-1592.
173. Fan, Q.; Gottfried, J. M.; Zhu, J., Surface-Catalyzed C–C Covalent Coupling Strategies toward the Synthesis of Low-Dimensional Carbon-Based Nanostructures. *Acc. Chem. Res.* **2015**, *48* (8), 2484-2494.
174. Zhang, Y.-Q.; Kepčija, N.; Kleinschrodt, M.; Diller, K.; Fischer, S.; Papageorgiou, A. C.; Allegretti, F.; Björk, J.; Klyatskaya, S.; Klappenberger, F.; Ruben, M.; Barth, J. V., Homo-coupling of terminal alkynes on a noble metal surface. *Nat. Commun.* **2012**, *3*, 1286.
175. Gao, H.-Y.; Wagner, H.; Zhong, D.; Franke, J.-H.; Studer, A.; Fuchs, H., Glaser Coupling at Metal Surfaces. *Angew. Chem. Int. Ed.* **2013**, *52* (14), 4024-4028.

176. Li, Q.; Yang, B.; Lin, H.; Aghdassi, N.; Miao, K.; Zhang, J.; Zhang, H.; Li, Y.; Duhm, S.; Fan, J.; Chi, L., Surface-Controlled Mono/Diselective ortho C–H Bond Activation. *J. Am. Chem. Soc.* **2016**, *138* (8), 2809-2814.
177. Wiengarten, A.; Seufert, K.; Auwärter, W.; Eciija, D.; Diller, K.; Allegretti, F.; Bischoff, F.; Fischer, S.; Duncan, D. A.; Papageorgiou, A. C.; Klappenberger, F.; Acres, R. G.; Ngo, T. H.; Barth, J. V., Surface-assisted Dehydrogenative Homocoupling of Porphine Molecules. *J. Am. Chem. Soc.* **2014**, *136* (26), 9346-9354.
178. Zhong, D.; Franke, J.-H.; Podiyanachari, S. K.; Blömker, T.; Zhang, H.; Kehr, G.; Erker, G.; Fuchs, H.; Chi, L., Linear Alkane Polymerization on a Gold Surface. *Science* **2011**, *334* (6053), 213-216.
179. Gao, H.-Y.; Held, P. A.; Knor, M.; Mück-Lichtenfeld, C.; Neugebauer, J.; Studer, A.; Fuchs, H., Decarboxylative Polymerization of 2,6-Naphthalenedicarboxylic Acid at Surfaces. *J. Am. Chem. Soc.* **2014**, *136* (27), 9658-9663.
180. Sun, Q.; Tran, B. V.; Cai, L.; Ma, H.; Yu, X.; Yuan, C.; Stöhr, M.; Xu, W., On-Surface Formation of Cumulene by Dehalogenative Homocoupling of Alkenyl gem-Dibromides. *Angew. Chem. Int. Ed.* **2017**, *129* (40), 12333-12337.
181. Sun, Q.; Cai, L.; Ma, H.; Yuan, C.; Xu, W., Dehalogenative Homocoupling of Terminal Alkynyl Bromides on Au(111): Incorporation of Acetylenic Scaffolding into Surface Nanostructures. *ACS Nano* **2016**, *10* (7), 7023-7030.
182. Kolmer, M.; Zuzak, R.; Ahmad Zebari, A. A.; Godlewski, S.; Prauzner-Bechcicki, J. S.; Piskorz, W.; Zasada, F.; Sojka, Z.; Bléger, D.; Hecht, S.; Szymonski, M., On-surface polymerization on a semiconducting oxide: aryl halide coupling controlled by surface hydroxyl groups on rutile TiO₂(011). *Chem. Commun.* **2015**, *51* (56), 11276-11279.
183. Gutzler, R.; Perepichka, D. F., π -Electron Conjugation in Two Dimensions. *J. Am. Chem. Soc.* **2013**, *135* (44), 16585-16594.
184. Batra, A.; Cvetko, D.; Kladnik, G.; Adak, O.; Cardoso, C.; Ferretti, A.; Prezzi, D.; Molinari, E.; Morgante, A.; Venkataraman, L., Probing the mechanism for graphene nanoribbon formation on gold surfaces through X-ray spectroscopy. *Chem. Sci.* **2014**, *5* (11), 4419-4423.
185. Simonov, K. A.; Vinogradov, N. A.; Vinogradov, A. S.; Generalov, A. V.; Zagrebina, E. M.; Mårtensson, N.; Cafolla, A. A.; Carpy, T.; Cunniffe, J. P.; Preobrajenski, A. B., Effect of Substrate Chemistry on the Bottom-Up Fabrication of Graphene Nanoribbons: Combined Core-Level Spectroscopy and STM Study. *J. Phys. Chem. C* **2014**, *118* (23), 12532-12540.
186. Morchutt, C.; Björk, J.; Krotzky, S.; Gutzler, R.; Kern, K., Covalent coupling via dehalogenation on Ni(111) supported boron nitride and graphene. *Chem. Commun.* **2015**, *51* (12), 2440-3.

187. Wu, Y. J.; Wang, W. H.; Chiang, C. M., Identification of surface allenyl and its transformation into propargyl with C₃H₃Br adsorption by RAIRS on Ag(111). *Langmuir* **2002**, *18* (5), 1449-1452.
188. Migani, A.; Illas, F., A systematic study of the structure and bonding of halogens on low-index transition metal surfaces. *J. Phys. Chem. B* **2006**, *110* (24), 11894-11906.
189. Cirera, B.; Björk, J.; Otero, R.; Gallego, J. M.; Miranda, R.; Ecija, D., Efficient Lanthanide Catalyzed Debromination and Oligomeric Length-Controlled Ullmann Coupling of Aryl Halides. *J. Phys. Chem. C* **2017**, *121* (14), 8033-8041.
190. Hanke, F.; Björk, J., Structure and local reactivity of the Au(111) surface reconstruction. *Phys. Rev. B* **2013**, *87* (23).
191. Henkelman, G.; Jónsson, H., Improved tangent estimate in the nudged elastic band method for finding minimum energy paths and saddle points. *J. Chem. Phys.* **2000**, *113* (22), 9978-9985.
192. Henkelman, G.; Uberuaga, B. P.; Jónsson, H., A climbing image nudged elastic band method for finding saddle points and minimum energy paths. *J. Chem. Phys.* **2000**, *113* (22), 9901-9904.
193. Pham, T. A.; Song, F.; Nguyen, M. T.; Li, Z.; Studener, F.; Stohr, M., Comparing Ullmann Coupling on Noble Metal Surfaces: On-Surface Polymerization of 1,3,6,8-Tetrabromopyrene on Cu(111) and Au(111). *Chem. Eur. J.* **2016**, *22* (17), 5937-44.
194. Fan, Q.; Gottfried, J. M., Topology-Selective Ullmann Coupling on Metal Surfaces by Precursor Design and Adsorbate-Substrate Interaction: Towards the Control over Polymer versus Macrocyclic Formation. *ChemPhysChem* **2019**, *20* (18), 2311-2316.
195. Moreno-López, J. C.; Mowbray, D. J.; Pérez Paz, A.; de Campos Ferreira, R. C.; Ceccatto dos Santos, A.; Ayala, P.; de Siervo, A., Roles of Precursor Conformation and Adatoms in Ullmann Coupling: An Inverted Porphyrin on Cu(111). *Chem. Mater.* **2019**, *31* (8), 3009-3017.
196. Li, H.; Wu, J.; Huang, X.; Yin, Z.; Liu, J.; Zhang, H., A Universal, Rapid Method for Clean Transfer of Nanostructures onto Various Substrates. *ACS Nano* **2014**, *8* (7), 6563-6570.
197. Bennett, P. B.; Pedramrazi, Z.; Madani, A.; Chen, Y.-C.; de Oteyza, D. G.; Chen, C.; Fischer, F. R.; Crommie, M. F.; Bokor, J., Bottom-up graphene nanoribbon field-effect transistors. *Appl. Phys. Lett.* **2013**, *103* (25), 253114.
198. Abbas, A. N.; Liu, G.; Liu, B.; Zhang, L.; Liu, H.; Ohlberg, D.; Wu, W.; Zhou, C., Patterning, Characterization, and Chemical Sensing Applications of Graphene Nanoribbon Arrays Down to 5 nm Using Helium Ion Beam Lithography. *ACS Nano* **2014**, *8* (2), 1538-1546.

199. Tapasztó, L.; Dobrik, G.; Lambin, P.; Biró, L. P., Tailoring the atomic structure of graphene nanoribbons by scanning tunnelling microscope lithography. *Nat. Nanotechnol.* **2008**, *3* (7), 397-401.
200. Jiao, L.; Zhang, L.; Wang, X.; Diankov, G.; Dai, H., Narrow graphene nanoribbons from carbon nanotubes. *Nature* **2009**, *458* (7240), 877-880.
201. Bronner, C.; Marangoni, T.; Rizzo, D. J.; Durr, R. A.; Jørgensen, J. H.; Fischer, F. R.; Crommie, M. F., Iodine versus Bromine Functionalization for Bottom-Up Graphene Nanoribbon Growth: Role of Diffusion. *J. Phys. Chem. C* **2017**, *121* (34), 18490-18495.
202. Narita, A.; Chen, Z.; Chen, Q.; Müllen, K., Solution and on-surface synthesis of structurally defined graphene nanoribbons as a new family of semiconductors. *Chem. Sci.* **2019**, *10* (4), 964-975.
203. Radocea, A.; Sun, T.; Vo, T. H.; Sinitskii, A.; Aluru, N. R.; Lyding, J. W., Solution-Synthesized Chevron Graphene Nanoribbons Exfoliated onto H:Si(100). *Nano Lett.* **2017**, *17* (1), 170-178.
204. Yang, X.; Dou, X.; Rouhanipour, A.; Zhi, L.; Räder, H. J.; Müllen, K., Two-Dimensional Graphene Nanoribbons. *J. Am. Chem. Soc.* **2008**, *130* (13), 4216-4217.
205. Narita, A.; Feng, X.; Hernandez, Y.; Jensen, S. A.; Bonn, M.; Yang, H.; Verzhbitskiy, I. A.; Casiraghi, C.; Hansen, M. R.; Koch, A. H. R.; Fytas, G.; Ivasenko, O.; Li, B.; Mali, K. S.; Balandina, T.; Mahesh, S.; De Feyter, S.; Müllen, K., Synthesis of structurally well-defined and liquid-phase-processable graphene nanoribbons. *Nat. Chem.* **2014**, *6* (2), 126-132.
206. Yang, W.; Lucotti, A.; Tommasini, M.; Chalifoux, W. A., Bottom-Up Synthesis of Soluble and Narrow Graphene Nanoribbons Using Alkyne Benzannulations. *J. Am. Chem. Soc.* **2016**, *138* (29), 9137-9144.
207. Han, D.; Fan, Q.; Dai, J.; Wang, T.; Huang, J.; Xu, Q.; Ding, H.; Hu, J.; Feng, L.; Zhang, W.; Zeng, Z.; Gottfried, J. M.; Zhu, J., On-Surface Synthesis of Armchair-Edged Graphene Nanoribbons with Zigzag Topology. *J. Phys. Chem. C* **2020**.
208. Yu, X.; Cai, L.; Bao, M.; Sun, Q.; Ma, H.; Yuan, C.; Xu, W., On-surface synthesis of graphyne nanowires through stepwise reactions. *Chem. Commun.* **2020**, *56* (11), 1685-1688.
209. Teeter, J. D.; Costa, P. S.; Mehdi Pour, M.; Miller, D. P.; Zurek, E.; Enders, A.; Sinitskii, A., Epitaxial growth of aligned atomically precise chevron graphene nanoribbons on Cu(111). *Chem. Commun.* **2017**, *53* (60), 8463-8466.
210. Bushell, J.; Carley, A. F.; Coughlin, M.; Davies, P. R.; Edwards, D.; Morgan, D. J.; Parsons, M., The Reactive Chemisorption of Alkyl Iodides at Cu(110) and Ag(111) Surfaces: A Combined STM and XPS Study. *J. Phys. Chem. B* **2005**, *109* (19), 9556-9566.

211. Berndt, W., Iodine Adsorption on Silver (111) Studied by LEED. *Jpn. J. Appl. Phys.* **1974**, *13* (S2), 653.
212. Dou, R.-F.; Ma, X.-C.; Xi, L.; Yip, H. L.; Wong, K. Y.; Lau, W. M.; Jia, J.-F.; Xue, Q.-K.; Yang, W.-S.; Ma, H.; Jen, A. K. Y., Self-Assembled Monolayers of Aromatic Thiols Stabilized by Parallel-Displaced π - π Stacking Interactions. *Langmuir* **2006**, *22* (7), 3049-3056.
213. Moreno, C.; Vilas-Varela, M.; Kretz, B.; Garcia-Lekue, A.; Costache, M. V.; Paradinas, M.; Panighel, M.; Ceballos, G.; Valenzuela, S. O.; Peña, D.; Mugarza, A., Bottom-up synthesis of multifunctional nanoporous graphene. *Science* **2018**, *360* (6385), 199.
214. Haiss, W.; Sass, J. K.; Gao, X.; Weaver, M. J., Iodine adlayer structures on Au(111) as discerned by atomic-resolution scanning tunnelling microscopy: relation to iodide electrochemical adsorption. *Surf. Sci.* **1992**, *274*, L593-L598.
215. Gao, X.; Weaver, M. J., Probing redox-induced molecular transformations by atomic-resolution scanning tunneling microscopy: iodide adsorption and electrooxidation on gold(111) in aqueous solution. *J. Am. Chem. Soc.* **1992**, *114* (22), 8544-8551.
216. Lattice Constants of the elements. <https://periodictable.com/Properties/A/LatticeConstants.st.log.html> (2019/10/24).
217. Sun, Q.; Zhang, C.; Kong, H.; Tan, Q.; Xu, W., On-surface aryl-aryl coupling via selective C-H activation. *Chem. Commun.* **2014**, *50* (80), 11825-11828.
218. Otero, G.; Biddau, G.; Sánchez-Sánchez, C.; Caillard, R.; López, M. F.; Rogero, C.; Palomares, F. J.; Cabello, N.; Basanta, M. A.; Ortega, J.; Méndez, J.; Echavarren, A. M.; Pérez, R.; Gómez-Lor, B.; Martín-Gago, J. A., Fullerenes from aromatic precursors by surface-catalysed cyclodehydrogenation. *Nature* **2008**, *454* (7206), 865-868.
219. Frisch, M. J.; Trucks, G. W.; Schlegel, H. B.; Scuseria, G. E.; Robb, M. A.; Cheeseman, J. R.; Scalmani, G.; Barone, V.; Petersson, G. A.; Nakatsuji, H.; Li, X.; Caricato, M.; Marenich, A. V.; Bloino, J.; Janesko, B. G.; Gomperts, R.; Mennucci, B.; Hratchian, H. P.; Ortiz, J. V.; Izmaylov, A. F.; Sonnenberg, J. L.; Williams, F.; Ding, F.; Lipparini, F.; Egidi, F.; Goings, J.; Peng, B.; Petrone, A.; Henderson, T.; Ranasinghe, D.; Zakrzewski, V. G.; Gao, J.; Rega, N.; Zheng, G.; Liang, W.; Hada, M.; Ehara, M.; Toyota, K.; Fukuda, R.; Hasegawa, J.; Ishida, M.; Nakajima, T.; Honda, Y.; Kitao, O.; Nakai, H.; Vreven, T.; Throssell, K.; Montgomery Jr., J. A.; Peralta, J. E.; Ogliaro, F.; Bearpark, M. J.; Heyd, J. J.; Brothers, E. N.; Kudin, K. N.; Staroverov, V. N.; Keith, T. A.; Kobayashi, R.; Normand, J.; Raghavachari, K.; Rendell, A. P.; Burant, J. C.; Iyengar, S. S.; Tomasi, J.; Cossi, M.; Millam, J. M.; Klene, M.; Adamo, C.; Cammi, R.; Ochterski, J. W.; Martin, R. L.; Morokuma, K.; Farkas, O.; Foresman, J. B.; Fox, D. J. *Gaussian 16 Rev. B.01*, Wallingford, CT, 2016.
220. Kresse, G.; Furthmüller, J., Efficient iterative schemes for ab initio total-energy calculations using a plane-wave basis set. *Phys. Rev B* **1996**, *54* (16), 11169-11186.

221. Dion, M.; Rydberg, H.; Schroder, E.; Langreth, D. C.; Lundqvist, B. I., van der Waals density functional for general geometries. *Phys. Rev. Lett.* **2004**, *92* (24), 246401.
222. Hamada, I., van der Waals density functional made accurate. *Phys. Rev B* **2014**, *89* (12).
223. Björk, J.; Stafstrom, S., Adsorption of large hydrocarbons on coinage metals: a van der Waals density functional study. *Chemphyschem* **2014**, *15* (13), 2851-8.
224. Liu, X.; Xie, Y.; Zhao, H.; Cai, X.; Wu, H.; Su, S.-J.; Cao, Y., Star-shaped isoindigo-based small molecules as potential non-fullerene acceptors in bulk heterojunction solar cells. *New J. Chem.* **2015**, *39* (11), 8771-8779.
225. Blöchl, P. E., Projector augmented-wave method. *Phys. Rev. B* **1994**, *50* (24), 17953-17979.
226. Kästner, J.; Sherwood, P., Superlinearly converging dimer method for transition state search. *J. Chem. Phys.* **2008**, *128* (1), 014106.

Publications

1. The influence of *ortho*-methyl substitution in organometallic self-assembly – a comparative study on Cu(111) vs. Ag(111)
M. Fritton, K. Otte, J. Björk, P. K. Biswas, W. M. Heckl, M. Schmittel, M. Lackinger, *Chem. Commun.*, 54, 9745-9748, 2018.
2. The role of kinetics versus thermodynamics in surface-assisted Ullmann coupling on gold and silver surfaces
M. Fritton, D. A. Duncan, P. S. Deimel, A. Rastgoo-Lahrood, F. Allegretti, J. V. Barth, W. M. Heckl, J. Björk, M. Lackinger, *J. Am. Chem. Soc.*, 141 (12), 4824-4832, 2019.
3. Post-synthetic decoupling of on-surface-synthesized covalent nanostructures from Ag(111)
A. Rastgoo-Lahrood, J. Björk, M. Lischka, J. Eichhorn, S. Kloft, **M. Fritton**, T. Strunskus, D. Samanta, M. Schmittel, W. M. Heckl, M. Lackinger, *Angew. Chem. Int. Ed.*, 55 (27), 7650-7654, 2016.
4. On-surface polymerization of 1,8-Dibromo-3,6-diiodopyrene – a comparative study on Au(111) versus Ag(111) by STM, XPS, and NEXAFS
M. Lischka, **M. Fritton**, J. Eichhorn, V. S. Vyas, T. Strunskus, B. V. Lotsch, J. Björk, W. M. Heckl, and M. Lackinger, *J. Chem. Phys. C*, 122, 5967–5977, 2018.
5. Competitive metal coordination of hexaaminotriphenylene on Cu(111) by intrinsic copper versus extrinsic nickel adatoms
M. Lischka, R. Dong, M. Wang, **M. Fritton**, L. Grossmann, N. Martsinovich, W. M. Heckl, X. Feng, and M. Lackinger, *Chem. Eur. J.*, 25, 1975, 2019.
6. Formation of a thermally stable bilayer of coadsorbed intact and deprotonated thymine exploiting the surface corrugation of rutile TiO₂(110)
D. A. Duncan, J. H. K. Pfisterer, P. S. Deimel, R. G. Acres, **M. Fritton**, P. Feulner, J. V. Barth, and F. Allegretti, *Phys. Chem. Chem. Phys.*, 18, 20433-20442, 2016.

Curriculum Vitae

Massimo Enrico Fritton

10/2014–12/2019	Doktorand, Physik Technische Universität München (TUM) Deutsches Museum
10/2011–04/2014	Masterstudium, Geomaterialien und Geochemie Ludwig-Maximilian-Universität (LMU)
10/2007–10/2011	Bachelorstudium, Geowissenschaften Technische Universität München (TUM)
09/2006–06/2007	Zivildienst Falken-Freizeitstättenverein München e.V.
07/2006	Allgemeine Hochschulreife Rupprecht-Gymnasium München

Acknowledgments

An dieser Stelle möchte ich allen beteiligten Personen, die zum Gelingen meiner Doktorarbeit beigetragen haben, meinen großen Dank aussprechen. Ohne Eure Hilfe wäre die Anfertigung der Dissertation nicht möglich gewesen

Vor allem möchte ich mich bei meinem Doktorvater Prof. Dr. Markus Lackinger bedanken, der mir die Möglichkeit gegeben hat, diese Doktorarbeit in seiner Arbeitsgruppe anzufertigen. Während der gesamten Zeit genoss ich eine ausgezeichnete Betreuung, von der Umsetzung der Projekte im Labor und deren Interpretation bis hin zur Gliederung und Formulierung der Publikationen. Auch Prof. Dr. Wolfgang Heckl gilt mein Dank für die Möglichkeit, an der Technischen Universität München in Physik zu promovieren.

Besonders danken möchte ich Atena, die mir die grundlegenden Abläufe in unseren Laboren gezeigt hat. Weiter möchte ich mich bei Stephan und Olli für die Entwicklung und Konstruktion zuverlässiger Rastertunnelmikroskope bedanken. Bei dieser Gelegenheit will ich außerdem Olli meinen herzlichen Dank äußern, der sich bei technischen Fragen jederzeit extrem hilfsbereit gezeigt hat. Auch Lukas, mein Laborpartner, war mir ein sehr hilfreicher und unterstützender Kollege, danke für die zahlreichen wissenschaftlichen und gesellschaftlichen Diskussionen. Ferner möchte ich Matthias meinen Dank aussprechen, der mir die Abläufe an seiner UHV-Anlage sehr strukturiert erklärt hat. Nicht zuletzt möchte ich mich bei der gesamten Arbeitsgruppe für den produktiven wissenschaftlichen Austausch und die gute Arbeitsatmosphäre bedanken.

Auch Günter und der gesamten feinmechanischen Werkstatt der LMU gilt mein Dank für die Anfertigung verschiedenster Bauteile.

Meinen Eltern, meiner Schwester und meiner gesamten Familie danke ich für ihre Unterstützung während der Arbeit an dieser Dissertation. Zum Schluss will ich mich noch bei meiner Freundin und Tochter bedanken, die mir besonders in der letzten Zeit viel Freude und einen entspannten Ausgleich zur wissenschaftlichen Arbeit beschert haben.